Departamento de Biología Molecular
Facultad de Ciencias
Universidad Autónoma de Madrid

AXON INITIAL SEGMENT CYTOSKELETON, COMPOSITION AND PLASTICITY REGULATION BY FORMINS

Tesis Doctoral

Wei Zhang

2019

Trabajo dirigido por el Dr. Juan José Garrido Jurado

Instituto Cajal
Departamento de Biología Molecular
Facultad de Ciencias
Universidad Autónoma de Madrid

Memoria de Investigación presentada por

Wei Zhang

Para optar al grado de

Doctor en Biología Molecular por la Universidad Autónoma de Madrid.

Trabajo dirigido por el Dr. Juan José Garrido Jurado (Instituto Cajal-CSIC).

Vº.Bº del director de Tesis,

Juan José Garrido Jurado

El doctorando,

Wei Zhang

Instituto Cajal
Departamento de Biología Molecular
Facultad de Ciencias
Universidad Autónoma de Madrid

Dr. Juan José Garrido Jurado, Científico Titular del Instituto Cajal (CSIC)

CERTIFICA:

Que la presente tesis doctoral, que lleva por título “Axon initial segment cytoskeleton, composition and plasticity regulation by formins” que presenta Wei Zhang para optar al grado de Doctor por la Universidad Autónoma de Madrid ha sido realizada bajo mi dirección en el Instituto Cajal (CSIC) y que cumple todos los requisitos paqra su defensa pública, reuniendo, a mi juicio el suficiente rigor científico para optar al grado de doctor.

Madrid, a 23 de Septiembre de 2019

Fdo: Dr. Juan José Garrido Jurado

Acknowledgements

In these 4 years in Spain, I gained more knowledge on neuroscience and a precious abroad experience. Here, I saw the cultural diversity and another way of life-style. Importantly, I found lots of nice people. I appreciate all the people who once helped me and supported me along this travel to arrive to this point.

I thank Dr. Juan José Garrido Jurado, my director of PhD study. Thanks for his supervision on my research work, his understanding of our discussions about research and continuous support on my work. Without his coaching, I could not have reached this step. From him, I got a better understanding of how to properly organize scientific projects and focus on my research direction.

I thank Dr. Aixa Morales and Prof. María José Benítez for their kind help and advices in daily life. I especially thank Dr. Pablo Méndez García and Dr. Jose Mª Frade López and for their help on my research work.

I would like to thank our excellent technicians Maria Ciorraga and Diana Retana for their assistance on my research. And of course, I do not forget the support of all technical services at Cajal Institute, specially the people of confocal and imaging unit, Carmen and Belén.

I thank my family, in particular, my wife Lingling Li who has been with me through this challengeable period and always encourages me to pursue my scientific dreams. In the rest of my life, we will continue to share joys and tears and built our bright future. Besides, I got lots of silent supports from my parents, parents-in-law, my brother, brothers-in-law, my sister, sister-in-law. It is their understanding and encouragement that promotes me to make progress toward my ideal.

I thank my friends. In particular, Dr. Shaoliang Zhang, Yuwen Chen, Chaska C. Walton, Yu Wang, Ting Wang and Da Guang. Thanks for making my life colorful in Madrid.

This is the end of my PhD study, while it is also the starting point of my scientific career. And I do believe that tomorrow will be better.

“If A is a success in life, then A equals x plus y plus z.

Work is x; y is play; and z is keeping your mouth shut.”

—Albert Einstein

INDEX

Abstract 1

Presentación 3

Abbreviations 6

Introduction 9

1. The Axon Initial Segment (AIS) 10
    1.1. The AIS structure 11
        1.1.1. AnkyrinG: the key AIS organizer 11
        1.1.2. Other AIS enriched proteins 12
            1.1.2.1. Voltage-gated ion channels 12
            1.1.2.2. Cell adhesion molecules 13
        1.1.3. AIS cytoskeleton 14
            1.1.3.1. Actin cytoskeleton in the AIS 14
            1.1.3.2. Microtubules cytoskeleton in the AIS 16
    1.2. AIS development and maturation 18
2. AIS plasticity and regulation 19
    2.1. AIS plasticity during neuronal development 19
    2.2. Activity dependent AIS plasticity 20
    2.3. Potential mechanisms for AIS plasticity 21
3. The AIS in neurological disorders 22
4. Formin homology proteins (Formins) 23
    4.1. Mammalian formin family members and protein domains 24
    4.2. Physiological functions of formins 25
        4.2.1. Actin filament nucleation and elongation 25
        4.2.2. Microtubule binding and stabilization 27
        4.2.3. Formins regulation 28
        4.2.4. Formins in neurons and neurological disorders 28

Objectives 30

Materials and Methods 32

1. Animals 33
2. Reagents 33
    2.1. Chemicals 33
    2.2. Antibodies 34
    2.3. Oligonucleotides and recombinant DNA 35
3. Hippocampal Cultures 35
4. Neuronal transfection 37
5. Immunocytochemistry 38

6. Detergent extraction of hippocampal neurons 38
7. Fluorescence recovery after photobleaching (FRAP) 39
8. Immunohistochemistry 40
9. AIS length and fluorescence intensity measurements 41
10. Axon and dendrites morphology analysis 42
11. Electrophysiology 42
12. Statistical analysis 43

Results 44

1. Formins inhibition disrupts AIS integrity 45
2. Formins inhibition alters AIS actin and microtubules cytoskeleton 50
3. Blocking formins activity results in loss of neuronal polarity and alterations in axonal trafficking 53
4. mDia1 localizes at the AIS 56
5. mDia1 is necessary for AIS assembly 57
6. mDia1 is required for AIS maintenance and plasticity in vitro 63
7. mDia1 activity is essential for AIS structural plasticity in vivo 69
8. Deciphering mDia1 mediated AIS regulation pathway 72
    8.1. Rho is not the upstream regulator of mDia1 for AIS regulation 72
    8.2. mDia1 mediated AIS components loss is independent of calpain signaling 74
    8.3. mDia1 mediated AIS integrity is related with F-actin dynamics regulation 75
    8.4. Microtubule properties contribute to AIS components loss caused by mDia1 inhibition or suppression 77
    8.5. mDia1 inactivity induced ankyrinG loss can be rescued by exogenous EB1 expression or dynein inhibition 80
9. Formins inhibition decreases intrinsic excitability 82

Discussion 84

1. Formins activity maintains AIS structure 85
2. AIS cytoskeleton and formins 88
3. mDia1 role on AIS regulation 90
4. Formins and AIS plasticity 92
5. Potential mechanisms for mDia1 mediated AIS regulation 93

Conclusions 98

Conclusiones 100

Bibliography 102

Annexes: Research Articles 115

FIGURES INDEX

Introduction

Figure I1. Developmental stages of cultured hippocampal neurons 10
Figure I2. Axon Initial Segment (AIS) structure and compositions 11
Figure I3. Domain organization of formin subfamilies and the regulation and function of DRFs 24

Materials and Methods

Table M1. Drugs used for pharmacological experiments 33
Table M2. Antibodies used for immunofluorescence 34
Figure M1. Three steps for preparing hippocampal neuronal cultures 36

Results

Figure R1. Formins inhibition decreases AIS components in hippocampal neurons 46
Figure R2. Formins inhibition reduces ankyrinG and βIV-spectrin intensity in hippocampal neurons detergent extracted at 37 ºC 47
Figure R3. Formins inhibition has long-term effects on ankyrinG decrease 48
Figure R4. Formins inhibition decreases ankyrinG-GFP accumulation in the AIS 49
Figure R5. Formins inhibition decreases F-actin intensity in the AIS 51
Figure R6. Formins inhibition reduces tubulin acetylation in the AIS 52
Figure R7. Formins inhibition disrupts neuronal polarity 54
Figure R8. The absence of formins activity alters the distribution of KIF5C along the neuron 55
Figure R9. mDia1 localizes at the AIS 57
Figure R10. mDia1 location in neuronal early developmental stages 58
Figure R11. Identification of efficient mDia1 interference shRNAs 58
Figure R12. Suppression of mDia1 by interference shRNAs has no effects on axon and dendrites growth in hippocampal neurons 59
Figure R13. Expression of a constitutively active form of mDia1 decreases axon specification and axon growth 60
Figure R14. Suppression of mDia1 by interference shRNAs decreases AIS proteins accumulation 61
Figure R15. Formins inhibition does not further decrease ankyrinG intensity in neurons with decreased mDia1 expression 63
Figure R16. mDia1 interference shRNA or constitutively active mDia1 expression in hippocampal neurons after AIS development decreases ankyrinG intensity 64
Figure R17. mDia1 suppression or inhibition shortens AIS length 65
Figure R18. AnkyrinG decrease caused by mDia1 inhibition or suppression is partially due to AIS length shortening 68
Figure R19. Formins inhibition decreases ankyrinG intensity and shortens AIS length in brain slices of cerebral cortex 70
Figure R20. Formins inhibition decreases ankyrinG intensity of hippocampal AISs in brain

slices 72
Figure R21. RhoA is not the upstream regulator of mDia1 for ankyrinG accumulation..... 73
Figure R22. Calpain inhibition does not avoid ankyrinG decrease induced by formins inhibition..... 74
Figure R23. Disruption of actin dynamics leads to ankyrinG reduction 76
Figure R24. HDAC6 inhibition or suppression rescues ankyrinG loss in hippocampal neurons after mDia1 inhibition or knockdown..... 78
Figure R25. Over-expression of EB1 rescues ankyrinG loss induced by mDia1 inhibition in hippocampal neurons..... 80
Figure R26. Dynein inhibition partially rescues ankyrinG loss in mDia1 inhibited hippocampal neurons..... 82
Figure R27. Formins inhibition decreases neuronal intrinsic excitability in hippocampal neurons 83

Abstract

The axon initial segment (AIS) is a specialized compartment crucial for generating action potentials and maintaining neuronal polarity. An integrated structure composed of a high concentration of voltage gated ion channels, a specific cytoskeleton architecture, as well as, scaffold proteins like ankyrinG and βIV-spectrin, contributes to these functions. Recent studies have revealed that AIS is dynamically regulated in molecular composition, length and location in response to neuronal activity alterations both in physiological and pathological conditions. Some mechanisms acting on AIS plasticity have been uncovered lately, which include calcium dependent calpain or calcineurin modulation, as well as, modifications of cytoskeleton proteins. However, it is not clear how AIS is regulated in its structure and functions, and which proteins may regulate AIS cytoskeleton. In this study, using pharmacological methods we found that formins modulate AIS maintenance in vitro and in vivo. Formins are a group of proteins involved in cytoskeleton regulation. Currently, 15 formin members are identified in mammals. In neurons, different formins show differential distribution and regulation mechanisms. Only a few studies have revealed that formin members play different roles in neurons, such as axonal and dendritic development, spine morphogenesis and synapse modulation. Regarding brain diseases, some mutations in formin proteins were found in patients suffering mental retardation, Alzheimer's disease, seizures and schizophrenia, suggesting that formins may play some important roles on neuronal activity. Our study demonstrates that formins inhibition modifies AIS cytoskeleton properties and their associated structural proteins and function. Interestingly, we found that mDia1 is at least one major formin family member that functions both in the AIS assembly and maintenance. mDia1 inhibition or suppression affects AIS length and structural and functional AIS proteins. Consistently, after blocking mDia1 activity, the action potential is affected, as well as, axonal polarity maintenance. These effects are due to the deficiency of AIS structural stability and alterations in axonal protein traffic, which can be compensated through expression or modulation of microtubules and microfilaments regulators. Taken together, our results indicate a new AIS regulator involved in AIS formation, maintenance and plasticity, which provides new insights on AIS regulation mechanisms. Further experiments will be necessary to completely understand mDia1 regulation at the AIS, and its implications in brain activity related diseases.

Presentación

El segmento inicial del axón (AIS) es un compartimento especializado crucial para generar potenciales de acción y mantener la polaridad neuronal. Una estructura integrada compuesta por una alta concentración de canales iónicos activados por voltaje, una arquitectura específica del citoesqueleto, así como proteínas de andamio como ankyrinG y βIV-spectrin, contribuyen a estas funciones. Estudios recientes han revelado que el AIS está regulado dinámicamente en la composición molecular, la longitud y la ubicación en respuesta a las alteraciones de la actividad neuronal tanto en condiciones fisiológicas como patológicas. Recientemente se han descubierto algunos mecanismos que actúan sobre la plasticidad AIS, que incluyen la modulación de la calpaína o la calcineurina dependientes de calcio, así como las modificaciones de las proteínas del citoesqueleto. Sin embargo, no está claro cómo AIS está regulado en su estructura y funciones, y qué proteínas pueden regular el citoesqueleto AIS. Este citoesqueleto, esencial para mantener la integridad del AIS, está compuesto por microtúbulos, que incluyen modificaciones postraduccionales de tubulina, y micofilamentos con diferentes tipos de estructuras. En este estudio, utilizando métodos farmacológicos, encontramos que las forminas modulan el mantenimiento de AIS in vitro e in vivo. Las forminas son un grupo de proteínas involucradas en la regulación del citoesqueleto, tanto de microtúbulos como de actina, y por tanto, candidatos potenciales para la regulación del AIS. Actualmente, se han identificado 15 miembros de formina en mamíferos. En las neuronas, las diferentes forminas muestran mecanismos diferenciales de distribución y regulación. Solo unos pocos estudios han revelado que los miembros de formina juegan diferentes roles en las neuronas, como el desarrollo axonal y dendrítico, la morfogénesis de las espinas dendríticas y la modulación de las sinapsis. Con respecto a las enfermedades cerebrales, se han encontrado algunas mutaciones en las forminas en pacientes que sufren retraso mental, enfermedad de Alzheimer, convulsiones y esquizofrenia, lo que sugiere que las forminas pueden desempeñar algunas funciones importantes en la actividad neuronal. Nuestro estudio demuestra que la inhibición de las forminas modifica las propiedades del citoesqueleto AIS y sus funciones y proteínas estructurales asociadas. Curiosamente, descubrimos que mDia1 es al menos un miembro importante de la familia que funciona tanto en el ensamblaje como en el mantenimiento del AIS. La inhibición o supresión de mDia1 afecta la longitud del AIS y las proteínas AIS estructurales y funcionales.

Consistentemente, después de bloquear la actividad de mDia1, el potencial de acción se ve afectado, así como el mantenimiento de la polaridad axonal. Estos efectos se deben a la deficiencia de la estabilidad estructural AIS y las alteraciones en el tráfico de proteínas axonales, que se pueden compensar mediante la expresión o la modulación de microtúbulos y reguladores de microfilamentos. Tomados en conjunto, nuestros resultados indican un nuevo regulador del AIS involucrado en la formación, mantenimiento y plasticidad del AIS, lo que proporciona nuevas ideas sobre los mecanismos de regulación del AIS. Se necesitarán más experimentos para comprender completamente la regulación mDia1 en el AIS y sus implicaciones en las enfermedades relacionadas con la actividad cerebral.

Abbreviations

ADAM22: a disintegrin and metalloproteinase domain-containing protein 22

AIS: axon initial segment

ALS: amyotrophic lateral sclerosis

APC: adenomatous polyposis coli

AraC: 1-β-D-arabinofuranosylcytosine

Arp2/3: actin related protein 2/ 3 complex

ATP: adenosine triphosphate

CA: constitutively active

CAMs: cell adhesion molecules

Caspr2: contactin-associated protein-like 2

CK2α: casein kinase 2α

CLASPs: CLIP-associated proteins

CLIPs: cytoplasmic linker proteins

CMF: correct mean fluorescence

CO: cisternal organelle

C-terminal: carboxy terminal

CTF: correct total fluorescence

DAAM: dishevelled associated activator of morphogenesis

DAD: diaphanous autoregulatory domain

Dia/ DIAPH: diaphanous related formins

DID: diaphanous inhibitory domain

DN: dominant negative

DRFs: 4 subclasses of formins, including Dia, DAAM, FMNL, FHOD

EB: microtubule plus-end binding protein

ECM: extracellular matrix molecules

EDTA: ethylenediaminetetraacetic acid

EGTA: ethylene glycol-bis(β-aminoethyl ether)-N, N, N ′, N ′-tetraacetic acid

F-actin: filamentous actin

FH1: formin homology 1 domain

FH2: formin homology 2 domain

INF1: inverted formin 1

FHOD: formin homology 2 domain containing

FMN: formin

FMNL: formin-like subtypes

Formins: formin homology proteins

FRAP: fluorescence recovery after photobleaching

FSI: formin-spire interaction domain

GBD: GTPase-binding domain

GRID2IP: grid2 interacting protein

GSK3: glycogen synthase kinase 3

HBSS: Ca^{2+}/Mg^{2+} free Hank's buffered salt solution

HDAC6: histone deacetylase 6

IC: immunocytochemistry

IH: immunohistochemistry

IP3R1: inositol 1,4,5-triphosphate receptor 1

KCC2: K^{+}/Cl^{-} cotransporter 2

L1CAM: L1 cell adhesion molecule protein

LGI1: leucine-rich glioma inactivated protein 1

Lis1: lissencephaly-1 homolog

LTD: long-term depression

MAP: microtubule-associated protein

MAP2: microtubule-associated protein 2

MEM: minimum essential medium

N/A: not applicable

NDEL1: nuclear distribution protein nudE-like 1

NF186: neurofascin 186

NrCAM: neuron-glia-related cell-adhesion molecule

N-terminal: amino terminal

OCD: obsessive-compulsive disorder

PanNaCh: pan voltage gated sodium channels

PB: phosphate buffer

PBS: phosphate buffered saline

PDZ: PSD95-Dlg1-Zo-1 domain

PFA: paraformaldehyde

pMLC: phosphorylated myosin light chain

PSD: postsynaptic density protein

PTSD: post-traumatic stress disorder

ROCK: Rho-associated kinase

RT: room temperature

shRNA: short hairpin RNA

SNPs: single nucleotide polymorphisms

STORM: stochastic optical reconstruction microscopy

Tag-1: transient axonal glycoprotein-1

+TIPs: microtubule plus-end-tracking proteins

TRIM46: tripartite motif-containing protein 46

WH2: Wiskott-Aldrich homology 2

WHIF1: WH2 domain-containing formin 1

WT: wild type

Introduction

Neuronal development has been thoroughly studied in hippocampal cultured neurons (Barnes and Polleux, 2009; Kaech and Banker, 2006), which in somehow reflects the neuronal development observed "in vivo". During hippocampal neuronal development in vitro, five different stages have been described (Fig. I1). After plating, neurons extend an actin lamella all around the cell body (Stage 1). Then, minor neurites begin to extend in the cell periphery (Stage 2). In this stage, cell retains its symmetric appearance and lasts for 12-36 h. Next, one neurite grows for an extended period without retraction and acquires axonal characteristics (Stage 3). After 3-4 days in culture, the remaining minor neurites slowly elongate to become dendrites. At roughly the same time, AIS forms in the axon in a tiny domain proximal to the soma, being first detected by early AIS protein ankyrinG and voltage gated ion channels (Alpizar et al., 2019; Nakada et al., 2003). The AIS turns to be mature rapidly in two weeks (Stage 4) with the addition of more components, such as potassium channels (Sanchez-Ponce et al., 2012b), and the maturation of the diffusion barrier (Brachet et al., 2010).

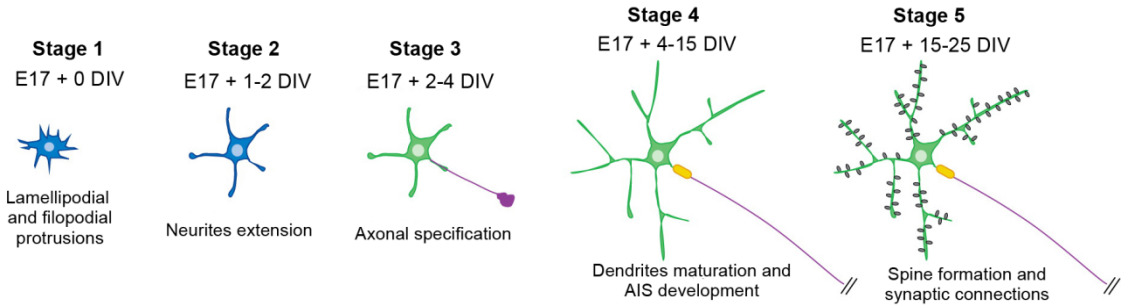

Figure I1. Developmental stages of cultured hippocampal neurons. Adapted from (Barnes and Polleux, 2009).

1. The Axon Initial Segment (AIS)

The axon initial segment (AIS) is a highly specialized neuronal compartment located in between axonal and somatodendritic domains (Fig. I2). It contains a high concentration of different sodium, potassium and calcium voltage gated ion channels, which allows its function as the site of action potential generation. The AIS is also characterized by a high density of cell adhesion molecules (CAMs), such as neurofascin. Both, voltage gated ion channels and CAMs are anchored to the AIS cytoskeleton by the scaffold proteins ankyrinG, βIV-spectrin and PSD93. Among them, ankyrinG is the main scaffold protein and it is extremely important for the maintenance of the whole structure, keeping AIS integrity and function. AnkyrinG and βIV-scpectrin also serve as the linker with the AIS cytoskeleton, which is composed by different actin structures and bundled microtubules with specific characteristics. This cytoskeleton,

together with membrane proteins maintains axonal polarization to exclude somatodendritic proteins entrance into the axon.

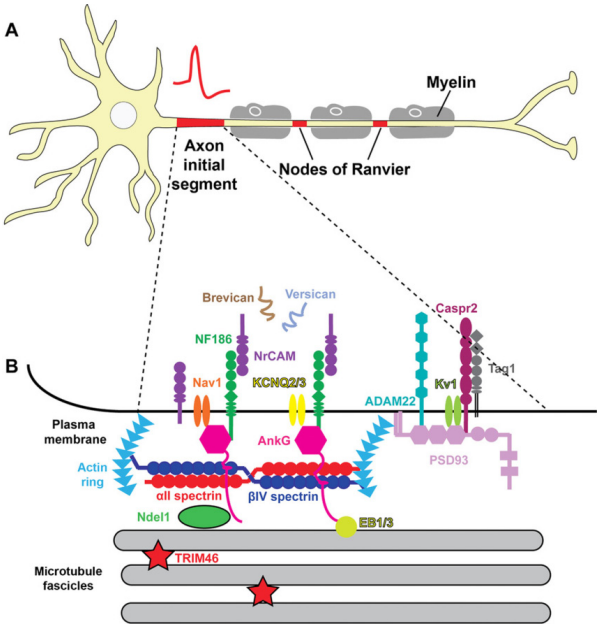

Figure I2. Axon Initial Segment (AIS) structure and compositions. AIS is the place of action potential initiation. It contains a high density of sodium (Nav) and potassium channels (Kv and KCNQ2/3), which are anchored by ankyrinG (AnkG) and βIV-αII-spectrins to the actin and microtubules cytoskeleton. Its membrane also contains a high density of adhesion molecules (NF186, ADAM22, Caspr2 or NrCAM). These molecules are associated with extracellular glicoproteins, such as Brevican or Versican. This whole complex structure maintains somatodendritic-axonal polarization, and is the site of action potential generation, which is maintained and propagated by nodes of Ranvier. From (Huang and Rasband, 2018).

1.1. The AIS structure

1.1.1. AnkyrinG: the key AIS organizer

AnkyrinG is a submembranous scaffold protein in the AIS. In mammals, three ankyrin genes were discovered (Bennett and Baines, 2001) and ankyrinG is the third member of the ankyrin family (*ANK3*), which is expressed in the brain, heart, muscle and epithelial cells. In neurons, there are three splice variants of ankyrinG. The largest isoform of ankyrinG is a 480 kDa protein (giant ankyrinG), which contains several major domains (Bennett and Lorenzo, 2013): a membrane-binding domain for cell adhesion molecules and ion channels interaction, a spectrin-binding domain for β-spectrin interaction, an unstructured serine-rich domain for microtubules interaction (Freal et al., 2016), a tail domain and a C-terminal containing a death domain. The medium isoform of ankyrinG is a 270 kDa protein, which lacks of the tail domain. And the smallest isoform of ankyrinG is a 190 kDa protein, which only has N-terminal amino acids and lacks the serine-rich domain and the tail domain. However, only the largest and the medium isoform of ankyrinG are specifically localized in the AIS and nodes of Ranvier in neurons (Jenkins et al., 2015; Kordeli et al., 1995). As a scaffold, βIV-spectrin contributes to anchoring ankyrinG to the cytoskeleton (Komada and Soriano, 2002), but also maintaining plasma membrane adhesion and membrane polarization through binding to phosphoinositides

(Lemmon et al., 2002). Consistently, mutant mice lacking βIV-spectrin causes axonal molecules L1CAM and ankyrinG to mislocalize to the somatodendrites both in vitro and in vivo (Komada and Soriano, 2002; Nishimura et al., 2007).

Shortly after axon and dendrites specification, ankyrinG starts to cluster at the proximal axon and then recruits other AIS components (Hedstrom et al., 2007; Yang et al., 2019). An amino acids motif (AIS motif) in voltage gated sodium (Nav) and potassium ($Kv7_)$ channels has been described that target these channels to the AIS through interaction with ankyrinG (Garrido et al., 2003; Pan et al., 2006). As a master regulator, ankyrinG controls both ion channels clustering and the maintenance of neuronal polarity. Previous studies in knockout mice and cultured neurons have shown that the loss of ankyrinG is associated with loss of voltage gated ion channels, cell adhesion molecules and the loss of AIS integrity (Hedstrom et al., 2007; Jenkins and Bennett, 2001; Zhou et al., 1998). Moreover, ankyrinG concentration at the AIS is necessary to maintain axonal polarity and impairs somatodendritic proteins to enter the axon. In fact, absence of ankyrinG in cultured hippocampal neurons dismantles the AIS structure and causes somatodendritic proteins (MAP2, KCC2, PSD95) to redistribute and enter the axon, where spine-like structures and postsynaptic densities can even develop (Hedstrom et al., 2008). This is corroborated by in vivo experiments in ankyrinG knockout of Purkinje neurons, which develop dendritic spines enriched with postsynaptic proteins in the axons (Sobotzik et al., 2009).

1.1.2. Other AIS enriched proteins

1.1.2.1. Voltage-gated ion channels

Voltage-gated ion channels are one of major constituents concentrated in the AIS. AIS is enriched with multiple types of voltage gated sodium channels, potassium channels and calcium channels. These channels play varied roles in action potential initiation and shaping the spike waveforms (Bender and Trussell, 2012; Kole and Stuart, 2012). Sodium channels α subunit, the pore-forming subunit, directly interacts with ankyrinG through the AIS motif in cytoplasmic II-III loop and is recruited to the AIS domain (Garrido et al., 2003; Lemaillet et al., 2003; Zhou et al., 1998). The phosphorylation of several serine residues (S1112, S1124, and S1126) at AIS motif tightens the interaction between ankyrinG and Nav1.2, which further contributes to the sodium channels clustering in the AIS (Brechet et al., 2008).

In neurons of central nervous system, there are three major subtypes of sodium channels at the AIS: Nav1.1, Nav1.2 and Nav1.6 (Boiko et al., 2003; Duflocq et al., 2008). Each type of neurons contains a different combination of voltage gated ion channels (Debanne et al., 2011). Nav1.6 is the dominant isoform of sodium channels in the AIS for mature neurons both in rodent (Kress et al., 2010; Lorincz and Nusser, 2008; Van Wart et al., 2007) and human (Inda et al., 2006; Tian et al., 2014). In immature neurons, Nav1.2 is more abundantly expressed in the AIS (Boiko et al., 2003). Nav1.1 channels have also been detected in motoneurons (Duflocq et al., 2008), cortical interneurons (Ogiwara et al., 2007; Van Wart et al., 2007) and cerebellar Purkinje cells (Xiao et al., 2013). Those different subunits of sodium channels can play different roles for the generation of action potentials (Hu et al., 2009). Potassium channels are also richly expressed in the AIS (Lorincz and Nusser, 2008; Pan et al., 2006). In addition to Kv7.2/7.3 channels clustered by ankyrinG, Kv1.1 channels are clustered at the AIS through binding to the scaffold protein PSD93 (Ogawa et al., 2008). Kv7.2/7.3 is not clustered at the AIS in ankyrinG knock-out mice of cerebellum (Pan et al., 2006; Rasmussen et al., 2007). Previous studies have established that potassium channels affect resting membrane potential as well as repolarization by shaping the width and repetitive spiking of action potentials (Clark et al., 2009; Kole et al., 2007; Shah et al., 2008).

Voltage-gated calcium channels Cav2.1 (P/Q-type current) and Cav2.2 (N-type) also concentrate along the AIS of ferret prefrontal cortical neurons (Yu et al., 2010). Cav3.1/3.2 (T-type) channels at the AIS are identified in pyramidal cells of primary somatosensory cortex layer 5b and cerebellar Purkinje cells in mice through electrophysiology techniques (Bender and Trussell, 2009). Ca^{2+} influx in the AIS is mediated by low voltage-activated (LVA) Ca^{2+} channels, including T- and R-type isoforms. However, the knowledge of these calcium channels at the AIS is limited.

1.1.2.2. Cell adhesion molecules

Several cell adhesion molecules (CAMs) are richly expressed in the AIS. NrCAM, neurofascin (NF186) and L1CAMs are recruited in the AIS by ankyrinG through their cytoplasmic FIGQY motif (Davis and Bennett, 1994). Phosphorylation of the tyrosine (Y) in the FIGQY motif decreases L1CAMs-ankyrin interactions (Jenkins et al., 2001; Tuvia et al., 1997).

Indeed, knocking down either of those CAMs has no effects on other AIS components clustering in the AIS (Hedstrom et al., 2007). Consistently, ablating NF186 can not modify overall enrichment of sodium channels and its distribution (Alpizar et al., 2019). However, the loss of NF186 perturbs ankyrinG accumulation, which indicates that NF186 may play vital roles for AIS components recruitment. Besides, NF186 is responsible for the collection of extracellular matrix molecules (ECM) to the AIS, such as brevican, versican and aggrecan, and thereby links the intracellular cytoskeleton to the ECM (Bruckner et al., 2006; Hedstrom et al., 2007; John et al., 2006). In the cerebellum, NF186 contributes to the innervations by basketball interneurons in Purkinje neurons AIS (Ango et al., 2004). Some CAMs are specifically clustered at the distal AIS region, including Caspr2 (contactin-associated protein-like 2), Tag-1 (transient axonal glycoprotein-1) and a disintegrin and metalloproteinase domain-containing protein 22 (ADAM22). Those proteins are recruited directly or indirectly by PSD93 (Ogawa et al., 2008). PSD93 as well as NF186 and NrCAM can be modified by lipids (El-Husseini et al., 2000; Ogawa et al., 2008; Ren and Bennett, 1998). These lipid modifications facilitate protein interactions with lipid bilayers and regulate protein sorting, localization and function in specialized lipid microdomains (el-Husseini Ael and Bredt, 2002). Consistent with the finding of ADAM22 in the AIS (Ogawa et al., 2010), its ligand, the secreted leucine-rich glioma inactivated protein 1 (LGI1) is enriched at the AIS and colocalizes with Kv1 channels in cultured hippocampal neurons. LGI1 deficiency decreases Kv1 channels expression and leads to neuronal intrinsic excitability (Seagar et al., 2017).

1.1.3. AIS cytoskeleton

1.1.3.1. Actin cytoskeleton in the AIS

F-Actin structures function as a barrier in the AIS both for membrane components and intracellular vesicles (Song et al., 2009; Winckler et al., 1999). Disruption of F-actin abolishes AIS barrier and leads to a redistribution of membrane proteins, which is accompanied by the entrance of macromolecules to the axon.

F-actin orchestrates the AIS in several different ways. At least three types of actin structures have been idenditifed in the AIS: actin rings, actin patches and actin trails. Actin can bind to ankyrinG through βIV-spectrin. βIV-spectrin stabilizes ankyrinG by binding to its spectrin repeat, while the interaction with actin cytoskeleton is via an actin-binding domain at

the N-terminal. Recent studies using stochastic optical reconstruction microscopy (STORM) reveal that actin in the AIS forms a periodic structure with actin filament rings spaced 190 nm intervals (Leterrier et al., 2015; Xu et al., 2013). Actin rings are connected by βIV-spectrin in a mode of head-to-head. A current study revealed that contractile myosin II activator, pMLC, is associated with actin rings (Berger et al., 2018). The function of this actin rings structure is unknown, but it may be involved in the stabilization of AIS due to their strong resistance to actin destabilizing drugs (Abouelezz et al., 2019; Leterrier et al., 2015). Together with actin rings, other AIS components such as ankyrinG, sodium channels and NF186 in the AIS are also periodic (Xu et al., 2013). In addition to actin rings in the AIS, 2-3 μm actin patches are reported in the AIS (Watanabe et al., 2012). Those actin patches are present shortly after neuronal specification with a highly dynamic modulation (Balasanyan et al., 2017). Actin patches loss induced by inhibition of the actin nucleator Arp2/3 activity results in the mislocation of somatodendritic proteins to the axon. In the AIS, actin patches function to block dendritic protein vesicles entry in the axon. In fact, somatodendritic proteins are much more likely to stop and reverse their movement direction in regions occupied by the actin patches (Watanabe et al., 2012).

Actin related proteins are expressed in the AIS and allow the identification in the AIS of another small sized and actin condensed structure, the cisternal organelle (CO) (Sanchez-Ponce et al., 2012a). The CO is identified as patches in the AIS of variable size and is thought to be a calcium store in neocortical and hippocampal neurons (Bas Orth et al., 2007; Benedeczky et al., 1994; Sanchez-Ponce et al., 2011a). Besides, other calcium regulation related molecules, such as inositol 1,4,5-triphosphate receptor 1 (IP_3R1), annexin 6 and SERCA-type Ca^{2+} pump (Benedeczky et al., 1994; Sanchez-Ponce et al., 2011a) have been identified at the AIS. Apart from those molecules, actin binding or associated proteins α-actinin and synaptopodin are also expressed in the CO (Sanchez-Ponce et al., 2012a). Synaptopodin knockout mice are characterized by the lack of CO in CA1 pyramidal cells, but without altering neuronal excitability (Bas Orth et al., 2007). Recent studies revealed a dynamic remodeling of CO along with AIS length modifications during visual cortex development (Hofflin et al., 2017; Schluter et al., 2017). Visual deprivation leads to an increase of CO patches size and AIS length in

pyramidal neurons of layers II/III in visual cortex (Schluter et al., 2017). This is also observed in retinal ganglion cells (Schluter et al., 2019). However, AIS shortening is observed in synaptopodin-deficient mice lacking the CO after visual deprivation. The relation of CO and AIS can also be supported by a study that CO integrity depends on the ankyrinG expression in the AIS (Sanchez-Ponce et al., 2011a). This suggests that the CO is an essential part of the AIS machinery required for AIS plasticity in response to changes in network activity. However, our knowledge of this structure is limited.

Using platinum replica electron microscopy, short, stable filaments and slightly longer dynamic filaments are previously identified in the AIS (Jones et al., 2014). Stable actin filaments together with other known AIS proteins function as a diffusion barrier to prevent mixing of axonal and dendritic proteins, whereas dynamic actin may promote AIS coat remodeling and allows for selective passage of vesicles during establishment of neuron polarity. Another form of dynamic actin filaments known as actin trails is found along the axon including the AIS. Those actin trails originate from "actin hotspots" and spurt bidirectionally along axons. Formins are responsible for actin trails regulation and loss of formins activity attenuates these actin trails (Ganguly et al., 2015).

1.1.3.2. Microtubules cytoskeleton in the AIS

Microtubules are uniformly oriented with their plus ends pointing to the distal axon, both in the AIS and the axon, whereas in dendrites microtubule orientations are mixed (Baas et al., 1988; Stepanova et al., 2003; Stone et al., 2008). Microtubules in the AIS are tightly packed into fascicles, a composition absent from other neuronal regions, even the similar excitable structure, the nodes of Ranvier (Palay et al., 1968). Recently, a microtubule associated protein (MAP), TRIM46, is identified and enriches in the AIS, which function is to maintain the uniform axonal microtubule orientation and microtubules fasciculation (Harterink et al., 2019; Palay et al., 1968; van Beuningen et al., 2015). Depletion of TRIM46 results in a mixed microtubule polarity and a decrease of axonal trafficking efficiency. TRIM46 partly overlaps with ankyrinG and maintains the uniform plus-end outward microtubule fascicles. And loss of ankyrinG greatly disrupts the distribution of TRIM46.

AIS microtubules together with other AIS scaffold and membrane proteins form a

submembranous coat to maintain AIS stability (Jones et al., 2014). Indeed, microtubules are tightly related with AIS master protein ankyrinG. It is reported that fasciculated microtubules are absent in the proximal axon of ankyrinG knock-out mice in the cerebellum (Sobotzik et al., 2009). In addition, ankyrinG binds to microtubules via the microtubule plus-end-binding proteins EB1 and EB3 (Leterrier et al., 2011). EB proteins are localized in the AIS and contribute to AIS assembly and maintenance through interaction with ankyrinG (Freal et al., 2016; Leterrier et al., 2011). Although EB proteins can recruit other plus-end-tracking proteins (+TIPs) such as CLASPs and CLIPs (Akhmanova and Steinmetz, 2010), no signal is observed for CLIP170, CLASP1/2 and APC in the AIS of mature cultured rat hippocampal neurons (Leterrier et al., 2011).

Microtubules properties can be regulated by post-translational modifications, such as tyrosination, detyrosination, polyglutamylation, polyglycylation. Detyrosinated and acetylated tubulin are more resistant to depolymerization agents and are considered as more stable microtubules (Baas and Black, 1990). Indeed, a stable pool of microtubules was identified in the AIS, which is characterized by higher level of acetylated and detyrosinated microtubules in cultured hippocampal neurons (Tapia et al., 2010). Several mechanisms and proteins have been identified to modify tubulin post-translational modifications at the AIS. HDAC6 is a tubulin deacetylase and it is involved in the AIS assembly through α-tubulin deacetylation in the distal axon, conferring AIS specific higher acetylation (Tapia et al., 2010). Casein kinase 2α (CK2α) clusters at the AIS and its inhibition blocks sodium channels and ankyrinG assembly and maintenance, which is accompanied by the increase of tubulin acetylation in the AIS (Sanchez-Ponce et al., 2011b). In addition, an important regulator of microtubules, glycogen synthase kinase 3 (GSK3), was also identified in the AIS. It is known that inhibition of GSK3β results in the increase of tubulin acetylation, detyrosination, and polyglutamylation (Hammond et al., 2010), but also decreases the levels of ankyrinG and sodium channels at the AIS (Tapia et al., 2013).

This structural and regulatory complex cytoskeleton is necessary not only to anchor AIS proteins, but also to decide which motor proteins can go into the axon to transport axonal cargoes. Among them, kinesins and dyneins are the most studied. Kinesins are generally plus-

end-directed microtubule motors driving long-distance movement in neurons. They are a large superfamily, organized in 14 families, being kinesin1 family the main one responsible for the anterograde transport into the axon and AIS (Konishi and Setou, 2009; Reed et al., 2006). Kinesin1 mediated axonal transportation is related with microtubule stability binding to acetylated and detyrosinated microtubules at the AIS and along the axon. Long-term increase of tubulin acetylation disrupts KIF5C redistribution between somatodendritic and axonal compartments and alters AIS components accumulation (Tapia et al., 2010). For the retrograde transport in the AIS and axon, dynein counteracts mislocalized somatodendritic cargoes and redirects them to the soma and dendrites along the minus-end microtubules. In addition, dynein regulator NDEL1 stably binds to ankyrinG at the AIS and cooperates with its effector Lis1 for efficient local cargo reversal (Klinman et al., 2017; Kuijpers et al., 2016; Waterman-Storer et al., 1995). Depletion either of them leads to both cell-wide and local defects, including the non-polarized trafficking of dendritic cargos through the AIS (Kuijpers et al., 2016).

1.2. AIS development and maturation

Previous studies have provided a few clues for AIS early assembly. The specific accumulation in the AIS of ankyrinG, as the master and organizer protein for AIS assembly, determines the fate of AIS formation (Rasband, 2010). Several hypotheses have been proposed for AIS establishment. First, a distal axonal submembranous cytoskeleton composed of ankyrinB, αII-spectrin, and βII-spectrin, defines ankyrinG location in the proximal axon (Galiano et al., 2012). Second, local higher acetylation of microtubules in the AIS due to distal axon expression of the tubulin deacetylase HDAC6, allows AIS components clustering in the AIS (Tapia et al., 2010). Moreover, the cooperation of microtubule end-binding proteins (EBs) and giant ankyrinG is decisive for AIS assembly and neuronal polarity (Freal et al., 2016). In fact, disrupting the interaction between giant ankyrinG and βIV-spectrin impairs AIS composition targeting to the AIS (Yang et al., 2019). A current study also found that an actin motor, myosin II, contributes to the assembly of AIS (Berger et al., 2018). Interestingly, myosin II activator pMLC (phosphorylated myosin light chain) is richly expressed in the AIS and controls ankyrinG accumulation.

The AIS initially appears between stage 3 and stage 4 in cultured hippocampal neurons

(Barnes and Polleux, 2009; Kaech and Banker, 2006) after axon has started its elongation. Thus, AIS assembly and axon specification are two different events. Consistently, knocking down ankyrinG before axon specification does not impair a morphological neuronal differentiation into axons and dendrites (Sanchez-Ponce et al., 2011b). However, once AIS is formed, it starts to maintain neuronal polarity by preventing somatodendritic proteins from entering axonal domains (Rasband, 2010; Sobotzik et al., 2009). Along with AIS development, various transmembrane proteins, such as, voltage gated sodium channels, neurofascin, scaffold proteins continuously assemble in the AIS (Alpizar et al., 2019; Jones et al., 2014; Nakada et al., 2003). In addition, AIS actin and microtubules cytoskeleton turn to be more stable along with AIS development (Jones et al., 2014). During this maturation period, AIS becomes a diffusion barrier, between 4 and 10 DIV, and a place of axonal traffic control that contributes to maintenance of neuronal polarity. Finally, between 14 and 21 DIV, all kinds of voltage gated ion channels are established at the AIS and action potential properties are fully mature.

2. AIS plasticity and regulation

Despite AIS has a highly stable and specialized cytoskeletal architecture, recent studies have highlighted that the AIS possesses a high plasticity characterized by dynamic alterations in its molecular compositions, changes of distance to the soma or changes in its length. These structural and compositional modifications happen in response to changes in neuronal activity input during development or from pathological alterations.

2.1. AIS plasticity during neuronal development

Different types of neurons may have distinct AIS ion channels, locations and lengths that tune the electrophysiological properties of each specific cell type (Hofflin et al., 2017; Lorincz and Nusser, 2008; Yoshimura and Rasband, 2014). To be functionally developed, the AIS undergoes changes in its structure and compositions during AIS maturation along with neuronal development. In retinal ganglion cells, Nav1.2 channels expression precedes that of Nav1.6 channels and Nav1.6 turns to be the major Na^+ channel subtype when the neuron is mature (Boiko et al., 2003). Similarly, in cerebellar granule cells, Nav1.2 accumulates rapidly in the AIS at early stages, while Nav1.6 clusters at AIS from P21 to P40 and later co-localizes with Nav1.2 (Osorio et al., 2010). Besides the sodium channels, notable changes in AIS length and

thickness throughout cell maturation have been described (Bolos et al., 2019). Also, in developing visual cortex, AIS length undergoes dynamic changes along postnatal development, increasing its length till postnatal day 15. Later and coinciding with the critical period with the highest sensitivity to input imbalance, the AIS becomes shorter around P28, but increases its length around P35 till adult stage (Gutzmann et al., 2014). Among the factors and receptors controlling initial development of the AIS, purinergic P2Y1 and cannabinoids CB1 receptors are essential to properly start AIS development (Tapia et al., 2017; Zhang et al., 2019).

2.2. Activity dependent AIS plasticity

AIS modeling during development could be due to the activity alterations (Gutzmann et al., 2014; Kuba et al., 2014; Kuba et al., 2006). Several works have demonstrated that neuronal activity contributes to the AIS plasticity. Computer modeling analysis first showed that AIS length and location are optimized to reduce the threshold of spike generation (Kuba et al., 2006). This was indeed proved in a study in chicken audiotry cortical neurons, that were deprived of their inputs from cochlear neurons (Kuba et al., 2010). Deprivation of auditory inputs leads to nucleus magnocellularis neurons AIS elongation, which was accompanied by changes of ankyrinG and sodium channels distribution along the AIS. In addition, the input deprived cells become more excitable to compensate for the lost of input and to maintain a maximum of efficiency. Consistent with theses findings, chronic increase neuronal activity using high extracellular potassium or photostimulation results in a significant shift of AIS position along the axon away from the soma in cultured hippocampal neurons (Grubb and Burrone, 2010). Those neurons with distal shift of AIS are characterized by higher current thresholds to respond and compensate this higher neuronal ongoing excitability.

Abnormal neuronal firing often happens in neuropathological conditions. AIS plasticity in response to neuronal excitability is also applicable to this situation. With aging, neurons from visual cortex of aged individuals show an increased excitation (Ding et al., 2017; Hua et al., 2006; Leventhal et al., 2003). A recent research showed that the primary visual cortex neurons in layer II/III of aged rats have shorter AIS length and less Nav1.6 channels intensity, indicating that AIS plasticity is a mechanism to compensate for age-related enhancement of neuronal excitation in the visual cortex (Ding et al., 2018). Changes in AIS length have been described in

Alzheimer's disease models (Marin et al., 2016) and a mouse model of *Angelman syndrome* shows an increased ankyrinG and sodium channels expression at the AIS (Kaphzan et al., 2011).

2.3. Potential mechanisms for AIS plasticity

Neurons can sculpture AIS in order to meet their specific functional requirements. However, the mechanisms involved in the control of AIS structure and composition changes during AIS rearrangements in physiological and pathological conditions remain mostly unknown. There are several proposed mechanisms for AIS plasticity with calcium signaling as a common mediator. Given the presence of cisternal organelles (Benedeczky et al., 1994) and calcium channels (Bender and Trussell, 2009) at the AIS, calcium-dependent pathways may have profound impacts on AIS plasticity. AIS location distal shifting after induction of long-term depolarization can be blocked in pyramidal hippocampal neurons by T- and/or L-type voltage-gated calcium channels antagonists (Grubb and Burrone, 2010). However, this elevated neuronal activity shortens the AIS length in dentate granule cells mediated through L-type Cav1 calcium channels (Evans et al., 2015). In the other hand, even higher extracellular potassium concentration reduces AIS components expression within minutes in hippocampal neurons. This quick effect can be blocked by extracellular calcium chelation with EGTA (Berger et al., 2018). This reduction in AIS proteins has also been described after activation of P2X7 purinergic receptor by ATP, which triggers calcium influx. Consistently, the reduction of ankyrinG and sodium channels mediated by ATP-P2X7 activation can be inhibited through chelating extracellular calcium ions by EGTA (Del Puerto et al., 2015). Some calcium related proteins, including calcium-modulated protein calmodulin (Liu and Devaux, 2014), calcium-activated phosphatase calcineurin (Evans et al., 2013) and calcium-dependent cysteine protease calpain (Del Puerto et al., 2015; Schafer et al., 2009) have been described as mediators of AIS plasticity. While calmodulin enhances the heteromeric association of Kv7 heteromers and their clustering at the AIS (Liu and Devaux, 2014), slow activity-dependent AIS relocation and rapid activity-dependent AIS shortening both rely on calcineurin activity (Evans et al., 2013). Instead, calpain is involved in AIS components degradation after neuronal injury or abnormal enhanced neuronal excitability, and its inhibition is sufficient to preserve the molecular organization of the AIS (Del Puerto et al., 2015).

In addition, a recent research showed that actin destabilization could be a late-stage event that underlies activity-dependent AIS disassembly (Berger et al., 2018). Consistent with this finding, actin stabilization recoveries the decrease of AIS components caused by loss of P2Y1 purinergic receptors (Zhang et al., 2019). Besides, myosin II and its activator pMLC have major roles in neuronal activity dependent AIS plasticity (Berger et al., 2018; Evans et al., 2017). Inhibition of myosin II ATPase activity blocks AIS long-term relocation and more rapid shortening in dentate granule cells.

AIS plasticity is a complex process. It can occur over the course of hours or days. Besides, numerous stimuli can alter AIS both in nervous system development and pathologies. As a stable compartment in neurons, the AIS changes may need several coordinators. However, based on the current knowledge, our understanding of AIS plasticity processes is very limited. Therefore, it is necessary to identify new AIS plasticity regulators in order to get a better understanding of AIS homeostatic plasticity in physiology and pathology.

3. The AIS in neurological disorders

Given the vital roles of AIS on action potential generation and polarity maintenance, mutations or single nucleotide polymorphisms (SNPs) in genes responsible for the expression of AIS components could be a risk factor leading to some neurological disorders related to neuronal function. Some AIS proteins mutations cause neurological disorders. AnkyrinG abnormal expression or incorrect splicing of *ANK3* are related with lots of neuronal pathologies. Multiple genome-wide association studies revealed that *ANK3* is among the most frequently reported risk genes in bipolar disorder (Leussis et al., 2013; Leussis et al., 2012; Psychiatric, 2011), with further evidence for association with other psychiatric disorders including schizophrenia (Schizophrenia Psychiatric Genome-Wide Association Study, 2011) and autism spectrum disorder (Codina-Sola et al., 2015). βIV-spectrin is another an important scaffolding protein in the AIS. Functional loss of βIV-spectrin gene (*Spnb4*) in mutant mice have phenotypes of ataxia and central auditory deafness (Parkinson et al., 2001). In patients, *Spnb4* mutants have myopathies and central auditory deficiency disorders (Knierim et al., 2017). Moreover, different autoantibodies against AIS proteins have been detected in different autoimmune diseases, such as, encephalopaties (LGI1), multiple sclerosis (NF186), Morvan

syndrome (Kv channels) or neuropathic pain (Nav channels) (Buffington and Rasband, 2011; Seagar et al., 2017).

In addition, AIS alterations could occur in response to the abnormality of neuronal activity or microenvironments. Inflammatory or genetic diseases generate changes in AIS integrity and plasticity. For example, AIS components in ischemic brains are completely lost due to proteolysis of ankyrinG and βIV-spectrin by the Ca^{2+} dependent protease calpain in stroke brains (Del Puerto et al., 2015; Schafer et al., 2009). Within the peri-infarct cortex, AIS length decreases from the distal end (Hinman et al., 2013). In a blast wave induced mild traumatic brain injury model, the AIS shortens in both the cortex and hippocampus, although there is no change of AIS components (Baalman et al., 2013). *Angelman syndrome* is associated with a series of symptoms consisting of epilepsy, autism, intellectual disability and motor abnormalities. A mouse model for *Angelman syndrome* generated by knockout of ubiquitin ligase UBE3A gene exhibits upregulated ankyrinG and Nav1.6 channels together with longer AIS. Besides, severe AIS disruption and even loss of the AIS were observed in the neocortex of *experimental autoimmune encephalomyelitis* mice model, which can be impaired through inhibiting microglia activity (Clark et al., 2016). In line with the finding that microglia activity affects AIS integrity, higher densities of microglia surrounding Aβ plaques may also damage the AIS (Marin et al., 2016). Given type-2 diabetes associated with cognitive and mood impairments, a more current study showed that AIS shortening occurs in the absence of altered AIS protein levels in diabetic mice (Yermakov et al., 2018). All together, AIS alterations could be a relatively common feature in nervous diseases and injuries, suggesting that AIS could be regarded as a possible target for therapeutic intervention in some brain diseases and disorders.

4. Formin homology proteins (Formins)

Actin and microtubules are key players in the AIS maintenance and their regulation and modifications are necessary for AIS plasticity and maintenance of neuronal polarity. Many regulatory proteins play an important role in actin or/and microtubules dynamics in different neuronal domains. However, the knowledge of how AIS actin and microtubules cytoskeleton is regulated remains elusive. Formins family members are potential candidates for AIS cytoskeleton regulation due to their ability to modulate actin and microtubules structures

(Bartolini and Gundersen, 2010; Courtemanche, 2018), their roles in maintaining apico-basal polarity in neuroepithelial and epithelial cells (Acharya et al., 2017; Herzog et al., 2011; Thumkeo et al., 2011), and their function in maintaining axonal actin structures (Ganguly et al., 2015).

4.1. Mammalian formin family members and protein domains

Formins are defined by their most conserved formin homology 2 (FH2) domain (Higgs and Peterson, 2005). They are evolutionarily conserved in eukaryotes throughout a wide range of species, including slime molds, yeast, plants, mollusca, annelida, platyhelminthes, arthropoda, nematode, echinodermata and chordate (Higgs and Peterson, 2005; Pruyne, 2016). However, a different number of formin subtypes exist in different species, being 15 in mammals. These 15 mammalian formins are further subdivided into eight different subfamilies based on their sequences and domain architectures (Schonichen and Geyer, 2010). Specifically, there are 3 Diaphanous related formin subtypes (Dia1, Dia2, Dia3), 2 Dishevelled associated activator of morphogenesis subtypes (DAAM1, DAAM2), 3 formin-like subtypes (FMNL1, FMNL2, FMNL3), 2 formin homology 2 domain containing subtypes (FHOD1, FHOD3), 2 formin subtypes (FMN1, FMN2), as well as, WH2 domain-containing formin 1 (WHIF1), inverted formin 1 (INF1) and Grid2 interacting protein (GRID2IP).

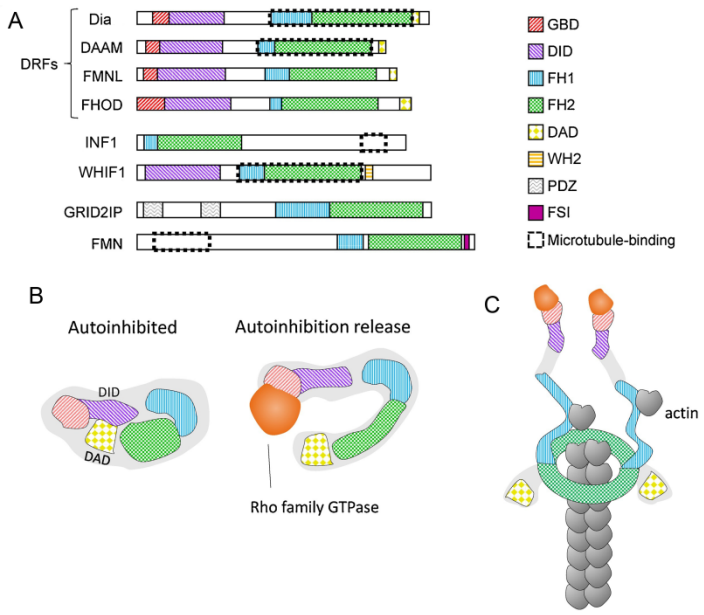

Figure I3. Domain organization of formin subfamilies and the regulation and function of DRFs. A. Formin subfamilies classification based on the sequence similarity of the FH2 domain. GBD: GTPase-binding domain. DID: diaphanous inhibitory domain. FH1: formin homology 1 domain. FH2: formin homology 2 domain. DAD: diaphanous autoregulatory domain. WH2: Wiskott-Aldrich homology 2. FSI: formin-spire interaction domain. PDZ: PSD95-Dlg1-Zo-1 domain. **B.** General mechanism of DRFs autoinhibition via DID-DAD intramolecular binding and release by RhoGTPase-binding to the GBD domain. **C.** When elongating actin, dimerized FH2 domains form a ring-like structure near the barbed end of the actin filament, with the more flexible FH1 domains continuously adding actin monomers. Adapted from (Kawabata Galbraith and Kengaku, 2019).

Formins are large and multi-domain proteins with more than 1000 amino acids (Fig. I3). The most conserved domain, FH2 domain, is a sequence of around 400 amino acids and

typically localizes in the C-terminal. FH2 domain is often immediately preceded by a proline-rich formin homology 1 (FH1) domain. In C-terminal tail regions, many formins also encode additional actin-binding sites, including Wiskott-Aldrich syndrome protein homology-2 (WH2)-like motifs in WHIF1 and FMNL3 (Chhabra and Higgs, 2006; Heimsath and Higgs, 2012) and formin-spire interaction domain in FMN1 and FMN2 (Pechlivanis et al., 2009). Most formins share an N-terminal diaphanous inhibitory domain (DID) and C-terminal diaphanous autoregulatory domain (DAD). A dimerization domain (DD) is adjacent to the DID and followed by coiled-coil domain. Four formin subtypes Dia, DAAM, FMNL and FHOD share a similar domain organization and belong to the DRFs. The other formins family members are non-DRFs that diverge from this pattern of domain organization. Among them, one or more conserved N-terminal domains are absent, instead replaced by other folds, such as PSD95-Dlg1-Zo-1 domain (PDZ) of GRID2IP and microtubule-binding domains of FMN1 and FMN2 (Kawabata Galbraith and Kengaku, 2019).

FH2 domain is the core element for formins' physiological functions through actin and microtubules regulation (Bartolini and Gundersen, 2010). However, the flanking regions of the FH2 domain vary considerably between individual formins, likely resulting in different cellular functions and regulation mechanisms. FH1 can bind to profilin-actin complexes and enhance the delivery of new actin monomers onto the growing filaments (Paul and Pollard, 2008; Romero et al., 2004). FH1, FH2 and C-terminal domains also contribute to the dynamics of microtubule regulation in some formins, such as Dia, DAAM, INF1 and WHIF1 (Bartolini and Gundersen, 2010). Formins in resting state are autoinhibited through the binding of DID and DAD, which is disrupted by binding of RhoGTPase in the formins GTPase-binding domain (GBD) (Kuhn and Geyer, 2014). Disruption of this DID-DAD interaction results in releasing intramolecular autoinhibition and partially activating the actin polymerization abilities.

4.2. Physiological functions of formins

4.2.1. Actin filament nucleation and elongation

Formins play various cellular roles and the most common one is on actin filament nucleation and elongation. A ring-like head-to-tail FH2 dimer binds directly to G- and F-actin and nucleates actin molecules, which is followed by actin filaments elongation (Goode and Eck, 2007). During this process, FH1 domain recruits G-actin molecules through interaction with

profilin and affects the actin polymerization rate (Kovar et al., 2006; Romero et al., 2004). Dimerized FH2 domains robustly stimulate actin nucleation rates in bulk kinetic assays (Courtemanche, 2018). In some formins, specific factors can contribute to the nucleation activity. For example, the C-terminal WH2 motif of FMNL3 enhances nucleation through binding actin monomers, which is independent of the actin subunits recruited by FH2 dimers (Thompson et al., 2013). The C-terminal DAD motif is another domain binding actin monomers and increases rates of nucleation, which is found in mammalian formins mDia1 and DAAM1 (Gould et al., 2011). Besides, other ligands of formin C-terminal tail regions can also enhance or inhibit formin nucleation activities, such as the enhancement of Disheveled on DAAM1, APC on mDia1, Spire on FMN formins and the inhibition of Ena/Vasp on Dia formins (Courtemanche, 2018).

Apart form actin nucleation, formins also function on actin elongation (Higashida et al., 2004). A "gating" model was proposed to explain the formin-mediated actin elongation. In this model, FH2 domains are in rapid equilibrium among "open" and "closed" conformations that allow or block actin addition. Thus, the elongation rate is dictated by the probability that incoming actin monomers find the FH2-barbed end complex in an open conformation (Vavylonis et al., 2006). Indeed, the inhibition ability of elongation varies widely among formins from 99% in mammalian GRID2IP (Dutta et al., 2017; Silkworth et al., 2018) to about 5-10% in mouse mDia1 (Kovar et al., 2006). Additionally, the elongation rate mediated by formins could be affected by the application of force, but in isoform-specific ways. For example, the application of force speeds up the elongation by mDia1 (Yu et al., 2017), but not by mDia2 (Zimmermann et al., 2017). Indeed, mDia1 is mechanosensitive and can efficiently elongate actin filaments in response to mechanical tensions, suggesting a mechanical protection role of mDia1 for cellular morphology (Jegou et al., 2013).

In addition to actin nucleation and elongation, some formins have access to bind along the length of actin filaments. This can leads to actin filament bundling through binding actin filament sides. FH2 domain alone is sufficient for the bundling mediated by mammalian formin FMNL1 or mDia2. However, there is no polarity of bundled actin filaments mediated by those formins (Harris et al., 2006). Interstingly, WHIF1 is identified with the ability to accelerate both

actin polymerization and depolymerization and the latter effect is due to filament severing ability (Chhabra and Higgs, 2006; Gurel et al., 2014).

4.2.2. Microtubule binding and stabilization

So far, 6 mammalian formins have been shown to bind microtubules directly, such as mDia1, mDia2, INF1, WHIF1, FMN1 and FMN2. Except for INF1 and FMN1, the rest formins mDia1, mDia2, WHIF1 and FMN2 require the FH2 domain for microtubule binding. Constructs containing FH1, FH2, and C-terminal domains of mDia1, mDia2 and WHIF1 bind microtubules with high similar affinities (Gaillard et al., 2011). mDia2 FH1 and FH2 domains binds directly to microtubules and decreases tubulin dissociation rates in vitro (Bartolini et al., 2008). FMN2 directly interacts with polymerized microtubules in vitro via FH2 domain (Kwon et al., 2011). INF1 encompassing the conserved FH1 and FH2 domains in its N-terminal, associates discretely with microtubules through its novel C-terminal microtubule-binding domain (Young et al., 2008). In contrast, a novel microtubule-binding peptide was identified in the N-terminal of FMN1, which is sufficient for microtubule binding, while loss of FH1-FH2 domains in FMN1 has no effects on microtubule binding capability (Zhou et al., 2006).

In addition to direct binding of microtubule lattice, mDia1 also associates with microtubules indirectly via microtubule plus end binding proteins. Among them, microtubule end binding protein EB1 and cytoplasmic linker protein CLIP170 are two important interacting partners of mDia1 (Lewkowicz et al., 2008; Wen et al., 2004). CLIP170-mDia1 complexes can be recruited to the growing microtubule ends by EB1 with the advanced actin filament elongation. This enhancement is also applicable to other formins such as mDia2, DAAM1, INF1, and WHIF1 (Henty-Ridilla et al., 2016).

Formins can also modulate microtubule properties through post-translational modifications. It is reported that it is a general formins' feature to induce microtubule acetylation in NIH 3T3 fibroblasts (Thurston et al., 2012). Besides, some formins are also reported to affect microtubule detyrosination. mDia1 or WHIF1 knockdown decreases detyrosinated microtubules in NIH3T3 fibroblasts (Bartolini et al., 2016). Overexpression of mDia2 induces stable detyrosinated microtubules in serum-starved NIH3T3 fibroblasts (Bartolini et al., 2008). Interestingly, mDia1 is also necessary to maintain the level of detyrosinated microtubules in hippocampal neurons

(Qu et al., 2017). Besides, the microtubule regulation mediated by mDia1 in turn affect actin filament polymerization and alignment (Gaillard et al., 2011).

4.2.3. Formins regulation

As above described, DRFs formins contains a GTPase binding domain in their N-terminal. DRFs formins are activated by RhoGTPase binding through releasing intramolecular autoinhibition. Rho, Rac and Cdc42 are three well studied GTPase in formins (Kuhn and Geyer, 2014). mDia1 and mDia2 can also be regulated by another small RhoGTPase Rif during filopodium formation (Goh et al., 2011). In addition, RhoGTPase signaling is also involved in the regulation of formins' membrane localization. FMNL2 and FMNL3 can undergo protein N-myristoylation, which affects their localization and activity (Moriya et al., 2012). Interestingly, phospholipids can regulate mDia1 localization and activity (Ramalingam et al., 2010). Moreover, phosphorylation through serine/threonine kinases affects mDia3 and FMNL2 activation (Cheng et al., 2011; Wang et al., 2015).

4.2.4. Formins in neurons and neurological disorders

Given the vital roles of formins on actin and microtubule dynamics, formins are involved in general cell functions such as cell division, migration, vesicle and organelle trafficking, membrane receptor trafficking, and polarization (Breitsprecher and Goode, 2013). Although formins have not been extensively studied in nervous system cells, some works point to an important role of formins in neuronal development and function. In neurons, several specific formins have been identified with a function in different compartments. Knocking down mDia1 increases hippocampal dendritic spines number (Qu et al., 2017). However, loss of FMN2 leads to the decrease of spine density in hippocampal dentate granule neurons. Functional mutation of FMN2 also leads to synaptic density decrease (Law et al., 2014). Similarly, mDia2 knockdown results in a decrease of dendritic protrusion density with slight effects on spine morphology distribution (Hotulainen et al., 2009). Consistently, the aberrant lengthening of dendritic protrusions and gradual retraction of dendrites were observed after expression of constitutive active DAAM1 in Purkinje cells (Kawabata Galbraith and Kengaku, 2019). For dendrite development, mDia1 is involved in the regulation of dendrite architecture, which may be mediated through Golgi deployment (Hong et al., 2018). FMN1 overexpression induces an

increase of primary dendrites as well as glutamatergic synaptic inputs (Simon-Areces et al., 2011). Several formins like mDia1, mDia3, FMN2 and DAAM have been linked to axon growth cone maintenance and pathfinding (Kawabata Galbraith and Kengaku, 2019). At the presynapse, DAAM1 loss of function impairs activity dependent F-actin assembly in hippocampal pyramidal cells. At the postsynapse, GRID2IP interacts with glutamate receptor δ2 (GluRδ2) and loss of GRID2IP reduces Ca^{2+} requirement for LTD induction.

The importance of formins in nervous system has been further demonstrated in neurological disorders. Several formin genes have been identified as risk factors, such as FMN2 in sporadic amyotrophic lateral sclerosis (ALS) (Schymick et al., 2007), DAAM2 in schizophrenia (Kuzman et al., 2009) and FMN1 in early-onset obsessive-compulsive disorder (OCD) (Cappi et al., 2014). Moreover, loss of function or mutation of certain formins results in neurological deficiency. Patients with loss of functional DIAPH1 (mDia1) have symptoms of microcephaly, severe vision impairment, early-onset epilepsy and intellectual disability (Al-Maawali et al., 2016; Ercan-Sencicek et al., 2015). Formins deficiency of FMNL2 or FMNL3 may also lead to mental retardation in patients (Kumar et al., 2015; Lybaek et al., 2009). Mutants of FMN2 can even have intellectual disability and severe hearing loss symptoms. Mutations in WHIF1 were identified in patients with Charcot-Marie-Tooth disease, a hereditary peripheral neuropathy affecting motor and sensory nerves (Boyer et al., 2011; Mademan et al., 2013).

Objectives

The axon initial segment (AIS) has an extremely important role for the maintenance of neuronal polarity and action potential initiation. Recent studies have highlighted the role of AIS alterations in mental disorders and neurodegenerative diseases. Due to the complexity of AIS structure and the limited knowledge of its regulation and protein composition, it is still elusive how AIS structure is regulated and which regulators are involved in the AIS assembly, maintenance and plasticity in physiological and pathological conditions. Given AIS cytoskeleton is the basement of AIS control of axonal traffic and polarity, it is important to understand which proteins and mechanisms modulate actin and microtubules within the AIS. A few studies have described some proteins at the AIS, related to actin or microtubules regulation, such as synaptopodin or TRIM46. Previous studies have also shown that alterations of actin dynamics or microtubules post-translational modifications affect AIS integrity. However, we are far away to understand AIS cytoskeleton regulation. In this context, we hypothesized that formin family proteins may function as AIS cytoskeleton regulators. Formins are a group of proteins capable of regulating actin microfilaments and microtubules. The sparse knowledge of this family of proteins in brain indicates that these proteins are related to mental and neurodegerative diseases. Furthermore, one of its members, mDia1, is involved in axonal growth, epithelial cells polarity maintenance and interacts with proteins previously described at the AIS, such as β-catenin. Moreover, mDia1, not only modulates F-actin polymerization, but also affects microtubule acetylation.Thus, we studied formins as potential candidates for AIS actin and microtubules regulation.

The objectives of this study were:

Objective 1: To explore how formins may affect AIS cytoskeleton, compositions, plasticity or function, using a general formins inhibitor, SMIFH2.

Objective 2: Analysis of formins expression at the AIS and their roles on AIS assembly and maintenance. This objective was tackled using immunofluorescence, interference shRNA or over-expression plasmids to decrease or increase formins expression, and analyze their effects on AIS compositions and plasticity.

Objective 3: To identify potential candidates for formins regulation at the AIS and mechanisms related to formins that can contribute to the fine regulation of the AIS.

Materials and Methods

1. Animals

Animals were housed in the Experimental Animal Center of the Cajal Institute at controlled temperature and relative humidity with alternating 12 h light and dark cycles and free access to food and water. All animals were taken care in accordance with the appropriate national legislation (53/2013, BOE no. 1337) and guidelines of the Council of the European Communities (2010/63/UE). Protocols were previously approved by the CSIC bioethics committee.

2. Reagents

2.1. Chemicals

Pharmacological experiments were carried out in cultured hippocampal neurons or brain slices. Only SMIFH2 was used for acute treatments in brain slices. The reagents and their concentrations are listed in the following table:

Chemicals	Function	Concentration	Source	Identifier
SMIFH2	Formins inhibitor	Cultured neurons: 15 µM; Brain slices: 15, 30 µM	Sigma-Aldrich	Cat# 4826
SMIFH2	Formins inhibitor	Cultured neurons: 15 µM; Brain slices: 15, 30 µM	TOCRIS	Cat# 4401
Latrunculin A	Actin assembly inhibitor	0.5, 1 µM	TOCRIS	Cat# 3973
Jasplakinolide	Actin filaments stabilizer	5, 10, 25 nM	TOCRIS	Cat# 2792
Tubastatin A hydrochloride	HDAC6 inhibitor	10 µM	Sigma-Aldrich	Cat# SML0044
Ciliobrevin D	Dynein inhibitor	20 µM	Calbiochem	Cat# 250401
MDL 28170	Calpain inhibitor	50 nM, 1 µM	TOCRIS	Cat# 1146
Y-27632 dihydrochloride	ROCK inhibitor	40 µM	Sigma-Aldrich	Cat# Y0503
Y-27632 dihydrochloride	ROCK inhibitor	40 µM	TOCRIS	Cat# 1254
CT04	Rho inhibitor	1.0 µg/ml	Cytoskeleton	Cat# T04

Table M1. Drugs used for pharmacological experiments.

2.2. Antibodies

Antibodies information and the dilution used for immunocyto- or immunohistochemistry is provided in the following table. The antibody dilution is for immunocytochemistry, unless explicitly stated.

Antibodies	Dilution	Source	Identifier
Rabbit polyclonal anti-mDia1	1:70	Thermo Fisher Scientific	Cat# PA5-27607
Mouse monoclonal anti-AnkG (IgG2a)	IC/IH: 1:150	NeuroMab	clone N106/36
Mouse monoclonal anti-AnkG (IgG2b)	1:500	NeuroMab	clone N106/65
Mouse monoclonal anti-PanNaCh (IgG1)	1:100	Sigma-Aldrich	Cat# S8809
Rabbit polyclonal anti-pMLC	1:200	Thermo Fisher Scientific	Cat# PA5-17727
Rabbit polyclonal anti-βIV-Spectrin	1:1000	Dr. Matthew Rasband, Baylor College of Medicine	N/A
Chicken polyclonal anti-MAP2	1:5000	Abcam	Cat# ab5392
Rabbit polyclonal anti-GFP	1:1000	Thermo Fisher Scientific	Cat# A-6455
Mouse monoclonal anti-α-Acetylated tubulin (IgG2b)	1:5000	Sigma-Aldrich	Cat# T7451
Mouse monoclonal anti-α-Tubulin (IgG1)	1:5000	Sigma-Aldrich	Cat# T6199
Rabbit polyclonal anti-Kinesin 5C	1:200	Abcam	Cat# ab5630
Mouse monoclonal anti-Tau1 (IgG2a)	1:1000	Millipore	Cat# MAB3420
Rabbit polyclonal anti-Synaptopodin	1:500	Sigma-Aldrich	Cat# S9442
Alexa Fluor 568 Phalloidin	1:100	Thermo Fisher Scientific	Cat# A12380
bisBenzimide H 33342 trihydrochloride	IH: 5 μg/ml	Sigma-Aldrich	Cat# B2261
Alexa Fluor 488, Alexa Fluor 568, Alexa Fluor 647 goat anti-mouse IgG2a	IC: 1:1000 IH: 1:500	Thermo Fisher Scientific	Cat# A21131; A21134; A21241
Alexa Fluor 488, Alexa Fluor 568, Alexa Fluor 647 goat anti-mouse IgG2b	1:1000	Thermo Fisher Scientific	Cat# A21141; A21144; A21242
Alexa Fluor 488, Alexa Fluor 568, Alexa Fluor 647 goat anti-mouse IgG1	1:1000	Thermo Fisher Scientific	Cat# A21121; A21124; A21240
Alexa Fluor 488, Alexa Fluor 594, Alexa Fluor 647 donkey anti-rabbit IgG (H+L)	1:1000	Thermo Fisher Scientific	Cat# A21206; A21207; A31573
Alexa Fluor 647 goat anti-chicken IgY (H+L)	1:1000	Thermo Fisher Scientific	Cat# A21449

Table M2. Antibodies used for immunofluorescence.

2.3. Oligonucleotides and recombinant DNA

The interference RNA plasmids of mouse for mDia1 were purchased from Origene with the RFP expression element. Two effective targets were identified: 5'-TGCCACTGACGAGAAGGACAAGTTTGTTG-3' (Cat# TF500527D, shmDia1-1) and 5'-GAAGGAATCCTACTGCTGGTCAGAGCCAT-3' (Cat# TF500527A, shmDia1-2). HDAC6 interference RNA plasmid with GFP expression element is kept in the laboratory and has been previously described (Tapia et al., 2010). AnkyrinG-GFP (270 kD) plasmid was a kind gift from Dr. Van Bennett laboratory. pEGFP-N1, as a control plasmid of recombinant DNA expression was bought from Clontech (Cat# 6085-1). The GFP-CA-mDia1 vector expressing a constitutively active form of mDia1 was a gift from Klaus Hahn & Ronen Zaidel-Bar (Addgene plasmid # 45583). The pEFmEGFP-mDia2 vector expressing mDia2 was a gift from Arthur Alberts (Addgene plasmid # 25407). Three plasmids of EGFP-RhoA-WT (wild type, Addgene plasmid # 12965), EGFP-RhoA-T19N (dominant negative type, Addgene plasmid #12967) and EGFP-RhoA-Q63L (constitutively active type, Addgene plasmid # 12968) were all from Gary Bokoch. The recombinant vector of EB1-GFP was a gift from Tim Mitchison & Jennifer Tirnauer (Addgene plasmid # 39299).

Plasmids were first transformed into competent DH5α bacteria. Transformed bacteria were selected on LB agar plates with appropriate antibiotics. Individual colonies were used for storing and replicating plasmids. HiSpeed Plasmid Maxi Kit (QIAGEN, Cat# 12663) was utilized for plasmids extraction and the plasmids quality was tested via agarose gel electrophoresis and spectrophotometer. Plasmids mainly presented as supercoiled DNA with a range of A260/280 ratio (1.8-2.0) read by NanoDrop-1000 were used for transfection.

3. Hippocampal Cultures

Mouse hippocampal neurons were prepared as previously described (Fig. M1)(Kaech and Banker, 2006). Briefly, neurons were cultured on polylysine-treated coverslips, which were suspended above an astrocyte feeder layer and maintained in serum-free medium. Astrocytes from cortex of embryonic day 17 (E17) CD-1 mouse were prepared 2 weeks in advance and used for co-culturing with neurons when they reach 60%-70% confluence. Neurons were obtained from E17 CD-1 mouse hippocampi, which were incubated in a 0.25% trypsin solution

in Ca^{2+}/Mg^{2+} free

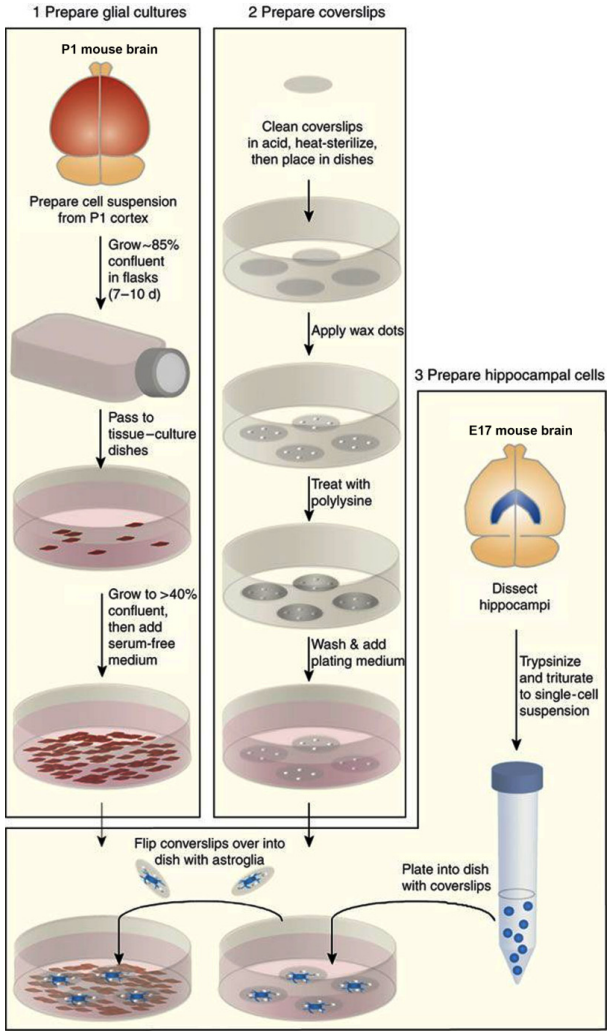

Figure M1. Three steps for preparing hippocampal neuronal cultures. Adapted from (Kaech and Banker, 2006).

Hank's buffered salt solution (HBSS) and dissociated using fire-polished Pasteur pipettes. The cells were plated on polylysine coated coverslips (1 mg/ml) at a density of 6,000 cells/cm^2 for 2 h in plating medium (minimum essential medium [MEM], 10% horse serum, 0.6% glucose and Glutamax-I). Then coverslips were inverted and transferred to culture dishes containing astrocytes. Astrocytes medium was replaced by neuronal culture medium 24 h before neuronal culture (Neurobasal medium, B27 supplement, Glutamax-I). To avoid contact between neurons and astrocytes, paraffin beads were placed on coverslips before neuronal plating.

5 µM 1-β-D-arabinofuranosylcytosine (AraC) was added after 2 days in culture to curb glial cells proliferation. One third of neuronal medium was replaced every week. Pharmacological treatments were described in the results section. In the case of pharmacological treatments in the absence of glial cell layer, coverslips were transferred to plates containing glial cells conditioned medium. Conditioned medium was prepared from 24 h maintenance of 60%-70% glia using neuronal culture medium. For FRAP experiments, hippocampal neurons were plated directly on the glass bottom of µ-Dish 35 mm culture dishes treated with polylysine (Ibidi). Neurons were plated at a density of 20,000 cells/cm^2 and glia cells were prepared on the coverslips with a diameter of 24 mm. Before plating glia cells, coverslips were treated with polylysine (0.1 mg/ml) and placed with paraffin beads.

4. Neuronal transfection

In this study, primary hippocampal neurons were transfected through two approaches: nucleofection and lipofection.

Nucleofection was done using the P3 Primary Cell 4D-Nucleofector^{TM} X Kit L for primary mammalian neural cells (Cat# V4XP-3012, Lonza) according to the manufacturer's instructions. Namely, nucleofection for scrRFP, shmDia1-1, shmDia1-2, GFP, GFP-CA-mDia1, EGFP-mDia2, EGFP-RhoA-WT, EGFP-RhoA-T19N, EGFP-RhoA-Q63L or shHDAC6 was performed using 3 μg of total DNA and 3× 10^{6} cells for each nucleofection. Given the similar molecular weight of plasmids between shmDia1-1 and shHDAC6, co-nucleofection was achieved using 1.5 μg of DNA for each. After nucleofection, neurons were plated at a density of 15,000 cells/cm^2 and cultured as above described.

Lipofection experiments were performed as follows, hippocampal neurons with a density of 20,000 cells/cm^2 were transfected at 8-14 DIV with Lipofectamine 2000 (Cat#11668-030, Invitrogen) and maintained for another 24 or 48 h. Lipoplexes were prepared at a ratio of 1 μl of Lipofectamine per 1 μg of DNA. Total transfected DNA per 35 mm culture dish for GFP, GFP-CA-mDia1, scrRFP, shmDia1-1, EGFP-RhoA-WT, EGFP-RhoA-T19N, EGFP-RhoA-Q63L or EB1-GFP was 2 μg and for ankyrinG-GFP it was 5 μg. Specifically, coverslips coated with neurons were quickly inverted and transferred into a clean 35 mm culture dishes or 6-well plates in 2 ml mixed medium (1 ml conditioned medium and 1 ml Neurobasal medium). Lipofectamine and DNA were mixed with Neurobasal to a final volume of 50 μl per culture dish respectively and left for 3-5 min. Next, plasmid DNA solution was added to Lipofectamine solution and gently mixed and left for 20 min at room temperature (RT). Thereafter, 100 μl of the mix was dropwise added to each culture dish or well and left for 90 min in the incubator. Lipofectamine was then washed out 3 times with 2 ml Neurobasal medium pre-warmed to 37 °C. After washout, coverslips were transferred back to the original 35 mm culture dishes for continuous culture. For FRAP experiments, neuronal culture medium and coverslips coated with glia were removed before lipofection and kept in the incubator. After washout of Lipofectamine, neuronal culture medium and coverslips were transferred back to the original μ-Dish 35 mm culture dishes for continuous culture.

5. Immunocytochemistry

Neurons were fixed in 4% paraformaldehyde (PFA) for 15 min and washed in phosphate buffered saline (PBS). After 3 washes, coverslips were treated with 50 mM NH_4Cl and incubated in blocking buffer for 1 h (0.22% gelatin, 0.1% Triton X-100 in PBS) to avoid non-specific binding. The cells were then incubated for 1 h with primary antibodies diluted in blocking buffer. Following 3 additional washes, coverslips were then incubated with appropriate secondary antibodies in blocking buffer for 45 min, followed by 2 washes in blocking buffer and 2 washes in PBS. F-actin was stained using Alexa-Fluor-568-conjugated Phalloidin. After staining, the coverslips were mounted with Fluoromount-G (Southern-Biotech). All above described procedures were performed at RT. Images were acquired on a Leica fluorescence inverted microscope DMI6000B (40x, oil immersion, 1.00 N.A.) or Leica SP5 confocal microscopes (40x, oil immersion, 1.25 N.A.). For quantitative analysis in different conditions, coverslips in each experiment were stained with freshly diluted antibodies at the same time and experienced the same procedures for labelling. Besides, samples from every experiment were photographed with the same settings of microscopes and all measurements taken under the same criteria. To validate the efficiency of mDia1 shRNAs, neurons were nucleofected with control scrRFP or mDia1 inteference shRNAs and fixed at 10 DIV. Hippocampal neurons were stained with mDia1 antibody as above described. The staining intensity was calculated by measuring the total mDia1 intensity in the soma and the background was subtracted. AIS measurements were separately described below. Figures were prepared for presentation using the Adobe CS4 software.

6. Detergent extraction of hippocampal neurons

13, 14 or 20 DIV neurons were first rinsed in phosphate buffer (PB) and incubated in the extraction buffer (pH 7.0, 30 mM PIPES, 1 mM $MgCl_2$, 5 mM EDTA, 0.5% Triton X-100) for 5 minutes at 37 °C as previously described (Garrido et al., 2003). After extraction, neurons were rinsed in PB and fixed in 4% PFA for immunocytochemistry. For 4 °C extraction experiments, the same manipulations were performed except that neurons were incubated in the extraction buffer for 20 min on ice. Coverslips were photographed on an upright Leica SP5 confocal microscope using Leica DM6000B 40x 1.25 N.A. oil objective with 1024 x 1024 pixels. In the

case of deconvolution process, images with all stacks were processed by blind iterative deconvolution with 10 iterations according to standard procedures in Leica SP5 3D deconvolution software. Figures were prepared for presentation using the Adobe CS4 software.

7. Fluorescence recovery after photobleaching (FRAP)

Neurons were lipofected with AnkG-GFP at 8 DIV as above described and treated with 15 μM SMIFH2 1 h prior to being applied to FRAP at 9 or 10 DIV. Live imaging was performed on a Leica SP5 inverted confocal microscope, equipped with Leica DMI6000B 63x 1.40 N.A. oil objective, live cell chamber and FRAP Wizard system. μ-Dish 35 mm culture dishes were mounted on an adaptor and maintained at 37 °C and 5% CO_2 in the live cell chamber. Time-lapse images were acquired using bidirectional scan at 1400 Hz with the format of 256 x 256 pixels and the pinhole size was 2 airy units. AIS were distinguished through stronger GFP signal of AnkG-GFP. Besides, the morphological differences between axon and dendrites contribute to the AIS identification. A ROI with an area of 5 μm x 5 μm on the AIS was photobleached at 100% 488-nm Laser Line Visible with 25% Argon Laser Power, reducing local fluorescence by 80-95%. FRAP was performed with 10 frames of 0.1 s interval for Pre-bleach and 15 s for Bleach with 0.1 s interval, followed by Post-bleach with 240 frames of 0.5 s interval. For FRAP analysis, fluorescence signal was background subtracted using the formula 'I(t) = I_indicated region(t) – I_background(t)' frame by frame. The normalization of recovery R_norm(t) was calculated in the bleached ROI region according to the formula 'R_norm(t) = (I_bleached region(t) - I_bleached region(0))/(I_bleached region(Δt) - I_bleached region(0))', in which I_bleached region(0) indicates the region's mean intensity directly after bleaching, and I_bleached region(Δt) indicates the intensity averaged over last five frames before bleaching. To account for the bleaching due to imaging itself, additional correction was performed using intensity of neighboring nonbleached regions in the AIS according to the equation 'R(t) = R_norm(t) x (I_control(Δt)/I_control(t))', where I_control corresponds to the mean fluorescence intensity subtracted background of the non-bleached region and I_control(Δt) denotes the average intensity from last five frames before bleaching. The recovery curve was generated by pooling together at least 15 neurons in each condition and averaging each frame the recovery rate. The maximum recovery percentage was obtained through averaging recovery data in 20 s

at the plateau from every neuron in Sigmaplot v12.5 (Systat Software Inc., San Jose, CA, USA).

8. Immunohistochemistry

Brains from mice P26-P30 days old were quickly removed and acute coronal slices (300 µm) containing sensorimotor cortex were cut with a vibratome (4 °C) in a solution containing: 234 mM sucrose, 11 mM glucose, 26 mM $NaHCO_3$, 2.5 mM KCl, 1.25 mM NaH_2PO_4, 10 mM $MgSO_4$, and 0.5 mM $CaCl_2$ (equilibrated with 95% O_2–5% CO_2). SMIFH2 treatment was carried out at a concentration of 15 or 30 µM for 3 h and the same volume of vehicle DMSO was used as control. Treated brain slices were fixed for immunohistochemistry using 4% PFA for 30 min at RT and washed in PBS. To block antibody unspecific binding, slices were incubated for 2 h at RT with PBS containing 0.1% TritonX-100 and 10% goat serum. Thereafter, slices were immersed overnight at 4 °C with mouse monoclonal anti-AnkG (IgG2a, 1:150) in PBS containing 0.1% TritonX-100 and 1% goat serum on a small shaker, followed by 5 washes using antibody diluents with 1 h interval for each time. The secondary antibody goat anti-mouse IgG2a conjugated with Alexa Fluor 488 (1:500) was incubated for 2 h at RT. After 5 additional washes, sections were counterstained with bisBenzimide for nuclei staining before mounted in Fluoromount G. Images were acquired on an upright Leica SP5 confocal microscope using Leica DM6000B 40x 1.25 N.A. oil objective with 1024 x 1024 pixels. To capture ankyrinG signal entirely and increase the number of in-focus AIS, sections were imaged in z stacks of 70 steps with a 0.5-µm step size. For qualitative analysis, a Z-projection (maximum intensity projection) was obtained in Fiji-ImageJ software and fluorescence signal was background subtracted. We measured cortical AIS in layers II/III, layer IV and layers V/VI. Cortical layers were distinguished according to nuclei patterns. In the case of CA1 staining quantification, every generated Z-projected image produces one datum. Correct total fluorescence (CTF) and correct mean fluorescence (CMF) were used to examine the ankyrinG changes according to the following formulas: ‘CTF = Integrated intensity - (Mean background x Area)’ and ‘CMF = Mean intensity - Mean background’, where Mean background denotes the intensity averaged over 6 mean background values along the whole selected AIS plexus. Figures were prepared for presentation using the Adobe CS4 software.

9. AIS length and fluorescence intensity measurements

Hippocampal neurons were imaged using a Leica fluorescence inverted microscope DMI6000B (40x, oil immersion) or Leica SP5 confocal microscopes (40x, oil immersion). The settings were adjusted to prevent signal saturation and the images were taken in z stacks with a 0.5-μm step size using confocal microscopes. Z stack images were projected into a single plane using maximum intensity projections, followed by AIS analysis in Fiji-ImageJ software. To compare fluorescence intensity, all the parameters were exactly the same to all conditions in one experiment. 8-bit images were used for AIS components and position measurement. For ankyrinG measurement, we drew a line starting at the limit of soma identified by MAP2 staining, and extended it along the the axon, past the AIS. Data were smoothed every 1 μm using Sigma Plot 12.5 software, followed by the normalization according to the value of maximum mean fluorescence in control neurons to be 100%. AIS start and end positions were determined at the proximal and distal axonal positions respectively, where the normalized profile declined to 33% of maximum fluorescence intensity, as described previously (Grubb and Burrone, 2010). Then total ankyrinG fluorescence within AIS was obtained by adding intensity values from the start to the end position. To obtain the mean fluorescence per 1 μm, the normalized total ankyrinG intensity within AIS was then divided by the length. The sum of fluorescent intensity values added in the proximal axon of 30 μm length was used for total ankyrinG intensity comparations, unless explicitly stated. Likewise, PanNaCh, pMLC and βIV-Spectrin were compared and presented as 100% in the control. For other AIS measurement, ankyrinG staining was employed to identify the AIS position. In the case of acetylated α-tubulin analysis, integrated acetylated α-tubulin was obtained from extracted hippocampal neurons. In the case of hippocampal neurons without extraction, the fluorescent intensity of acetylated α-tubulin and total α-tubulin in the AIS and neighboring dendrites was collected from the same neuron respectively as above described. The ratio profile of acetylated α-tubulin / α-tubulin was first obtained every 0.12 μm, then was smoothed and normalized considering the starting value in control neurons to be 1. To study the ratio value of total acetylated α-tubulin / total α-tubulin, both signals were quantified respectively in the AIS or proximal dendrites within 30 μm length and then divided. The ratio value was normalized against control. In the case of F-actin analysis,

smoothed data were normalized taking the averaged F-actin intensity of the start position in control neurons to be 100%. Then total F-actin intensity was obtained by adding 30 μm intensity values along the AIS. In the case of cisternal organelle analysis, we labelled synaptopodin and ankyrinG to identify cisternal organelles and AIS respectively. Counting was performed on Leica SP5 confocal microscopes with 40x objectives. We randomly evaluated AIS positive neurons whether it is cisternal organelle positive or negative. Every 30-40 neurons generated one percentage datum and data were from 3 times independent experiments. In the case of KIF5C analysis, a line was drawn along the entire axon and started at the limit of soma. To compare somal KIF5C signal, integrated intensity of soma was measured and normalized against control. To compare axonal KIF5C, average intensity of the entire axon was calculated and normalized against control. To study the distribution of KIF5C in axons, we calculated total KIF5C intensity in the proximal and distal 50 μm length from the same axon respectively, followed by the division of proximal/distal axon.

10. Axon and dendrites morphology analysis

Nucleofected neurons were fixed at 3 DIV or 7 DIV for axon or dendrites analysis. Positive cells were randomly chosen and photographed with 40x Leica SP5 confocal microscopes in z stacks with a 1-μm step size. The settings were adjusted to prevent signal saturation and applied to all conditions in every experiment. Z-projected images were used for the following evaluation. Tau1 staining served to identify axons for 3 DIV nucleofected neurons. According to the number of axons for each neuron, three categories were performed: no axon, 1 axon and axons ≥ 2. Every 30 neurons from each coverslip generated one percentage datum for each category. MAP2 signaling served to identify dendrites for 7 DIV nucleofected neurons. To quantify axonal or dendritic length and ramifications, lines were semi-automatically traced along the entire extension of axons or dendrites and their branches using NeuronJ program in Fiji software. Data were from 3 times independent experiments.

11. Electrophysiology

Whole-cell patch clamp recordings were obtained from CA3 hippocampal neurons. The external solution contained (mM): 125 NaCl, 26 $NaHCO_3$, 3 $CaCl_2$, 2.5 KCl, 2 $MgCl_2$, 0.8 NaH_2PO_4, and 10 D-glucose, and was equilibrated with 95% O_2-CO_2. Patch pipettes (5-10 MΩ)

were filled with a solution containing (mM): 120 potassium gluconate, 20 KCl, 0.5 EGTA, 10 HEPES, 2 Na_2ATP, 0.3 NaGTP and 2 $MgCl_2$, pH 7.4. Recordings were made at RT. The voltage and current signals were low-pass filtered (3 kHz) and acquisition of sequences (500-1,500 ms) was performed at a frequency of 0.1 Hz with P-clamp 8 or 10 (Axon Instruments). Sodium currents were evoked by a voltage step (50 ms) from -70 to 0 mV. The capacitive and leak components of the evoked current were subtracted with a conventional P/4 protocol. Intrinsic neuronal excitability was monitored with depolarizing current pulses (1 s) of increasing amplitude (from +10/+500 pA).

12. Statistical analysis

All statistical analyses were carried out in GraphPad Prism 5 and Sigmaplot v12.5. All data were collected and analyzed from at least 3 independent experiments. All statistical details including the number of experiments and statistical tests performed can be found in each figure and figure legends. Sample distributions were first assessed for normality using the D'Agostino and Pearson omnibus test or Shapiro-Wilk test. Statistical analysis was performed by two tailed t-test for two group comparisons: unpaired t test for normally distributed data and Mann-Whitney test for non-normally distributed data. For multiple group comparisons, One-way analysis of variance with Tukey post test and Kruskal-Wallis with Dunn's post test were performed for normally and non-normally distributed data respectively. Graphs were represented as the mean ± SEM. And the p value less than 0.05 was considered a significant difference, which was expressed as follows: *$p < 0.05$, **$p < 0.01$, ***$p < 0.001$.

Results

1. Formins inhibition disrupts AIS integrity

Actin and microtubules cytoskeleton plays an important role in the development, maintenance and function of the Axon Initial Segment (AIS). However, to our knowledge this cytoskeleton regulation on AIS is very limited. In this context, formins are known to control actin trails in the axon, and are able to regulate both actin and microtubules in different cellular compartments of different cell types (Ganguly et al., 2015; Palazzo et al., 2001; Qu et al., 2017; Soykan et al., 2017; Thurston et al., 2012). Thus, we hypothesized that formins may be involved in the regulation of the AIS.

To determine the effects of formins activity on AIS structure and composition, we employed SMIFH2, an inhibitor of FH2 domain, a functional conserved region in formins (Bartolini and Gundersen, 2010; Courtemanche, 2018; Rizvi et al., 2009). First, we tested the optimal and non-toxic SMIFH2 concentration and time of treatment. The vehicle of DMSO was solvent and the same volume of DMSO was applied as the corresponding control. Our observations indicated that treatments with a SMIFH2 concentration higher than 15 μM for more than 3 h were deleterious for cultured hippocampal neurons. Morphologically, no difference was observed between control and SMIFH2 groups treated with a concentration of 15 μM for 3 h (Fig. R1A). However, ankyrinG, the master protein of AIS, decreased after 3 h treatment of SMIFH2 during neuronal development (7, 14 and 21 DIV) (Fig. R1A, B). The reduction of ankyrinG intensity was pronounced at 7 DIV (68.47 ± 2.96% *vs* 100 ± 2.80% in control neurons, Mann Whitney test, $p < 0.0001$) and modest at 14 DIV (74.07 ± 1.90% *vs* 100 ± 2.10% in control neurons, Mann Whitney test, $p < 0.0001$), while more mature neurons at 21 DIV showed 86.81 ± 2.68% total ankyrinG intensity after treatment compared to 100 ± 3.38% in the corresponding control neurons (Mann Whitney test, $p = 0.0078$). This suggests that increased maturity of the AIS along development makes AIS less susceptible to the loss of formins activity.

Next, we shortened the treating duration of SMIFH2 ranging from 30 min to 3 h to examine how quickly this process takes place. 14 DIV neurons were treated for 30 min, 1 h, 2 h and 3 h (Fig. R1C). A significant decrease of total ankyrinG was detected as soon as 30 min after SMIFH2 treatment (85.56 ± 1.58% *vs* 100 ± 1.54% for 0 h, $p < 0.001$), that was maintained

for treatments of 1 h and 2 h (82.43 ± 1.44% and 84.63 ± 1.65%, respectively). The reduction of ankyrinG continuously increased after 3 h treatment (76.99 ± 1.53%), indicating a time-dependent effect of lack of formins activity on ankyrinG intensity.

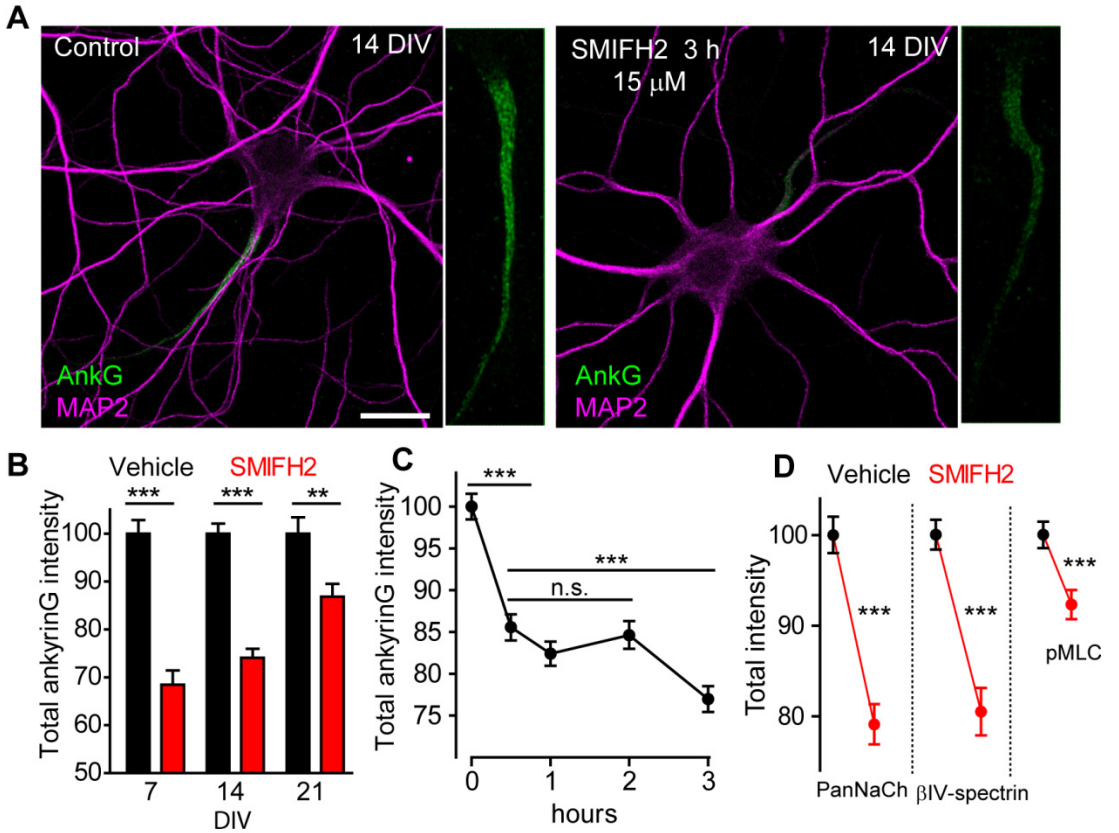

Figure R1. Formins inhibition decreases AIS components in hippocampal neurons. (**A**) Neurons were cultured for 14 DIV and then treated for 3 h with vehicle DMSO or 15 µM SMIFH2. Neurons were fixed and stained with MAP2 (magenta) and ankyrinG antibodies (green). Magnification of AIS in each condition is shown in adjacent panels. Scale bar = 20 µm. (**B**) 7, 14 and 21 DIV hippocampal neurons were treated for 3 h with vehicle or 15 µM SMIFH2 respectively. Total ankyrinG fluorescence intensity was quantified and normalized to their respective vehicle treated neurons at each developmental stage. **p < 0.01, ***p < 0.0001, Mann Whitney test. (**C**) 14 DIV neurons were treated with DMSO or 15 µM SMIFH2 and fixed after 0, 0.5, 1, 2 and 3 h respectively. Total ankyrinG fluorescence intensity was normalized to the control (0 h). n.s., not significant, ***p < 0.001, Kruskal-Wallis, Dunn's multiple comparison test. (**D**) Quantification of AIS total voltage gated sodium channels (PanNaCh), βIV-spectrin and phospho-myosin light chain (pMLC) fluorescence intensity in 14 DIV neurons treated with DMSO or 15 µM SMIFH2 for 3 h. ***p < 0.001, unpaired t test. All data were acquired from three independent experiments and represented as the mean ± SEM.

In addition, we checked other richly accumulated AIS components, such as, βIV-spectrin, voltage-gated sodium channels (PanNaCh) and the newly AIS identified actin related phospho-myosin light chain (pMLC). Neurons were treated for 3 h at 14 DIV and labeled with PanNaCh, βIV-spectrin or pMLC antibodies. In line with the decrease of total ankyrinG intensity at the AIS, the signal of PanNaCh, βIV-spectrin or pMLC was remarkably reduced after blocking formins activity (PanNaCh, 79.15 ± 2.24% *vs* 100 ± 2.02% in control neurons, p < 0.0001; βIV-spectrin, 80.48 ± 2.63% *vs* 100 ± 1.65% in control neurons, p < 0.0001; pMLC, 92.3 ± 1.60% *vs*

100 ± 1.44% in control neurons, p = 0.0004; Fig. R1D).

To corroborate the decrease of AIS components after inhibiting formins activity, we took advantage of the AIS property to be resistant to detergent extraction (Garrido et al., 2003; Winckler et al., 1999). Neurons at 13 DIV were treated with DMSO or SMIFH2, followed by the extraction of live neurons using 0.5% TritonX-100 at 37 ºC for 5 min. After fixation and immunoflurescence, the remaining AIS components were evaluated. Consistent with the results obtained previously from non-extracted neurons, formins inhibition decreased the intensity of ankyrinG (71.34 ± 3.51% *vs* 100 ± 10.61% in control neurons, Mann Whitney test, p = 0.0273) and βIV-spectrin (56.33 ± 3% *vs* 100 ± 11.45% in control neurons, Mann Whitney test, p = 0.0001) (Fig. R2A, B).

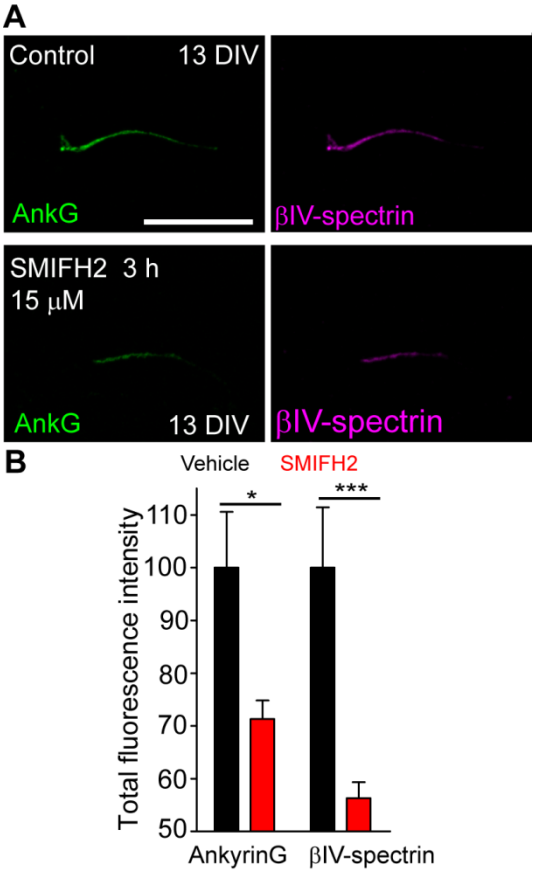

Figure R2. Formins inhibition reduces ankyrinG and βIV-spectrin intensity in hippocampal neurons detergent extracted at 37 ºC. (**A**) After 3 h treatment with DMSO or 15 μM SMIFH2, 13 DIV neurons were extracted using extraction buffer containing 0.5% TritonX-100 at 37 ºC for 5 minutes. Fixed neurons were stained with ankyrinG (green) and βIV-spectrin (magenta) antibodies. Scale bar = 20 μm. (**B**) Quantification of total ankyrinG and βIV-spectrin fluorescence intensity. *p < 0.05, ***p < 0.001, Mann Whitney test. Data in graphs were acquired from three independent experiments and represented as the mean ± SEM.

Formins expression is not limited to neurons, but also expressed in glia cells (Gardberg et al., 2010; Williams et al., 2018). In our co-culture model, both neurons and glia cells lost formins activity when samples were applied to the treatment with SMIFH2. To exclude that formins inhibition in glial cells could be responsible for the effects on AIS, 14 DIV neurons were placed in glia cell conditioned medium without astrocytes, before treatment with SMIFH2 for 3 h. A similar decrease trend of total ankyrinG intensity was observed after blocking formins activity (71.2 ± 1.89% *vs* 100 ± 1.75% in control neurons, Mann Whitney test, p < 0.0001; Fig. R3A). This trend was corroborated in the cumulative fraction plot of individual neuron values for total ankyrinG intensity (Fig. R3A).

We have shown that formins inhibition reduces AIS components expression. Given AIS is characterized by a dynamic short- and long-term structural plasticity, we tested whether neurons could recover AIS composition after SMIFH2 inhibition. Thus, a set of neurons, previously treated with SMIFH2 or DMSO for 3 h, were washed and transferred to new plates in glia cell conditioned medium containing astrocytes as feeder layer for another 6 h in the absence of SMIFH2. Other set of neurons were fixed after 3 h SMIFH2 or DMSO treatment and used as control neurons. Consistent with above observations, 3 h treatment with SMIFH2 clearly decreased total ankyrinG intensity (68.79 ± 2.72%, Fig. R3B). After additional 6 h in the absence of SMIFH2, ankyrinG expression was not recovered and instead another 15% significant decrease (53.86 ± 2.30%) was observed compared to neurons directly fixed after SMIFH2 treatment (68.79 ± 2.72%, Fig. R3B). However, ankyrinG intensity in DMSO treated neurons did not change after 6 h (97.4 ± 3.17% *vs* 100 ± 2.79% in only 3 h DMSO treated neurons, Fig. R3B).

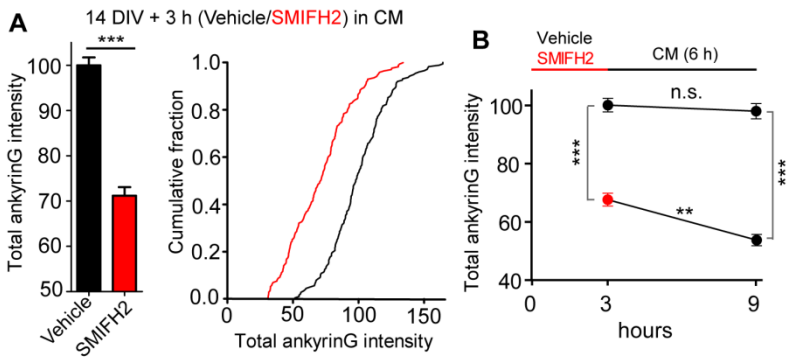

Figure R3. Formins inhibition has long-term effects on ankyrinG decrease. (**A**) 14 DIV hippocampal neurons were treated with DMSO or 15 µM SMIFH2 for 3 h in glia cell conditioned medium without astrocytes. Quantification of total ankyrinG fluorescence intensity. ***p < 0.0001, Mann Whitney test. In the right panel, a cumulative fraction plot shows a distribution of normalized total ankyrinG intensity. (**B**) Neurons were treated with DMSO or 15 µM SMIFH2 for 3 h. Then neurons were washed and cultured for another 6 h in glia cell conditioned medium containing astrocytes. Total ankyrinG intensity was quantified and normalized to DMSO treated neurons before maintenance in conditioned medium. n.s., not significant, **p < 0.01, ***p < 0.001, Kruskal-Wallis, Dunn's multiple comparison test. All data were acquired from three independent experiments and represented as the mean ± SEM.

Together, all these immunofluorescence quantification data indicate that neuronal formins activity is required for AIS components maintenance. In order to ascertain this role of formins on AIS, we tested whether SMIFH2 inhibition had the same effect on ankyrinG-GFP expressing neurons. To this end, we first studied the impacts of formins on exogenous ankyrinG-GFP accumulation in the AIS. In brief, 10 DIV hippocampal neurons were transfected with a plasmid expressing ankyrinG-GFP, and after 48 h expression, neurons were treated with SMIFH2 for 3 h. AnkyrinG-GFP mainly accumulated in the AIS and decreased after formins inhibition (Fig. R4A-C), which further confirmed the results obtained from endogenous ankyrinG. Namely, total

GFP signal of ankyrinG-GFP in the AIS reduced by 34% (65.54 ± 6.50% *vs* 100 ± 6.93% in control neurons, unpaired t test, p = 0.0008, Fig. R4B). Analysis of the average GFP signal revealed the decrease profile along the AIS (Fig. R4C).

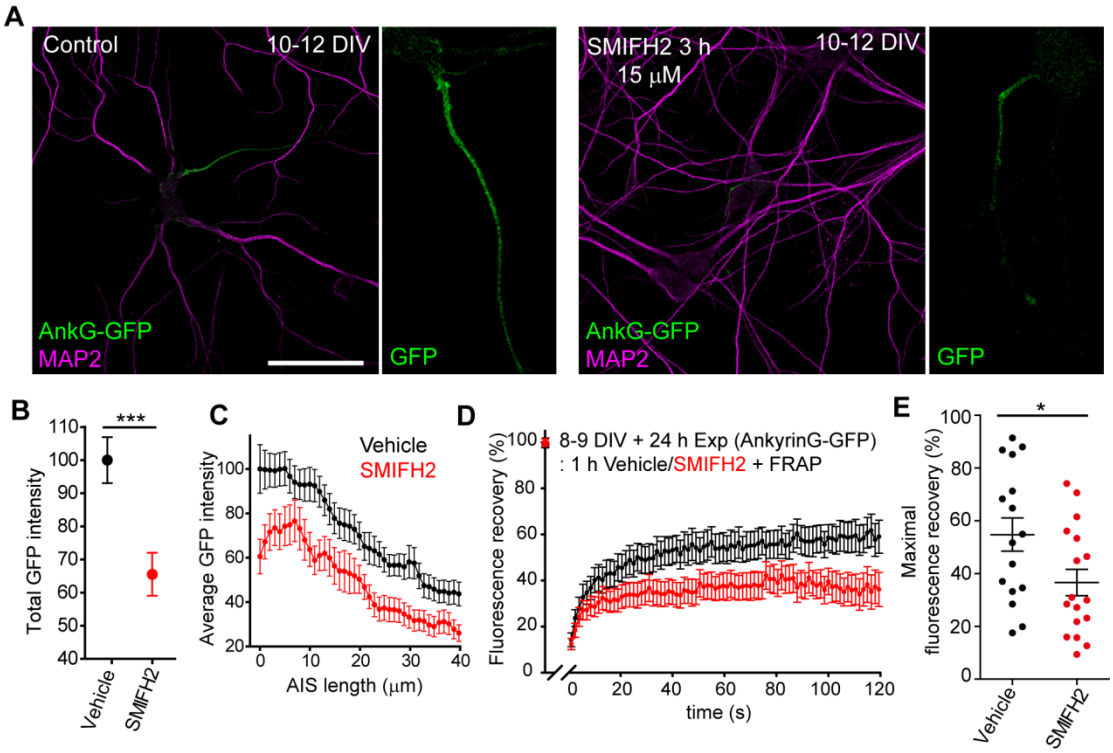

Figure R4. Formins inhibition decreases ankyrinG-GFP accumulation in the AIS. (**A**) 10 DIV hippocampal neurons were transfected with ankyrinG-GFP for 48 h and then exposed to DMSO or 15 µM SMIFH2 for 3 h. The neurons were stained with MAP2 antibody (magenta). AnkyrinG-GFP was richly expressed in the AIS. AIS magnification and ankyrinG-GFP signal for each condition are shown in adjacent panels. Scale bar = 50 µm. (**B**) Quantification of total GFP fluorescence intensity in the AIS in vehicle (black) or SMIFH2 treated neurons (red). ***p < 0.001, unpaired t test. (**C**) Normalized average GFP intensity profile along the AIS in the presence (red) or absence (black) of 15 µM SMIFH2 treatments. (**D**) Percentage of AIS ankyrinG-GFP fluorescence recovery for 120 s after photobleaching. Hippocampal neurons were transfected with ankyrinG-GFP plasmids at 8-9 DIV and kept in culture for 24 h before exposing them to DMSO (black) or 15 µM SMIFH2 (red) treatment for 1 h, and posterior FRAP experiments. (**E**) The graph represents the mean ± SEM of the maximal GFP recovery capability for each neuron. *p < 0.05, unpaired t test. All data were acquired from three independent experiments and represented as the mean ± SEM.

After this confirmation, we took advantage of the possibility to analyze live ankyrinG-GFP expressing neurons after DMSO or SMIFH2 treatments. Thus, we performed FRAP experiments to analyze ankyrinG-GFP mobility at the AIS in DMSO or SMIFH2 treated neurons. 8-9 DIV neurons were transfected with ankyrinG-GFP and left for 24 h before being treated with DMSO or SMIFH2 for 1 h prior to confocal live imaging. Next, we performed ankyrinG-GFP photobleaching on a section of 5 µm of the AIS and analyzed GFP signal during the whole processes of live imaging. The maximal ankyrinG-GFP signal recovery was significantly lower in SMIFH2 treated neurons (36.6 ± 5.01% *vs* 54.77 ± 6.32% in DMSO treated neurons,

unpaired t test, p = 0.0305, Fig. R4D, E). These results suggest that formins inhibition affects ankyrinG-GFP diffusion and tethering at the AIS. Nevertheless, it may also reflect the possibility of alterations on ankyrinG traffic at the AIS.

2. Formins inhibition alters AIS actin and microtubules cytoskeleton

In view of our results, and taking in account that AIS cytoskeleton integrity and dynamics is essential for AIS components tethering and trafficking, we analyzed the AIS actin and microtubules cytoskeleton after formins inhibition. We first studied F-actin at the AIS using fluorescent Phallodin. To do so, 14 DIV neurons were treated with DMSO or SMIFH2 for 3 h and stained with Phalloidin. AIS identification was done by ankyrinG staining and F-actin intensity was quantified in the ankyrinG positive area in confocal sections of control or SMIFH2 treated neurons. Consistent with other reports (Jones et al., 2014), F-actin signal in the AIS was not high in mature neurons (Fig. R5A). AIS F-actin was distributed in patches along the AIS (Fig. R5A). Formins inhibition with SMIFH2 decreased 18% of total F-actin intensity at the AIS (81.59 ± 1.94% *vs* 100 ± 2.27% in control neurons, Mann Whitney test, p < 0.0001; Fig. R5B, C). In line with this, the average profile along the AIS also showed a reduction of F-actin intensity (Fig. R5D).

Interestingly, the AIS contains an actin related structure, the cisternal organelle (CO) (Sanchez-Ponce et al., 2012a). To corroborate the above findings, we took advantage of this structure. To this end, we treated mature neurons at 21 DIV for 3 h and labeled CO using the synaptopodin marker. AIS was identified by ankyrinG staining. While 89.83 ± 2.50% of control neurons had an identificable synaptopodin positive CO, only 25.41 ± 4.61% of neurons treated with SMIFH2 were synaptopodin positive (p = 0.0022, Mann Whitney test; Fig. R5F). Thus, formins inhibition dramatically reduced synaptopodin intensity in the AIS (Fig. R5E, F), further suggesting a change on AIS F-actin cytoskeleton.

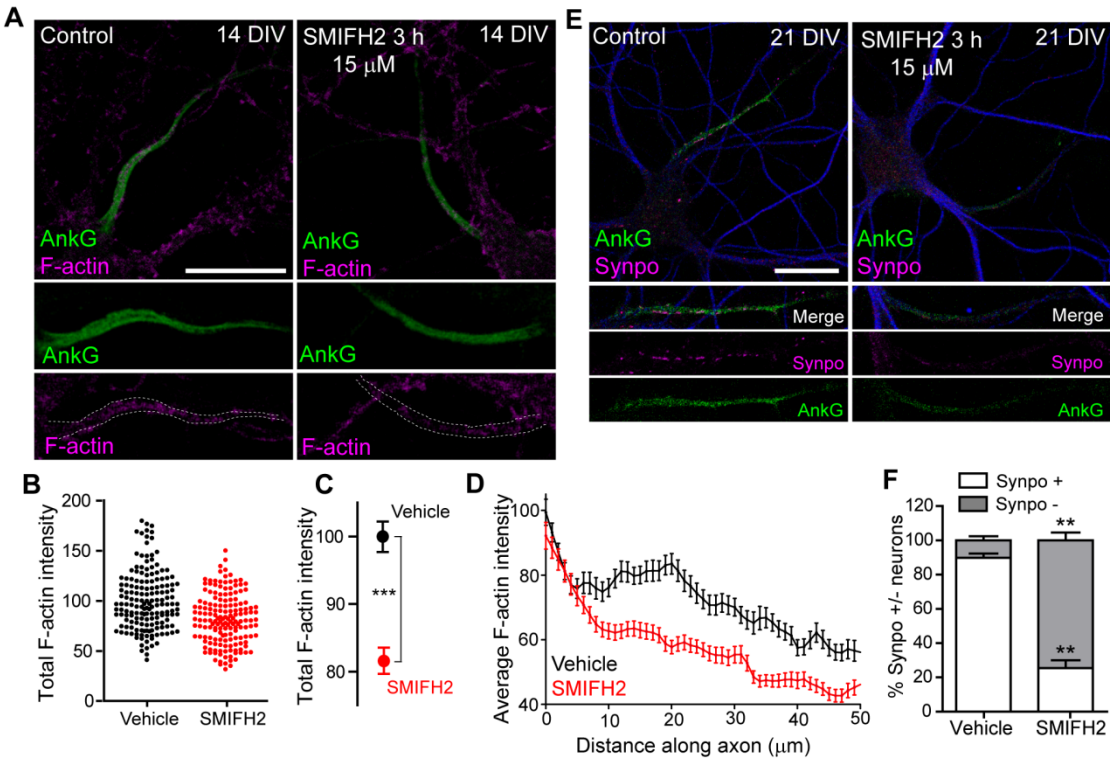

Figure R5. Formins inhibition decreases F-actin intensity in the AIS. (**A**) 14 DIV neurons were treated with vehicle DMSO or 15 µM SMIFH2 for 3 h. Neurons were fixed and stained with ankyrinG antibodies (green) for AIS identification. F-actin was labeled by Alexa Fluor 568 Phalloidin (magenta). Magnification of AIS in each condition is shown under each image. Scale bar = 20 µm. (**B**) Quantification of total F-actin intensity in the AIS in vehicle (black) or SMIFH2 treated neurons (red). (**C**) Graph represents mean ± SEM normalized total F-actin intensity of data represented in B. ***p < 0.0001, Mann Whitney test. (**D**) Normalized average F-actin intensity profile along the AIS in the presence (red) or absence (black) of 15 µM SMIFH2 treatments. (**E**) 21 DIV hippocampal neurons treated for 3 h with vehicle DMSO or 15 µM SMIFH2. Neurons were fixed and stained with synaptopodin (magenta) and ankyrinG antibodies (green). Synaptopodin puncta were used to identify cisternal organelles and ankyrinG signal was used to identify AIS. Magnification of AIS is shown under each image. Scale bar = 20 µm. (**F**) Quantification of the percentage of neurons with or without synaptopodin puncta in the AIS. **p < 0.01, Mann Whitney test. All data were acquired from three independent experiments and represented as the mean ± SEM.

Next, we analyzed whether microtubule properties were modified on AIS after formins activity inhibition. It has been described that formins can stabilize microtubules and modify tubulin acetylation in different cell types (Qu et al., 2017; Thurston et al., 2012). Previous studies have demonstrated that tubulin acetylation at the AIS is important to maintain AIS composition and integrity (Tapia et al., 2010). We first analyzed α-tubulin acetylation in dendrites and the AIS. To do this, 14 DIV neurons treated with DMSO or SMIFH2 for 3 h and labeled with acetylated-α-tubulin and α-tubulin antibodies, as well as ankyrinG for AIS identification. We found a clear reduction of acetylated-α-tubulin / α-tubulin ratio in the AIS after blocking formins activity (0.82 ± 0.025 *vs* 1 ± 0.021 in DMSO treated neurons, unpaired t test, $p < 0.0001$; Fig. R6A). This reduction was detectable all along the AIS (Fig. R6B). To check whether this effect is only related to AIS or is a general phenotype in other neuronal compartments, we analyzed acetylated-α-tubulin / α-tubulin ratio in proximal dendrites. After 3

h formins inhibition this ratio did not significantly change (0.95 ± 0.027 *vs* 1 ± 0.018 in DMSO treated neurons, unpaired t test, p = 0.1484; Fig. R6C), which is in accordance with the profile of this ratio along dendrites (Fig. R6D). These results suggest that formins activity is important to regulate microtubules characteristics in the AIS.

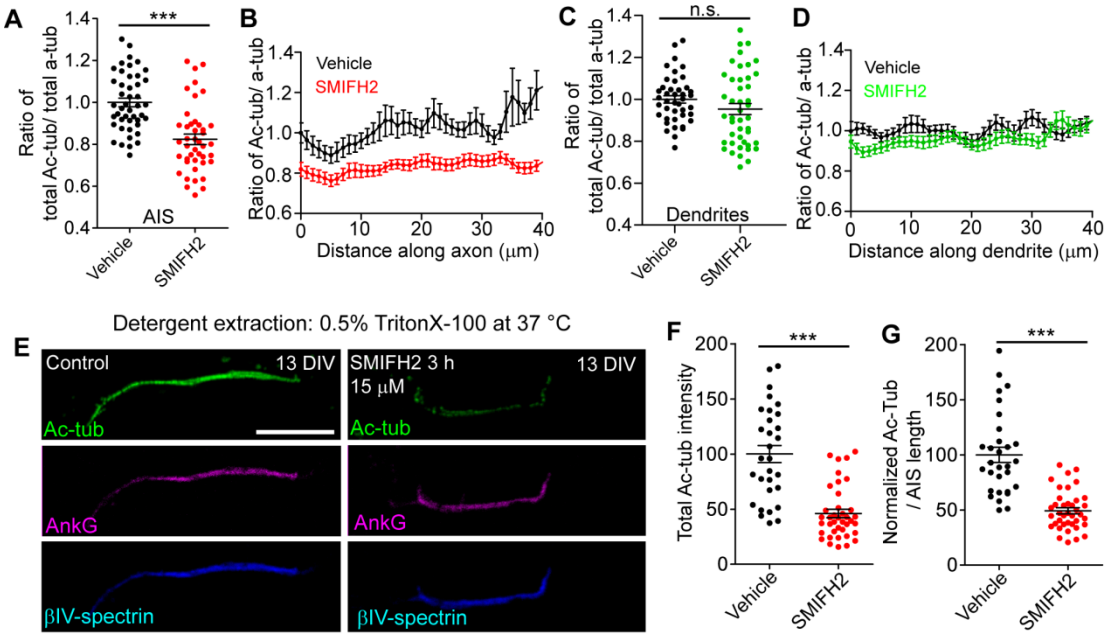

Figure R6. Formins inhibition reduces tubulin acetylation in the AIS. (**A, C**) 14 DIV neurons were treated with vehicle DMSO or 15 μM SMIFH2 for 3 h. Graphs represent the quantification of the total intensity ratio of acetylated-α-tubulin / α-tubulin in the AIS (A) or in the proximal dendrites (C) in the presence or absence of 15 μM SMIFH2 treatments. (**B, D**) Normalized average ratio of acetylated-α-tubulin / α-tubulin profile along the AIS (B) or the proximal dendrite in 40 μm (D). n.s., not significant, ***p < 0.0001, unpaired t test. (**E**) Images of control and SMIFH2 treated 13 DIV neurons after detergent extraction. After treatment, neurons were extracted using extraction buffer containing 0.5% TritonX-100 at 37 ºC for 5 minutes before fixation. Fixed neurons were stained with acetylated-α-tubulin (green), ankyrinG (magenta) and βIV-spectrin (blue) antibodies. Scale bar = 10 μm. (**F**) Quantification of total acetylated-α-tubulin fluorescence intensity of neurons shown in E. ***p < 0.0001, Mann Whitney test. (**G**) Normalized ratio of total acetylated-α-tubulin / AIS length for each neuron. ***p < 0.0001, unpaired t test. All data were acquired from three independent experiments and represented as the mean ± SEM.

To further ascertain this data, we took advantage of the stability and detergent extraction resistance of AIS proteins. Thus, 13 DIV neurons were treated for 3 h with SMIFH2 or DMSO and then incubated in extraction buffer for 5 min at 37 ºC and fixed. Neurons were stained with acetylated-α-tubulin antibodies, and ankyrinG or βIV-spectrin staining was used for AIS identification (Fig. R6E). We observed a clear reduction of acetylated α-tubulin after inhibiting formins activity (46.13 ± 3.85% *vs* 100 ± 7.77% in control neurons, Mann Whitney test, p < 0.0001; Fig. R6F), which was accompanied by a lower intensity of ankyrinG and βIV-spectrin staining (Fig. R6E). To avoid differences due to variability of neuronal AIS length after extraction, we normalized each AIS data to its length. Normalized acetylated α-tubulin of every μm AIS showed a similar reduction by 50% (49.27 ± 2.84% *vs* 100 ± 6.87% in DMSO treated

neurons, unpaired t test, $p < 0.0001$; Fig. R6G). Together, all these data demonstrate that formins activity is necessary to maintain AIS cytoskeleton dynamics. The absence of formins activity may then affect neuronal polarity and axonal trafficking.

3. Blocking formins activity results in loss of neuronal polarity and alterations in axonal trafficking

The AIS is essential to maintain neuronal polarization and serves as a membrane and cytoplasmic barrier to exclude somatodendritic proteins from the axon (Hedstrom et al., 2008; Sobotzik et al., 2009; Winckler et al., 1999). Thus, we analyzed whether formins inhibition may affect the distribution of a main somatodendritic protein, MAP2. To do so, 13 DIV neurons were treated with DMSO or SMIFH2 for 3 h, and then washed in neuronal medium and maintained in new plates with astrocytes and conditioned medium for 6 h or 24 h. Neurons were fixed and stained for MAP2 and ankyrinG. No difference was found for the percentage of ankyrinG positive neurons after 3 h treatment (97.43% for SMIFH2 group *vs* 98.13% for vehicle group; Fig. R7B), although ankyrinG intensity was significantly reduced (Fig. R1B). After additional 6 h in conditioned medium, ankyrinG intensity decreased even more (Fig. R3B), but we were not able to detect MAP2 entering the axon. However, after 24 h we found that lots of neurons lost ankyrinG staining in pre-treated SMIFH2 group (Fig. R7B). Only 23% of neurons showed detectable and low ankyrinG intensity, in which concomitantly MAP2 signal was detected in the axon (Fig. R7A-D). MAP2 intensity profile along the axon showed a high level of MAP2 signal, particularly in the proximal region (Fig. R7C). Cell to cell analysis of total ankyrinG and MAP2 intensity within AIS revealed that control neurons had low MAP2 intensity and high ankyrinG intensity, while neurons pre-treated with SMIFH2 showed higher MAP2 intensity and lower ankyrinG intensity (Fig. R7D).

In order to ascertain that formins inhibition can affect AIS barrier and neuronal polarization, we treated neurons with SMIFH2 at 5 DIV, when the AIS barrier is in the process of maturation (Nakada et al., 2003). 5 DIV neurons were treated for 3 h and labeled with ankyrinG and the somatodendritic marker MAP2. In control neurons, ankyrinG was enriched at the AIS and cytoplasmic MAP2 defined the somatodendritic domain and was absent from the axon (Fig. R7E). However, MAP2 signal extended into the AIS and continued along the axon in

SMIFH2 treated neurons, meanwhile a reduced accumulation of ankyrinG was observed in the AIS (Fig. R7E). Combined, these results indicate that formins activity is required to exclude somatodendritic proteins and maintains AIS barrier functionality.

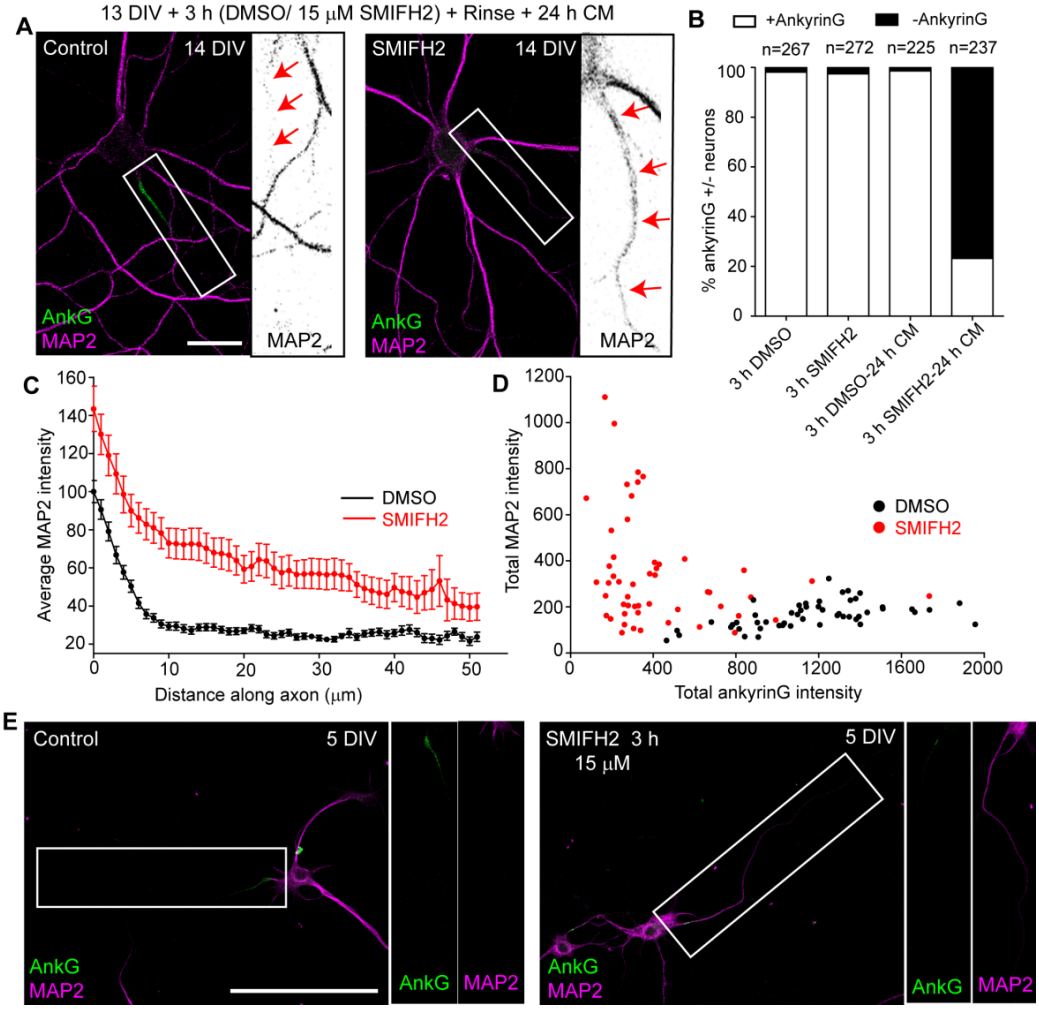

Figure R7. Formins inhibition disrupts neuronal polarity. (**A**) 13 DIV neurons were treated with DMSO or 15 μM SMIFH2 for 3 h. Then neurons were washed and cultured for another 24 h in glia cell conditioned medium containing astrocytes. Neurons were stained with MAP2 (magenta) and ankyrinG antibodies (green). Magnification of boxed AIS regions are shown in adjacent panels. Red arrows indicate the MAP2 signal in the proximal axon. Scale bar = 20 μm. (**B**) Quantification of the percentage of ankyrinG positive neurons in the AIS before and after maintenance in the conditioned medium for 24 h. (**C**) Normalized average MAP2 intensity profile along the proximal axon after 24 h maintenance in the conditioned medium. (**D**) Cell-to-cell analysis of the relationship between total ankyrinG intensity and total MAP2 intensity at the AIS after 24 h maintenance in the conditioned medium. (**E**) 5 DIV hippocampal neurons were treated with DMSO or 15 μM SMIFH2 for 3 h before AIS barrier completely forms. Fixed neurons were stained with MAP2 (magenta) and ankyrinG antibodies (green). Magnification of boxed regions including AIS in each condition is shown in adjacent panels. Scale bar = 100 μm. Data were acquired from three independent experiments and represented as the mean ± SEM.

The AIS is also essential to control and allow the traffic of axonal cargoes (Song et al., 2009). Kinesin-1 is one of the main proteins in charge of axonal cargoes transportation. Its entrance in the AIS depends on microtubules acetylation and detyrosination (Konishi and Setou, 2009; Reed et al., 2006). Given our previous results revealed that misregulation of tubulin acetylation in the AIS redistributes kinesin-1 location (Tapia et al., 2010) and our above data

showed that formins inhibition decreased tubulin acetylation in the AIS, we investigated whether kinesin-1 is altered following the inhibition of formins activity. To this end, we analyzed KIF5C staining and distribution, a major kinesin-1 family member functioning in the axonal transportation (Nakata and Hirokawa, 2003; Tapia et al., 2010). 5 DIV neurons were treated with SMIFH2 or DMSO for 3 h and labeled with KIF5C antibody. To analyze KIF5C signal distribution, its intensity was traced along the axon and the integrated intensity of KIF5C in the soma was also measured. Our results showed that KIF5C was significantly increased in the soma of SMIFH2 treated neurons (124 ± 4.63% *vs* 100 ± 4.39% in control neurons, unpaired t test, p = 0.0003; Fig. R8A, B), while it was reduced along the axon (88.99 ± 3.97% *vs* 100 ± 3.17% in control neurons, unpaired t test, p = 0.0418; Fig. R8A, C). To further analyze KIF5C distribution in the axon, the ratio of KIF5C intensity in the proximal versus distal 50 µm axon was evaluated in both conditions. A relatively higher KIF5C signal was observed in the proximal axon of SMIFH2 treated neurons (129.7 ± 9.79%) compared to the vehicle treated

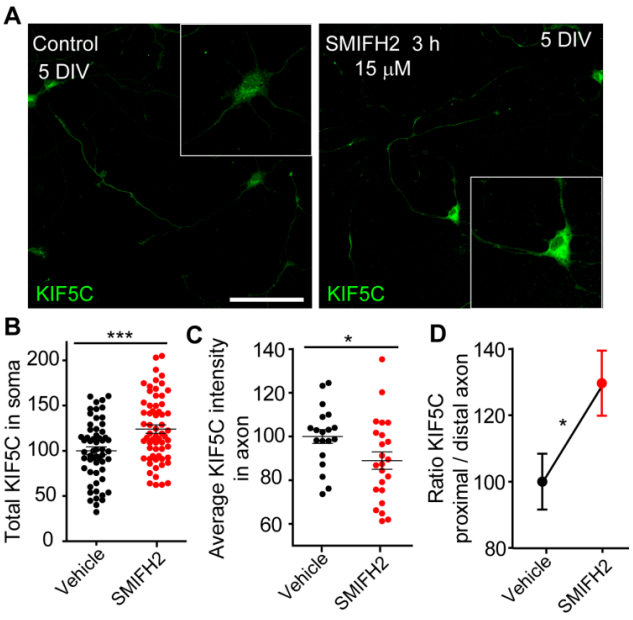

Figure R8. The absence of formins activity alters the distribution of KIF5C along the neuron. (**A**) 5 DIV neurons treated for 3 h with DMSO or 15 µM SMIFH2. Neurons were fixed and stained with KIF5C antibodies (green). KIF5C expression in the soma is magnified in the boxes. Scale bar = 100 µm. (**B, C**) Quantification of total KIF5C fluorescence intensity in the soma (B) or along the entire axon (C) in vehicle (black) or SMIFH2 treated neurons (red). *p < 0.05, ***p < 0.001, unpaired t test. (**D**) Quantification of KIF5C intensity ratio between proximal and distal 50 µm axon. *p < 0.05, Mann Whitney test. All data were acquired from three independent experiments and represented as the mean ± SEM.

neurons (100 ± 8.42%, Mann Whitney test, p = 0.0231; Fig. R8D). Combined, these data indicate that formins activity is necessary to maintain proper axonal transportation. Taken together, formins inhibition affected AIS cytoskeleton and structural integrity and resulted in defects on AIS barrier and axonal traffic. Mammalian animals consist of 15 formins. Therefore, this raises a question on which formin family members are involved in this process and how it works.

4. mDia1 localizes at the AIS

Next, we asked which formin family members may mediate AIS regulation. Our knowledge of formins in brain is still very limited, and only a few works have revealed the role of formins in brain functions (Kawabata Galbraith and Kengaku, 2019). In this context, mDia1 is able to regulate axon growth in cultured cerebellar granule neurons (Arakawa et al., 2003), and it is an important regulatory protein to maintain polarity in epithelial or neuroepithelial cells (Acharya et al., 2017; Thumkeo et al., 2011). Besides, mDia1 is ubiquitously expressed in neurons and has been detected in dendrites, axon, dendritic spines and synapses (Qu et al., 2017; Soykan et al., 2017). mDia1 exerts its functions through regulating actin dynamics and microtubules stability (Ishizaki et al., 2001). This makes mDia1 a suitable candidate among formin members for AIS regulation. First, we tested whether mDia1 localizes in the AIS. Mature neurons at 14 DIV were labeled with an mDia1 antibody that has been previously used in other studies (Neuhaus et al., 2017). Our results showed that mDia1 signal was observed mainly in the soma with a perinuclear staining, as well as, in dendrites and axon (Fig. R9A). Meanwhile, mDia1 puncta were also detected in the AIS along ankyrinG staining (Fig. R9A). To corroborate these findings, neurons were transfected at 10 DIV with a GFP-mDia1 plasmid, which harbors its constitutive active form (GFP-CA-mDia1), and neurons were kept for another 48 h in culture. GFP signal was detected in the soma with a perinuclear signal, but also in the AIS, along the axon and in dendrites (Fig. R9B), as found with mDia1 antibody staining. Indeed, GFP signal and mDia1 antibody staining were colocalized in the same regions, as observed in the AIS and axon (Fig. R9C).

To further confirm mDia1 location at the AIS, we took advantage of the detergent resistance properties of AIS proteins. As actin and microtubules cytoskeleton dynamics are sensitive to temperature changes, we performed detergent extraction experiments at 4 and 37 ºC (Winckler et al., 1999). Detergent extraction was initially applied to 14 DIV using 0.5% TritonX-100 at 4 ºC. After extraction, mDia1 signal was detected as puncta in the AIS, identified by ankyrinG staining (Fig. R9D). Next, we extracted 20 DIV neurons at 37 ºC. Consistent with the findings at 4 ºC, mDia1 localized along the AIS as puncta (Fig. R9E). Together, these data indicate that mDia1 is localized in the AIS and is a potential formin family candidate for AIS

regulation.

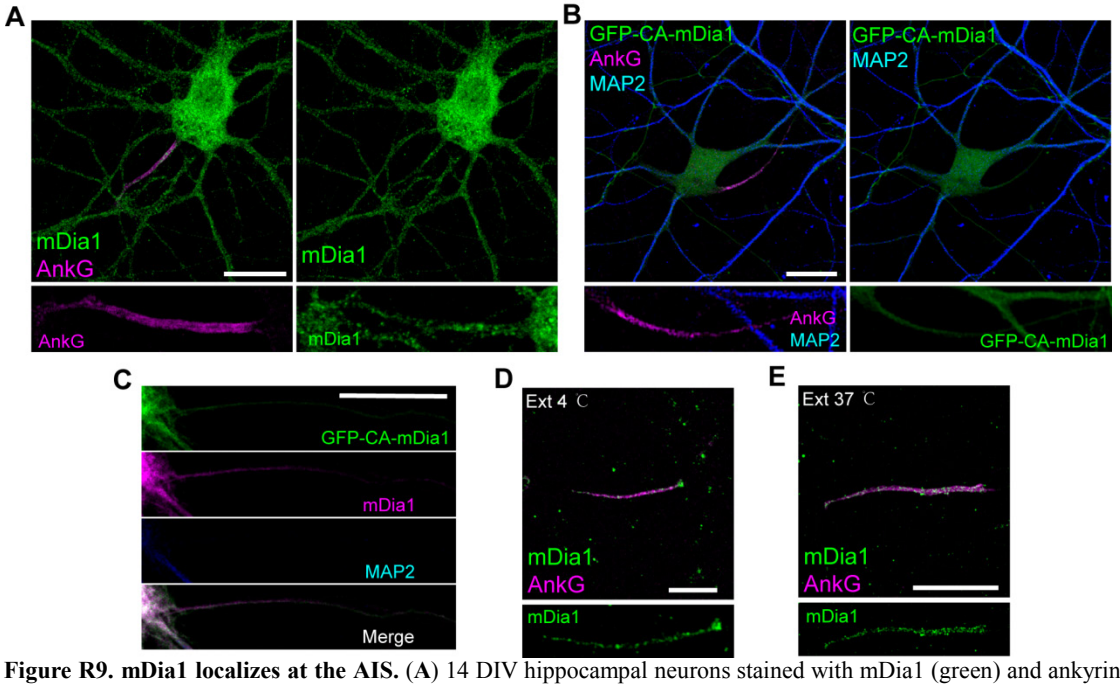

Figure R9. mDia1 localizes at the AIS. (**A**) 14 DIV hippocampal neurons stained with mDia1 (green) and ankyrinG (magenta) antibodies. AIS region is magnified under the image. Scale bar = 20 μm. (**B**) GFP-CA-mDia1 transfected 10 DIV hippocampal neurons stained with MAP2 (blue) and ankyrinG (magenta) antibodies. AIS region is magnified under the image. Scale bar = 20 μm. (**C**) GFP-CA-mDia1 transfected 9 DIV hippocampal neurons stained with MAP2 (blue) and mDia1 (magenta) antibodies. A representative image of proximal axon is shown. Scale bar = 20 μm. (**D**) Detergent extracted 14 DIV neurons at 4 ºC for 20 minutes. (**E**) Detergent extracted 20 DIV neurons at 37 ºC for 5 minutes. Neurons were fixed and stained with mDia1 (green) and ankyrinG (magenta) antibodies. Scale bar = 20 μm.

5. mDia1 is necessary for AIS assembly

AIS regulation includes AIS assembly and maintenance. AIS starts to assemble since axon specification at 3-4 DIV (Kaech and Banker, 2006) and turns to be premature when AIS barrier is formed at 10 DIV (Nakada et al., 2003). Thus, we questioned whether mDia1 plays roles in the AIS formation. Before addressing this question, we first examined the expression of mDia1 in hippocampal neurons at 3 DIV and 7 DIV respectively. Similar to mature neurons, mDia1 was mainly expressed in the soma with a perinuclear staining, as well as, in dendrites and in the nascent axon of hippocampal neurons (Fig. R10A, C). mDia1 staining was also observed in the AIS of 7 DIV neurons, identified by ankyrinG staining (Fig. R10C). However, we found a relatively higher signal of mDia1 in the axon compared to neurites at 3 DIV (Fig. R10A, B) and this difference disappeared at 7 DIV along dendrites development (Fig. R10C). These data imply that mDia1 may play some roles during AIS assembly as well as on axonal and dendritic development.

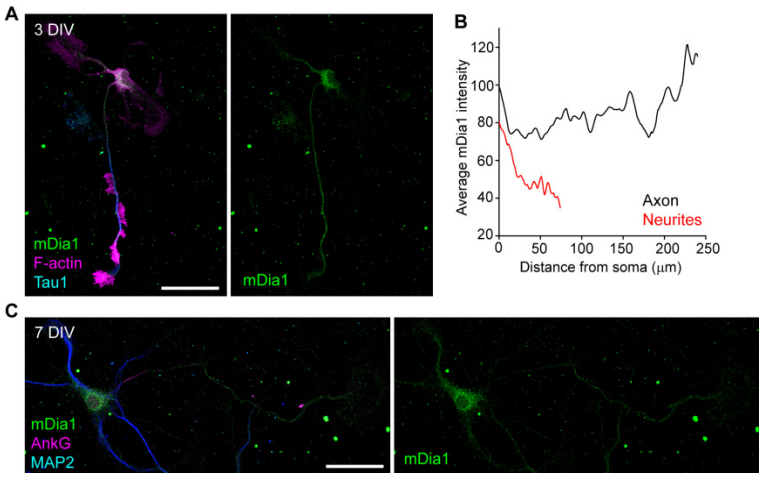

Figure R10. mDia1 location in neuronal early developmental stages. (**A**) 3 DIV neurons were stained with mDia1 (green) and Tau1 (blue) antibodies. F-actin was labeled by Alexa Fluor 568 Phalloidin (magenta). Scale bar = 50 µm. (**B**) Normalized average mDia1 intensity along the axon or neurites (axon, n = 41; neurites, n = 51). Data in graphs were acquired from three independent experiments. (**C**) 7 DIV neurons were stained with mDia1 (green), ankyrinG (magenta) and MAP2 (blue) antibodies. Scale bar = 50 µm.

Previous studies reported that the complexity of neuronal morphology can affect AIS development (Hamada et al., 2016; Tapia et al., 2017). Moreover, the time window of AIS assembly matches with initial dendritic development. Therefore, it is necessary to study the contribution of mDia1 during axon and dendrites growth prior to AIS assembly study. We employed knockdown experiments to reduce endogenous mDia1 expression before neuronal polarization starts. First, we analyzed 4 different vectors harboring short hairpin RNAs specific for mDia1 that co-express the red fluorescent protein (RFP). As a control we used scrambled RNA sequences (scrRFP). After screening, we found two efficient vectors to knock down mDia1 (shmDia1-1 and shmDia1-2).

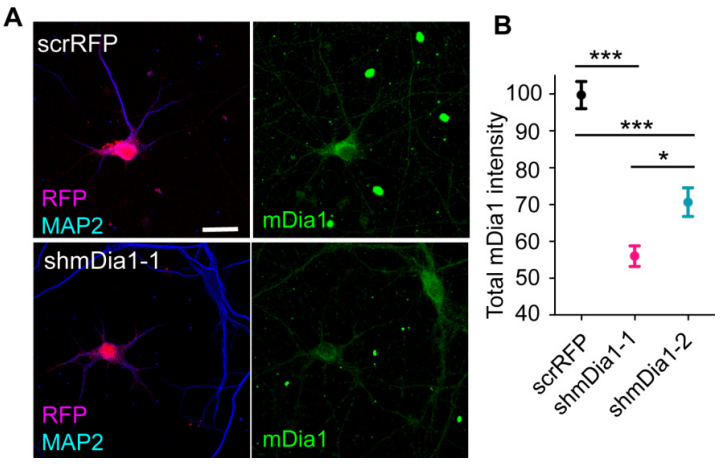

Figure R11. Identification of efficient mDia1 interference shRNAs. (**A**) 10 DIV hippocampal neurons were nucleofected with scrambled interference RNA (scrRFP) or mDia1 interference RNA (shmDia1-1, shmDia1-2). Nucleofected neurons were identified based on RFP fluorescence (magenta). Neurons were stained with mDia1 (green) and MAP2 (blue) antibodies. Scale bar = 20 µm. (**B**) Quantification of total mDia1 fluorescence intensity in the soma of 10 DIV hippocampal neurons nucleofected with scrRFP, shmDia1-1 or shmDia1-2 plasmids. *p < 0.05, ***p < 0.001, One-way analysis of variance, Tukey's multiple comparison test. Data in graphs were acquired from three independent experiments and represented as the mean ± SEM.

Neurons were nucleofected before plating and fixed at 10 DIV. Nucleofected neurons were identified based on RFP fluorescence. Samples were labeled with mDia1 antibody and the total mDia1 intensity in the soma was measured to evaluate the knocking down efficiency. We found a significant reduction of mDia1 signal in shmDia1-1 nucleofected neurons (56.15 ± 2.82%) and

shmDia1-2 nucleofected neurons (70.85 ± 3.88%) compared to mDia1 signal in scrRFP nucleofected control neurons (100 ± 3.71%, One-way analysis of variance, Tukey's multiple comparison test, $p < 0.001$; Fig. R11A, B).

Next, we took advantage of the higher efficiency of shmDia1-1 vector capable of depleting mDia1 for axonal and dendritic studies. Neurons were nucleofected with scrRFP or shmDia1-1 and fixed at 3 DIV and 7 DIV respectively. 3 DIV neurons were used for studying axon polarity and axon length. Axon polarity was assessed by the percentage of Tau1 positive nucleofected neurons among all the nucleofected neurons identified by RFP (Fig. R12A). We found that knocking down mDia1 has no effects on axon specification (Fig. R12A).

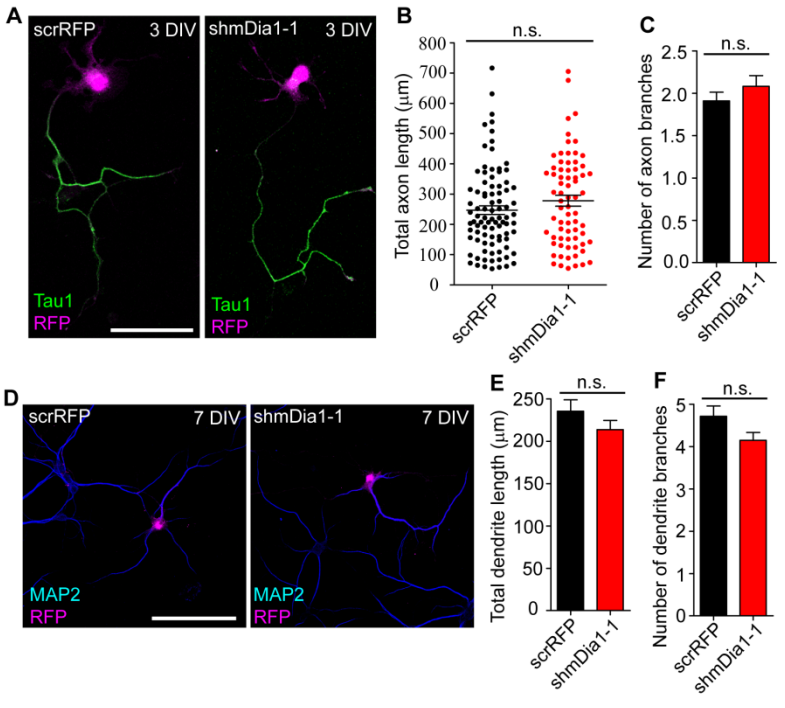

Figure R12. Suppression of mDia1 by interference shRNAs has no effects on axon and dendrites growth in hippocampal neurons. (**A**) 3 DIV hippocampal neurons nucleofected with scrambled interference RNA (scrRFP) or mDia1 interference RNA (shmDia1-1). Neurons were stained with Tau1 (green) antibody. Scale bar = 50 μm. (**B**) Quantification of total axon length of 3 DIV hippocampal neurons nucleofected with scrRFP or shmDia1-1 plasmids. n.s., not significant, Mann Whitney test. (**C**) Quantification of total axon branches in the same neurons. n.s., not significant, Mann Whitney test. (**D**) 7 DIV hippocampal neurons nucleofected with scrRFP or shmDia1-1 plasmids. Neurons were stained with MAP2 (blue) antibody. Scale bar = 100 μm. (**E**) Quantification of total dendrites length of 7 DIV hippocampal neurons nucleofected with scrRFP or shmDia1-1 plasmids. n.s., not significant, Mann Whitney test. (**F**) Quantification of total dendrites branches of 7 DIV hippocampal neurons nucleofected with scrRFP or shmDia1-1 plasmids. n.s., not significant, unpaired t test. Nucleofected neurons were identified based on RFP fluorescence (magenta). All data were acquired from three independent experiments and represented as the mean ± SEM.

No significant difference was observed in total axon length (278.3 ± 18.04 μm for shmDia1-1 nucleofected neurons *vs* 247.3 ± 14.64 μm for scrRFP nucleofected neurons, Mann Whitney test, $p = 0.1907$; Fig. R12B), neither a change was observed for the number of axonal branches (2.08 ± 0.13 for shmDia1-1 nucleofected neurons *vs* 1.91 ± 0.10 for scrRFP nucleofected neurons, Mann Whitney test, $p = 0.3093$; Fig. R12C). Meanwhile, 7 DIV neurons were used for dendritic study. Visually, we did not find any change of dendrites based on the

MAP2 staining (Fig. R12D). This was confirmed by our quantitative data showing comparable dendrites length (213.9 ± 10.89 µm for shmDia1-1 nucleofected neurons *vs* 235.5 ± 13.44 µm for scrRFP nucleofected neurons, Mann Whitney test, p = 0.4177; Fig. R12E) and total dendritic branches (4.15 ± 0.19 for shmDia1-1 nucleofected neurons *vs* 4.72 ± 0.24 for scrRFP nucleofected neurons, unpaired t test, p = 0.0669; Fig. R12F).

We have shown that mDia1 reduction has no significant effects on initial axon and dendrites growth. Thus, we asked whether increasing mDia1 expression or enhancing mDia1 activity on early neuronal development may have effects on neuronal growth. To this end, hippocampal neurons were nucleofected using a plasmid that expresses a constitutively active form of mDia1 (GFP-CA-mDia1). GFP was used as a control vector for nucleofection. Nucleofected neurons were fixed at 3 DIV and labeled with Tau1 for axon identification (Fig. R13A). Neurons expressing GFP-CA-mDia1 significantly reduced axon polarity, and 59.50 ± 7.40% did not develop an axon compared to 9.79 ± 1.35% in GFP nucleofected neurons (Mann Whitney test, p = 0.0022).

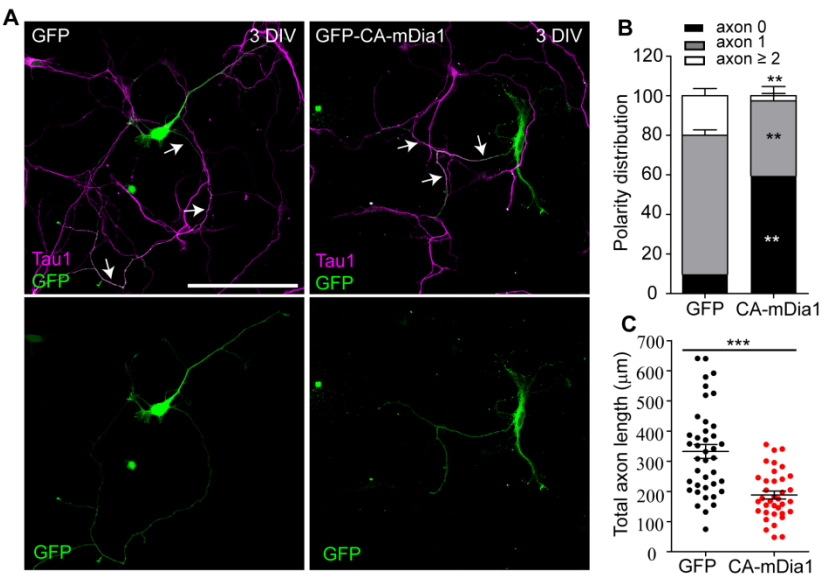

Figure R13. Expression of a constitutively active form of mDia1 decreases axon specification and axon growth. (**A**) 3 DIV hippocampal neurons nucleofected with GFP or GFP-CA-mDia1 plasmids. Nucleofected neurons were identified based by GFP signal. Neurons were stained with Tau1 (magenta) antibody. Arrows indicate axons of nucleofected neurons. Scale bar = 100 µm. (**B**) Percentage of neurons without or with 1, ≥ 2 axons in 3 DIV hippocampal neurons nucleofected with GFP or GFP-CA-mDia1 plasmids. **p < 0.01, Mann Whitney test. (**C**) Quantification of total axon length in 3 DIV polarized GFP or GFP-CA-mDia1 positive neurons. ***p < 0.0001, unpaired t test. All data were acquired from three independent experiments and represented as the mean ± SEM.

Meanwhile, 37.98 ± 7.21% developed one axon, and 2.52 ± 1.19% were able to develop two or more axons, compared to 70.24 ± 2.74% and 19.97 ± 3.67%, respectively, in GFP nucleofected neurons (Mann Whitney test, p = 0.0081 and p = 0.0022, respectively, Fig. R13B). We further analyzed GFP-CA-mDia1 polarized neurons and we found a significant reduction of

total axon length (187.9 ± 13.40 µm *vs* 332.6 ± 23.04 µm in GFP polarized neurons, unpaired t test, $p < 0.0001$; Fig. R13A, C). These data suggest that mDia1 is not strictly necessary to develop the axon, but its enhanced expression and activity affect initial neuronal polarization.

Given that knocking down mDia1 has no effects on early neuronal development in axon and dendrites, we took advantage of this approach to specifically study the role of mDia1 on AIS assembly. Neurons were nucleofected with two efficient mDia1 knockdown vectors shmDia1-1 and shmDia1-2, or scrRFP vector as control. Nucleofected neurons were cultured until 10 DIV when AIS diffusion barrier is formed. Fixed samples were labeled with ankyrinG antibody and its fluorescence intensity in the AIS along 30 µm was analyzed for comparing total ankyrinG expression. We found that ankyrinG intensity was reduced in both shmDia1-1 (65.09 ± 1.51%) and shmDia1-2 nucleofected neurons (78.31 ± 2.15%) compared to 100.0 ± 2.44% in scrRFP nucleofected neurons ($p < 0.001$; Fig. R14A, B).

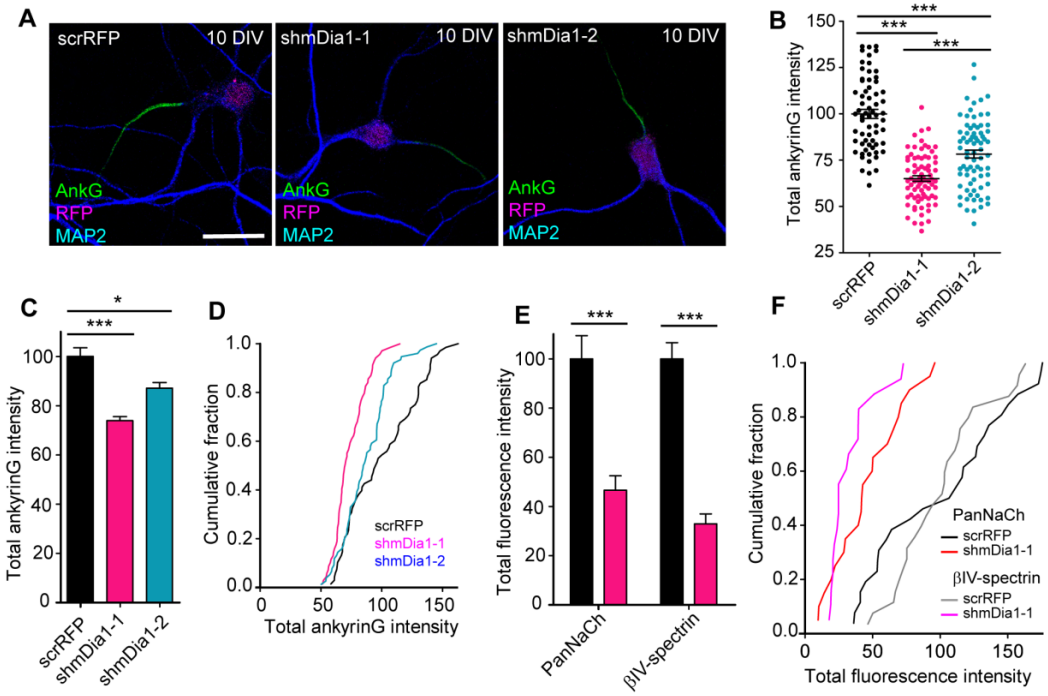

Figure R14. Suppression of mDia1 by interference shRNAs decreases AIS proteins accumulation. (**A**) 10 DIV hippocampal neurons nucleofected with scrambled interference RNA (scrRFP) or mDia1 interference RNAs (shmDia1-1, shmDia1-2). Nucleofected neurons were identified based on RFP fluorescence (magenta). Neurons were stained with ankyrinG (green) and MAP2 (blue) antibodies. Scale bar = 20 µm. (**B**) Quantification of total ankyrinG fluorescence intensity in the AIS of scrRFP, shmDia1-1 or shmDia1-2 10 DIV nucleofected hippocampal neurons. ***$p < 0.001$, One-way analysis of variance, Tukey's multiple comparison test. (**C**) Quantification of total ankyrinG fluorescence intensity in the AIS of 7 DIV hippocampal neurons nucleofected with plasmids of scrRFP, shmDia1-1 or shmDia1-2. *$p < 0.05$, ***$p < 0.001$, Kruskal-Wallis, Dunn's multiple comparison test. (**D**) Cumulative fraction plot of the normalized total ankyrinG intensity of neurons quantified in C. (**E**) Quantification of total voltage gated sodium channels (PanNaCh) and βIV-spectrin fluorescence intensity in the AIS of 7 DIV hippocampal neurons nucleofected with scrRFP or shmDia1-1 plasmids. ***$p < 0.001$, Mann Whitney test. (**F**) Cumulative fraction plot shows the normalized total PanNaCh and βIV-spectrin intensity distribution of neurons quantified in E. All data were acquired from three independent experiments and represented as the mean ± SEM.

The reduction of ankyrinG intensity in both mDia1 shRNAs was in line with the higher efficiency of shmDia1-1 to deplete mDia1 expression in hippocampal neurons (Fig. R11A, B). These data suggest that mDia1 is necessary to assemble AIS components. In order to ascertain this data, we analyzed ankyrinG expression in 7 DIV nucleofected neurons, when AIS diffusion barrier and AIS maturity is not complete (Nakada et al., 2003). Consistently, our data showed that total ankyrinG intensity in the AIS was significantly decreased in shmDia1-2 (87.13 ± 2.29%) and even more in shmDia1-1 nucleofected neurons (73.89 ± 1.65%) compared to 100 ± 3.54% in scrRFP nucleofected neurons (Kruskal-Wallis, Dunn's multiple comparison test, $p < 0.001$; Fig. R14C). The decrease trend was corroborated by the cumulative fraction plot of total ankyrinG intensity in individual neurons (Fig. R14D). In addition, we further analyzed other AIS components using 7 DIV nucleofected samples. We found a ~53% reduction of total PanNaCh (46.63 ± 5.84%, Mann Whitney test, $p = 0.0003$; Fig. R14E) and a ~67% reduction of total βIV-spectrin (32.99 ± 3.97%, Mann Whitney test, $p < 0.0001$; Fig. R14E) in shmDia1-1 nucleofected neurons compared to scrRFP nucleofected neurons. The cumulative fraction plot of total PanNaCh and βIV-spectrin further confirmed the reduction of AIS components after knocking down mDia1 (Fig. R14F). These results suggest that mDia1 is involved in AIS modulation before and after the diffusion barrier is formed.

We have shown that formins inhibition causes AIS structural disruption and mDia1 suppression disturbs AIS structural integrity. To further ascertain that the effects of SMIFH2 on AIS are due to mDia1 inhibition, neurons were nucleofected with scrRFP or shmDia1-1 plasmids and cultured until 10 DIV, followed by 3 h treatment with DMSO or 15 μM SMIFH2. Fixed neurons were labeled with ankyrinG antibody and total ankyrinG intensity in 30 μm AIS was quantified and analyzed. In line with above results, both, SMIFH2 treatment and mDia1 suppression, alone or in combination, significantly decreased ankyrinG intensity (One-way analysis of variance, Tukey's multiple comparison test, $p < 0.001$; Fig. R15A, B). SMIFH2 treated neurons and shmDia-1-1 nucleofected neurons shared a similar reduction of ankyrinG level (68.32 ± 2.02% for neurons in scrRFP-SMIFH2 group *vs* 72.83 ± 3.17% for neurons in shmDia1-1-DMSO group, n.s.; Fig. R15A, B). Besides, when shmDia1-1 nucleofected neurons were treated with SMIFH2, no further reduction of total ankyrinG intensity was observed in

shmDia1-1 nuclefected neurons (66.85 ± 3.01% *vs* 72.83 ± 3.17% for neurons in shmDia1-1-DMSO group, Fig. R15A, B). Together, these results indicate that mDia1 is the primary target of SMIFH2 in hippocampal neurons during AIS development. Thus, mDia1 is a regulator of AIS assembly and potentially involved in its maintenance.

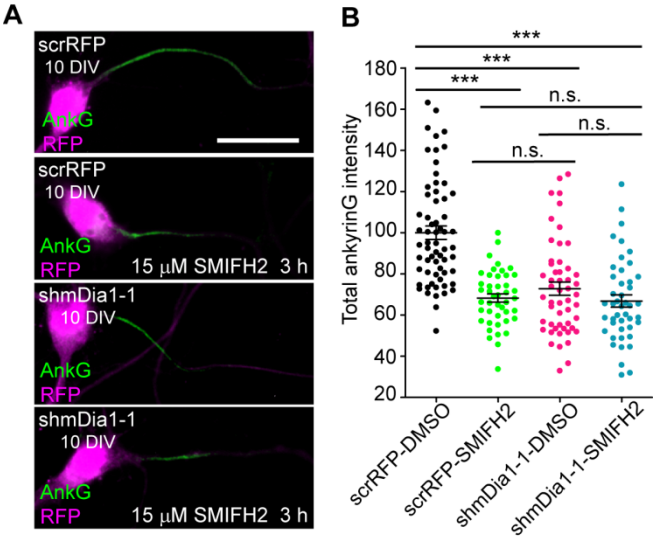

Figure R15. Formins inhibition does not further decrease ankyrinG intensity in neurons with decreased mDia1 expression. (**A**) 10 DIV hippocampal neurons were nucleofected with scrambled interference RNA (scrRFP) or mDia1 interference RNA (shmDia1-1) and then treated for 3 h with DMSO or 15 μM SMIFH2. Nucleofected neurons were identified based on RFP fluorescence (magenta). Neurons were stained with ankyrinG (green) antibody. Scale bar = 20 μm. (**B**) Quantification of total ankyrinG fluorescence intensity in the AIS of 10 DIV hippocampal neurons in every experimental condition. n.s., not significant, ***p < 0.001, One-way analysis of variance, Tukey's multiple comparison test. Data in graph were acquired from three independent experiments and represented as the mean ± SEM.

6. mDia1 is required for AIS maintenance and plasticity in vitro

Next, we asked whether mDia1 contributes to AIS maintenance. To address this question, neurons were left to develop AIS till 10 DIV and then transfected with plasmids expressing shmDia1-1 or scrRFP. Transfected neurons were fixed after 24 or 48 h before analyzing ankyrinG expression in the AIS. mDia1 interference RNA dramatically reduced ankyrinG expression after 48 h (Fig. R16A). Indeed, ankyrinG intensity was significantly reduced after 24 h suppression of mDia1 (85.71 ± 4.32% *vs* 100 ± 3.83% for scrRFP transfected neurons, unpaired t test, p = 0.0148; Fig. R16B). AnkyrinG reduction was even higher after 48 h (72.37 ± 3.70% *vs* 100 ± 4.58% for scrRFP transfected neurons, unpaired t test, p < 0.0001; Fig. R16B). To further decipher the role of mDia1 in the AIS maintenance, we transfected 10 DIV neurons with GFP-CA-mDia1 to constitutively express active form of mDia1. Transfected neurons were fixed after 24 or 48 h expression of exogenous plasmids GFP or GFP-CA-mDia1. After 48 h, GFP-CA-mDia1 transfected neurons had slightly lower ankyrinG intensity (87.24 ± 3.29% *vs* 100 ± 3.85% for GFP transfected neurons, unpaired t test, p = 0.014; Fig. R16C, D). However, no significant difference of ankyrinG signal was observed after 24 h in GFP-CA-mDia1 transfected neurons (97.37 ± 7.31% *vs* 100 ± 6.78% for GFP transfected neurons, unpaired t

test, p = 0.7938; Fig. R16D). These results demonstrate that the appropriate expression and activity of mDia1 is essential to maintain AIS components integrity, suggesting again that mDia1 is a fine regulator of AIS.

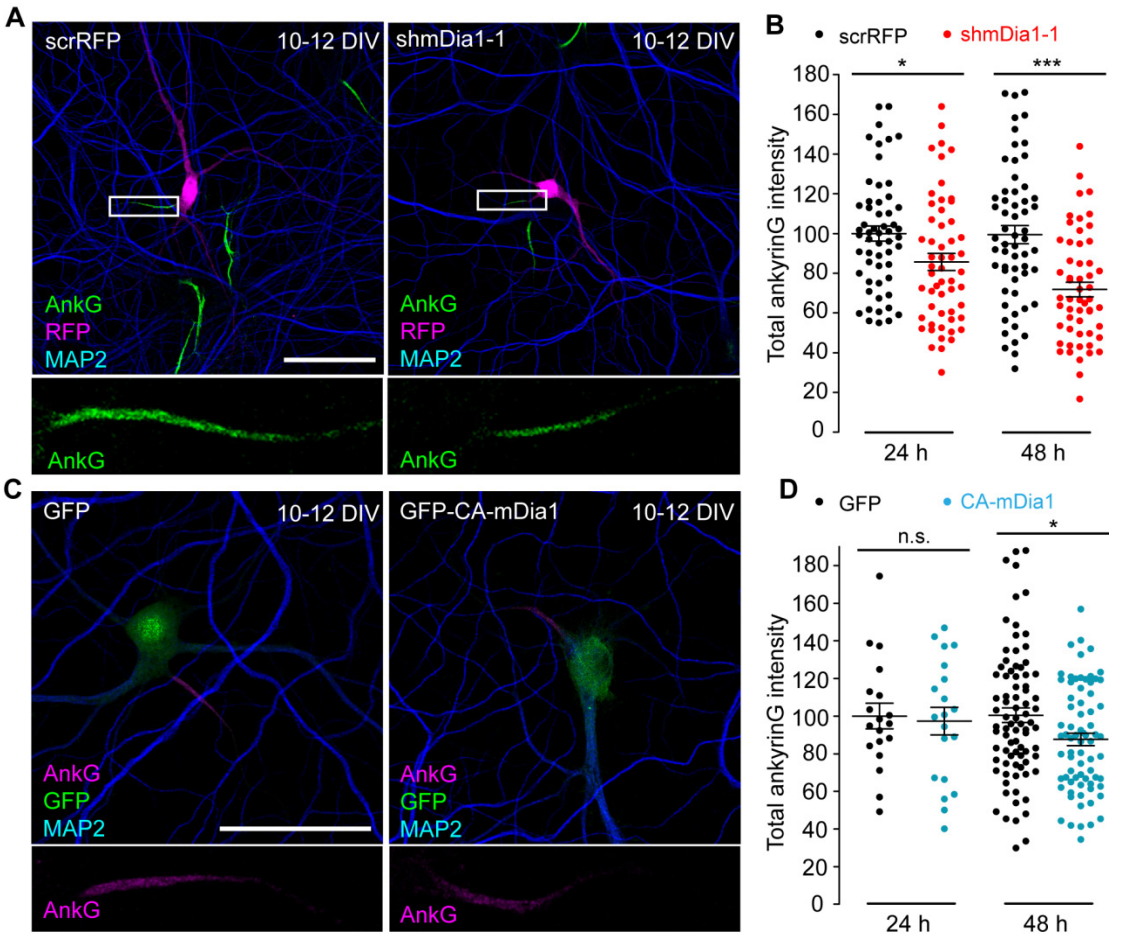

Figure R16. mDia1 interference shRNA or constitutively active mDia1 expression in hippocampal neurons after AIS development decreases ankyrinG intensity. (**A, C**) 10 DIV hippocampal neurons transfected with scrambled interference RNA (scrRFP) or mDia1 interference RNA (shmDia1-1) plasmids (A), and GFP or a constitutively active form of mDia1 (GFP-CA-mDia1) plasmids (C). Transfected neurons were identified based on RFP (magenta, A) or GFP (green, C) fluorescence. Neurons were stained with MAP2 (blue) and ankyrinG (green in A, magenta in B) antibodies. The boxed AIS region is amplified and shown under each image. Scale bar = 50 µm. (**B, D**) Quantification of total ankyrinG fluorescence intensity in the AIS. 10 DIV hippocampal neurons were transfected with scrRFP or shmDia1-1 plasmids (B) or GFP or GFP-CA-mDia1 plasmids (D) and analyzed after 24 and 48 h. Data were normalized to their respective scrRFP or GFP transfected neurons at each interval. *p < 0.05, ***p<0.0001, unpaired t test in B, and n.s., not significant, *p < 0.05, unpaired t test in D. Data in graph were acquired from three independent experiments and represented as the mean ± SEM.

AIS plasticity consists of the dynamic changes of molecular composition, length and location. Our results have highlighted that mDia1 is necessary to maintain AIS composition. To test whether mDia1 is a mediator on AIS length and position, we used 10 DIV neurons transfected with shmDia1-1 and scrRFP plasmids, and kept them for additional 48 h in culture due to the higher decrease of ankyrinG components in the AIS at that time. The average ankyrinG intensity profile obtained from all the normalized smooth data showed an overall

ankyrinG reduction along the AIS (Fig. R17A). To quantify whether AIS length is modified, we employed a well documented protocol (Grubb and Burrone, 2010), where ankyrinG profile from each neuron was smoothed into every 1 µm and a 33% of maximum fluorescence intensity reference was applied to define the AIS start and end position. Using this approach, we first analyzed AIS length in the average ankyrinG intensity profile of scrRFP and shmDia1-1 transfected neurons (Fig. R17A). We found that AIS length was reduced after knocking down mDia1 (Fig. R17A), as observed in shmDia1-1 transfected neurons (Fig. R16A).

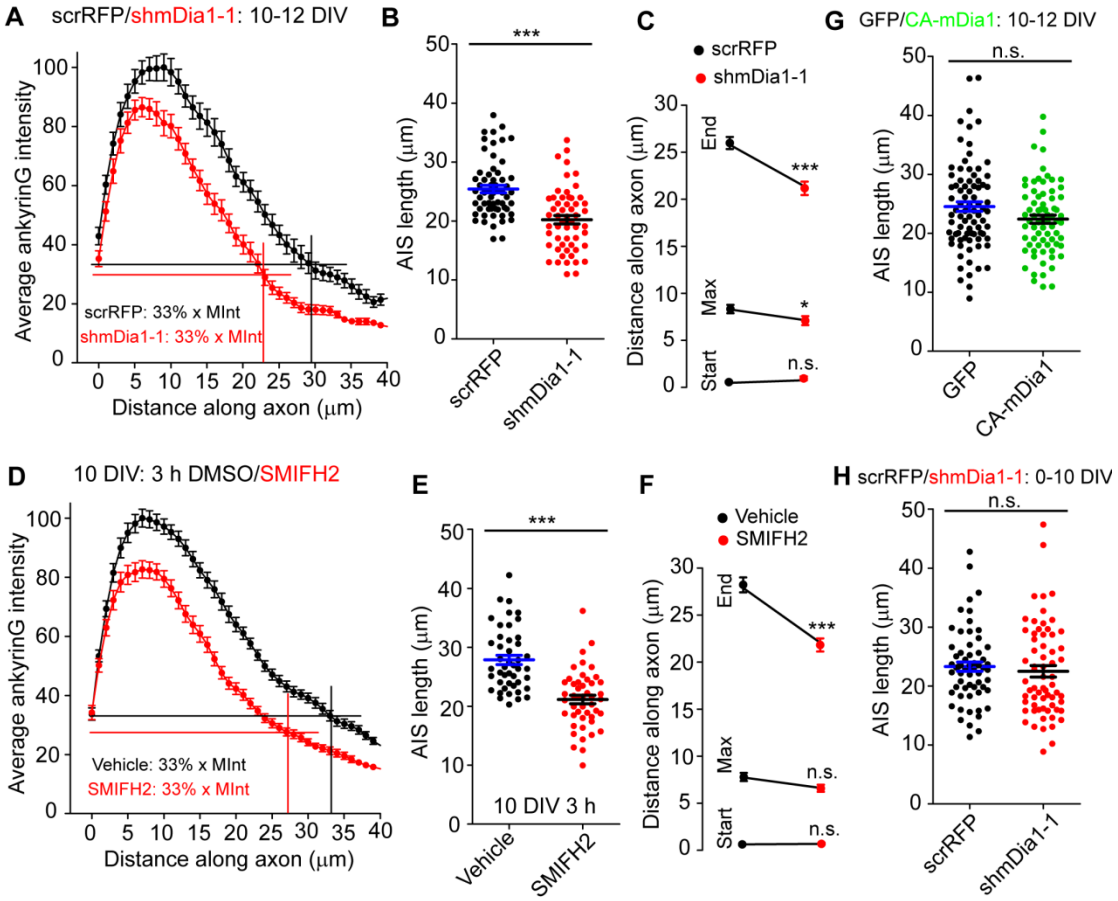

Figure R17. mDia1 suppression or inhibition shortens AIS length. (**A, D**) Normalized average ankyrinG intensity profile along the AIS of 12 DIV hippocampal neurons transfected at 10 DIV (A) with scrambled interference RNA (scrRFP, black) or mDia1 interference RNA (shmDia1-1, red), and the same profile for 10 DIV hippocampal neurons in the presence (red) or absence (black) of 15 µM SMIFH2 (D) treatments. A 33% of maximum fluorescence intensity reference was applied to define the AIS start and end position in the profile. (**B, E**) Quantification of AIS length in transfected neurons shown in A or inhibited neurons shown in D. ***p < 0.0001, unpaired t test. (**C, F**) Quantification of AIS starting, maximum intensity and end positions in transfected (C) or inhibited neurons (F) shown in B or E, n.s., not significant, *p < 0.05, ***p < 0.0001, Mann Whitney test in C, and n.s., not significant, Mann Whitney test; ***p < 0.0001, unpaired t test in F. (**G**) Quantification of AIS length in 12 DIV hippocampal neurons transfected at 10 DIV with GFP (black) or GFP-CA-mDia1 (green) plasmids. n.s., not significant, Mann Whitney test. (**H**) Quantification of AIS length in 10 DIV hippocampal neurons nucleofected with scrRFP (black) or shmDia1-1 (red) plasmids. n.s., not significant, Mann Whitney test. All data were acquired from three independent experiments and represented as the mean ± SEM.

To ascertain this data, AIS length was analyzed independently neuron by neuron in their own ankyrinG intensity smooth profile. A significant reduction was observed after knocking

down mDia1 (20.21 ± 0.72 μm *vs* 25.43 ± 0.63 μm for scrRFP transfected neurons, unpaired t test, $p < 0.0001$; Fig. R17B). Next, in order to further analyze whether the change in length is related to changes in ankyrinG distribution along the AIS, we analyzed the start, maximum intensity and end position in each neuron. Our study revealed that AIS end position remarkably shifted towards the soma in shmDia1-1 transfected neurons (21.17 ± 0.70 μm *vs* 26 ± 0.64 μm for scrRFP transfected neurons, Mann Whitney test, $p < 0.0001$; Fig. R17C), accompanied by slightly significant movement of maximal ankyrinG intensity position (7.10 ± 0.47 μm for shmDia1-1 transfected neurons *vs* 8.33 ± 0.46 μm for scrRFP transfected neurons, Mann Whitney test, $p = 0.0487$; Fig. R17C). No change was found for AIS starting position (Mann Whitney test, $p=0.4389$; Fig. R17C). In order to corroborate these results, we analyzed AIS length after mDia1 inhibition with SMIFH2. 10 DIV neurons were treated for 3 h with DMSO or 15 μM SMIFH2. Fixed samples were labeled with ankyrinG antibody for AIS length and position analysis. Using the same analysis procedures, we found a decrease of AIS length in the average ankyrinG intensity profile of SMIFH2 treated neurons, accompanied by a reduction of ankyrinG intensity along AIS (Fig. R17D). AIS length from every neuron was analyzed and a similar reduction was found in SMIFH2 treated neurons (21.15 ± 0.72 μm *vs* 27.86 ± 0.79 μm for control neurons, unpaired t test, $p < 0.0001$; Fig. R17E). Consistent with mDia1 knockdown experiments, AIS end position shifted forward to the soma in SMIFH2 treated neurons (21.83 ± 0.70 μm *vs* 28.21 ± 0.80 μm for DMSO treated neurons, unpaired t test, $p < 0.0001$; Fig. R17F). No significant change was found in ankyrinG maximal fluorescence position (Mann Whitney test, $p = 0.0984$), but it was slightly closer to the soma as happened in transfected neurons (6.58 ± 0.37 μm *vs* 7.79 ± 0.44 μm for DMSO treated neurons; Fig. R17F). No significant difference was found in AIS starting position (Mann Whitney test, $p = 0.9784$; Fig. R17F).

Given mDia1 suppression or inhibition decreases AIS length, we next analyzed the effects of increased mDia1 expression and activity on AIS plasticity. 10 DIV neurons were transfected with GFP-CA-mDia1 or GFP and fixed after 48 h. AIS length analysis showed that no significant change was found in GFP-CA-mDia1 transfected neurons (22.40 ± 0.70 μm *vs* 24.53 ± 0.82 μm for GFP transfected neurons, Mann Whitney test, $p = 0.0821$; Fig. R17G). These data suggest that mDia1 lack of function on AIS has detrimental consequences for AIS length, but

increasing its expression does not modify AIS length at short-term.

Next, we asked whether mDia1 participates in the long-term AIS plasticity. To do so, neurons were nucleofected with shmDia1-1 or scrRFP and cultured until 10 DIV. AIS length was checked in shmDia1-1 or scrRFP nucleofected neurons. We found that AIS length was similar in both conditions and the difference did not reach statistical significance (Mann Whitney test, $p = 0.2864$; Fig. R17H). This result indicates that mDia1 is related with short-term changes in AIS length and some other mechanisms may compensate AIS length changes at long-term.

In view of our results, short-term mDia1 suppression or inhibition decreased both AIS components and AIS length. Thus, we explored whether AIS components reduction were related to the shortening of AIS length in the same set of neurons used for AIS length analysis. To test this hypothesis, cell to cell analysis was performed regarding to the AIS length and the total ankyrinG intensity within AIS. First, we examined the relation between AIS length and total ankyrinG intensity after blocking mDia1 activity. 10 DIV neurons were treated with SMIFH2 or DMSO for 3 h. AIS length and total ankyrinG intensity within AIS were measured. Our results showed that there was a positive correlation between these two parameters in SMIFH2 treated neurons (Pearson $r = 0.4319$, $p = 0.0027$; Fig. R18A) and a similar correlation was also found in DMSO treated neurons (Pearson $r = 0.468$, $p = 0.001$; Fig. R18A). Then, we analyzed the ratio of normalized total ankyrinG intensity within AIS / AIS length. Our statistical analysis of this ratio revealed a significant reduction after SMIFH2 treatment ($87.24 \pm 3.01\%$ *vs* $100 \pm 2.76\%$, unpaired t test, $p = 0.0024$; Fig. R18B). Next, we explored the relationship between AIS length and total ankyrinG intensity after knocking down mDia1. 10 DIV neurons were transfected with scrRFP or shmDia1-1 and fixed after 48 h. We also found a positive correlation of these two parameters both in scrRFP transfected neurons (Pearson $r = 0.627$, $p < 0.0001$; Fig. R18D) and shmDia1-1 transfected neurons (Pearson $r = 0.7085$, $p < 0.0001$; Fig. R18D). To further analyze these data, we compared the ratio of normalized total ankyrinG intensity within AIS / AIS length. Although the difference of this ratio did not reach statistical significance (unpaired t test, $p = 0.0672$), a decrease trend was found in shmDia1-1 transfected neurons ($90.61 \pm 3.32\%$ *vs* $100 \pm 3.81\%$ for scrRFP transfected neurons; Fig. R18E).

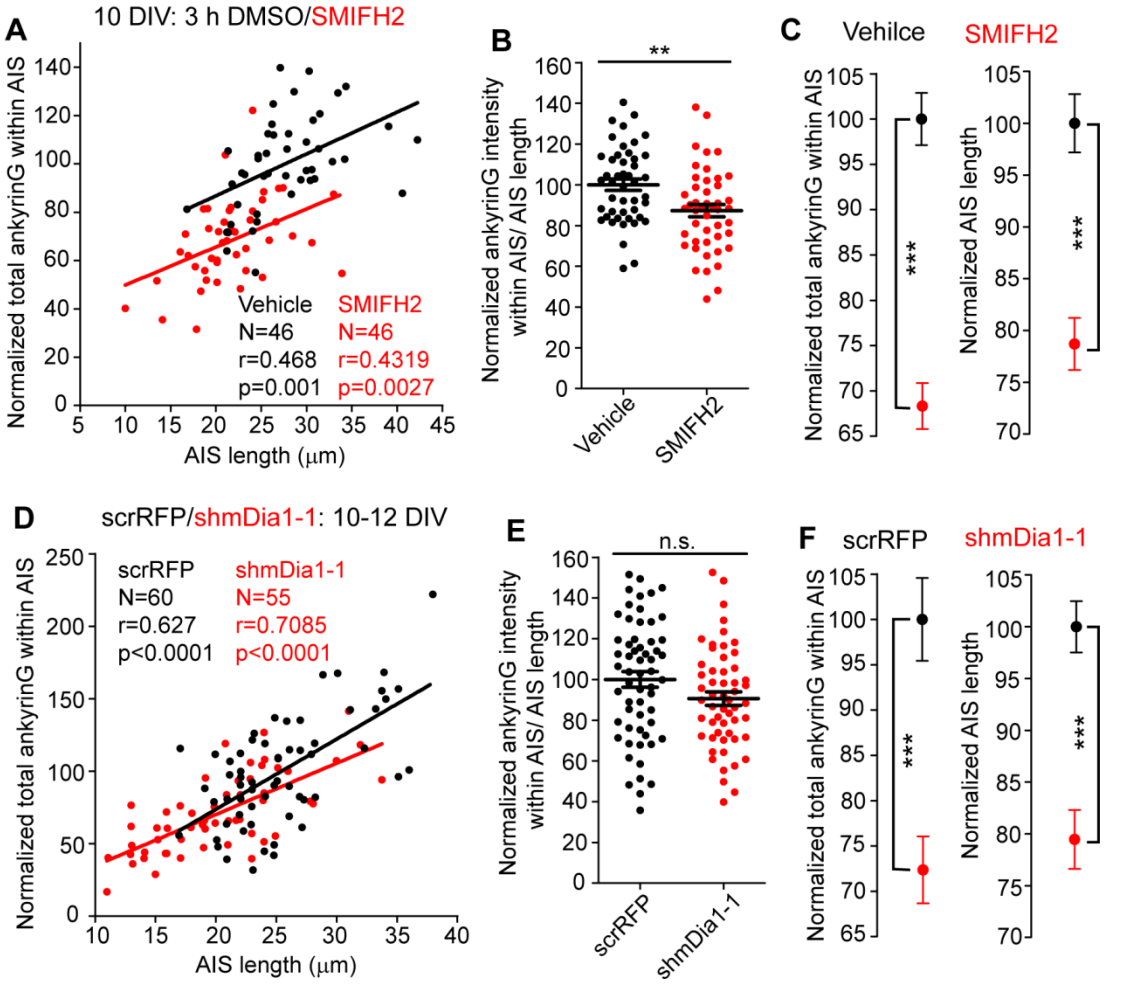

Figure R18. AnkyrinG decrease caused by mDia1 inhibition or suppression is partially due to AIS length shortening. (**A, D**) Cell-to-cell analysis of the relationship between normalized total ankyrinG intensity and AIS length of 10 DIV hippocampal neurons in the presence (red) or absence (black) of 15 μM SMIFH2 treatments (A) and 12 DIV hippocampal neurons transfected at 10 DIV (D) with interference RNAs scrRFP (black) or shmDia1-1 (red). Data fit a normal distribution and Pearson correlation test was performed. The number of neurons, Pearson r coefficient and p values are indicated in the graph. (**B, E**) Quantification of the ratio of normalized total ankyrinG intensity within AIS versus AIS length. Quantified neurons are from (A or D). n.s., not significant, p = 0.0672, **p < 0.01, unpaired t test. (**C, F**) Graphs show the normalized ankyrinG intensity within AIS and AIS length. Quantified neurons are from (A or D). ***p < 0.0001, unpaired t test. All data were acquired from three independent experiments and represented as the mean ± SEM.

To explore the reason that leads to the statistical difference of the ratio between mDia1 inhibition and mDia1 suppression, we re-analyzed ankyrinG intensity within AIS and AIS length in both conditions. We found a ~21% decrease of AIS length after SMIFH2 acute treatment (78.69 ± 2.52%; Fig. R18C) and mDia1 short-term suppression (79.47 ± 2.85%; Fig. R18F). However, SMIFH2 treated neurons showed 68.33 ± 2.54% of total ankyrinG intensity within AIS (n=46; Fig. R18C), while mDia1 suppressed neurons had 72.37 ± 3.70% of total ankyrinG intensity within AIS (n=55; Fig. R18F). A slightly less reduction of total ankyrinG intensity leads to the statistical difference of average ankyrinG intensity between mDia1 knockdown experiments and mDia1 inhibition experiments. Combined, the total ankyrinG

intensity is positively correlated with AIS length in all the conditions. In addition, an AIS length independent ankyrinG decrease was also observed, as shown in the reduction of average ankyrinG intensity in mDia1 inhibited or suppressed neurons.

Together, all these data demonstrate that mDia1 expression and activity are required to maintain AIS structural integrity and plasticity in hippocampal neurons.

7. mDia1 activity is essential for AIS structural plasticity in vivo

Our data in cultured hippocampal neurons demonstrate that loss of mDia1 activity and expression decreases AIS components and shortens AIS length. To further understand whether mDia1 has the same function in more complex brain models, we employed brain slices and blocked mDia1 activity through acute SMIFH2 treatment using 15 μM or 30 μM concentrations. Coronal sensorimotor cortex slices (300 μm) from mice P26-P30 were treated with SMIFH2 or DMSO for 3 h in a solution buffer equilibrated with 95% O_2-5% CO_2. Fixed brain slices were labeled with ankyrinG antibody and bisBenzimide to stain nuclei and to identify specific regions of cerebral cortex and hippocampus. We analyzed AIS length and ankyrinG staining. Images were acquired from 40x oil objective of confocal microscope (1024 × 1024 pixels) spanning 35 μm thickness with a 0.5-μm step size.

AIS was first traced one by one in the z-projected image of cerebral cortex. Taken into account that AIS may differ in different layers, first we explored the total ankyrinG intensity and AIS length in three regions of the cerebral cortex (layers II/III, layer IV and layers V/VI). In control brain slices, no significant change was observed in ankyrinG intensity between these regions using layers II/III as a reference (layers II/III, 100 ± 4.30%; layer IV, 107.5 ± 3.68%; layers V/VI, 107.2 ± 2.52%; Kruskal-Wallis, Dunn's multiple comparison test; Fig. R19B). However, AIS length were significantly different in all the categorized layers (19.39 ± 0.41 μm for layers II/III, 21.49 ± 0.48 μm for layer IV, 23.04 ± 0.28 μm for layers V/VI, Kruskal-Wallis, Dunn's multiple comparison test; Fig. R19C).

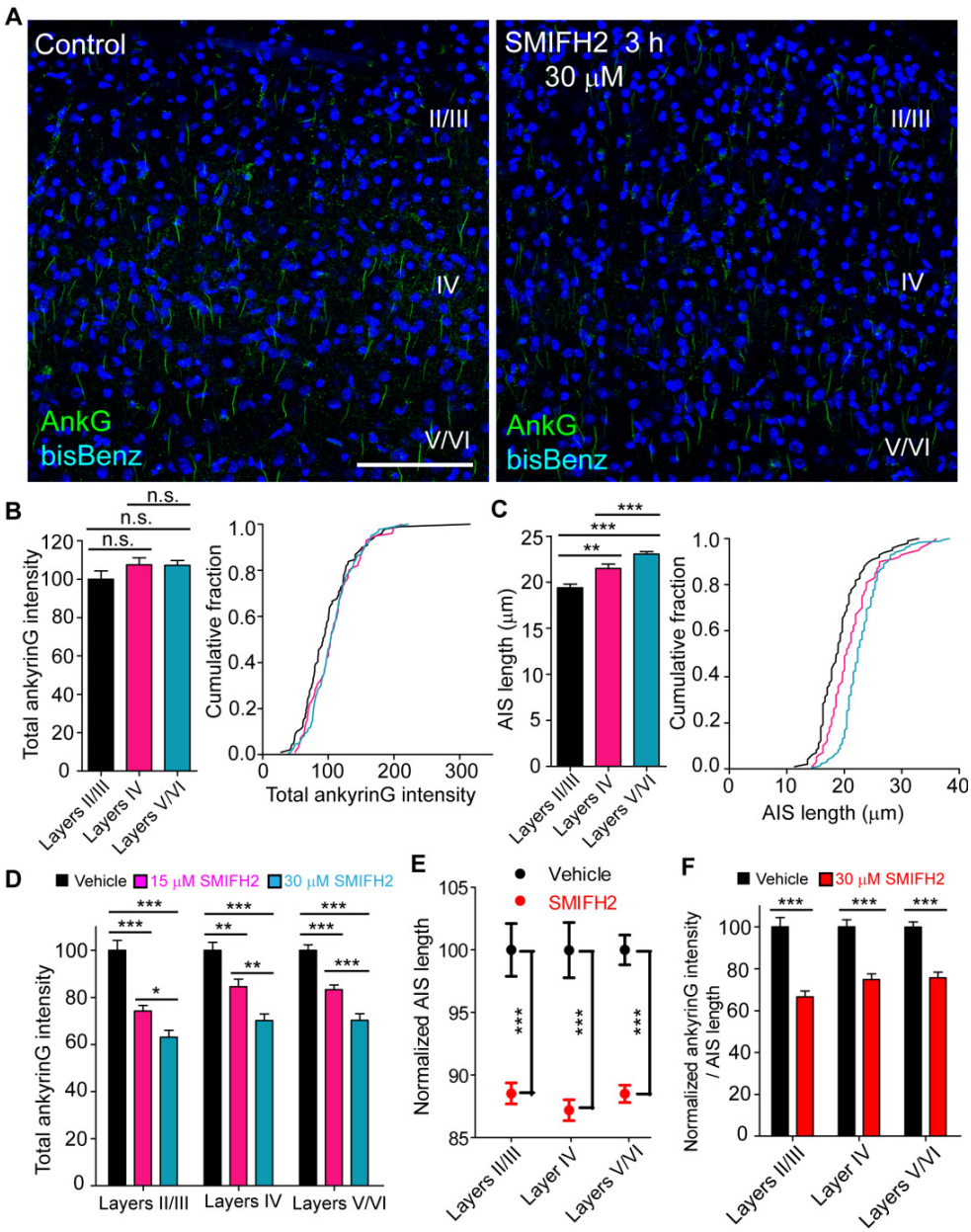

Figure R19. Formins inhibition decreases ankyrinG intensity and shortens AIS length in brain slices of cerebral cortex. (**A**) Coronal sensorimotor cortex slices (300 μm) from P30 mice were treated with DMSO or 30 μM SMIFH2 for 3 h. Fixed brain slices were labeled with ankyrinG (green) antibody and bisBenzimide (blue) to stain nuclei. Layers were categorized into layers II/III, layer IV and layers V/VI, as shown in images. Scale bar = 100 μm. (**B**) Quantification of total ankyrinG intensity in layers II/III, layer IV and layers V/VI of coronal sensorimotor cortex in P30 mice. n.s., not significant, Kruskal-Wallis, Dunn's multiple comparison test. In the right panel, a cumulative fraction plot shows a distribution of normalized total ankyrinG intensity. (**C**) Quantification of AIS length based on ankyrinG intensity in layers II/III, layer IV and layers V/VI of coronal sensorimotor cortex in P30 mice. $^{**}p < 0.01$, $^{***}p < 0.001$, Kruskal-Wallis, Dunn's multiple comparison test. In the right panel, a cumulative fraction plot shows a distribution of AIS length. (**D**) Quantification of total ankyrinG intensity in the presence or absence (dark) of 15 μM (magenta) or 30 μM (light blue) SMIFH2 in layers II/III, layer IV and layers V/VI of coronal sensorimotor cortex in P30 mice. $^{*}p < 0.05$, $^{**}p < 0.01$, $^{***}p < 0.001$, Kruskal-Wallis, Dunn's multiple comparison test. (**E**) Quantification of AIS length based on ankyrinG intensity in the presence (red) or absence (dark) of 30 μM SMIFH2 in layers II/III, layer IV and layers V/VI of coronal sensorimotor cortex in P30 mice. $^{***}p < 0.0001$, Mann Whitney test. (**F**) Quantification of the ratio of normalized total ankyrinG intensity / AIS length in the presence (red) or absence (dark) of 30 μM SMIFH2 in layers II/III, layer IV and layers V/VI of coronal sensorimotor cortex in P30 mice. $^{***}p < 0.0001$, Mann Whitney test. All data were acquired from three independent experiments and represented as the mean ± SEM.

To precisely evaluate the SMIFH2 effects on AIS, we compared AIS intensity and length according to the categorized layers. We found that 15 μM SMIFH2 treatment significantly decreased ankyrinG intensity in all the layers (Kruskal-Wallis, Dunn's multiple comparison test; Fig. R19D) and the decrease was even higher in 30 μM SMIFH2 treated brain slices (layers II/III, 63.11 ± 2.94% *vs* 74.22 ± 2.34% for 15 μM SMIFH2 treated brain slices; layer IV, 70.19 ± 2.76% *vs* 84.52 ± 3.24% for 15 μM SMIFH2 treated brain slices; layers V/VI, 70.24 ± 2.79% *vs* 83.34 ± 1.99% for 15 μM SMIFH2 treated brain slices; Fig. R19D). Thus, 30 μM SMIFH2 was used for the following experiments in brain slices. 30 μM SMIFH2 treatment significantly reduced AIS length in layers II/III (88.53 ± 0.84% *vs* 100 ± 2.11% for DMSO treated neurons, Mann Whitney test, $p < 0.0001$), layer IV (87.19 ± 0.84% *vs* 100 ± 2.21% for DMSO treated neurons, Mann Whitney test, $p < 0.0001$) and layers V/VI (88.50 ± 0.69% *vs* 100 ± 1.20% for DMSO treated neurons, Mann Whitney test, $p < 0.0001$; Fig. R19E). A similar AIS length decrease was observed in all layers of treated neurons (Fig. R19E). To study the average ankyrinG intensity versus AIS length, the ratio of normalized total ankyrinG intensity / AIS length was analyzed. We found a ~25% reduction of this ratio in all the analyzed layers after SMIFH2 treatment (Mann Whitney test, $p < 0.0001$; Fig. R19F).

In order to ascertain the data from cerebral cortex, CA1 regions of hippocampi were used for ankyrinG intensity analysis. As above described, images were acquired from 40x oil objective of SP5 spanning 35 μm thickness with a 0.5-μm step size. The whole AIS regions were selected from one z-projected images according to ankyrinG staining and background was subtracted, due to the complexity of analyzing individual AIS in hippocampi. We found that 30 μM SMIFH2 dramatically reduced ankyrinG intensity of CA1 regions after 3 h treatment (Fig. R20A). Corrected total fluorescence intensity showed that SMIFH2 treated neurons had lower ankyrinG intensity (79.11 ± 5.22%) compared to DMSO treated neurons (100 ± 3.00%, unpaired t test, $p = 0.0022$; Fig. R20B). To exclude the influence of selected area size, correct mean fluorescence intensity was measured. Consistently, our results showed a significant reduction of average ankyrinG intensity in SMIFH2 treated neurons (79.77 ± 3.95% *vs* 100 ± 3.51% for DMSO treated neurons, unpaired t test, $p = 0.0005$; Fig. R20C). Combined, these data demonstrate that mDia1 inhibition disrupts AIS structural integrity and plasticity in vivo at

short-term. This raises the question that how mDia1 is regulated and contributes to the regulation of AIS.

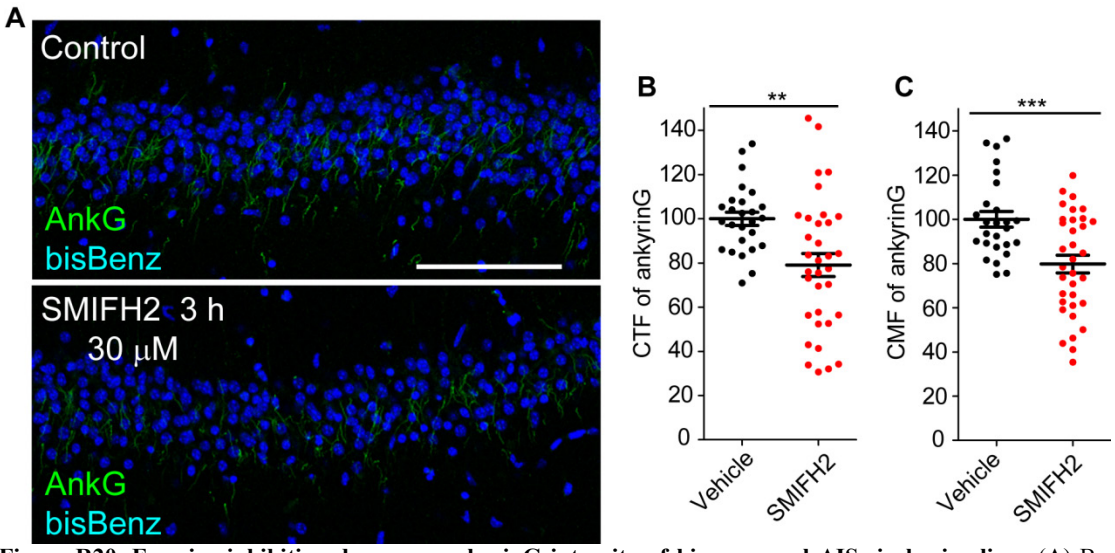

Figure R20. Formins inhibition decreases ankyrinG intensity of hippocampal AISs in brain slices. (**A**) Brain slices (300 μm) containing hippocampi from P26-P30 mice were treated with DMSO or 30 μM SMIFH2 for 3 h. Fixed brain slices were labeled with ankyrinG (green) antibody and bisBenzimide (blue) to stain nuclei. Scale bar = 100 μm. (**B**) Quantification of corrected total fluorescence intensity (CTF) in CA1 regions. **p < 0.01, unpaired t test. (**C**) Quantification of correct mean fluorescence intensity (CMF) in CA1 regions. ***p < 0.001, unpaired t test. All data were acquired from three independent experiments and represented as the mean ± SEM.

8. Deciphering mDia1 mediated AIS regulation pathway

8.1. Rho is not the upstream regulator of mDia1 for AIS regulation

Our above data have demonstrated that mDia1 regulates AIS components through downstream cytoskeleton regulation. This leads us to question which is the mDia1 upstream regulator. Previous studies have shown that RhoA-mDia1 signaling participates in many physiological processes both in neurons and in non-neuronal cells through actin and microtubules regulation (Qu et al., 2017; Zilberman et al., 2011). Furthermore, RhoA is involved in both neuro-epithelial and epithelial apico-basal polarity regulation (Acharya et al., 2017; Herder et al., 2013; Herzog et al., 2011). Taken all these into account, we investigated whether RhoA is the upstream regulator of mDia1 on AIS regulation. Given RhoA affects early neuronal development (Chen and Firestein, 2007; Fujita and Yamashita, 2014), we modified RhoA expression and activity after AIS had already formed. 10 DIV hippocampal neurons were transfected with RhoA plasmids and its mutants coupled to EGFP protein and fixed at 12 DIV. RhoA-T19N is a dominant negative construct and RhoA-Q63L is a constitutively active construct. Neurons were stained with ankyrinG antibody and total intensity was analyzed. We did not find any change of ankyrinG intensity in neurons with over-expressed RhoA (93.49 ± 4.40%),

neither in the case of RhoA-T19N (97.95 ± 4.95%) or RhoA-Q63L (97.83 ± 4.41%) compared to GFP transfected neurons (100 ± 4.05%, One-way analysis of variance, Tukey's multiple comparison test, n.s.; Fig. R21A).

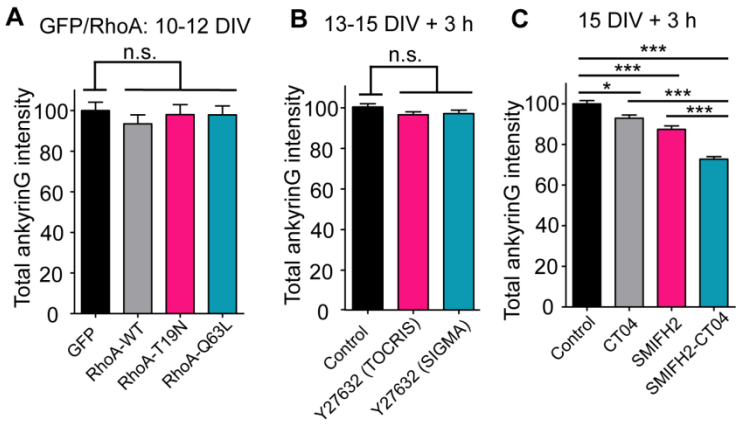

Figure R21. RhoA is not the upstream regulator of mDia1 for ankyrinG accumulation. (**A**) Quantification of total ankyrinG fluorescence intensity of 12 DIV hippocampal neurons transfected at 10 DIV with plasmids of GFP, RhoA wild-type (RhoA-WT), RhoA dominant negative form (RhoA-T19N) and RhoA constitutively active form (RhoA-Q63L). n.s., not significant, One-way analysis of variance, Tukey's multiple comparison test. (**B**) Quantification of total ankyrinG fluorescence intensity of 13-15 DIV hippocampal neurons treated with vehicle or 40 μM Y27632 (ROCK inhibitor) for 3 h. n.s., not significant, Kruskal-Wallis, Dunn's multiple comparison test. (**C**) Quantification of total ankyrinG fluorescence intensity of 15 DIV hippocampal neurons treated for 3 h with 1.0 μg/ml CT04 (Rho inhibitor), 15 μM SMIFH2 or the combination of both. *p < 0.05, ***p < 0.001, Kruskal-Wallis, Dunn's multiple comparison test. All data were acquired from three independent experiments and represented as the mean ± SEM.

To corroborate these data, we took advantage of the canonical RhoA effector, Rho-associated kinase (ROCK) (Schmandke et al., 2007). 13-15 DIV neurons were treated with 40 μM Y27632 (ROCK inhibitor) for 3 h. Two commercial Y27632 drugs were employed and we did not find any change of ankyrinG intensity in Y27632 treated neurons (96.08 ± 1.54% for TOCRIS drug treated neurons, 96.62 ± 1.76% for SIGMA drug treated neurons) compared to control neurons (100 ± 1.53%, Kruskal-Wallis, Dunn's multiple comparison test, n.s.; Fig. R21B).

Our data exhibited that it was not RhoA that signals mDia1 to regulate AIS integrity (Fig. R21A, B). However, previous studies have shown that apart from RhoA, RhoB and RhoC can also bind to mDia1 in its N-terminal region (Watanabe et al., 1999). Besides, RhoB and RhoC can remodel cellular cytoskeleton (Fernandez-Borja et al., 2005; Luo et al., 2017). Thus, we employed a general Rho inhibitor CT04 to explore whether other Rho proteins are mDia1 upstream regulators. 15 DIV neurons were treated for 3 h and total ankyrinG intensity was analyzed. We found that ankyrinG intensity showed a slightly significant decrease after treatment with 1.0 μg/ml CT04 (92.93 ± 1.56%) compared with vehicle treated neurons (100 ± 1.62%, p < 0.05; Fig. R21C). SMIFH2 treatment decreased ankyrinG intensity (87.42 ± 1.69%), while neurons co-treated with SMIFH2 and CT04 remarkably decreased ankyrinG accumulation

in the AIS (72.69 ± 1.30%, $p < 0.001$; Fig. R21C). Statistical analysis revealed that ankyrinG intensity in co-treated neurons was significantly lower compared to either CT04 treated neurons or SMIFH2 treated neurons (Kruskal-Wallis, Dunn's multiple comparison test, $p < 0.001$; Fig. R21C). Together, our data suggest that Rho is not the upstream modulator of mDia1 in the process of AIS regulation. Further study is needed to decipher the upstream regulator and perfect mDia1 cell signaling.

8.2. mDia1 mediated AIS components loss is independent of calpain signaling

Previous studies reported that calcium-dependent calpain signaling is responsible for AIS components degradation (Schafer et al., 2009). Inhibition of calpain activity by 50 nM MDL 28170 can rescue AIS composition loss caused from calcium influx (Del Puerto et al., 2015). Therefore, we investigated whether the loss of ankyrinG caused by mDia1 inhibition is related to calpain activation. 14 DIV neurons were pre-treated with 50 nM or 1 µM MDL 28170 or DMSO for 1 h, followed by 3 h treatment with 15 µM SMIFH2. Consistent with previous results, we found a significant reduction of total ankyrinG intensity in SMIFH2 treated neurons (80.87 ± 2.31% *vs* 100 ± 2.11% for vehicle treated neurons, $p < 0.001$; Fig. R22A). However, MDL 28170 pre-treatment did not block ankyrinG decrease after SMIFH2 treatment (78.01 ± 2.07% for 50 nM MDL 28170 pre-treated neurons, 76.44 ± 2.03% for 1 µM MDL 28170 pre-treated neurons *vs* 80.87 ± 2.31% for only SMIFH2 treated neurons, Kruskal-Wallis, Dunn's multiple comparison test, n.s.; Fig. R22A). This was confirmed by the cumulative fraction plot of total ankyrinG intensity (Fig. R22B).

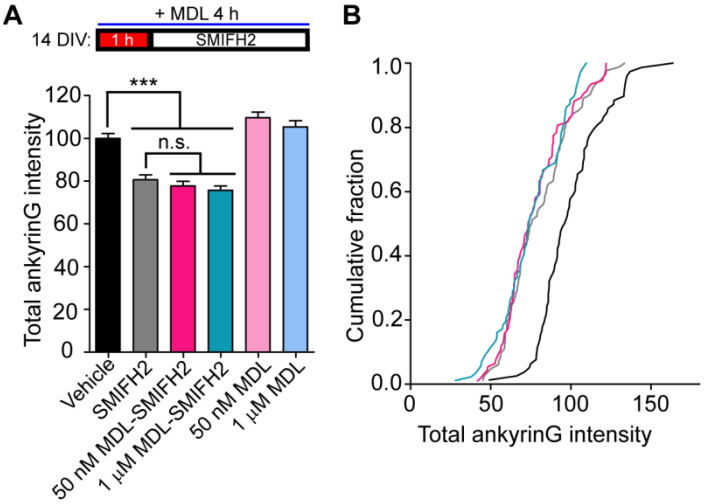

Figure R22. Calpain inhibition does not avoid ankyrinG decrease induced by formins inhibition. (**A**) Quantification of total ankyrinG fluorescence intensity. 14 DIV hippocampal neurons were treated with vehicle DMSO or 50 nM or 1 µM MDL 28170 (MDL, calpain inhibitor) for 1 h prior to 3 h treatment with vehicle DMSO or 15 µM SMIFH2. n.s., not significant, ***$p < 0.001$, Kruskal-Wallis, Dunn's multiple comparison test. (**B**) A cumulative fraction plot shows a distribution of normalized total ankyrinG intensity quantified in A of vehicle, SMIFH2, 50 nM MDL-SMIFH2 and 1 µM MDL -SMIFH2 conditions. Data were acquired from three independent experiments and represented as the mean ± SEM.

8.3. mDia1 mediated AIS integrity is related with F-actin dynamics regulation

In view of these results, we decided to assess whether AIS cytoskeleton regulatory factors may be linked to mDia1 AIS regulation. AIS cytoskeleton modulation contributes to AIS assembly and maintenance (Berger et al., 2018; Tapia et al., 2010). Our results have shown that mDia1 inhibition destabilized F-actin (Fig. R5) and microtubules (Fig. R6). We systematically studied how stabilization/destabilization of actin or microtubules contributes to AIS integrity in relation to mDia1. First, we analyzed actin dynamics. For this purpose, we used an F-actin stabilizing agent, Jasplakinolide, and and actin destabilizing agent, Latrunculin A. We found that F-actin destabilization triggered by Latrunculin A decreased ankyrinG intensity (85.09 ± 1.63% for 0.5 μM Latrunculin A treated neurons, 86.10 ± 1.48% for 1 μM Latrunculin A treated neurons *vs* 100 ± 1.41% for DMSO treated neurons; One-way analysis of variance, Tukey's multiple comparison test, $p < 0.001$; Fig. R23A-C). Interestingly, enhancement of F-actin stability by Jasplakinolide also significantly reduced ankyrinG accumulation in the AIS (89.74 ± 1.07% for 10 nM Jasplakinolide treated neurons, 86.27 ± 1.30% for 25 nM Jasplakinolide treated neurons *vs* 100 ± 1.09% for DMSO treated neurons; Kruskal-Wallis, Dunn's multiple comparison test, $p < 0.001$; Fig. R23A, D, E). Given our results that actin dynamics are essential to maintain AIS structural integrity and mDia1 inhibition destabilizes actin filaments, we tested whether AIS deficiency in SMIFH2 treated neurons could be ameliorated through stabilizing F-actin. 14 DIV neurons were treated with 15 μM SMIFH2, 10 nM Jasplakinolide or both reagents for 3 h and total ankyrinG intensity in 30 μm AIS was quantified. We found that ankyrinG intensity did not change between SMIFH2 treated neurons (91.05 ± 2.34%) and SMIFH2-Jasplakinolide co-treated neurons (86.90 ± 2.20%, n.s.; Fig. R23F). Taken into account that sequence of drugs application might affect F-actin stabilization efficiency, we first stabilized F-actin 1 h in advance using Jasplakinolide and then treated with SMIFH2 for another 3 h. Similarly, Jasplakinolide pre-treatment failed to rescue ankyrinG reduction in SMIFH2 treated neurons (90.68 ± 1.24% *vs* 88.43 ± 1.27% for only SMIFH2 treated neurons, n.s.; Fig. R23G). Due to this unexpected result and in order to get a better understanding of actin in the AIS, we analyzed whether an AIS actin related structure, the cisternal organelle (CO), was affected by Jasplakinolide and SMIFH2 treatments.

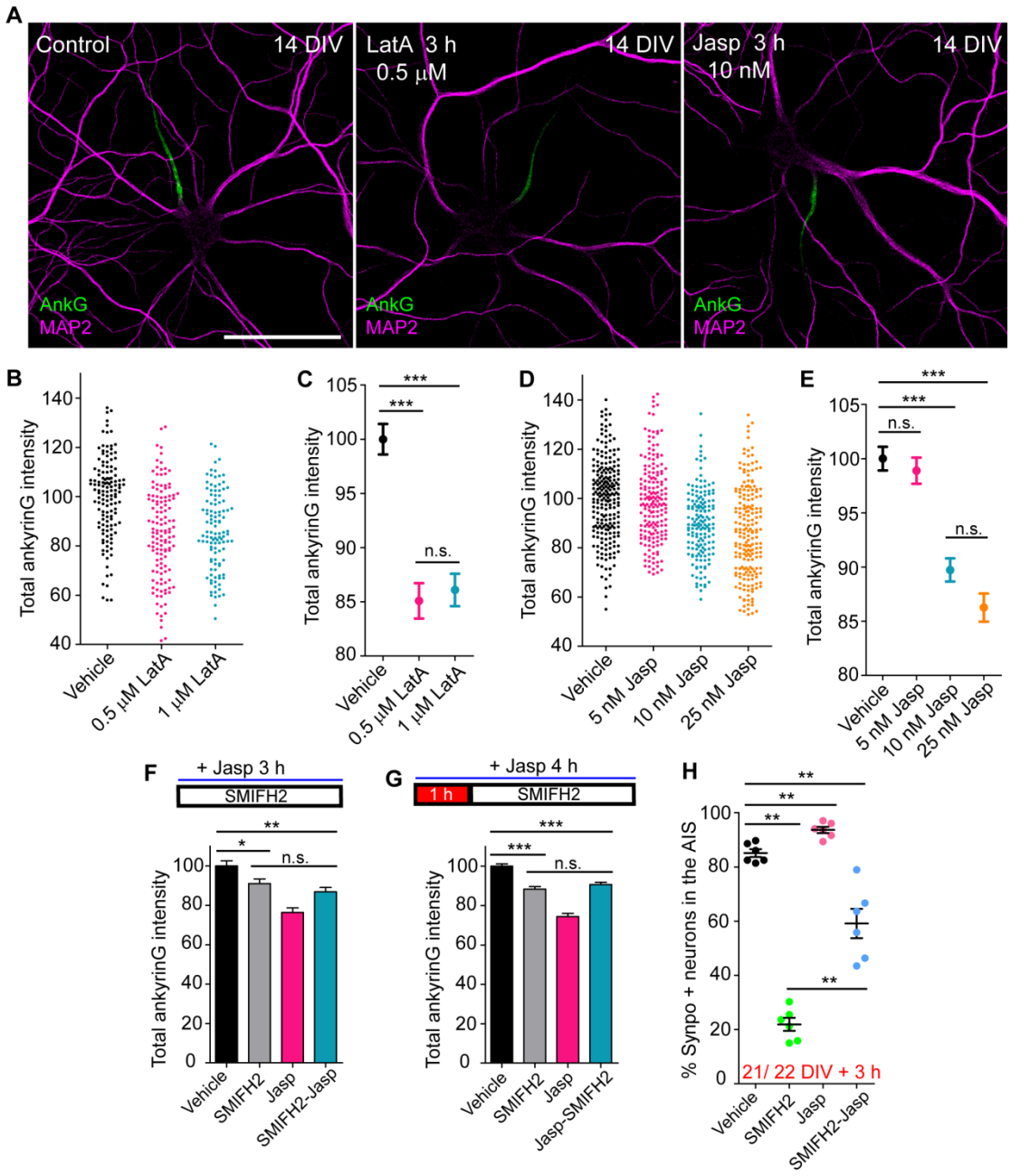

Figure R23. Disruption of actin dynamics leads to ankyrinG reduction. (**A**) Hippocampal neurons were cultured for 14 DIV and then treated for 3 h with vehicle DMSO, 0.5 µM Latrunculin A (LatA, actin destabilizing agent) or 10 nM Jasplakinolide (Jasp, F-actin stabilizing agent). Neurons were fixed and stained with MAP2 (magenta) and ankyrinG antibodies (green). Scale bar = 50 µm. (**B, C**) Quantification of total ankyrinG fluorescence intensity of 14 DIV neurons treated for 3 h with vehicle DMSO, 0.5 µM or 1 µM Latrunculin A. n.s., not significant, ***p < 0.001, One-way analysis of variance, Tukey's multiple comparison test. (**D, E**) Quantification of total ankyrinG fluorescence intensity of 14 DIV neurons treated for 3 h with vehicle DMSO, 5 nM, 10 nM or 25 nM Jasplakinolide. n.s., not significant, ***p < 0.001, Kruskal-Wallis, Dunn's multiple comparison test. (**F, G**) Quantification of total ankyrinG fluorescence intensity of 14 DIV hippocampal neurons treated for 3 h with 10 nM Jasplakinolide, 15 µM SMIFH2 or the combination of both (F), or treated with vehicle DMSO or 10 nM Jasplakinolide for 1 h prior to 3 h treatment with vehicle DMSO or 15 µM SMIFH2 (G), n.s., not significant, *p < 0.05, **p < 0.01, Kruskal-Wallis, Dunn's multiple comparison test in F, or n.s., not significant, ***p < 0.001, One-way analysis of variance, Tukey's multiple comparison test in G. (**H**) Quantification of the percentage of synaptopodin puncta positive neurons in the AIS. 21 or 22 DIV hippocampal neurons were treated for 3 h with 10 nM Jasplakinolide, 15 µM SMIFH2 or the combination of both. **p < 0.01, Mann Whitney test. All data were acquired from three independent experiments and represented as the mean ± SEM.

To test this, 21 or 22 DIV hippocampal neurons were treated with SMIFH2, Jasplakinolide or the combination of both reagents for 3 h and the percentage of CO positive neurons in the AIS was evaluated. CO was identified by synaptopodin marker and ankyrinG staining was used to identify the AIS. SMIFH2 treatment significantly decreased CO positive neurons in the AIS (21.93 ± 2.38% *vs* 85.13 ± 1.44% for vehicle treated neurons, Mann Whitney test, $p = 0.005$), which was partially rescued by the co-treatment of SMIFH2 and Jasplakinolide (59.15 ± 5.45%, Mann Whitney test, $p < 0.01$; Fig. R23H). Indeed, more percentage of neurons had CO in the AIS after Jasplakinolide treatment (93.65 ± 1.16% *vs* 85.13 ± 1.44% for vehicle treated neurons, Mann Whitney test, $p = 0.0081$; Fig. R23H). These data propose a participation of mDia1 in actin dynamics regulation at the AIS such as modulating actin related structures, the cisternal organelle. However, the fact that ankyrinG intensity is not recovered by F-actin stabilization, which suggests that other AIS cytoskeleton components may participate on mDia1 mediated modulation.

8.4. Microtubule properties contribute to AIS components loss caused by mDia1 inhibition or suppression

As aforementioned, mDia1 inhibition decreased tubulin acetylation in the AIS (Fig. R6). Thus, we asked whether balancing the level of acetylated tubulin can rescue AIS deficiency caused by mDia1 inhibition. HDAC6 is a tubulin deacetylase and functions in the AIS regulation through tubulin deacetylation (Tapia et al., 2010). To increase the level of acetylated tubulin, we used 10 μM Tubastatin A, an inhibitor of HDAC6. 14 DIV neurons were treated with SMIFH2, Tubastatin A, SMIFH2-Tubastatin A or vehicle for 3 h. We analyzed ankyrinG intensity, as well as, AIS length. Acute Tubastatin A treatment did not change ankyrinG intensity (101 ± 1.80%) compared to vehicle treated neurons (100 ± 1.51%), while SMIFH2 treated neurons showed a significant reduction (81.33 ± 1.45%, $p < 0.001$; Fig. R24A). However, ankyrinG intensity was rescued by Tubastatin A in SMIFH2 treated neurons (95.69 ± 1.63%) compared to SMIFH2 treated neurons (81.33 ± 1.45%, $p < 0.001$; Fig. R24A). Consistently, the ratio of normalized total ankyrinG intensity within AIS / AIS length revealed that Tubastatin A treatment prevented ankyrinG decrease in SMIFH2 treated neurons along AIS (106 ± 2.59% for co-treated neurons *vs* 84.13 ± 1.99% for SMIFH2 treated neurons, $p < 0.001$; Fig. R24B). These

data suggest that microtubules regulation through HDAC6 is related to mDia1 and at least regulates ankyrinG expression at the AIS.

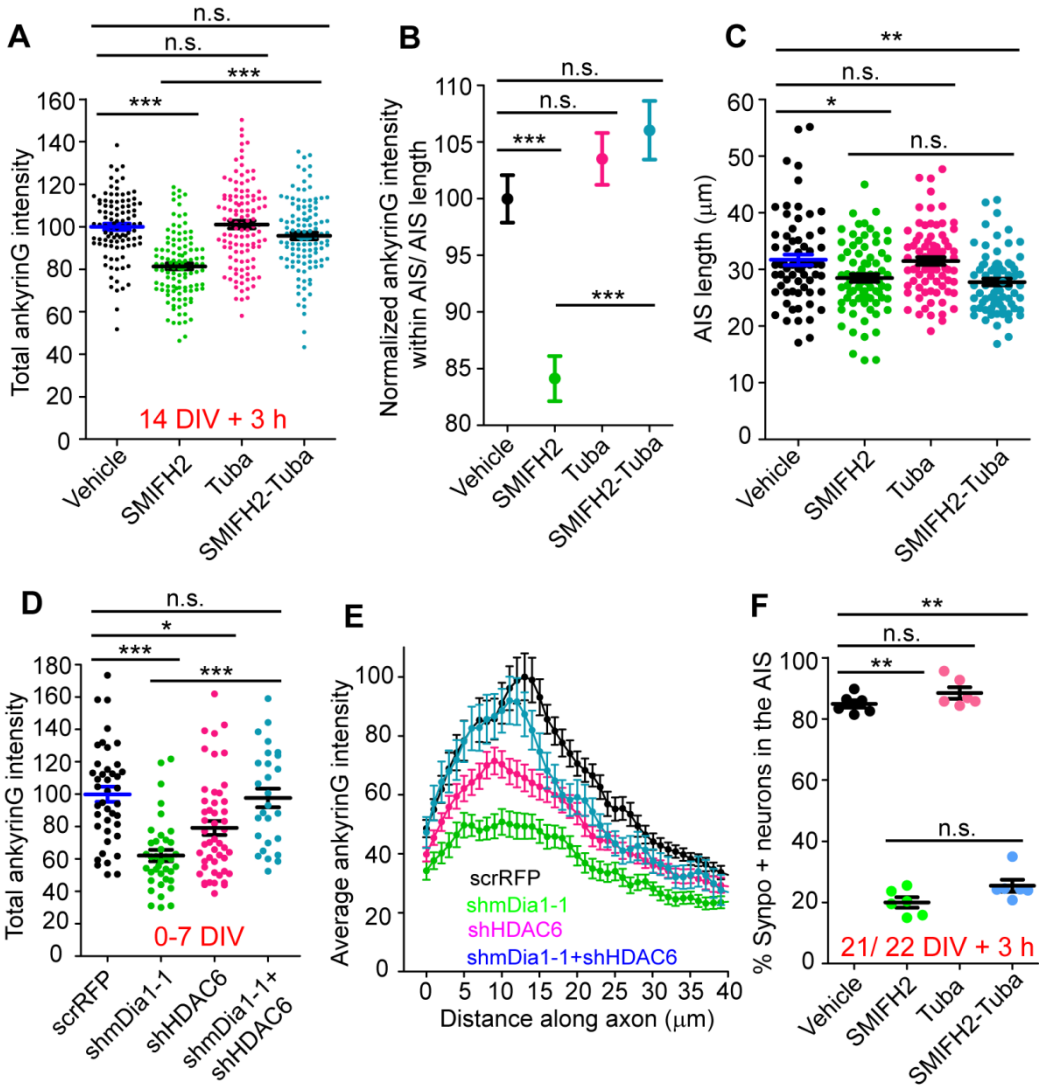

Figure R24. HDAC6 inhibition or suppression rescues ankyrinG loss in hippocampal neurons after mDia1 inhibition or knockdown. (**A**) Quantification of total ankyrinG fluorescence intensity in 14 DIV hippocampal neurons treated for 3 h with 10 μM Tubastatin A (Tuba, HDAC6 inhibitor), 15 μM SMIFH2 or the combination of both. n.s., not significant, ***p < 0.001, One-way analysis of variance, Tukey's multiple comparison test. (**B**) Mean ± SEM ratio of normalized total ankyrinG intensity within AIS / AIS length. Quantified neurons are from A. n.s., not significant, ***p < 0.001, Kruskal-Wallis, Dunn's multiple comparison test. (**C**) AIS length of neurons quantified in B. n.s., not significant, *p < 0.05,**p < 0.01, Kruskal-Wallis, Dunn's multiple comparison test. (**D**) Quantification of total ankyrinG fluorescence intensity of 7 DIV hippocampal neurons nucleofected with mDia1 interference RNA (shmDia1-1), HDAC6 interference RNA (shHDAC6) or the combination of both. Neurons nucleofected with scrambled interference RNA (scrRFP) are used as control. n.s., not significant, *p < 0.05, ***p < 0.001, Kruskal-Wallis, Dunn's multiple comparison test. (**E**) Normalized average ankyrinG intensity profile along the AIS of 7 DIV hippocampal neurons nucleofected with scrRFP, shmDia1-1, shHDAC6 or the combination of shmDia1-1 and shHDAC6. (**F**) Quantification of the percentage of synaptopodin puncta positive neurons in the AIS. 21 or 22 DIV hippocampal neurons were treated for 3 h with 10 μM Tubastatin A, 15 μM SMIFH2 or the combination of both. n.s., not significant, **p < 0.01, Mann Whitney test. All data were acquired from three independent experiments and represented as the mean ± SEM.

Next, we explored whether Tubastatin A can recover AIS length due to mDia1 inhibition. Our previous results have shown that AIS length shortens after SMIFH2 treatment in 10 DIV

neurons (Fig. R17D-F). In this set of experiments, SMIFH2 treatment also significantly decreased AIS length in 14 DIV neurons (28.49 ± 0.68 μm *vs* 31.71 ± 0.95 μm for vehicle treated neurons, $p < 0.05$; Fig. R24C). However, Tubastatin A treatment did not rescue AIS length shortening in SMIFH2 treated neurons (27.80 ± 0.61 μm for co-treated neurons *vs* 28.49 ± 0.68 μm for SMIFH2 treated neurons, n.s.; Fig. R24C).

To corroborate these results, instead we used interference RNA plasmids for HDAC6 and mDia1. Neurons were nucleofected with interference RNA plasmids: shHDAC6-GFP, shmDia1-1-RFP, shHDAC6 and shmDia1-1 in combination or scrRFP and fixed at 7 DIV. As happened with HDAC6 inhibition using Tubastatin A in SMIFH2 treated neurons, we found that co-nucleofected neurons expressing shmDia1-1 and shHDAC6 plasmids prevented ankyrinG decrease observed in shmDia1-1 nucleofected neurons (62.16 ± 3.54%) compared to 97.72 ± 5.80% in shmDia1-1/shHDAC6 nucleofected neurons ($p < 0.001$; Fig. R24D). In contrast to the results that 3 h inhibition of HDAC6 had no effect on ankyrinG (Fig. R24A, B), shHDAC6 nucleofection decreased ankyrinG intensity after 7 DIV (79.17 ± 4.33%, $p < 0.05$) compared to control scrRFP nucleofected neurons (100 ± 4.71%; Fig. R24D). These results and the difference in ankyrinG intensity were confirmed, as observed in the plot profile of average ankyrinG intensity along the AIS (Fig. R24E).

To assess whether this rescue mediated by increasing acetylated tubulin has relation with actin filaments integrity, 21 or 22 DIV hippocampal neurons were treated with SMIFH2, Tubastatin A or combined reagents for 3 h and the percentage of CO positive neurons in the AIS was evaluated, as previously performed for the study of actin dynamics (Fig. R23H). Neurons were labeled with synaptopodin and ankyrinG antibodies to identify CO and AIS respectively. A significant decrease of CO positive neurons in the AIS was found both in SMIFH2 treated neurons (20.02 ± 1.70%) and SMIFH2-Tubastatin A co-treated neurons (25.48 ± 1.99%) compared to vehicle treated neurons respectively (84.90 ± 1.26%, Mann Whitney test, $p < 0.01$; Fig. R24F). The percentage of CO positive neurons in the AIS did not show any difference between SMIFH2 and Tubastatin A co-treated neurons and SMIFH2 treated neurons (Mann Whitney test, $p = 0.0649$; Fig. R24F), indicating that microtubules modifications might not be related to cisternal organelle alterations due to mDia1 inhibition, in contrast to what observed in

actin related experiments.

8.5. mDia1 inactivity induced ankyrinG loss can be rescued by exogenous EB1 expression or dynein inhibition

All above data point to that mDia1 modulation of AIS is through regulation of actin and microtubules structure and functions. As described in the introduction section, formins and specifically, mDia1, is able to modulate actin dynamics and tubulin acetylation (Acharya et al., 2017; Bartolini et al., 2016). Thus, in order to understand whether an AIS component common to actin and microtubules is linked to mDia1 mediated AIS regulation, we studied EB1 as a potential link to mDia1. End binding (EB) protein EB1 has been reported to contribute to the maintenance of the AIS structure and participation in the AIS assembly (Freal et al., 2016; Leterrier et al., 2011). EB1 stabilizes microtubules and promotes actin filaments elongation through directly or indirectly binding to mDia1 (Henty-Ridilla et al., 2016; Wen et al., 2004). Thus, we transfected 9-11 DIV hippocampal neurons with EB1-GFP or GFP respectively and maintained neurons for another 48 h. Neurons were treated with SMIFH2 or DMSO for 3 h before fixation. Total ankyrinG intensity in 30 µm AIS was analyzed. We found that EB1-GFP expression prevented ankyrinG reduction observed in GFP transfected neurons after SMIFH2 treatment (89.84 ± 3.74% for EB1-SMIFH2 neurons *vs* 65.40 ± 4.24% for GFP-SMIFH2 neurons, $p < 0.01$; Fig. R25A). EB1-GFP expression had no effect on ankyrinG accumulation in the AIS (97.58 ± 3.76% for EB1-GFP-DMSO neurons *vs* 100 ± 4.23% for GFP-DMSO neurons; Fig. R25A). This effect was confirmed along the AIS in the average ankyrinG intensity plot profile (Fig. R25B).

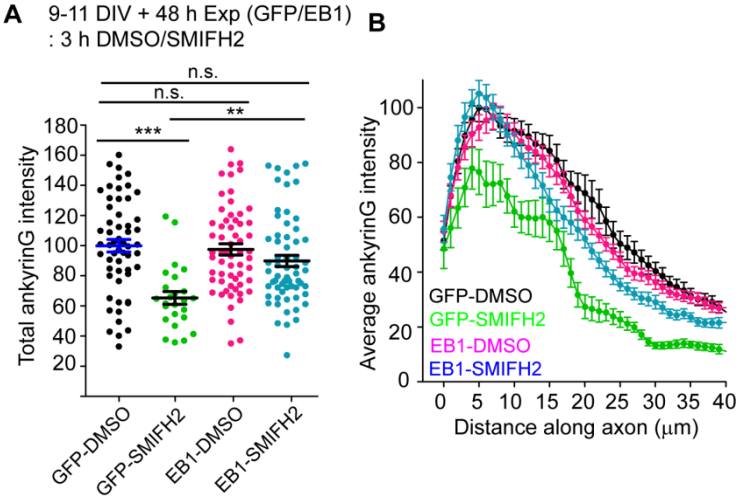

Figure R25. Over-expression of EB1 rescues ankyrinG loss induced by mDia1 inhibition in hippocampal neurons. (**A**) Quantification of total ankyrinG fluorescence intensity in the AIS. 9-11 DIV hippocampal neurons were transfected with GFP or EB1-GFP for 48 h and then exposed to DMSO or 15 µM SMIFH2 for 3 h. n.s., not significant, **p < 0.01, ***p < 0.001, Kruskal-Wallis, Dunn's multiple comparison test. (**B**) Normalized average ankyrinG intensity profile along the AIS of hippocampal neurons shown in A. All data were acquired from three independent experiments and represented as the mean ± SEM.

Then, we took advantage of this normalized smooth ankyrinG intensity profile and assessed AIS length according to the reference of 33% of maximal ankyrinG intensity. However, AIS length was not rescued in EB1 transfected neurons after SMIFH2 treatment as happened after HDAC6 inhibition (~34 μm, ~23 μm, ~33 μm, ~25 μm for neurons in conditions of GFP-DMSO, GFP-SMIFH2, EB1-GFP-DMSO, and EB1-GFP-SMIFH2 respectively; Fig. R25B).

Our data have shown that mDia1 inhibition mediated ankyrinG loss at the AIS can be recovered by increased acetylation of microtubules and EB1 expression. Moreover, our results showed that KIF5C distribution is modified in neurons after mDia1 inhibition. Thus, one potential cause of ankyrinG loss is the alteration of the AIS cytoskeleton properties to control traffic towards the axon. Thus, we hypothesized that compensating the lack of anterograde transport of AIS components could reverse ankyrinG loss by inhibiting retrograde transport and keeping ankyrinG at the AIS. One of the important mediators of retrograde transport at the AIS is dynein (Kuijpers et al., 2016). Dynein participates on neuronal polarity maintenance avoiding the axonal entry of somatodendritic proteins through their retrograde transport in the AIS (Klinman et al., 2017; Kuijpers et al., 2016). In fact, dynein and its accessory complex dynactin interact with EB1 (Baumbach et al., 2017; Berrueta et al., 1999). Thus, we investigated whether dynein inhibition with Ciliobrevin D could rescue ankyrinG reduction in mDia1 inhibited neurons (Firestone et al., 2012). 14 DIV neurons were treated with 15 μM SMIFH2 and 20 μM Ciliobrevin D (Sainath and Gallo, 2015), SMIFH2-Ciliobrevin D or vehicle for 3 h and ankyrinG intensity was then analyzed. We found that Ciliobrevin D application partially prevented the reduction of ankyrinG intensity in SMIFH2 treated neurons (87.17 ± 1.56% *vs* 75.82 ± 1.38% for SMIFH2 treated neurons and 100 ± 1.41% for vehicle treated neurons, One-way analysis of variance, Tukey's multiple comparison test, $p < 0.001$, Fig. R26A). AnkyrinG intensity in Ciliobrevin D treated neurons was comparable to vehicle treated neurons after 3 h acute treatment (Fig. R26A). The partial rescue effect was corroborated by the average ankyrinG intensity along the AIS (Fig. R26B). However, Ciliobrevin D failed to rescue AIS length shortening according to the final smooth profile pooled from all the neurons in the corresponding conditions (~30 μm in SMIFH2 or SMIFH2-Ciliobrevin D treated neurons, ~34 μm in vehicle or Ciliobrevin D treated neurons; Fig. R26B). Combined, dynein inhibition

partially rescued AIS components integrity after loss of mDia1 activity.

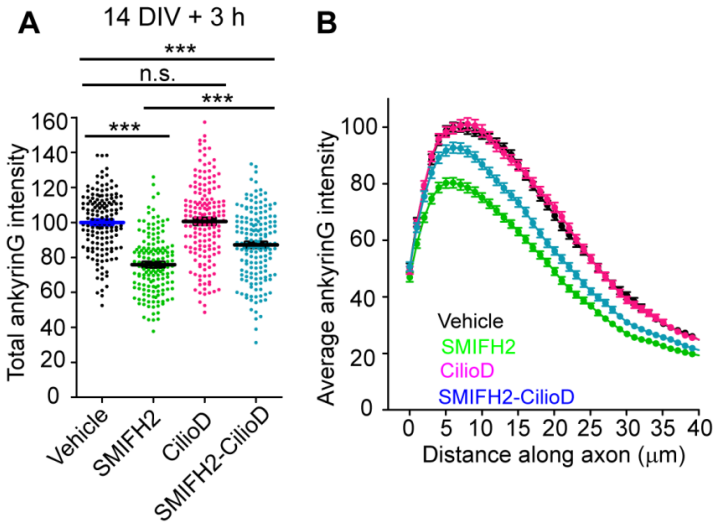

Figure R26. Dynein inhibition partially rescues ankyrinG loss in mDia1 inhibited hippocampal neurons. (**A**) Quantification of total ankyrinG fluorescence intensity of 14 DIV hippocampal neurons treated for 3 h with 20 μM Ciliobrevin D (CilioD, dynein inhibitor), 15 μM SMIFH2 or the combination of both. n.s., not significant, ***p < 0.001, One-way analysis of variance, Tukey's multiple comparison test. (**B**) Normalized average ankyrinG intensity profile along the AIS of hippocampal neurons shown in A.

All together, AIS components loss mediated by mDia1 inactivation can be recovered through cytoskeleton modulation as well as axonal motors regulation, in which both actin and microtubules are involved. However, the shortening of AIS length can not be rescued in our work, suggesting that a complex mechanism related with AIS stability and axonal traffic contributes to mDia1 mediated AIS integrity and plasticity. Although Rho proteins somewhat affect ankyrinG in the AIS, they are not the upstream regulator of mDia1. Additional studies are required to elucidate the cell signaling of mDia1 mediated AIS regulation.

9. Formins inhibition decreases intrinsic excitability

All these data suggest that changes in mDia1 expression and formins activity are important for the regulation of AIS composition and voltage gated sodium channels localization at the AIS, implicating a role of formins in the modulation of neuronal excitability. To corroborate the data obtained in hippocampal cultured neurons or brain slices and consolidate this latter hypothesis, hippocampal slice cultures containing the entorhinal cortex were used. Slices were treated with 30 μM SMIFH2 or DMSO, and kept for 2 hours before testing the electrophysiological properties of the neurons (Fig. R27). CA3 pyramidal neurons were used to analyze neuronal excitability and action potential number in current clamp. In accordance with our previous results showing an ankyrinG reduction after SMIFH2 treatment (Fig. R20), SMIFH2 treated neurons showed a significant reduction in the number of action potentials (Fig. R27A) and a higher rheobase (Fig. R27B), indicating that SMIFH2 treated neurons need a higher minimum

current to launch an action potential.

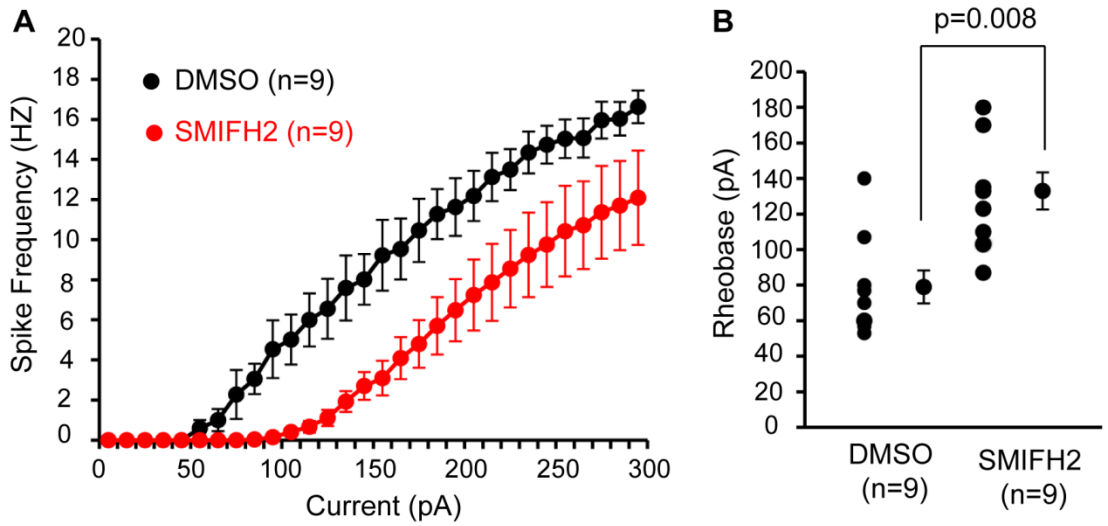

Figure R27. Formins inhibition decreases neuronal intrinsic excitability in hippocampal neurons. 350 μm brain slices containing the entorhinal cortex were used from P26-P30 mice. Intrinsic excitability was measured by current clamp in CA3 hippocampal neurons treated with 30 μM SMIFH2 or its vehicle DMSO for 2 h. (**A**) Input-output curves for control DMSO and SMIFH2 treated neurons. (**B**) Graph represents the mean ± SEM of the smallest injected current necessary to generate one action potential (Rheobase). *$p < 0.01$, Mann-Whitney test.

Discussion

The AIS is essential for action potential generation (Kole et al., 2008; Stuart et al., 1997) and neuronal polarity maintenance (Hedstrom et al., 2008; Sobotzik et al., 2009; Winckler et al., 1999). However, these functions require a fine regulation of its complex structure. Due to the complexity of AIS study, the knowledge of its molecular composition is still uncompleted, and it is still elusive how AIS performs its complex structural and functional regulation. Previous works have described some aspects of actin and microtubules structure at the AIS (Nirschl et al., 2017), however only a limited number of studies have proposed some potential regulatory mechanisms of AIS actin (Berger et al., 2018; Zhang et al., 2019) or microtubules cytoskeleton (Leterrier et al., 2011; Tapia et al., 2010). In this work, we have studied the potential role of formins on AIS regulation, as proteins that modulate both, actin and microtubules cytoskeletons. We demonstrate that formins take a role on maintaining AIS integrity. Formins inhibition decreases AIS expression of structural and functional proteins, such as, voltage-gated sodium channels. Among formins, mDia1 is the most studied formin family member. mDia1 is necessary to maintain cell polarity (Acharya et al., 2017; Herzog et al., 2011), cell growth and morphology (Arakawa et al., 2003; Ishizaki et al., 2001) in different cell models and tissues. In this sense, we identified mDia1 expression at the AIS and its function as a regulator of AIS assembly and axonal polarity maintenance. Moreover, unbalanced mDia1 activity or expression not only alters AIS assembly, integrity and plasticity, but also modifies action potential generation. Furthermore, AIS components loss after inhibition of mDia1 activity can be rescued by modulating AIS cytoskeleton and cytoskeleton related proteins. All these findings demonstrate that mDia1 participates in AIS integrity and function regulation.

1. Formins activity maintains AIS structure

This study demonstrates that formins activity inhibition disrupts AIS structure, modifying the expression of AIS scaffold proteins, such as ankyrinG and βIV-spectrin, and functional proteins, such as voltage gated sodium channels (Fig. R1). The data suggest that this modification is due to alterations on AIS microfilaments and microtubules cytoskeleton properties and structure (Fig. R5, 6). Formins are a group of large proteins with multiple domains, of which FH2 is the most conserved domain (Higgs and Peterson, 2005) and the core functional component (Bartolini and Gundersen, 2010; Courtemanche, 2018). In our work, we

used a potent FH2 domain inhibitor, SMIFH2 (Rizvi et al., 2009), to inhibit FH2 domain dependent formins activity. Indeed, SMIFH2 has been validated as a general formin inhibitor in previous studies in neurons (Ganguly et al., 2015; Qu et al., 2017) and nonneuronal cells (Rao and Zaidel-Bar, 2016). We found that formins activity is essential to keep AIS components both in vitro (Fig. R1-4) and in vivo (Fig. R19, 20). In fact, ankyrinG, βIV-spectrin, sodium channels and pMLC expression was significantly reduced in the AIS after SMIFH2 inhibition. This effect was observed as soon as 30 min (Fig. R1), strongly supporting a direct effect of SMIFH2 on AIS, not mediated by further transcriptional machinery.

AIS components reduction has been observed in different pathological conditions using in vivo animal models. Following ischemic injury, ankyrinG, βIV-spectrin and sodium channels are lost from the AIS in the cerebral cortex neurons (Schafer et al., 2009). Sodium channel Nav 1.6 reduces in the AIS of layer II/III neurons in primary visual cortex of aged rats (Ding et al., 2018). In addition, enhanced neuronal excitability induced by high concentration of extracellular KCl leads to a reduction of ankyrinG and pMLC in cultured hippocampal neurons (Berger et al., 2018). Interestingly, some neuronal receptors expression and activity also contribute to the maintenance of AIS components. For example, purinergic P2X7 receptor over-expression or hyperactivity decreases ankyrinG and sodium channels concentration in the AIS (Del Puerto et al., 2015). Conversely, loss of expression of purinergic receptor P2Y1 blocks AIS early development with reduction of ankyrinG, βIV-spectrin, sodium channels and pMLC expression (Zhang et al., 2019). In fact, a previous work from our laboratory has shown that P2Y1 suppression alters actin structures at the AIS (Zhang et al., 2019). Furthermore, cannabinoid receptors inhibition or suppression also decreases ankyrinG expression at the developing AIS (Tapia et al., 2017). It will be of interest to determine whether formins activity are been regulated by those receptors.

Our knowledge of formins in neurons is very limited. However, structures with similar function in other cells are regulated by formins. In this context, epithelial tight junctions or adherent junctions are important for establishing epithelial cells polarity, separating apical and basolateral domins (Grikscheit and Grosse, 2016), that were previously thought to be equivalent to axons and dendrites. These junctions participate in the control of polarized traffic and

maintenance of cell polarity. Indeed, formins are involved in the maintenance of these junctions and the expression of different proteins on them. It is reported that formins activity inhibition decreases E-cadherin at epithelial junctions (Rao and Zaidel-Bar, 2016). E-cadherin is a main protein to maintain adherent junctions and has been shown to interact with ankyrinG in epithelial cells in early embryos (Kizhatil et al., 2007). mDia1 knockdown decreases β-catenin in cell-cell junctions of epithelial cells (Carramusa et al., 2007). Interestingly, phosphorylated β-catenin localizes in the AIS of hippocampal neurons (Tapia et al., 2013). In addition, knocking down mDia1 or FMNL3 reduces E-cadherin at the adherens junctions of epithelial cells and weakens cell-cell adhesion and polarity (Rao and Zaidel-Bar, 2016). mDia1 knockdown also decreases vinculin, non-muscle myosins II A/B, and even another formin member mDia2 at epithelial junctions (Acharya et al., 2017). Non-muscle myosin II is an actin-binding protein that has actin cross-linking and contractile properties and is activated via MLC phosphorylation (pMLC) (Heissler and Sellers, 2014). pMLC is enriched at the AIS and involved in the activity-dependent plasticity of the AIS via actin destabilization during depolarization (Berger et al., 2018). In our work, we found a reduction of pMLC after formins inhibition (Fig. R1). Moreover, the junctional levels of epithelial constituent proteins, ZO-1, occludin, and Par3 all are reduced after losing mDia1 expression (Acharya et al., 2017). In neuroepithelial cells of mouse ventricular zone, loss of mDia1 activity results in the loss of apical N-cadherin and neuroepithilium organization is disrupted (Herzog et al., 2011). Together with our findings, this suggests that formins have capacity to maintain structural proteins in cellular specific compartments, such as the axon initial segment.

On the other hand, formins inducing ankyrinG loss leads to the loss of voltage gated sodium channels, which are highly enriched at the AIS and their high concentration is required for initiating action potentials (Kole et al., 2008; Zhou et al., 1998). AnkyrinG is required for normal action potential firing through clustering voltage gated sodium channels in the AIS (Zhou et al., 1998). Other studies have demonstrated that ankyrinG loss affects sodium channels concentration at the AIS (Hedstrom et al., 2007; Jenkins and Bennett, 2001). Accordingly, our data reveal an overall reduction of sodium channels in cultured neurons (Fig. R1). It is widely reported that loss of sodium channels in the AIS disables action potential generation and lowers

neuronal excitability (Del Puerto et al., 2015; Tapia et al., 2013). Consistently, we found a decrease in intrinsic neuronal excitability of hippocampal neurons after inhibiting formins activity in P26-P30 mice brain slices (Fig. R27), which is correlated with the fact that ankyrinG expression is reduced on these brain slices (Fig. R19, 20).

2. AIS cytoskeleton and formins

AnkyrinG, βIV-spectrin and sodium channels anchorage at the AIS depend on the integrity of AIS cytoskeleton (Berger et al., 2018; Tapia et al., 2010). Previous studies have shown that formins activity inhibition disrupts deep F-actin network in axons (Ganguly et al., 2015) and blocks synaptic vesicles endocytosis mediated by actin assembly (Soykan et al., 2017). In the case of microtubules, formins are featured to induce microtubule acetylation (Thurston et al., 2012). Formins inactivation or suppression results in microtubule instability (Qu et al., 2017). Moreover, formins' function can happen in actin or microtubules independently. Consistently, in our work, loss of formins activity destabilizes F-actin (Fig. R5) and alters microtubules properties (Fig. R6) in the AIS. Acute inhibition of formins activity for only 3 h remarkably disrupts microtubule stability, understood as a decrease in tubulin acetylation. While this happens in the AIS, no effect is detected in proximal dendrites (Fig. R6). Microtubules in the AIS are distinctive from other neuronal regions and they are tightly packed into fascicles (Palay et al., 1968), which may explain this different sensitivity of microtubules in the AIS and dendrites in our study. Previous studies showed that AIS assembly and integrity are tightly related with microtubule acetylation at the AIS. Enhanced microtubule acetylation in the distal axon by tubulin deacetylase HDAC6 inhibition or suppression, impairs the AIS to have specific local higher microtubules acetylation (Tapia et al., 2010). Similarly, the inhibition of Casein kinase 2, an AIS protein, also increases tubulin acetylation and decreases AIS composition (Sanchez-Ponce et al., 2011b). Some microtubules associated proteins, such as, microtubule cross-linking factor 1 (MTCL1) and TRIM46, are necessary to maintain microtubules bundles stability in the AIS, as a consequence of ankyrinG tethering (Satake et al., 2017; van Beuningen et al., 2015). In our work, we found that tubulin acetylation decreases in the AIS after formins activity inhibition, which is accompanied by a reduction of ankyrinG and βIV-spectrin in the AIS (Fig. R6). Interestingly, inhibiting or suppressing the activity of HDAC6 deacetylase we

were able to impair ankyrinG reduction in AIS (Fig. R24). HDAC6 inhibition has been previously shown as a way to protect neurons from external insults (Rivieccio et al., 2009). All these data demonstrate that microtubule dynamics in the AIS play an essential role in the AIS regulation, and our results suggest that formins play a role on these microtubules regulation.

In our work, we also found that actin dynamics play vital roles on AIS integrity (Fig. R23). Actin destabilization induced by Latrunculin A or enhanced actin stability induced by Jasplakinolide leads to a reduction of ankyrinG intensity. This phenomenon is also observed in actin trails in the axon using the same reagents (Ganguly et al., 2015). Here, we provide new insights of how actin cytoskeleton and related structures are modified by actin dynamic alterations mediated by formins. In fact, several studies have previously pointed out that actin related regulation is important for AIS components assembly and maintenance. For example, a previous study from our laboratory showed that stabilizing F-actin with Jasplakinolide recovers AIS components reduction due to P2Y1 receptor-mediated F-actin loss (Zhang et al., 2019). This actin loss is accompanied by a reduction of pMLC, an actin motor myosin II activator. In addition, it has been shown that pMLC reduction at the AIS, happens concomitantly with alterations in the space and organization of actin rings, and a decrease of ankyrinG expression in the AIS caused by enhanced neuronal excitability (Berger et al., 2018).

As mentioned in introduction section, different types of F-actin structures have been described in the AIS. Actin rings, actin patches and actin trails are involved in varied functions in the AIS, such as, structural maintenance or traffic control (Ganguly et al., 2015; Watanabe et al., 2012; Xu et al., 2013). In our data, we found that formins inhibition generates an overall reduction of F-actin signal in the AIS identified by phalloidin-bound fluorophore (Fig. R5). F-actin signal reduction contributes to the loss of the actin related structure termed cisternal organelles (Fig. R5). While the cisternal organelle is not necessary to maintain action potential generation, it has been shown that its size is modified with AIS plasticity during development. We found that cisternal organelles partially recovered at the AIS when stabilizing actin, but not when recovering tubulin acetylation, and after formins inhibition. Thus, further investigations will be necessary to better understand this proposed regulatory element in the AIS. However, a study described that actin patches are not modified by formins inhibition in mature neurons,

even if the formin FMN2 is expressed in the AIS of these cortical neurons. Instead, the study proposes that the actin nucleator Arp2/3 is required to maintain those actin patches in the AIS (Balasanyan et al., 2017). In fact, Arp2/3 and formins can cooperate for F-actin filaments formation and regulation, but can also act independently one from the other (Young et al., 2015). In this sense, we have identified the mDia1 formin at the AIS, which may function as a regulator of AIS actin structures as shown by other data using interference shRNAs. Other F-actin structures are localized at the AIS, short and stable actin filaments, as well as, longer dynamic actin filaments that can cooperate with other AIS enriched proteins to maintain AIS integrity (Jones et al., 2014). Given the longer dynamic actin filaments are sensitive to actin destabilizing drugs, and AIS enriched proteins decrease in our work, losing formins activity may at least reduce longer dynamic actin filaments. Using electron microscopy in the future in the context of formins and AIS will help to address this question.

In addition, actin rings are currently identified in the AIS (Xu et al., 2013). It is reported that actin rings are resistant to F-actin perturbations, although the overall amount of F-actin markedly decreases (Abouelezz et al., 2019). These rings in the AIS are connected by βIV-spectrins and potentially stabilize AIS structure and ankyrinG tethering (Leterrier et al., 2015; Zhong et al., 2014). In our work, ankyrinG reduction caused by the actin destabilizing reagent Latrunculin A is lower than that generated by the loss of formins activity (Fig. R1, 23). It will be of interest to determine whether actin rings in the AIS are affected after losing formins activity, but this will need a further STORM analysis.

3. mDia1 role on AIS regulation

Most of the data described above are based on pharmacological experiments using a general formins inhibitor. Taking advantage of the knowledge of mDia1 in epithelial cell polarity and the potential similarity with AIS, we found that mDia1 is expressed in patches along the AIS (Fig. R9). Although mDia1 is ubiquitously expressed along the neuron (Qu et al., 2017), a relatively higher expression of mDia1 was observed in the axon of early developing neurons (Fig. R10). Moreover, we could detect mDia1 signal after detergent extraction at the AIS (Fig. R9). mDia1 signal colocalizes with the signal of GFP-CA-mDia1 and ankyrinG, and we confirmed that AIS regulation observed in formins pharmacological experiments are due to

mDia 1 inhibition.

Previous studies have shown that axon growth or dendritic growth has a relation to AIS plasticity (Hamada et al., 2016; Tapia et al., 2017). Our work demonstrates that silencing mDia1 does not affect axon specification or dendrites growth in hippocampal neurons (Fig. R12). However, other studies have proposed that mDia1 silencing decreases axon elongation in cerebellar granule neurons (Arakawa et al., 2003) and dendrites length as well as dendritic arborization in hippocampal neurons (Hong et al., 2018). Conversely, mDia1 depletion increases dendritic complexity in post-developmental hippocampal neurons (Qu et al., 2017). These discrepancies may be the result of different times of mDia1 depletion or the varied percentage of mDia1 reduction in each study. In our work, we quantified a 30-40% reduction of endogenous mDia1, which probably allows axon development and AIS formation. Interestingly, constitutively active mDia1 expression is able to diminish axon and dendrites differentiation and growth during initial development of hippocampal neurons (Fig. R13). This is consistent with previous studies showing that axon length decreases after mDia1 hyperactivation in cultured cerebellar granule neurons (Arakawa et al., 2003) and which suggests that the control of mDia1 activity is essential to maintain a proper morphological neuronal development.

Regarding functions of mDia1 at the AIS, our results show that mDia1 participates in the AIS assembly (Fig. R14), maintenance (Fig. R16) and plasticity (Fig. R17). In fact, mDia1 suppression in neuronal early development leads to a decrease of AIS components, such as ankyrinG, βIV-spectrin and voltage gated sodium channels. This is the first study to describe a role of mDia1 in the AIS. Some studies have shown an early function of mDia1 in neuronal proliferation and migration in developmental cerebral cortex in mDia1/mDia3 knock-out mice model (Shinohara et al., 2012; Thumkeo et al., 2011). mDia1 homozygous loss in humans leads to microcephaly due to reduced neuronal cell precursors proliferation (Al-Maawali et al., 2016; Ercan-Sencicek et al., 2015). Thus, cultured hippocampal neurons in vitro is a good model to explore mDia1 functions in neuronal morphology development and AIS assembly and maintenance through modifying mDia1 expression. In fact, our results show that early suppression of mDia1 affects AIS properties along with the axonal and dendritic development. Taken these data, we hypothesized that mDia1 over-expression could increase AIS components.

However, the expression of a constitutively active mDia1 construct also slightly decreases ankyrinG expression (Fig. R16). In fact, the same effects are produced by increasing or decreasing mDia1 activity in other cell models, such as the axon length shortening in cultured cerebellar granule neurons (Arakawa et al., 2003).

4. Formins and AIS plasticity

Recent studies have highlighted the importance of AIS plasticity in the regulation of neuronal function in response to physiological or pathological changes affecting neuronal input. AIS plasticity occurs during neuronal development (Gutzmann et al., 2014) and after alterations of neuronal activity in mature neurons (Grubb and Burrone, 2010; Kuba et al., 2010). Structural AIS plasticity requires a re-arrangement of actin and microtubules cytoskeleton that is not well known neither understood. AIS elongation or movement away from the soma can only be understood following this re-arrangement. In this context, formins, and specifically mDia1, are known by their mechanosensitive function (Jegou et al., 2013; Zimmermann et al., 2017). Formins and mDia1 can sense forces and promote actin polymerization, but also modulate efficient contractile ring assembly. It has been described that pulling force of myosin II propagates through the actin filament impeding formin-mediated actin filament elongation in yeast (Zimmermann et al., 2017). Our study shows important changes in cytoskeleton after formins inhibition, which may be involved in AIS plasticity. In fact, our work demonstrates that short-term mDia1 inhibition or knockdown in mature neurons shortens AIS length (Fig. R17), as happens in cortical neurons in brain slices after formins inhibition (Fig. R19). However, long term knocking down mDia1 before AIS forms, does not change AIS length, but only decreases AIS components accumulation (Fig. R14, 17). This could be due to homeostatic compensation that may occur for 10 days in vitro before AIS is analyzed (Kuba et al., 2010; Schluter et al., 2017).

AIS plasticity can happen at short- or long-term (Grubb et al., 2011), involving other mechanisms, such as calcium regulation or channels expression. Moreover, the regulation of AIS structural plasticity and AIS composition may be mediated through different pathways. In fact, our results show that AIS composition can be recovered, while AIS length is not rescued (Fig. R24-26). Different mechanisms have been related to AIS structural or compositional

plasticity. For example, calcium-calpain activation through P2X7 activation decreases ankyrinG and sodium channels, but does not alter AIS length (Del Puerto et al., 2015), while KCl depolarization induces AIS movement or AIS length shortening in different cell types (Evans et al., 2015; Grubb and Burrone, 2010), without changing AIS components expression after 48 h. AIS plasticity also happens during development and seems to be related to changes in cisternal organelle (Schluter et al., 2017). In our work, we found a dramatic reduction of cisternal organelle clusters after short period of mDia1 inhibition together with AIS shortening (Fig. R5). In pyramidal neurons of layers II/III in visual cortex, visual deprivation leads to the size increase of cisternal organelle clusters, as well as AIS length increase (Schluter et al., 2017). However, loss of cisternal organelles due to synaptopodin knockout results in AIS length shortening after visual deprivation (Schluter et al., 2017). The increase of cisternal organelle clusters in number and size is also observed in retinal ganglion cells after sensory deprivation (Schluter et al., 2019). It would be interesting to determine whether cisternal organelles are involved in mDia1 mediated AIS length shortening in future studies. Moreover, the cisternal organelle is thought to regulate calcium, which intracellular increase is related to P2X7 mediated AIS components loss (Del Puerto et al., 2015).

Thus, formins may regulate AIS plasticity through the regulation of actin filaments elongation and shortening, affecting actin related strucutures and microtubules. How changes in neuronal input can modify AIS cytoskeleton needs further research.

5. Potential mechanisms for mDia1 mediated AIS regulation

To understand how formins regulate intrinsic neuronal excitability through AIS regulation, it is important to know which molecules or signaling pathways act as upstream regulators or play a parallel role as formins in AIS regulation. mDia1 is typically autoinhibited through DID and DAD interaction. In different models, it has been shown that the binding of GTP-bound RhoGTPases to GBD displaces the DAD domain and activates formins (Kuhn and Geyer, 2014). However, formins can also be regulated by other mechanisms, such as, phospholipids interaction, myristoylation, farnesylation or phosphorylation (Grikscheit and Grosse, 2016). Specifically, besides RhoGTPases regulation, activation and localization of mDia1 is regulated by phospholipids (Ramalingam et al., 2010). Rho-mDia1 pathway is involved in the regulation

of Golgi complex architecture and dynamics in HeLa cells and its polarization in hippocampal neurons (Hong et al., 2018; Zilberman et al., 2011). Indeed, this signal is also linked with many physiological functions, such as cell polarity, cell adhesion, cell migration, neuronal stem cell pool maintenance and axon growth (Arakawa et al., 2003; Herzog et al., 2011; Yamana et al., 2006; Zaoui et al., 2008). ROCK is another canonical effector of Rho and cooperates with mDia1 for cell adhesion and tangential migration of interneuron precursors through actin dynamics regulation (Acharya et al., 2017; Shinohara et al., 2012). However, we found that the expression of RhoA, activated RhoA or dominant negative RhoA plasmids has no effects on AIS modulation (Fig. R21). Furthermore, ROCK deactivation has no influence on AIS components (Fig. R21). However, mDia1 can interact with other Rho proteins, such as RhoB or RhoC (Wallar and Alberts, 2003). RhoA-C inhibition with CT04 slightly decreases ankyrinG intensity at the AIS compared to SMIFH2, and the double inhibition generates a much higher effect (Fig. R21). This may indicate parallel mechanisms of AIS regulation mediated by Rho and formins, not being Rho as the upstream regulator of mDia1. Other RhoGTPases could be responsible for mDia1 activation. In fact, RhoGTPase Rif binds to the N-terminal GBD domain of mDia1 (Fan et al., 2010). Through direct interaction within filopodia, Rif with mDia1 instead of with mDia2 regulates filopodial protrusion in the N1E115 mouse neuroblastoma cell line (Goh et al., 2011). In addition to RhoGTPase, tyrosine kinases src also has access to regulate formins activity (Rao and Zaidel-Bar, 2016). mDia1 activation is sufficient to rescue the effects of Src inhibition on E-cadherin levels at adherent junctions and prevent the loss of lateral junctions in epithelial cells (Rao and Zaidel-Bar, 2016). Regarding phospholipids regulation, N-terminal phospholipid-binding sites help to anchor mDia1 at the plasma membrane, and the interaction with phospholipids in the C-terminal functions as a switch for transient inactivation (Ramalingam et al., 2010). In this sense, AIS is characterized by a characteristic membrane that controls protein and lipids diffusion (Nakada et al., 2003). Future studies are needed to elucidate the cell signaling of mDia1 mediated AIS regulation.

Some studies have described that calcium regulation related receptors, such as, IP3R3 can regulate actin cytoskeletal reorganization through a signaling pathway including mDia1 (Vautrin-Glabik et al., 2018). In fact, IP3R1 is localized at the AIS (Sanchez-Ponce et al., 2011a).

As previously described, calcium-calpain mechanisms have been shown to modulate AIS composition. However, calpain inhibition is not able to impair ankyrinG decrease, excluding the possibility that formins regulation on AIS through calpain mechanisms. Given actin stabilization partially recovers the cisternal organelle after formins inhibition (Fig. R23), we can not exclude calcium involvement in these regulatory mechanisms.

Microtubules regulation and microtubules binding proteins related to formins may be an alternative way of AIS regulation by formins. Both, actin and microtubules act in a complex interplay for cytoskeleton regulation in different cellular structures (Dogterom and Koenderink, 2019). EB1 not only interacts with microtubules but may serve as a link to actin cytoskeleton (Dugina et al., 2016). End bind proteins EB1 and EB3 are expressed at the AIS and interact with ankyrinG (Leterrier et al., 2011). Moreover, mDia1 directly interact with EB1, which occurs independently of actin filaments and microtubules (Wen et al., 2004), suggesting a potential mechanisms for mDia1 location at the AIS. Previous studies have shown that EB proteins have access to associate with giant ankyrinG, and this interaction is crucial for AIS formation (Freal et al., 2016). In our work, EB1 over-expression recovers AIS components loss induced by acute inhibition of mDia1 activity (Fig. R25). EB1 over-expression may act by modulating AIS cytoskeleton and impairing changes produced by formins inhibition or somewhat contributing to ankyrinG stabilization.

In addition, local acetylation of microtubules in the AIS contributes to recruitment of AIS components (Tapia et al., 2010). The reduction of acetylated tubulin in the AIS inflicted by mDia1 inhibition might contribute to the deficiency of AIS assembly. Consistently, silencing HDAC6 rescues ankyrinG reduction caused by mDia1 knockdown during AIS formation (Fig. R24). It will be of interest to determine whether there exists a mutual regulation between mDia1 and HDAC6 and how they cooperates to maintain this local higher acetylated tubulin in the AIS. For instance, a relation between HDAC6 and mDia2 has been described in podosomes (Destaing et al., 2005).

In view of the AIS cytoskeleton modifications caused by formins inhibition, a final balance of AIS components due to changes in anterograde or retrograde traffic may contribute to AIS

integrity maintenance. AIS formation and maintenance rely on the proper axonal transportation (Kuijpers et al., 2016; Tapia et al., 2010; van Beuningen et al., 2015). Kinesin-1 is the primary motor for anterograde transportation of axons (Nakata and Hirokawa, 2003). KIF5C is one of identified kinesin-1 family members in the axon and AIS (Nakata and Hirokawa, 2003; Tapia et al., 2010). We found that KIF5C expression is disrupted both in the soma and axon in mDia1 inhibited neurons (Fig. R8). It is reported that microtubule acetylation or detyrosination promotes kinesin-1 binding and transport into axon (Konishi and Setou, 2009; Reed et al., 2006). Consistently, AIS components loss is corrected by increasing tubulin acetylation in mDia1 inactivated or suppressed neurons (Fig. R24). Currently, an AIS enriched microtubule binding protein TRIM46 is identified and functions in the formation and maintenance of parallel microtubule arrays. Loss of ankyrinG leads to a dramatic redistribution of TRIM46 (van Beuningen et al., 2015). Given the remarkable effects of mDia1 on AIS ankyrinG, TRIM46 may also be affected in our work and which could be another reason of anterograde disability in the axon.

Apart from anterograde transportation, we found a possible involvement of retrograde transportation in mDia1 mediated AIS regulation. Cytoplasmic dynein is responsible for microtubule-based transportation in a minus end direction (Hirokawa, 1998). In the AIS, dynein and its regulators control axonal cargos transportation through excluding somatodendritic proteins (Klinman et al., 2017; Kuijpers et al., 2016). Consistent with this, we found that mDia1 inhibition disrupts neuronal polarity with MAP2 entrance into the axon (Fig. R7), although we can not exclude contributions from F-actin destabilization and ankyrinG loss in our study (Sobotzik et al., 2009; Song et al., 2009; Winckler et al., 1999). However, dynein inhibitor Ciliobrevin D partially rescues AIS components loss inflicted by mDia1 inhibition (Fig. R26). Previous studies showed that actin filament depolymerization induces retrograde reorganization of the axonal cytoplasm, which is rescued by treatment with Ciliobrevin D (Sainath and Gallo, 2015). Together with our results and previous studies, we propose that formins inhibition can affect both anterograde and retrograde transport, generating an imbalance in AIS trafficking, which leads to reduced AIS proteins accumulation together with loss of these proteins tethering at the AIS. Additional studies are needed to elucidate the role of mDia1 on protein

transportation to the AIS.

In conclusion, we have demonstrated that mDia1 activity and expression is necessary for AIS assembly, maintenance and plasticity both in cultured hippocampal neurons and in brain slices. However, further studies are necessary to completely understand the mechanisms and how they are involved in neuronal excitability regulation and diseases. Homozygous mutations of DIAPH1, the gene coding mDia1, in humans generate microcephaly, but no study has focused on further neuronal activity in adults. In mice models, it has been observed that mice lack of mDia1 and mDia3 altogether causes impaired tangential migration of cortical interneurons as well as neuroblasts migration from the subventricular zone to the granule cell layer of the olfactory bulb (Shinohara et al., 2012). Double knockout mice also show aberrant midline crossing of axons of corticospinal neurons and spinal cord interneurons (Toyoda et al., 2013). In addition, loss of mDia1 and mDia3 in mice disrupts integrity of neuroepithelium and causes periventricular dysplasia (Thumkeo et al., 2011). However, these phenotypes can not be observed in mDia1 knockout mice (Ercan-Sencicek et al., 2015). To some extent, in mice models, mDia1 is redundant with mDia3 and lacking mDia1 or mDia3 alone in mice has no apparent abnormality (Shinohara et al., 2012; Toyoda et al., 2013).

Regarding Alzheimer's disease, mDia1 suppression or inhibition diminishes synaptotoxicity induced by oligomeric amyloid β1-42 by increasing microtubule dynamics (Qu et al., 2017). mDia1 regulates tau phosphorylation through affecting microtubules stability (Qu et al., 2017). Besides, the recent involvement of AIS as a potential link to Alzheimer's disease, AIS modifications by formins in this disease models are lacking. In addition, some other formin family members are related to brain disorders. For example, formin FMN2 is deregulated in post-traumatic stress disorder (PTSD) and Alzheimer's disease. The loss of FMN2 leads to accelerated age-associated memory impairment and amyloid-induced deregulation of gene expression (Agis-Balboa et al., 2017). Finally, more studies are necessary to understand the role of formins and their mechanisms on neurons or glial cells. Together, our current findings provide novel molecular insights into AIS regulation, which might suggest new therapeutic strategies aimed to AIS related neurodevelopmental and neurodegenerative diseases.

Conclusions

1. Formins activity is required for axon initial segment (AIS) cytoskeleton maintenance. Inhibition of formins activity decreases overall F-actin intensity and microtubules acetylation in the AIS.

2. Formins activity is essential to maintain AIS protein composition. Loss of formins activity decreases the concentration of structural and functional AIS proteins in cultured neurons and brain slices.

3. Formins activity is required to maintain AIS mediated neuronal polarity. Lack of formins activity allows the somatodendritic protein MAP2 to enter the axon.

4. One of formin family members, mDia1, is localized at the AIS.

5. mDia1 knockdown alters early AIS assembly, by decreasing the recruitment of AIS components.

6. Formins activity and mDia1 are required to maintain AIS composition integrity after AIS is fully assembled.

7. Alterations in formins activity or mDia1 expression generate AIS plasticity and lead to AIS shortening.

8. AIS integrity loss by formins inhibition can be recovered through increasing tubulin acetylation, over-expressing the microtubule associated protein EB1 or inhibiting retrograde transport through dynein inhibitors.

Conclusiones

1. La actividad de las forminas es necesaria para el mantenimiento del citoesqueleto del segmento inicial del axón (AIS). La inhibición de la actividad de las forminas disminuye la intensidad general de F-actina y la acetilación de los microtúbulos en el AIS.

2. La actividad de las forminas es esencial para mantener la composición proteíca del AIS. La pérdida de la actividad de las forminas disminuye la concentración de proteínas estructurales y funcionales del AIS en neuronas en cultivo y rodajas de cerebro.

3. Se requiere la actividad de las forminas para mantener la polaridad neuronal mediada por el AIS. La falta de actividad de las forminas permite que la proteína somatodendrítica MAP2 entre en el axón.

4. Uno de los miembros de la familia de las forminas, mDia1, está localizado en el AIS.

5. La disminución de la expresión de mDia1 altera el ensamblaje temprano del AIS, al disminuir el reclutamiento de componentes del AIS.

6. La actividad de las forminas y mDia1 son necesarias para mantener la integridad de la composición del AIS, cuando el AIS está completamente ensamblado.

7. Las alteraciones en la actividad de las forminas o la expresión de mDia1 generan plasticidad en el AIS y conducen a su acortamiento.

8. La pérdida de integridad del AIS por la inhibición de las forminas se puede recuperar aumentando la acetilación de la tubulina, sobreexpresando la proteína EB1 asociada a los microtúbulos o inhibiendo el transporte retrógrado mediante inhibidores de la dineína.

Bibliography

Abouelezz, A., D. Micinski, A. Lipponen, and P. Hotulainen. 2019. Sub-membranous actin rings in the axon initial segment are resistant to the action of latrunculin. *Biol Chem*. 400:1141-1146.

Acharya, B.R., S.K. Wu, Z.Z. Lieu, R.G. Parton, S.W. Grill, A.D. Bershadsky, G.A. Gomez, and A.S. Yap. 2017. Mammalian Diaphanous 1 Mediates a Pathway for E-cadherin to Stabilize Epithelial Barriers through Junctional Contractility. *Cell Rep*. 18:2854-2867.

Agis-Balboa, R.C., P.S. Pinheiro, N. Rebola, C. Kerimoglu, E. Benito, M. Gertig, S. Bahari-Javan, G. Jain, S. Burkhardt, I. Delalle, A. Jatzko, M. Dettenhofer, P.A. Zunszain, A. Schmitt, P. Falkai, J.C. Pape, E.B. Binder, C. Mulle, A. Fischer, and F. Sananbenesi. 2017. Formin 2 links neuropsychiatric phenotypes at young age to an increased risk for dementia. *EMBO J*. 36:2815-2828.

Akhmanova, A., and M.O. Steinmetz. 2010. Microtubule +TIPs at a glance. *J Cell Sci*. 123:3415-3419.

Al-Maawali, A., B.J. Barry, A. Rajab, M. El-Quessny, A. Seman, S.N. Coury, A.J. Barkovich, E. Yang, C.A. Walsh, G.H. Mochida, and J.M. Stoler. 2016. Novel loss-of-function variants in DIAPH1 associated with syndromic microcephaly, blindness, and early onset seizures. *Am J Med Genet A*. 170A:435-440.

Alpizar, S.A., A.L. Baker, A.T. Gulledge, and M.B. Hoppa. 2019. Loss of Neurofascin-186 Disrupts Alignment of AnkyrinG Relative to Its Binding Partners in the Axon Initial Segment. *Front Cell Neurosci*. 13:1.

Ango, F., G. di Cristo, H. Higashiyama, V. Bennett, P. Wu, and Z.J. Huang. 2004. Ankyrin-based subcellular gradient of neurofascin, an immunoglobulin family protein, directs GABAergic innervation at purkinje axon initial segment. *Cell*. 119:257-272.

Arakawa, Y., H. Bito, T. Furuyashiki, T. Tsuji, S. Takemoto-Kimura, K. Kimura, K. Nozaki, N. Hashimoto, and S. Narumiya. 2003. Control of axon elongation via an SDF-1alpha/Rho/mDia pathway in cultured cerebellar granule neurons. *J Cell Biol*. 161:381-391.

Baalman, K.L., R.J. Cotton, S.N. Rasband, and M.N. Rasband. 2013. Blast wave exposure impairs memory and decreases axon initial segment length. *J Neurotrauma*. 30:741-751.

Baas, P.W., and M.M. Black. 1990. Individual microtubules in the axon consist of domains that differ in both composition and stability. *J Cell Biol*. 111:495-509.

Baas, P.W., J.S. Deitch, M.M. Black, and G.A. Banker. 1988. Polarity orientation of microtubules in hippocampal neurons: uniformity in the axon and nonuniformity in the dendrite. *Proc Natl Acad Sci U S A*. 85:8335-8339.

Balasanyan, V., K. Watanabe, W.P. Dempsey, T.L. Lewis, Jr., L.A. Trinh, and D.B. Arnold. 2017. Structure and Function of an Actin-Based Filter in the Proximal Axon. *Cell Rep*. 21:2696-2705.

Barnes, A.P., and F. Polleux. 2009. Establishment of axon-dendrite polarity in developing neurons. *Annu Rev Neurosci*. 32:347-381.

Bartolini, F., L. Andres-Delgado, X. Qu, S. Nik, N. Ramalingam, L. Kremer, M.A. Alonso, and G.G. Gundersen. 2016. An mDia1-INF2 formin activation cascade facilitated by IQGAP1 regulates stable microtubules in migrating cells. *Mol Biol Cell*. 27:1797-1808.

Bartolini, F., and G.G. Gundersen. 2010. Formins and microtubules. *Biochim Biophys Acta*. 1803:164-173.

Bartolini, F., J.B. Moseley, J. Schmoranzer, L. Cassimeris, B.L. Goode, and G.G. Gundersen. 2008. The formin mDia2 stabilizes microtubules independently of its actin nucleation activity. *J Cell Biol*. 181:523-536.

Bas Orth, C., C. Schultz, C.M. Muller, M. Frotscher, and T. Deller. 2007. Loss of the cisternal organelle in the axon initial segment of cortical neurons in synaptopodin-deficient mice. *J Comp Neurol*. 504:441-449.

Baumbach, J., A. Murthy, M.A. McClintock, C.I. Dix, R. Zalyte, H.T. Hoang, and S.L. Bullock. 2017. Lissencephaly-1 is a context-dependent regulator of the human dynein complex. *Elife*. 6.

Bender, K.J., and L.O. Trussell. 2009. Axon initial segment Ca2+ channels influence action potential generation and timing. *Neuron*. 61:259-271.

Bender, K.J., and L.O. Trussell. 2012. The physiology of the axon initial segment. *Annu Rev Neurosci*. 35:249-265.

Benedeczky, I., E. Molnar, and P. Somogyi. 1994. The cisternal organelle as a Ca(2+)-storing compartment associated with GABAergic synapses in the axon initial segment of hippocampal pyramidal neurones. *Exp Brain Res*. 101:216-230.

Bennett, V., and A.J. Baines. 2001. Spectrin and ankyrin-based pathways: metazoan inventions for integrating cells into tissues. *Physiol Rev*. 81:1353-1392.

Bennett, V., and D.N. Lorenzo. 2013. Spectrin- and ankyrin-based membrane domains and the evolution of vertebrates. *Curr Top Membr*. 72:1-37.

Berger, S.L., A. Leo-Macias, S. Yuen, L. Khatri, S. Pfennig, Y. Zhang, E. Agullo-Pascual, G. Caillol, M.S. Zhu, E. Rothenberg, C.V. Melendez-Vasquez, M. Delmar, C. Leterrier, and J.L. Salzer. 2018. Localized Myosin II Activity Regulates Assembly and Plasticity of the Axon Initial Segment. *Neuron*. 97:555-570 e556.

Berrueta, L., J.S. Tirnauer, S.C. Schuyler, D. Pellman, and B.E. Bierer. 1999. The APC-associated protein EB1 associates with components of the dynactin complex and cytoplasmic dynein intermediate chain. *Curr Biol*. 9:425-428.

Boiko, T., A. Van Wart, J.H. Caldwell, S.R. Levinson, J.S. Trimmer, and G. Matthews. 2003. Functional specialization of the axon initial segment by isoform-specific sodium channel targeting. *J Neurosci*. 23:2306-2313.

Bolos, M., J. Terreros-Roncal, J.R. Perea, N. Pallas-Bazarra, J. Avila, and M. Llorens-Martin. 2019. Maturation Dynamics of the Axon Initial Segment (AIS) of Newborn Dentate Granule Cells in Young Adult C57BL/6J Mice. *J Neurosci*. 39:1605-1620.

Boyer, O., F. Nevo, E. Plaisier, B. Funalot, O. Gribouval, G. Benoit, E. Huynh Cong, C. Arrondel, M.J. Tete, R. Montjean, L. Richard, A. Karras, C. Pouteil-Noble, L. Balafrej, A. Bonnardeaux, G. Canaud, C. Charasse, J. Dantal, G. Deschenes, P. Deteix, O. Dubourg, P. Petiot, D. Pouthier, E. Leguern, A. Guiochon-Mantel, I. Broutin, M.C. Gubler, S. Saunier, P. Ronco, J.M. Vallat, M.A. Alonso, C. Antignac, and G. Mollet. 2011. INF2 mutations in Charcot-Marie-Tooth disease with glomerulopathy. *N Engl J Med*. 365:2377-2388.

Brachet, A., C. Leterrier, M. Irondelle, M.P. Fache, V. Racine, J.B. Sibarita, D. Choquet, and B. Dargent. 2010. Ankyrin G restricts ion channel diffusion at the axonal initial segment before the establishment of the diffusion barrier. *J Cell Biol*. 191:383-395.

Brechet, A., M.P. Fache, A. Brachet, G. Ferracci, A. Baude, M. Irondelle, S. Pereira, C. Leterrier, and B. Dargent. 2008. Protein kinase CK2 contributes to the organization of sodium channels in axonal membranes by regulating their interactions with ankyrin G. *J Cell Biol*. 183:1101-1114.

Breitsprecher, D., and B.L. Goode. 2013. Formins at a glance. *J Cell Sci*. 126:1-7.

Bruckner, G., S. Szeoke, S. Pavlica, J. Grosche, and J. Kacza. 2006. Axon initial segment ensheathed by extracellular matrix in perineuronal nets. *Neuroscience*. 138:365-375.

Buffington, S.A., and M.N. Rasband. 2011. The axon initial segment in nervous system disease and injury. *Eur J Neurosci*. 34:1609-1619.

Cappi, C., A.G. Hounie, D.B. Mariani, J.B. Diniz, A.R. Silva, V.N. Reis, A.F. Busso, A.G. Silva, F. Fidalgo, S.R. Rogatto, E.C. Miguel, A.C. Krepischi, and H. Brentani. 2014. An inherited small microdeletion at 15q13.3 in a patient with early-onset obsessive-compulsive disorder. *PLoS One*. 9:e110198.

Carramusa, L., C. Ballestrem, Y. Zilberman, and A.D. Bershadsky. 2007. Mammalian diaphanous-related formin Dia1 controls the organization of E-cadherin-mediated cell-cell junctions. *J Cell Sci*. 120:3870-3882.

Clark, B.D., E.M. Goldberg, and B. Rudy. 2009. Electrogenic tuning of the axon initial segment. *Neuroscientist*. 15:651-668.

Clark, K.C., A. Josephson, S.D. Benusa, R.K. Hartley, M. Baer, S. Thummala, M. Joslyn, B.A. Sword, H. Elford, U. Oh, A. Dilsizoglu-Senol, C. Lubetzki, M. Davenne, G.H. DeVries, and J.L. Dupree. 2016. Compromised axon initial segment integrity in EAE is preceded by microglial reactivity and contact. *Glia*. 64:1190-1209.

Codina-Sola, M., B. Rodriguez-Santiago, A. Homs, J. Santoyo, M. Rigau, G. Aznar-Lain, M. Del Campo, B. Gener, E. Gabau, M.P. Botella, A. Gutierrez-Arumi, G. Antinolo, L.A. Perez-Jurado, and I. Cusco. 2015. Integrated analysis of whole-exome sequencing and transcriptome profiling in males with autism spectrum disorders. *Mol Autism*. 6:21.

Courtemanche, N. 2018. Mechanisms of formin-mediated actin assembly and dynamics. *Biophys Rev*. 10:1553-1569.

Chen, H., and B.L. Firestein. 2007. RhoA regulates dendrite branching in hippocampal neurons by decreasing cypin protein levels. *J Neurosci*. 27:8378-8386.

Cheng, L., J. Zhang, S. Ahmad, L. Rozier, H. Yu, H. Deng, and Y. Mao. 2011. Aurora B regulates formin mDia3 in achieving metaphase chromosome alignment. *Dev Cell*. 20:342-352.

Chhabra, E.S., and H.N. Higgs. 2006. INF2 Is a WASP homology 2 motif-containing formin that severs actin filaments and accelerates both polymerization and depolymerization. *J Biol Chem*. 281:26754-26767.

Davis, J.Q., and V. Bennett. 1994. Ankyrin binding activity shared by the neurofascin/L1/NrCAM family of nervous system cell adhesion molecules. *J Biol Chem*. 269:27163-27166.

Debanne, D., E. Campanac, A. Bialowas, E. Carlier, and G. Alcaraz. 2011. Axon physiology. *Physiol Rev*. 91:555-602.

Del Puerto, A., L. Fronzaroli-Molinieres, M.J. Perez-Alvarez, P. Giraud, E. Carlier, F. Wandosell, D. Debanne, and J.J. Garrido. 2015. ATP-P2X7 Receptor Modulates Axon Initial Segment Composition and Function in Physiological Conditions and Brain Injury. *Cereb Cortex*. 25:2282-2294.

Destaing, O., F. Saltel, B. Gilquin, A. Chabadel, S. Khochbin, S. Ory, and P. Jurdic. 2005. A novel Rho-mDia2-HDAC6 pathway controls podosome patterning through microtubule acetylation in osteoclasts. *J Cell Sci*. 118:2901-2911.

Ding, Y., T. Chen, Q. Wang, Y. Yuan, and T. Hua. 2018. Axon initial segment plasticity accompanies enhanced excitation of visual cortical neurons in aged rats. *Neuroreport*. 29:1537-1543.

Ding, Y., Y. Zheng, T. Liu, T. Chen, C. Wang, Q. Sun, M. Hua, and T. Hua. 2017. Changes in GABAergic markers accompany degradation of neuronal function in the primary visual cortex of senescent rats. *Sci Rep*. 7:14897.

Dogterom, M., and G.H. Koenderink. 2019. Actin-microtubule crosstalk in cell biology. *Nat Rev Mol Cell Biol*. 20:38-54.

Duflocq, A., B. Le Bras, E. Bullier, F. Couraud, and M. Davenne. 2008. Nav1.1 is predominantly expressed in nodes of Ranvier and axon initial segments. *Mol Cell Neurosci*. 39:180-192.

Dugina, V., I. Alieva, N. Khromova, I. Kireev, P.W. Gunning, and P. Kopnin. 2016. Interaction of microtubules with the actin cytoskeleton via cross-talk of EB1-containing +TIPs and gamma-actin in epithelial cells. *Oncotarget*. 7:72699-72715.

Dutta, P., S. Das, and S. Maiti. 2017. Non diaphanous formin delphilin acts as a barbed end capping protein. *Exp Cell Res*. 357:163-169.

El-Husseini, A.E., J.R. Topinka, J.E. Lehrer-Graiwer, B.L. Firestein, S.E. Craven, C. Aoki, and D.S. Bredt. 2000. Ion channel clustering by membrane-associated guanylate kinases. Differential regulation by N-terminal lipid and metal binding motifs. *J Biol Chem*. 275:23904-23910.

el-Husseini Ael, D., and D.S. Bredt. 2002. Protein palmitoylation: a regulator of neuronal development and function. *Nat Rev Neurosci*. 3:791-802.

Ercan-Sencicek, A.G., S. Jambi, D. Franjic, S. Nishimura, M. Li, P. El-Fishawy, T.M. Morgan, S.J. Sanders, K. Bilguvar, M. Suri, M.H. Johnson, A.R. Gupta, Z. Yuksel, S. Mane, E. Grigorenko, M. Picciotto, A.S. Alberts, M. Gunel, N. Sestan, and M.W. State. 2015. Homozygous loss of DIAPH1 is a novel cause of microcephaly in humans. *Eur J Hum Genet*. 23:165-172.

Evans, M.D., A.S. Dumitrescu, D.L.H. Kruijssen, S.E. Taylor, and M.S. Grubb. 2015. Rapid Modulation of Axon Initial Segment Length Influences Repetitive Spike Firing. *Cell Rep*. 13:1233-1245.

Evans, M.D., R.P. Sammons, S. Lebron, A.S. Dumitrescu, T.B. Watkins, V.N. Uebele, J.J. Renger, and M.S. Grubb. 2013. Calcineurin signaling mediates activity-dependent relocation of the axon initial segment. *J Neurosci*. 33:6950-6963.

Evans, M.D., C. Tufo, A.S. Dumitrescu, and M.S. Grubb. 2017. Myosin II activity is required for structural plasticity at the axon initial segment. *Eur J Neurosci*. 46:1751-1757.

Fan, L., S. Pellegrin, A. Scott, and H. Mellor. 2010. The small GTPase Rif is an alternative trigger for the formation of actin stress fibers in epithelial cells. *J Cell Sci*. 123:1247-1252.

Fernandez-Borja, M., L. Janssen, D. Verwoerd, P. Hordijk, and J. Neefjes. 2005. RhoB regulates endosome transport by promoting actin assembly on endosomal membranes through Dia1. *J Cell Sci*. 118:2661-2670.

Firestone, A.J., J.S. Weinger, M. Maldonado, K. Barlan, L.D. Langston, M. O'Donnell, V.I. Gelfand, T.M. Kapoor, and J.K. Chen. 2012. Small-molecule inhibitors of the AAA+ ATPase motor cytoplasmic dynein. *Nature*. 484:125-129.

Freal, A., C. Fassier, B. Le Bras, E. Bullier, S. De Gois, J. Hazan, C.C. Hoogenraad, and F. Couraud. 2016. Cooperative Interactions between 480 kDa Ankyrin-G and EB Proteins Assemble the Axon Initial Segment. *J Neurosci*. 36:4421-4433.

Fujita, Y., and T. Yamashita. 2014. Axon growth inhibition by RhoA/ROCK in the central nervous system. *Front Neurosci*. 8:338.

Gaillard, J., V. Ramabhadran, E. Neumanne, P. Gurel, L. Blanchoin, M. Vantard, and H.N. Higgs. 2011. Differential interactions of the formins INF2, mDia1, and mDia2 with microtubules. *Mol Biol Cell*. 22:4575-4587.

Galiano, M.R., S. Jha, T.S. Ho, C. Zhang, Y. Ogawa, K.J. Chang, M.C. Stankewich, P.J. Mohler, and M.N. Rasband. 2012. A distal axonal cytoskeleton forms an intra-axonal boundary that controls axon initial segment assembly. *Cell*. 149:1125-1139.

Ganguly, A., Y. Tang, L. Wang, K. Ladt, J. Loi, B. Dargent, C. Leterrier, and S. Roy. 2015. A dynamic formin-dependent deep F-actin network in axons. *J Cell Biol*. 210:401-417.

Gardberg, M., K. Talvinen, K. Kaipio, K. Iljin, C. Kampf, M. Uhlen, and O. Carpen. 2010. Characterization of Diaphanous-related formin FMNL2 in human tissues. *BMC Cell Biol*. 11:55.

Garrido, J.J., P. Giraud, E. Carlier, F. Fernandes, A. Moussif, M.P. Fache, D. Debanne, and B. Dargent. 2003. A targeting motif involved in sodium channel clustering at the axonal initial segment. *Science*. 300:2091-2094.

Goh, W.I., T. Sudhaharan, K.B. Lim, K.P. Sem, C.L. Lau, and S. Ahmed. 2011. Rif-mDia1 interaction is involved in filopodium formation independent of Cdc42 and Rac effectors. *J Biol Chem*. 286:13681-13694.

Goode, B.L., and M.J. Eck. 2007. Mechanism and function of formins in the control of actin assembly. *Annu Rev Biochem*. 76:593-627.

Gould, C.J., S. Maiti, A. Michelot, B.R. Graziano, L. Blanchoin, and B.L. Goode. 2011. The formin DAD domain plays dual roles in autoinhibition and actin nucleation. *Curr Biol*. 21:384-390.

Grikscheit, K., and R. Grosse. 2016. Formins at the Junction. *Trends Biochem Sci*. 41:148-159.

Grubb, M.S., and J. Burrone. 2010. Activity-dependent relocation of the axon initial segment fine-tunes neuronal excitability. *Nature*. 465:1070-1074.

Grubb, M.S., Y. Shu, H. Kuba, M.N. Rasband, V.C. Wimmer, and K.J. Bender. 2011. Short- and long-term plasticity at the axon initial segment. *J Neurosci*. 31:16049-16055.

Gurel, P.S., P. Ge, E.E. Grintsevich, R. Shu, L. Blanchoin, Z.H. Zhou, E. Reisler, and H.N. Higgs. 2014. INF2-mediated severing through actin filament encirclement and disruption. *Curr Biol*. 24:156-164.

Gutzmann, A., N. Ergul, R. Grossmann, C. Schultz, P. Wahle, and M. Engelhardt. 2014. A period of structural plasticity at the axon initial segment in developing visual cortex. *Front Neuroanat*. 8:11.

Hamada, M.S., S. Goethals, S.I. de Vries, R. Brette, and M.H. Kole. 2016. Covariation of axon initial segment location and dendritic tree normalizes the somatic action potential. *Proc Natl Acad Sci U S A*. 113:14841-14846.

Hammond, J.W., C.F. Huang, S. Kaech, C. Jacobson, G. Banker, and K.J. Verhey. 2010. Posttranslational modifications of tubulin and the polarized transport of kinesin-1 in neurons. *Mol Biol Cell*. 21:572-583.

Harris, E.S., I. Rouiller, D. Hanein, and H.N. Higgs. 2006. Mechanistic differences in actin bundling activity of two mammalian formins, FRL1 and mDia2. *J Biol Chem*. 281:14383-14392.

Harterink, M., K. Vocking, X. Pan, E.M. Soriano Jerez, L. Slenders, A. Freal, R.P. Tas, W.J. van de Wetering, K. Timmer, J. Motshagen, S.F.B. van Beuningen, L.C. Kapitein, W.J.C. Geerts, J.A. Post, and C.C. Hoogenraad. 2019. TRIM46 Organizes Microtubule Fasciculation in the Axon Initial Segment. *J Neurosci*. 39:4864-4873.

Hedstrom, K.L., Y. Ogawa, and M.N. Rasband. 2008. AnkyrinG is required for maintenance of the axon initial segment and neuronal polarity. *J Cell Biol*. 183:635-640.

Hedstrom, K.L., X. Xu, Y. Ogawa, R. Frischknecht, C.I. Seidenbecher, P. Shrager, and M.N. Rasband. 2007. Neurofascin assembles a specialized extracellular matrix at the axon initial segment. *J Cell Biol*. 178:875-886.

Heimsath, E.G., Jr., and H.N. Higgs. 2012. The C terminus of formin FMNL3 accelerates actin polymerization and contains a WH2 domain-like sequence that binds both monomers and filament

barbed ends. *J Biol Chem*. 287:3087-3098.

Heissler, S.M., and J.R. Sellers. 2014. Myosin light chains: Teaching old dogs new tricks. *Bioarchitecture*. 4:169-188.

Henty-Ridilla, J.L., A. Rankova, J.A. Eskin, K. Kenny, and B.L. Goode. 2016. Accelerated actin filament polymerization from microtubule plus ends. *Science*. 352:1004-1009.

Herder, C., J.M. Swiercz, C. Muller, R. Peravali, R. Quiring, S. Offermanns, J. Wittbrodt, and F. Loosli. 2013. ArhGEF18 regulates RhoA-Rock2 signaling to maintain neuro-epithelial apico-basal polarity and proliferation. *Development*. 140:2787-2797.

Herzog, D., P. Loetscher, J. van Hengel, S. Knusel, C. Brakebusch, V. Taylor, U. Suter, and J.B. Relvas. 2011. The small GTPase RhoA is required to maintain spinal cord neuroepithelium organization and the neural stem cell pool. *J Neurosci*. 31:5120-5130.

Higashida, C., T. Miyoshi, A. Fujita, F. Oceguera-Yanez, J. Monypenny, Y. Andou, S. Narumiya, and N. Watanabe. 2004. Actin polymerization-driven molecular movement of mDia1 in living cells. *Science*. 303:2007-2010.

Higgs, H.N., and K.J. Peterson. 2005. Phylogenetic analysis of the formin homology 2 domain. *Mol Biol Cell*. 16:1-13.

Hinman, J.D., M.N. Rasband, and S.T. Carmichael. 2013. Remodeling of the axon initial segment after focal cortical and white matter stroke. *Stroke*. 44:182-189.

Hirokawa, N. 1998. Kinesin and dynein superfamily proteins and the mechanism of organelle transport. *Science*. 279:519-526.

Hofflin, F., A. Jack, C. Riedel, J. Mack-Bucher, J. Roos, C. Corcelli, C. Schultz, P. Wahle, and M. Engelhardt. 2017. Heterogeneity of the Axon Initial Segment in Interneurons and Pyramidal Cells of Rodent Visual Cortex. *Front Cell Neurosci*. 11:332.

Hong, E.H., J.Y. Kim, J.H. Kim, D.S. Lim, M. Kim, and J.Y. Kim. 2018. BIG2-ARF1-RhoA-mDia1 Signaling Regulates Dendritic Golgi Polarization in Hippocampal Neurons. *Mol Neurobiol*. 55:7701-7716.

Hotulainen, P., O. Llano, S. Smirnov, K. Tanhuanpaa, J. Faix, C. Rivera, and P. Lappalainen. 2009. Defining mechanisms of actin polymerization and depolymerization during dendritic spine morphogenesis. *J Cell Biol*. 185:323-339.

Hu, W., C. Tian, T. Li, M. Yang, H. Hou, and Y. Shu. 2009. Distinct contributions of Na(v)1.6 and Na(v)1.2 in action potential initiation and backpropagation. *Nat Neurosci*. 12:996-1002.

Hua, T., X. Li, L. He, Y. Zhou, Y. Wang, and A.G. Leventhal. 2006. Functional degradation of visual cortical cells in old cats. *Neurobiol Aging*. 27:155-162.

Huang, C.Y., and M.N. Rasband. 2018. Axon initial segments: structure, function, and disease. *Ann N Y Acad Sci*. 1420:46-61.

Inda, M.C., J. DeFelipe, and A. Munoz. 2006. Voltage-gated ion channels in the axon initial segment of human cortical pyramidal cells and their relationship with chandelier cells. *Proc Natl Acad Sci U S A*. 103:2920-2925.

Ishizaki, T., Y. Morishima, M. Okamoto, T. Furuyashiki, T. Kato, and S. Narumiya. 2001. Coordination of microtubules and the actin cytoskeleton by the Rho effector mDia1. *Nat Cell Biol*. 3:8-14.

Jegou, A., M.F. Carlier, and G. Romet-Lemonne. 2013. Formin mDia1 senses and generates mechanical forces on actin filaments. *Nat Commun*. 4:1883.

Jenkins, P.M., N. Kim, S.L. Jones, W.C. Tseng, T.M. Svitkina, H.H. Yin, and V. Bennett. 2015. Giant ankyrin-G: a critical innovation in vertebrate evolution of fast and integrated neuronal signaling. *Proc Natl Acad Sci U S A*. 112:957-964.

Jenkins, S.M., and V. Bennett. 2001. Ankyrin-G coordinates assembly of the spectrin-based membrane skeleton, voltage-gated sodium channels, and L1 CAMs at Purkinje neuron initial segments. *J Cell Biol*. 155:739-746.

Jenkins, S.M., K. Kizhatil, N.R. Kramarcy, A. Sen, R. Sealock, and V. Bennett. 2001. FIGQY phosphorylation defines discrete populations of L1 cell adhesion molecules at sites of cell-cell contact and in migrating neurons. *J Cell Sci*. 114:3823-3835.

John, N., H. Krugel, R. Frischknecht, K.H. Smalla, C. Schultz, M.R. Kreutz, E.D. Gundelfinger, and C.I. Seidenbecher. 2006. Brevican-containing perineuronal nets of extracellular matrix in dissociated

hippocampal primary cultures. *Mol Cell Neurosci*. 31:774-784.

Jones, S.L., F. Korobova, and T. Svitkina. 2014. Axon initial segment cytoskeleton comprises a multiprotein submembranous coat containing sparse actin filaments. *J Cell Biol*. 205:67-81.

Kaech, S., and G. Banker. 2006. Culturing hippocampal neurons. *Nat Protoc*. 1:2406-2415.

Kaphzan, H., S.A. Buffington, J.I. Jung, M.N. Rasband, and E. Klann. 2011. Alterations in intrinsic membrane properties and the axon initial segment in a mouse model of Angelman syndrome. *J Neurosci*. 31:17637-17648.

Kawabata Galbraith, K., and M. Kengaku. 2019. Multiple roles of the actin and microtubule-regulating formins in the developing brain. *Neurosci Res*. 138:59-69.

Kizhatil, K., J.Q. Davis, L. Davis, J. Hoffman, B.L. Hogan, and V. Bennett. 2007. Ankyrin-G is a molecular partner of E-cadherin in epithelial cells and early embryos. *J Biol Chem*. 282:26552-26561.

Klinman, E., M. Tokito, and E.L.F. Holzbaur. 2017. CDK5-dependent activation of dynein in the axon initial segment regulates polarized cargo transport in neurons. *Traffic*. 18:808-824.

Knierim, E., E. Gill, F. Seifert, S. Morales-Gonzalez, S.D. Unudurthi, T.J. Hund, W. Stenzel, and M. Schuelke. 2017. A recessive mutation in beta-IV-spectrin (SPTBN4) associates with congenital myopathy, neuropathy, and central deafness. *Hum Genet*. 136:903-910.

Kole, M.H., S.U. Ilschner, B.M. Kampa, S.R. Williams, P.C. Ruben, and G.J. Stuart. 2008. Action potential generation requires a high sodium channel density in the axon initial segment. *Nat Neurosci*. 11:178-186.

Kole, M.H., J.J. Letzkus, and G.J. Stuart. 2007. Axon initial segment Kv1 channels control axonal action potential waveform and synaptic efficacy. *Neuron*. 55:633-647.

Kole, M.H., and G.J. Stuart. 2012. Signal processing in the axon initial segment. *Neuron*. 73:235-247.

Komada, M., and P. Soriano. 2002. [Beta]IV-spectrin regulates sodium channel clustering through ankyrin-G at axon initial segments and nodes of Ranvier. *J Cell Biol*. 156:337-348.

Konishi, Y., and M. Setou. 2009. Tubulin tyrosination navigates the kinesin-1 motor domain to axons. *Nat Neurosci*. 12:559-567.

Kordeli, E., S. Lambert, and V. Bennett. 1995. AnkyrinG. A new ankyrin gene with neural-specific isoforms localized at the axonal initial segment and node of Ranvier. *J Biol Chem*. 270:2352-2359.

Kovar, D.R., E.S. Harris, R. Mahaffy, H.N. Higgs, and T.D. Pollard. 2006. Control of the assembly of ATP- and ADP-actin by formins and profilin. *Cell*. 124:423-435.

Kress, G.J., M.J. Dowling, L.N. Eisenman, and S. Mennerick. 2010. Axonal sodium channel distribution shapes the depolarized action potential threshold of dentate granule neurons. *Hippocampus*. 20:558-571.

Kuba, H., R. Adachi, and H. Ohmori. 2014. Activity-dependent and activity-independent development of the axon initial segment. *J Neurosci*. 34:3443-3453.

Kuba, H., T.M. Ishii, and H. Ohmori. 2006. Axonal site of spike initiation enhances auditory coincidence detection. *Nature*. 444:1069-1072.

Kuba, H., Y. Oichi, and H. Ohmori. 2010. Presynaptic activity regulates Na(+) channel distribution at the axon initial segment. *Nature*. 465:1075-1078.

Kuhn, S., and M. Geyer. 2014. Formins as effector proteins of Rho GTPases. *Small GTPases*. 5:e29513.

Kuijpers, M., D. van de Willige, A. Freal, A. Chazeau, M.A. Franker, J. Hofenk, R.J. Rodrigues, L.C. Kapitein, A. Akhmanova, D. Jaarsma, and C.C. Hoogenraad. 2016. Dynein Regulator NDEL1 Controls Polarized Cargo Transport at the Axon Initial Segment. *Neuron*. 89:461-471.

Kumar, R., M.A. Corbett, N.J. Smith, L.A. Jolly, C. Tan, D.J. Keating, M.D. Duffield, T. Utsumi, K. Moriya, K.R. Smith, A. Hoischen, K. Abbott, M.G. Harbord, A.G. Compton, J.A. Woenig, P. Arts, M. Kwint, N. Wieskamp, S. Gijsen, J.A. Veltman, M. Bahlo, J.G. Gleeson, E. Haan, and J. Gecz. 2015. Homozygous mutation of STXBP5L explains an autosomal recessive infantile-onset neurodegenerative disorder. *Hum Mol Genet*. 24:2000-2010.

Kuzman, M.R., V. Medved, J. Terzic, and D. Krainc. 2009. Genome-wide expression analysis of peripheral blood identifies candidate biomarkers for schizophrenia. *J Psychiatr Res*. 43:1073-1077.

Kwon, S., H. Shin, and H.J. Lim. 2011. Dynamic interaction of formin proteins and cytoskeleton in

mouse oocytes during meiotic maturation. *Mol Hum Reprod*. 17:317-327.

Law, R., T. Dixon-Salazar, J. Jerber, N. Cai, A.A. Abbasi, M.S. Zaki, K. Mittal, S.B. Gabriel, M.A. Rafiq, V. Khan, M. Nguyen, G. Ali, B. Copeland, E. Scott, N. Vasli, A. Mikhailov, M.N. Khan, D.M. Andrade, M. Ayaz, M. Ansar, M. Ayub, J.B. Vincent, and J.G. Gleeson. 2014. Biallelic truncating mutations in FMN2, encoding the actin-regulatory protein Formin 2, cause nonsyndromic autosomal-recessive intellectual disability. *Am J Hum Genet*. 95:721-728.

Lemaillet, G., B. Walker, and S. Lambert. 2003. Identification of a conserved ankyrin-binding motif in the family of sodium channel alpha subunits. *J Biol Chem*. 278:27333-27339.

Lemmon, M.A., K.M. Ferguson, and C.S. Abrams. 2002. Pleckstrin homology domains and the cytoskeleton. *FEBS Lett*. 513:71-76.

Leterrier, C., J. Potier, G. Caillol, C. Debarnot, F. Rueda Boroni, and B. Dargent. 2015. Nanoscale Architecture of the Axon Initial Segment Reveals an Organized and Robust Scaffold. *Cell Rep*. 13:2781-2793.

Leterrier, C., H. Vacher, M.P. Fache, S.A. d'Ortoli, F. Castets, A. Autillo-Touati, and B. Dargent. 2011. End-binding proteins EB3 and EB1 link microtubules to ankyrin G in the axon initial segment. *Proc Natl Acad Sci U S A*. 108:8826-8831.

Leussis, M.P., E.M. Berry-Scott, M. Saito, H. Jhuang, G. de Haan, O. Alkan, C.J. Luce, J.M. Madison, P. Sklar, T. Serre, D.E. Root, and T.L. Petryshen. 2013. The ANK3 bipolar disorder gene regulates psychiatric-related behaviors that are modulated by lithium and stress. *Biol Psychiatry*. 73:683-690.

Leussis, M.P., J.M. Madison, and T.L. Petryshen. 2012. Ankyrin 3: genetic association with bipolar disorder and relevance to disease pathophysiology. *Biol Mood Anxiety Disord*. 2:18.

Leventhal, A.G., Y. Wang, M. Pu, Y. Zhou, and Y. Ma. 2003. GABA and its agonists improved visual cortical function in senescent monkeys. *Science*. 300:812-815.

Lewkowicz, E., F. Herit, C. Le Clainche, P. Bourdoncle, F. Perez, and F. Niedergang. 2008. The microtubule-binding protein CLIP-170 coordinates mDia1 and actin reorganization during CR3-mediated phagocytosis. *J Cell Biol*. 183:1287-1298.

Liu, W., and J.J. Devaux. 2014. Calmodulin orchestrates the heteromeric assembly and the trafficking of KCNQ2/3 (Kv7.2/3) channels in neurons. *Mol Cell Neurosci*. 58:40-52.

Lorincz, A., and Z. Nusser. 2008. Cell-type-dependent molecular composition of the axon initial segment. *J Neurosci*. 28:14329-14340.

Luo, J., D. Li, D. Wei, X. Wang, L. Wang, and X. Zeng. 2017. RhoA and RhoC are involved in stromal cell-derived factor-1-induced cell migration by regulating F-actin redistribution and assembly. *Mol Cell Biochem*. 436:13-21.

Lybaek, H., K.H. Orstavik, T. Prescott, R. Hovland, H. Breilid, C. Stansberg, V.M. Steen, and G. Houge. 2009. An 8.9 Mb 19p13 duplication associated with precocious puberty and a sporadic 3.9 Mb 2q23.3q24.1 deletion containing NR4A2 in mentally retarded members of a family with an intrachromosomal 19p-into-19q between-arm insertion. *Eur J Hum Genet*. 17:904-910.

Mademan, I., T. Deconinck, A. Dinopoulos, T. Voit, U. Schara, K. Devriendt, B. Meijers, E. Lerut, P. De Jonghe, and J. Baets. 2013. De novo INF2 mutations expand the genetic spectrum of hereditary neuropathy with glomerulopathy. *Neurology*. 81:1953-1958.

Marin, M.A., J. Ziburkus, J. Jankowsky, and M.N. Rasband. 2016. Amyloid-beta plaques disrupt axon initial segments. *Exp Neurol*. 281:93-98.

Moriya, K., T. Yamamoto, E. Takamitsu, Y. Matsunaga, M. Kimoto, D. Fukushige, C. Kimoto, T. Suzuki, and T. Utsumi. 2012. Protein N-myristoylation is required for cellular morphological changes induced by two formin family proteins, FMNL2 and FMNL3. *Biosci Biotechnol Biochem*. 76:1201-1209.

Nakada, C., K. Ritchie, Y. Oba, M. Nakamura, Y. Hotta, R. Iino, R.S. Kasai, K. Yamaguchi, T. Fujiwara, and A. Kusumi. 2003. Accumulation of anchored proteins forms membrane diffusion barriers during neuronal polarization. *Nat Cell Biol*. 5:626-632.

Nakata, T., and N. Hirokawa. 2003. Microtubules provide directional cues for polarized axonal transport through interaction with kinesin motor head. *J Cell Biol*. 162:1045-1055.

Neuhaus, C., R. Lang-Roth, U. Zimmermann, R. Heller, T. Eisenberger, M. Weikert, S. Markus, M. Knipper, and H.J. Bolz. 2017. Extension of the clinical and molecular phenotype of DIAPH1-associated autosomal dominant hearing loss (DFNA1). *Clin Genet*. 91:892-901.

Nirschl, J.J., A.E. Ghiretti, and E.L.F. Holzbaur. 2017. The impact of cytoskeletal organization on the local regulation of neuronal transport. *Nat Rev Neurosci*. 18:585-597.

Nishimura, K., H. Akiyama, M. Komada, and H. Kamiguchi. 2007. betaIV-spectrin forms a diffusion barrier against L1CAM at the axon initial segment. *Mol Cell Neurosci*. 34:422-430.

Ogawa, Y., I. Horresh, J.S. Trimmer, D.S. Bredt, E. Peles, and M.N. Rasband. 2008. Postsynaptic density-93 clusters Kv1 channels at axon initial segments independently of Caspr2. *J Neurosci*. 28:5731-5739.

Ogawa, Y., J. Oses-Prieto, M.Y. Kim, I. Horresh, E. Peles, A.L. Burlingame, J.S. Trimmer, D. Meijer, and M.N. Rasband. 2010. ADAM22, a Kv1 channel-interacting protein, recruits membrane-associated guanylate kinases to juxtaparanodes of myelinated axons. *J Neurosci*. 30:1038-1048.

Ogiwara, I., H. Miyamoto, N. Morita, N. Atapour, E. Mazaki, I. Inoue, T. Takeuchi, S. Itohara, Y. Yanagawa, K. Obata, T. Furuichi, T.K. Hensch, and K. Yamakawa. 2007. Nav1.1 localizes to axons of parvalbumin-positive inhibitory interneurons: a circuit basis for epileptic seizures in mice carrying an Scn1a gene mutation. *J Neurosci*. 27:5903-5914.

Osorio, N., L. Cathala, M.H. Meisler, M. Crest, J. Magistretti, and P. Delmas. 2010. Persistent Nav1.6 current at axon initial segments tunes spike timing of cerebellar granule cells. *J Physiol*. 588:651-670.

Palay, S.L., C. Sotelo, A. Peters, and P.M. Orkand. 1968. The axon hillock and the initial segment. *J Cell Biol*. 38:193-201.

Palazzo, A.F., T.A. Cook, A.S. Alberts, and G.G. Gundersen. 2001. mDia mediates Rho-regulated formation and orientation of stable microtubules. *Nat Cell Biol*. 3:723-729.

Pan, Z., T. Kao, Z. Horvath, J. Lemos, J.Y. Sul, S.D. Cranstoun, V. Bennett, S.S. Scherer, and E.C. Cooper. 2006. A common ankyrin-G-based mechanism retains KCNQ and NaV channels at electrically active domains of the axon. *J Neurosci*. 26:2599-2613.

Parkinson, N.J., C.L. Olsson, J.L. Hallows, J. McKee-Johnson, B.P. Keogh, K. Noben-Trauth, S.G. Kujawa, and B.L. Tempel. 2001. Mutant beta-spectrin 4 causes auditory and motor neuropathies in quivering mice. *Nat Genet*. 29:61-65.

Paul, A.S., and T.D. Pollard. 2008. The role of the FH1 domain and profilin in formin-mediated actin-filament elongation and nucleation. *Curr Biol*. 18:9-19.

Pechlivanis, M., A. Samol, and E. Kerkhoff. 2009. Identification of a short Spir interaction sequence at the C-terminal end of formin subgroup proteins. *J Biol Chem*. 284:25324-25333.

Pruyne, D. 2016. Revisiting the Phylogeny of the Animal Formins: Two New Subtypes, Relationships with Multiple Wing Hairs Proteins, and a Lost Human Formin. *PLoS One*. 11:e0164067.

Psychiatric, G.C.B.D.W.G. 2011. Large-scale genome-wide association analysis of bipolar disorder identifies a new susceptibility locus near ODZ4. *Nat Genet*. 43:977-983.

Qu, X., F.N. Yuan, C. Corona, S. Pasini, M.E. Pero, G.G. Gundersen, M.L. Shelanski, and F. Bartolini. 2017. Stabilization of dynamic microtubules by mDia1 drives Tau-dependent Abeta1-42 synaptotoxicity. *J Cell Biol*. 216:3161-3178.

Ramalingam, N., H. Zhao, D. Breitsprecher, P. Lappalainen, J. Faix, and M. Schleicher. 2010. Phospholipids regulate localization and activity of mDia1 formin. *Eur J Cell Biol*. 89:723-732.

Rao, M.V., and R. Zaidel-Bar. 2016. Formin-mediated actin polymerization at cell-cell junctions stabilizes E-cadherin and maintains monolayer integrity during wound repair. *Mol Biol Cell*. 27:2844-2856.

Rasband, M.N. 2010. The axon initial segment and the maintenance of neuronal polarity. *Nat Rev Neurosci*. 11:552-562.

Rasmussen, H.B., C. Frokjaer-Jensen, C.S. Jensen, H.S. Jensen, N.K. Jorgensen, H. Misonou, J.S. Trimmer, S.P. Olesen, and N. Schmitt. 2007. Requirement of subunit co-assembly and ankyrin-G for M-channel localization at the axon initial segment. *J Cell Sci*. 120:953-963.

Reed, N.A., D. Cai, T.L. Blasius, G.T. Jih, E. Meyhofer, J. Gaertig, and K.J. Verhey. 2006. Microtubule acetylation promotes kinesin-1 binding and transport. *Curr Biol*. 16:2166-2172.

Ren, Q., and V. Bennett. 1998. Palmitoylation of neurofascin at a site in the membrane-spanning domain highly conserved among the L1 family of cell adhesion molecules. *J Neurochem*. 70:1839-1849.

Rivieccio, M.A., C. Brochier, D.E. Willis, B.A. Walker, M.A. D'Annibale, K. McLaughlin, A. Siddiq, A.P. Kozikowski, S.R. Jaffrey, J.L. Twiss, R.R. Ratan, and B. Langley. 2009. HDAC6 is a target for

protection and regeneration following injury in the nervous system. *Proc Natl Acad Sci U S A*. 106:19599-19604.

Rizvi, S.A., E.M. Neidt, J. Cui, Z. Feiger, C.T. Skau, M.L. Gardel, S.A. Kozmin, and D.R. Kovar. 2009. Identification and characterization of a small molecule inhibitor of formin-mediated actin assembly. *Chem Biol*. 16:1158-1168.

Romero, S., C. Le Clainche, D. Didry, C. Egile, D. Pantaloni, and M.F. Carlier. 2004. Formin is a processive motor that requires profilin to accelerate actin assembly and associated ATP hydrolysis. *Cell*. 119:419-429.

Sainath, R., and G. Gallo. 2015. The dynein inhibitor Ciliobrevin D inhibits the bidirectional transport of organelles along sensory axons and impairs NGF-mediated regulation of growth cones and axon branches. *Dev Neurobiol*. 75:757-777.

Sanchez-Ponce, D., L. Blazquez-Llorca, J. DeFelipe, J.J. Garrido, and A. Munoz. 2012a. Colocalization of alpha-actinin and synaptopodin in the pyramidal cell axon initial segment. *Cereb Cortex*. 22:1648-1661.

Sanchez-Ponce, D., J. DeFelipe, J.J. Garrido, and A. Munoz. 2011a. In vitro maturation of the cisternal organelle in the hippocampal neuron's axon initial segment. *Mol Cell Neurosci*. 48:104-116.

Sanchez-Ponce, D., J. DeFelipe, J.J. Garrido, and A. Munoz. 2012b. Developmental expression of Kv potassium channels at the axon initial segment of cultured hippocampal neurons. *PLoS One*. 7:e48557.

Sanchez-Ponce, D., A. Munoz, and J.J. Garrido. 2011b. Casein kinase 2 and microtubules control axon initial segment formation. *Mol Cell Neurosci*. 46:222-234.

Satake, T., K. Yamashita, K. Hayashi, S. Miyatake, M. Tamura-Nakano, H. Doi, Y. Furuta, G. Shioi, E. Miura, Y.H. Takeo, K. Yoshida, H. Yahikozawa, N. Matsumoto, M. Yuzaki, and A. Suzuki. 2017. MTCL1 plays an essential role in maintaining Purkinje neuron axon initial segment. *EMBO J*. 36:1227-1242.

Schafer, D.P., S. Jha, F. Liu, T. Akella, L.D. McCullough, and M.N. Rasband. 2009. Disruption of the axon initial segment cytoskeleton is a new mechanism for neuronal injury. *J Neurosci*. 29:13242-13254.

Schizophrenia Psychiatric Genome-Wide Association Study, C. 2011. Genome-wide association study identifies five new schizophrenia loci. *Nat Genet*. 43:969-976.

Schluter, A., D. Del Turco, T. Deller, A. Gutzmann, C. Schultz, and M. Engelhardt. 2017. Structural Plasticity of Synaptopodin in the Axon Initial Segment during Visual Cortex Development. *Cereb Cortex*. 27:4662-4675.

Schluter, A., S. Rossberger, D. Dannehl, J.M. Janssen, S. Vorwald, J. Hanne, C. Schultz, D. Mauceri, and M. Engelhardt. 2019. Dynamic Regulation of Synaptopodin and the Axon Initial Segment in Retinal Ganglion Cells During Postnatal Development. *Front Cell Neurosci*. 13:318.

Schmandke, A., A. Schmandke, and S.M. Strittmatter. 2007. ROCK and Rho: biochemistry and neuronal functions of Rho-associated protein kinases. *Neuroscientist*. 13:454-469.

Schonichen, A., and M. Geyer. 2010. Fifteen formins for an actin filament: a molecular view on the regulation of human formins. *Biochim Biophys Acta*. 1803:152-163.

Schymick, J.C., S.W. Scholz, H.C. Fung, A. Britton, S. Arepalli, J.R. Gibbs, F. Lombardo, M. Matarin, D. Kasperaviciute, D.G. Hernandez, C. Crews, L. Bruijn, J. Rothstein, G. Mora, G. Restagno, A. Chio, A. Singleton, J. Hardy, and B.J. Traynor. 2007. Genome-wide genotyping in amyotrophic lateral sclerosis and neurologically normal controls: first stage analysis and public release of data. *Lancet Neurol*. 6:322-328.

Seagar, M., M. Russier, O. Caillard, Y. Maulet, L. Fronzaroli-Molinieres, M. De San Feliciano, N. Boumedine-Guignon, L. Rodriguez, M. Zbili, F. Usseglio, C. Formisano-Treziny, F. Youssouf, M. Sangiardi, M. Boillot, S. Baulac, M.J. Benitez, J.J. Garrido, D. Debanne, and O. El Far. 2017. LGI1 tunes intrinsic excitability by regulating the density of axonal Kv1 channels. *Proc Natl Acad Sci U S A*. 114:7719-7724.

Shah, M.M., M. Migliore, I. Valencia, E.C. Cooper, and D.A. Brown. 2008. Functional significance of axonal Kv7 channels in hippocampal pyramidal neurons. *Proc Natl Acad Sci U S A*. 105:7869-7874.

Shinohara, R., D. Thumkeo, H. Kamijo, N. Kaneko, K. Sawamoto, K. Watanabe, H. Takebayashi, H. Kiyonari, T. Ishizaki, T. Furuyashiki, and S. Narumiya. 2012. A role for mDia, a Rho-regulated actin nucleator, in tangential migration of interneuron precursors. *Nat Neurosci*. 15:373-380, S371-372.

Silkworth, W.T., K.L. Kunes, G.C. Nickel, M.L. Phillips, M.E. Quinlan, and C.L. Vizcarra. 2018. The neuron-specific formin Delphilin nucleates nonmuscle actin but does not enhance elongation. *Mol Biol Cell*. 29:610-621.

Simon-Areces, J., A. Dopazo, M. Dettenhofer, A. Rodriguez-Tebar, L.M. Garcia-Segura, and M.A. Arevalo. 2011. Formin1 mediates the induction of dendritogenesis and synaptogenesis by neurogenin3 in mouse hippocampal neurons. *PLoS One*. 6:e21825.

Sobotzik, J.M., J.M. Sie, C. Politi, D. Del Turco, V. Bennett, T. Deller, and C. Schultz. 2009. AnkyrinG is required to maintain axo-dendritic polarity in vivo. *Proc Natl Acad Sci U S A*. 106:17564-17569.

Song, A.H., D. Wang, G. Chen, Y. Li, J. Luo, S. Duan, and M.M. Poo. 2009. A selective filter for cytoplasmic transport at the axon initial segment. *Cell*. 136:1148-1160.

Soykan, T., N. Kaempf, T. Sakaba, D. Vollweiter, F. Goerdeler, D. Puchkov, N.L. Kononenko, and V. Haucke. 2017. Synaptic Vesicle Endocytosis Occurs on Multiple Timescales and Is Mediated by Formin-Dependent Actin Assembly. *Neuron*. 93:854-866 e854.

Stepanova, T., J. Slemmer, C.C. Hoogenraad, G. Lansbergen, B. Dortland, C.I. De Zeeuw, F. Grosveld, G. van Cappellen, A. Akhmanova, and N. Galjart. 2003. Visualization of microtubule growth in cultured neurons via the use of EB3-GFP (end-binding protein 3-green fluorescent protein). *J Neurosci*. 23:2655-2664.

Stone, M.C., F. Roegiers, and M.M. Rolls. 2008. Microtubules have opposite orientation in axons and dendrites of Drosophila neurons. *Mol Biol Cell*. 19:4122-4129.

Stuart, G., N. Spruston, B. Sakmann, and M. Hausser. 1997. Action potential initiation and backpropagation in neurons of the mammalian CNS. *Trends Neurosci*. 20:125-131.

Tapia, M., A. Del Puerto, A. Puime, D. Sanchez-Ponce, L. Fronzaroli-Molinieres, N. Pallas-Bazarra, E. Carlier, P. Giraud, D. Debanne, F. Wandosell, and J.J. Garrido. 2013. GSK3 and beta-catenin determines functional expression of sodium channels at the axon initial segment. *Cell Mol Life Sci*. 70:105-120.

Tapia, M., A. Dominguez, W. Zhang, A. Del Puerto, M. Ciorraga, M.J. Benitez, C. Guaza, and J.J. Garrido. 2017. Cannabinoid Receptors Modulate Neuronal Morphology and AnkyrinG Density at the Axon Initial Segment. *Front Cell Neurosci*. 11:5.

Tapia, M., F. Wandosell, and J.J. Garrido. 2010. Impaired function of HDAC6 slows down axonal growth and interferes with axon initial segment development. *PLoS One*. 5:e12908.

Thompson, M.E., E.G. Heimsath, T.J. Gauvin, H.N. Higgs, and F.J. Kull. 2013. FMNL3 FH2-actin structure gives insight into formin-mediated actin nucleation and elongation. *Nat Struct Mol Biol*. 20:111-118.

Thumkeo, D., R. Shinohara, K. Watanabe, H. Takebayashi, Y. Toyoda, K. Tohyama, T. Ishizaki, T. Furuyashiki, and S. Narumiya. 2011. Deficiency of mDia, an actin nucleator, disrupts integrity of neuroepithelium and causes periventricular dysplasia. *PLoS One*. 6:e25465.

Thurston, S.F., W.A. Kulacz, S. Shaikh, J.M. Lee, and J.W. Copeland. 2012. The ability to induce microtubule acetylation is a general feature of formin proteins. *PLoS One*. 7:e48041.

Tian, C., K. Wang, W. Ke, H. Guo, and Y. Shu. 2014. Molecular identity of axonal sodium channels in human cortical pyramidal cells. *Front Cell Neurosci*. 8:297.

Toyoda, Y., R. Shinohara, D. Thumkeo, H. Kamijo, H. Nishimaru, H. Hioki, T. Kaneko, T. Ishizaki, T. Furuyashiki, and S. Narumiya. 2013. EphA4-dependent axon retraction and midline localization of Ephrin-B3 are disrupted in the spinal cord of mice lacking mDia1 and mDia3 in combination. *Genes Cells*. 18:873-885.

Tuvia, S., T.D. Garver, and V. Bennett. 1997. The phosphorylation state of the FIGQY tyrosine of neurofascin determines ankyrin-binding activity and patterns of cell segregation. *Proc Natl Acad Sci U S A*. 94:12957-12962.

van Beuningen, S.F.B., L. Will, M. Harterink, A. Chazeau, E.Y. van Battum, C.P. Frias, M.A.M. Franker, E.A. Katrukha, R. Stucchi, K. Vocking, A.T. Antunes, L. Slenders, S. Doulkeridou, P. Sillevis Smitt, A.F.M. Altelaar, J.A. Post, A. Akhmanova, R.J. Pasterkamp, L.C. Kapitein, E. de Graaff, and C.C. Hoogenraad. 2015. TRIM46 Controls Neuronal Polarity and Axon Specification by Driving the Formation of Parallel Microtubule Arrays. *Neuron*. 88:1208-1226.

Van Wart, A., J.S. Trimmer, and G. Matthews. 2007. Polarized distribution of ion channels within microdomains of the axon initial segment. *J Comp Neurol*. 500:339-352.

Vautrin-Glabik, A., B. Botia, P. Kischel, H. Ouadid-Ahidouch, and L. Rodat-Despoix. 2018. IP3R3 silencing induced actin cytoskeletal reorganization through ARHGAP18/RhoA/mDia1/FAK pathway in breast cancer cell lines. *Biochim Biophys Acta Mol Cell Res*. 1865:945-958.

Vavylonis, D., D.R. Kovar, B. O'Shaughnessy, and T.D. Pollard. 2006. Model of formin-associated actin filament elongation. *Mol Cell*. 21:455-466.

Wallar, B.J., and A.S. Alberts. 2003. The formins: active scaffolds that remodel the cytoskeleton. *Trends Cell Biol*. 13:435-446.

Wang, Y., A. Arjonen, J. Pouwels, H. Ta, P. Pausch, G. Bange, U. Engel, X. Pan, O.T. Fackler, J. Ivaska, and R. Grosse. 2015. Formin-like 2 Promotes beta1-Integrin Trafficking and Invasive Motility Downstream of PKCalpha. *Dev Cell*. 34:475-483.

Watanabe, K., S. Al-Bassam, Y. Miyazaki, T.J. Wandless, P. Webster, and D.B. Arnold. 2012. Networks of polarized actin filaments in the axon initial segment provide a mechanism for sorting axonal and dendritic proteins. *Cell Rep*. 2:1546-1553.

Watanabe, N., T. Kato, A. Fujita, T. Ishizaki, and S. Narumiya. 1999. Cooperation between mDia1 and ROCK in Rho-induced actin reorganization. *Nat Cell Biol*. 1:136-143.

Waterman-Storer, C.M., S. Karki, and E.L. Holzbaur. 1995. The p150Glued component of the dynactin complex binds to both microtubules and the actin-related protein centractin (Arp-1). *Proc Natl Acad Sci U S A*. 92:1634-1638.

Wen, Y., C.H. Eng, J. Schmoranzer, N. Cabrera-Poch, E.J. Morris, M. Chen, B.J. Wallar, A.S. Alberts, and G.G. Gundersen. 2004. EB1 and APC bind to mDia to stabilize microtubules downstream of Rho and promote cell migration. *Nat Cell Biol*. 6:820-830.

Williams, S.K., Z.P. Weiner, and R.D. Gilmore. 2018. Human neuroglial cells internalize Borrelia burgdorferi by coiling phagocytosis mediated by Daam1. *PLoS One*. 13:e0197413.

Winckler, B., P. Forscher, and I. Mellman. 1999. A diffusion barrier maintains distribution of membrane proteins in polarized neurons. *Nature*. 397:698-701.

Xiao, M., M.K. Bosch, J.M. Nerbonne, and D.M. Ornitz. 2013. FGF14 localization and organization of the axon initial segment. *Mol Cell Neurosci*. 56:393-403.

Xu, K., G. Zhong, and X. Zhuang. 2013. Actin, spectrin, and associated proteins form a periodic cytoskeletal structure in axons. *Science*. 339:452-456.

Yamana, N., Y. Arakawa, T. Nishino, K. Kurokawa, M. Tanji, R.E. Itoh, J. Monypenny, T. Ishizaki, H. Bito, K. Nozaki, N. Hashimoto, M. Matsuda, and S. Narumiya. 2006. The Rho-mDia1 pathway regulates cell polarity and focal adhesion turnover in migrating cells through mobilizing Apc and c-Src. *Mol Cell Biol*. 26:6844-6858.

Yang, R., K.K. Walder-Christensen, S. Lalani, H. Yan, I.D. Garcia-Prieto, S. Alvarez, A. Fernandez-Jaen, L. Speltz, Y.H. Jiang, and V. Bennett. 2019. Neurodevelopmental mutation of giant ankyrin-G disrupts a core mechanism for axon initial segment assembly. *Proc Natl Acad Sci U S A*.

Yermakov, L.M., D.E. Drouet, R.B. Griggs, K.M. Elased, and K. Susuki. 2018. Type 2 Diabetes Leads to Axon Initial Segment Shortening in db/db Mice. *Front Cell Neurosci*. 12:146.

Yoshimura, T., and M.N. Rasband. 2014. Axon initial segments: diverse and dynamic neuronal compartments. *Curr Opin Neurobiol*. 27:96-102.

Young, K.G., S.F. Thurston, S. Copeland, C. Smallwood, and J.W. Copeland. 2008. INF1 is a novel microtubule-associated formin. *Mol Biol Cell*. 19:5168-5180.

Young, L.E., E.G. Heimsath, and H.N. Higgs. 2015. Cell type-dependent mechanisms for formin-mediated assembly of filopodia. *Mol Biol Cell*. 26:4646-4659.

Yu, M., X. Yuan, C. Lu, S. Le, R. Kawamura, A.K. Efremov, Z. Zhao, M.M. Kozlov, M. Sheetz, A. Bershadsky, and J. Yan. 2017. mDia1 senses both force and torque during F-actin filament polymerization. *Nat Commun*. 8:1650.

Yu, Y., C. Maureira, X. Liu, and D. McCormick. 2010. P/Q and N channels control baseline and spike-triggered calcium levels in neocortical axons and synaptic boutons. *J Neurosci*. 30:11858-11869.

Zaoui, K., S. Honore, D. Isnardon, D. Braguer, and A. Badache. 2008. Memo-RhoA-mDia1 signaling controls microtubules, the actin network, and adhesion site formation in migrating cells. *J Cell Biol*. 183:401-408.

Zhang, W., A. Bonadiman, M. Ciorraga, M.J. Benitez, and J.J. Garrido. 2019. P2Y1 Purinergic Receptor

Modulate Axon Initial Segment Initial Development. *Front Cell Neurosci*. 13:152.

Zhong, G., J. He, R. Zhou, D. Lorenzo, H.P. Babcock, V. Bennett, and X. Zhuang. 2014. Developmental mechanism of the periodic membrane skeleton in axons. *Elife*. 3.

Zhou, D., S. Lambert, P.L. Malen, S. Carpenter, L.M. Boland, and V. Bennett. 1998. AnkyrinG is required for clustering of voltage-gated Na channels at axon initial segments and for normal action potential firing. *J Cell Biol*. 143:1295-1304.

Zhou, F., P. Leder, and S.S. Martin. 2006. Formin-1 protein associates with microtubules through a peptide domain encoded by exon-2. *Exp Cell Res*. 312:1119-1126.

Zilberman, Y., N.O. Alieva, S. Miserey-Lenkei, A. Lichtenstein, Z. Kam, H. Sabanay, and A. Bershadsky. 2011. Involvement of the Rho-mDia1 pathway in the regulation of Golgi complex architecture and dynamics. *Mol Biol Cell*. 22:2900-2911.

Zimmermann, D., K.E. Homa, G.M. Hocky, L.W. Pollard, E.M. De La Cruz, G.A. Voth, K.M. Trybus, and D.R. Kovar. 2017. Mechanoregulated inhibition of formin facilitates contractile actomyosin ring assembly. *Nat Commun*. 8:703.

Annexes: Research Articles

frontiers in Cellular Neuroscience

ORIGINAL RESEARCH
published: 24 April 2019
doi: 10.3389/fncel.2019.00152

P2Y1 Purinergic Receptor Modulate Axon Initial Segment Initial Development

Wei Zhang[1], *Angela Bonadiman*[1], *María Ciorraga*[1], *María José Benitez*[1,2] *and Juan José Garrido*[1]*

[1]Spanish National Research Council (CSIC), Department of Molecular, Cellular and Developmental Neurobiology, Instituto Cajal, Madrid, Spain, [2]Departamento de Química Física Aplicada, Universidad Autónoma de Madrid, Madrid, Spain

Morphological and functional polarization of neurons depends on the generation and maintenance of the axon initial segment (AIS). This axonal domain maintains axonal properties but is also the place where the action potential (AP) is generated. All these functions require the AIS, a complex structure that is not fully understood. An integrated structure of voltage-gated ion channels, specific cytoskeleton architecture, as well as, scaffold proteins contributes to these functions. Among them, ankyrinG plays a crucial role to maintain ion channels and membrane proteins. However, it is still elusive how the AIS performs its complex structural and functional regulation. Recent studies reveal that AIS is dynamically regulated in molecular composition, length and location in response to neuronal activity. Some mechanisms acting on AIS plasticity have been uncovered recently, including Ca^{2+}, calpain or calmodulin-mediated modulation, as well as post-translational modifications of cytoskeleton proteins and actin-associated proteins. Neurons are able to respond to different kind of physiological and pathological stimuli from development to maturity by adapting their AIS composition, position and length. This raises the question of which are the neuronal receptors that contribute to the modulation of AIS plasticity. Previous studies have shown that purinergic receptor P2X7 activation is detrimental to AIS maintenance. During initial axonal elongation, P2X7 is coordinated with P2Y1, another purinergic receptor that is essential for proper axon elongation. In this study, we focus on the role of P2Y1 receptor on AIS development and maintenance. Our results show that P2Y1 receptor activity and expression are necessary during AIS initial development, while has no role once AIS maturity is achieved. P2Y1 inhibition or suppression results in a decrease in ankyrinG, βIV-spectrin and voltage-gated sodium channels accumulation that can be rescued by actin stabilization or the modulation of actin-binding proteins at the AIS. Moreover, P2X7 or calpain inhibition also rescues ankyrinG decrease. Hence, a dynamic balance of P2Y1 and P2X7 receptors expression and function during AIS assembly and maturation may represent a fine regulatory mechanism in response to physiological or pathological extracellular purines concentration.

Keywords: axon initial segment, purinergic receptors, P2Y1, ankyrinG, axon, myosin

OPEN ACCESS

Edited by:
Haruyuki Kamiya,
Graduate School of Medicine,
Hokkaido University, Japan

Reviewed by:
Hiroshi Kuba,
Nagoya University, Japan
Matthew S. Grubb,
King's College London,
United Kingdom

***Correspondence:**
Juan José Garrido
jjgarrido@cajal.csic.es

Received: *14 February 2019*
Accepted: *08 April 2019*
Published: *24 April 2019*

Citation:
Zhang W, Bonadiman A, Ciorraga M, Benitez MJ and Garrido JJ (2019) P2Y1 Purinergic Receptor Modulate Axon Initial Segment Initial Development. Front. Cell. Neurosci. 13:152. doi: 10.3389/fncel.2019.00152

INTRODUCTION

The axon initial segment (AIS) plays a crucial role in neuronal physiology, being responsible for the coordination of the whole set of inputs that a neuron receives. This unique axonal domain generates the action potential (AP; Stuart et al., 1997; Kole et al., 2008) and has a high degree of plasticity that allows the control of AP amplitude and frequency. In fact, the AIS may undergo lengthening or shortening, changes in its composition and can move away from soma to control AP response (Grubb and Burrone, 2010; Kuba et al., 2010, 2015; Del Puerto et al., 2015). Further, axonal identity and neuronal polarity depend on AIS integrity (Schafer et al., 2009). Different mental disorders (e.g., bipolar disorder, schizophrenia) and genetic diseases (e.g., Angelman syndrome) are related to AIS alterations (Kaphzan et al., 2011; van der Werf et al., 2017; Zhu et al., 2017), as well as neurodegeneration related diseases, such as stroke, brain injury or Alzheimer's disease (Schafer et al., 2009; Sun et al., 2014; Del Puerto et al., 2015). Despite the importance of AIS, our knowledge is far from a complete understanding of its whole composition, structure and plasticity. In this sense, it remains mostly unknown which receptors and extracellular factors participate on AIS development, maintenance and modulation.

The AIS comprises around the first 20–60 microns of the axon, depending on the type of neuron and developmental stage (for a review see Leterrier, 2018). It is composed by a high density of voltage-gated sodium, potassium and calcium ion channels, and also contains among others, GABA, dopamine and serotonin receptors, which contribute to modulate APs (Rasband, 2010). These voltage-gated ion channels are anchored through interactions with AIS enriched scaffold proteins, such as AnkyrinG or PSD-93 (Garrido et al., 2003; Pan et al., 2006; Ogawa et al., 2008). AnkyrinG is the most important structural protein in the AIS and AnkyrinG suppression drives to the loss of polarity and axonal identity. Scaffold proteins also serve to anchor other membrane proteins, such as L1, neurofascin or ADAM-22 (Jenkins and Bennett, 2001; Ogawa et al., 2010). Other extracellular proteins, such as Lgi1 (Seagar et al., 2017) or brevican (Hedstrom et al., 2007) also contribute to this dense protein structure. This functional and structural membrane and submembranous scaffold are anchored to a complex cytoskeleton by βIV-spectrin (Komada and Soriano, 2002), which interacts with the actin cytoskeleton (Rasband, 2010). Although recent studies have contributed to a better knowledge of this actin cytoskeleton, whose roles in AIS maintenance, development and function are not well understood. The AIS contains regular actin rings and actin patches (Watanabe et al., 2012; Leterrier et al., 2015). Some AIS actin-interacting proteins are α-actinin-2 (Sánchez-Ponce et al., 2012), synaptopodin (Bas Orth et al., 2007) or myosins (Evans et al., 2017; Janssen et al., 2017). Also, the AIS contains a synaptopodin and actin-associated structure, the cisternal organelle (Benedeczky et al., 1994), which function is still elusive despite, changes in cisternal organelle structure occurs during development and AIS plasticity (Schlüter et al., 2017). Finally, a differential microtubules cytoskeleton supports this whole structure and contributes to axonal trafficking. This microtubules cytoskeleton contains acetylated and detyrosinated tubulin that confers a higher degree of stability to this cytoskeleton (Konishi and Setou, 2009; Tapia et al., 2010).

While our knowledge of this complex interplay between important structural and functional proteins of the AIS increases, we still have little information about the external regulatory mechanisms modulating the AIS and its structural and composition plasticity.

Recent studies have highlighted the role of some receptors at the AIS and outside the AIS on the control of AIS composition, integrity and structural plasticity. The function and plasticity of AIS seem to depend on the excitatory or inhibitory profile of hippocampal neurons, as well as the input they receive and their developmental stage (Grubb et al., 2011). However, the extracellular factors, receptors, and mechanisms controlling these adaptive modifications are unknown. This raises the question of what factors contribute to a physiological development and maintenance of the AIS. Recent results show that neurotransmitter receptors participate in AIS regulation. Dopamine, through D3R receptors, modulates T-type Ca^{2+} channels at the AIS contributing to neuronal output (Bender et al., 2010; Clarkson et al., 2017). Serotonin receptors (5-HT1A) also contribute to the control of AP threshold by modulating AIS cyclic-nucleotide-gated channels (HCN1) in the medial superior olive (Ko et al., 2016). In addition, 5-HT1A receptors modulate $Na_v1.2$ voltage-gated sodium channels in the AIS of cortical neurons, decreasing the success rate of AP generation (Yin et al., 2017). Cannabinoid receptor 1 (CB1R) is necessary to achieve a proper ankyrinG clustering at the AIS in the early developmental stages of AIS (Tapia et al., 2017). Other neurotransmitters such as ATP, through the purinergic receptor P2X7, modulate AIS composition (Del Puerto et al., 2015). Purinergic receptors are a wide family of receptors expressed in neurons and glial cells and are important regulators of neuronal excitability. They can be divided into three subfamilies, adenosine, P2X and P2Y receptors, all activated by different neuronal and glial secreted purines (Del Puerto et al., 2013). They have an important role not only in physiological but also in pathological processes (Burnstock, 2017). Among them, the ionotropic P2X7 receptors are activated by high concentrations of extracellular ATP, while the metabotropic P2Y1 receptor is preferentially activated by ADP (Burnstock, 2007). P2X7 and P2Y1 purinergic receptors have an antagonistic role and are coordinated during initial axon elongation (del Puerto et al., 2012). While P2X7 has a detrimental effect on axonal elongation, P2Y1 promotes axonal elongation during the first stages of axonal growth. These antagonistic actions are regulated by P2X7-mediated calcium entry that inhibits adenylate cyclase 5 (AC5), and P2Y1-mediated Gq-PKCζ activation of AC5. This generates a balance that controls cAMP production and modulates PI3K-Akt-GSK3 pathway activity. Our previous work demonstrated that P2X7 activation is detrimental for ankyrinG and voltage-gated sodium channels accumulation in AIS of mature neurons (Del Puerto et al., 2015). However, P2Y1 role on AIS regulation has not been studied. The objective of our study was to investigate whether P2Y1 purinergic receptor

participates on AIS development or modulation. Our results show that P2Y1 activity is necessary for initial AIS development and ankyrinG accumulation while having no significant role in mature neuron AIS. Decreased ankyrinG accumulation due to P2Y1 suppression can be prevented through P2X7 or calpain inhibition, revealing the crosstalk of P2Y1 and P2X7 during AIS development. Further, P2Y1 suppression alters F-actin distribution in AIS and decreases phosphorylation of myosin light chain (pMLC) and ankyrinG which can be prevented by F-actin stabilizing agent Jasplakinolide or protein phosphatase 1 and 2A inhibitor Calyculin A. Together with previous results on purinergic regulation (del Puerto et al., 2012; Del Puerto et al., 2015), our results suggest a necessary role for P2Y1 for the early development of the AIS. However, with neuronal maturation, the importance of P2Y1 decreases while P2X7 gains and increasing relevance in AIS maintenance and modulation.

MATERIALS AND METHODS

Reagents and Plasmids

Reagents were obtained from the following manufacturers: Adenosine 5'-diphosphate sodium ADP (A2754), P2X7 antagonist, BBG (B0770), AC5 inhibitor, NKY80 (N2165) and PP1/PP2A phosphatases inhibitor calyculin A (C5552) were obtained from Sigma-Aldrich. P2Y Antagonist II (BPTU; 504187) was obtained from EMD Millipore. 2-Methylthioadenosine diphosphate trisodium salt (2-MeSADP; 1624), (N)-methanocarba-2MeSADP (MRS 2365; 2157), the calpain inhibitor MDL 28170 and jasplakinolide were obtained from Tocris. P2Y1 shRNA and scrambled shRNA plasmids have been previously published and validated (del Puerto et al., 2012).

Animals

Animals were housed in a room at controlled temperature and relative humidity with alternating 12 h light and dark cycles and free access to food and water "*ad libitum*." Animal care protocols used in our laboratory are in conformity with the appropriate national legislation (53/2013, BOE no. 1337) and guidelines of the Council of the European Communities (2010/63/UE). All protocols were previously approved by the CSIC bioethics committee.

Neuronal Culture

Mouse hippocampal neurons were prepared as previously described (del Puerto et al., 2012; Del Puerto et al., 2015). Neurons were obtained from E17 mouse hippocampi, which were incubated in a 0.25% trypsin solution in Ca^{2+}/Mg^{2+} free Hank's buffered salt solution (HBSS) and dissociated using fire-polished Pasteur pipettes. The cells were plated on polylysine-coated coverslips (1 mg/ml) at a density of 5,000 cells/cm^2 for 2 h in plating medium [minimum essential medium (MEM), 10% horse serum, 0.6% glucose and Glutamax-I]. Then coverslips were inverted and transferred to culture dishes containing astrocytes. Astrocytes medium was replaced by neuronal culture medium 24 h before neuronal culture (Neurobasal medium, B27 supplement, Glutamax-I). To avoid contact between neurons and astrocytes, paraffin beads were placed on coverslips before neuronal plating. Five micromolar 1-β-D-arabinofuranosylcytosine (AraC) was added after 2 days in culture to avoid glial cells proliferation. One-third of neuronal medium was replaced every week. Pharmacological treatments were applied as described in the "Results" section. In the case of pharmacological treatments in the absence of glial cell layer, coverslips were transferred to plates containing glial cells-conditioned medium. Primary hippocampal neurons were nucleofected using the Amaxa nucleofector kit for primary mammalian neural cells (Amaxa Bioscience) according to the manufacturer's instructions. Nucleofection was performed using 3 μg of total DNA and 3×10^6 cells for each nucleofection. Neurons were plated at a density of 10,000 cells/cm^2 as described above. Nucleofection efficiency was ∼15% of neurons, based on the number of GFP-positive neurons. For lipofection, neurons were plated at a density of 20,000 cells/cm^2 and transfected at 7 or 10 DIV. Lipofection was performed using Lipofectamine 2000 (Life Technologies) and 3 μg of total DNA following manufacturer instructions.

Immunofluorescence

Neurons from each experiment, containing all experimental conditions to be compared, were fixed in 4% PFA. To standardize staining, all these coverslips were treated at the same time for immunofluorescence following the same conditions. Briefly, coverslips were treated for 10 min with 50 mM NH_4Cl and incubated in blocking buffer (0.22% gelatine, 0.1% Triton X-100 in PBS) for 30 min, before incubation with primary antibodies for 1 h at room temperature in blocking buffer. The primary antibodies used were: chicken anti-MAP2 (1:10,000, Abcam, ab5392), mouse anti-ankyrinG (1:100) from NeuroMab (clone N106/36), mouse anti-pan sodium channel (1:100) from Sigma (clone K58/35), rabbit anti-pMLC (1:200) from Thermo Fisher (PA5-17727) and rabbit βIV-spectrin (1:1,000; a gift from Dr. M. Rasband, Baylor College of Medicine, Houston, TX, USA). The secondary antibodies used were a goat or donkey anti-mouse, anti-rabbit or anti-chicken Alexa-Fluor 488, 594, or 647 (1:1,000). Phalloidin Alexa-Fluor 594 was used at a concentration of 1:100. Images from each immunofluorescence were acquired on a Leica SP5 confocal microscope maintaining the same acquisition parameters to compare intensities. Figures were prepared for presentation using the Adobe CS4 software.

Dendrites and AIS Measurements

Quantification of fluorescence intensity at the AIS was performed on confocal images of neurons from at least three independent experiments. Neurons were randomly acquired without any bias by scanning each coverslip from top to bottom. All confocal images within the same experiment and immunofluorescence were acquired using exactly the same parameters of laser intensity, excitation and emission detection during the same working session for each Alexa fluorophore. Parameters were set in control neurons and maintained for the other experimental groups. After completing images acquisition of all conditions, ankyrinG and other AIS proteins staining were quantified using ImageJ software. We drew a line starting at the limit of neuronal soma identified by MAP2 staining and extended it along the

ankyrinG staining or the GFP signal of the axon. Data from every 0.16 μm along the first 40 μm were obtained and smoothed using the Sigmaplot software to obtain average ankyrinG fluorescence intensity every 1 μm. Data were normalized in each neuron, within the same immunofluorescence, considering the value of maximum mean fluorescence in control neurons to be 100%. Total fluorescence intensity for each neuron was obtained by adding ankyrinG fluorescence values from 0 to 40 μm. In some experiments, the total ankyrinG intensity was calculated within each AIS length and data normalized to AIS length of each neuron. AIS start, end and maximum fluorescence intensity were determined following the criteria described in Grubb and Burrone (2010). Taking 100% fluorescence as the maximum fluorescence intensity point, start and end points were defined as the points were fluorescence intensity is lower than 33%. For actin patches quantification, neurons were stained with Phalloidin-Alexa 594 (1:100) and ankyrinG to detect the AIS. Puncta of relatively uniform diameter of less than 3 μm within AIS were considered to be patches (Balasanyan et al., 2017). To avoid any possible loss of actin patches by lower F-actin intensity, image intensity was increased for the purpose of identification and quantification of all possible actin patches.

Dendrites lengths were obtained based on MAP2 staining using NeuronJ software to measure the length of the dendritic arbor in each neuron. All dendrites and ramifications in each neuron were traced using NeuronJ and their total length added. GFP signal of neurons under analysis allowed discriminating from crossing dendrites from other neurons. In order to study correlations between dendrites and AIS fluorescence, both data were obtained from the same neurons.

Statistical Analysis

All statistical analyses were carried out in Sigmaplot v12.5 (Systat Software Inc.) and Prism 5 (GraphPad Software, Inc., La Jolla, CA, USA). Data for each independent sample were obtained from at least three independent experiments. For pharmacological experiments, data from each experiment were collected from at least 30 cells (between 30 and 50 cells) in each experimental condition. For nucleofection or lipofection experiments around 25 neurons from each experiment in each experimental condition were analyzed. Statistical analysis was performed by *t*-test for two group comparisons and one-way ANOVA for multiple group comparisons. When data were non-normally distributed, non-parametric tests were used: Mann-Whitney Rank test for two independent samples and Kruskal-Wallis for analysis of multiple groups. In the analysis of multiple comparisons, a *post hoc* analysis was performed using Dunn's test. All *p*-values were adjusted to account for multiple comparisons. Cell-to-cell analysis of dendrite length and ankyrinG fluorescence was performed using Prism 5 and Sigmaplot v12.5. First, we tested the normality of data distribution on each variable using a Shapiro-Wilk or Kolmogorov-Smirnov normality test. As not all data passed normality test, the correlation was analyzed using the Pearson correlation function or Spearman correlation function when data failed normality test. Differences were considered significant when $p < 0.05$.

RESULTS

ADP Activation of P2Y1 Increases AnkyrinG Levels in the Developing Axon Initial Segments

A previous study demonstrated that the AIS of mature cultured hippocampal neurons (21 DIV) is regulated by ATP and P2X7 receptor (Del Puerto et al., 2015). Due to the coordinated action of ATP and ADP during initial axon elongation, we have investigated whether ADP and P2Y1 play a role in AIS regulation. Hippocampal neurons were treated with vehicle or ADP 10 μM during the 3 days prior fixation at 10, 14 or 21 DIV. AnkyrinG levels were then analyzed after immunofluorescence (**Figures 1A–D**). ADP treatment increased ankyrinG fluorescence intensity at the AIS in neurons treated from 7 to 10 DIV (146.74 ± 2.48%) compared to 10 DIV control neurons (100 ± 1.76%). However, ADP treatment in 14 DIV neurons had no significant effect in ankyrinG levels (113.74 ± 3.81%) vs. 14 DIV control neurons (100 ± 3.78%), as also happened for ADP treatment in 21 DIV neurons (110.38 ± 3.89% vs. AIS of 10 and 21 DIV neurons (**Figures 1B,C**). Next, we treated neurons with two more P2Y1 agonists, 2MeSADP (10 μM) and MRS-2365 (10 μM). Both agonists also increased significantly ankyrinG intensity at the AIS of 7–10 DIV treated neurons (**Figures 1E,F**), suggesting a P2Y1 mediated effect of ADP.

P2Y1 Receptor Suppression or Inhibition Decreases AnkyrinG Accumulation at the AIS During Initial Developmental Stages

In order to ensure that ADP effect was due to P2Y1 receptor activation, we nucleofected neurons before plating using scrambled (shscr) or P2Y1 (shP2Y1) interference RNAs that also express GFP. Neurons were left in culture for 4, 7, 14 or 21 DIV, fixed and stained with MAP2 and ankyrinG antibodies (**Figures 2A–D**). P2Y1 interference RNA significantly decreased ankyrinG intensity between 4 and 14 DIV (**Figure 2E**), with the maximum reduction found at 7 DIV (77.07 ± 3.79%) compared to 100 ± 4.75% in sh scrambled 7 DIV control neurons. Fourteen DIV neurons recovered when compared to 7 DIV neurons (86.58 ± 2.36%), and no significant change was observed in 21 DIV neurons. To ascertain that ADP treatment has no effect on ankyrinG intensity after P2Y1 suppression, nucleofected 7 DIV neurons were treated with ADP 10 μM for 3 days. Neurons nucleofected with scramble shRNA increased ankyrinG intensity after ADP treatment, while those expressing shP2Y1 did not respond to ADP treatment (**Figure 2F**). Next, we checked whether the fluorescence intensity of ankyrinG interacting proteins, βIV-spectrin and voltage-gated sodium channels, was also reduced in 7 DIV neurons (**Figure 2G**). Both proteins significantly decreased their expression at the AIS after P2Y1 suppression (72.19 ± 5.67%, panNaCh and 70.69 ± 6.46%, βIV-spectrin) and the percentage was similar to ankyrinG (**Figure 2E**). To rule out the possibility that shP2Y1 efficiency was progressively lost during *in vitro* development, we introduced

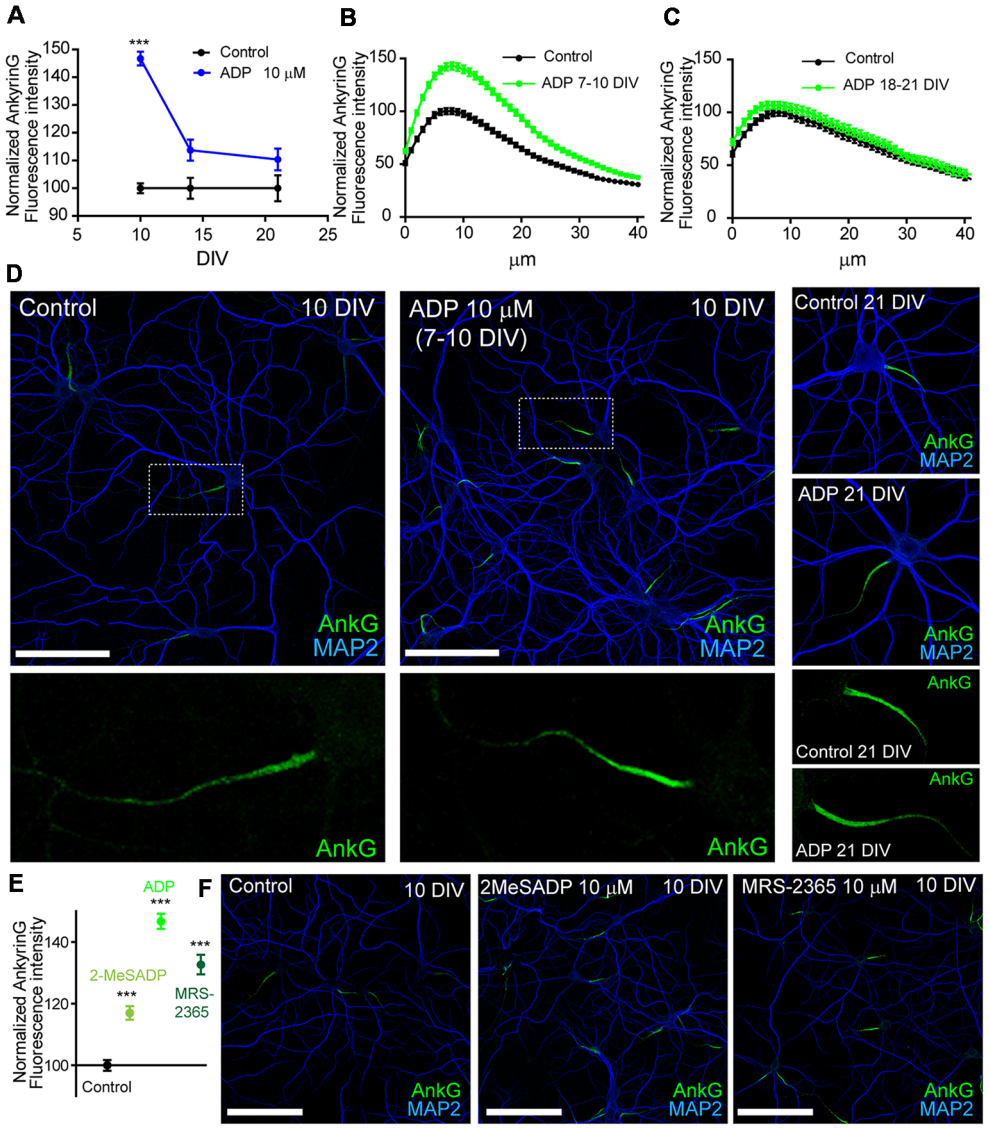

FIGURE 1 | ADP and P2Y1 agonists potentiates ankyrinG expression during early axon initial segment (AIS) development. **(A)** Normalized ankyrinG fluorescence intensity in 10, 14 and 21 DIV hippocampal neurons. Neurons were treated with ADP for 3 days before fixation (blue symbols). Data were acquired from three independent experiments (30 neurons/experimental condition in each experiment). Same pool of neurons was used for each experiment and fixed at different times. All images were acquired by confocal microscopy using the same fluorescence parameters. Statistical differences were analyzed by a Kruskal-Wallis test followed by a Dunn's multiple comparisons post-test. Adjusted p values: $^{***}p < 0.001$. **(B,C)** Normalized AnkyrinG intensity profile along the AIS of 10 DIV **(B)** and 21 DIV **(C)** hippocampal neurons in the presence (green line) or absence (black line) of 10 μM ADP treatments. **(D)** Control and ADP treated 10 DIV and 21 DIV neurons stained with MAP2 (blue) and ankyrinG antibodies (green). Scale bar = 100 μm. Four times-magnification of the ankyrinG staining (green) at the AIS is shown below images. **(E)** Normalized ankyrinG intensity at the AIS of 10 DIV neurons treated with ADP and P2Y1 agonists 2-methylthioadenosine diphosphate trisodium salt (2MeSADP) or MRS-2365 from 7 to 10 DIV. Data were acquired from three independent experiments (30 neurons/experimental condition in each experiment). $^{***}p < 0.001$, two-tail t-test. **(F)** 10 DIV hippocampal neurons stained with MAP2 (blue) and ankyrinG antibodies (green) treated with 2MeSADP (10 μM) or MRS-2365 (10 μM). Data in graphs are represented as the mean ± SEM.

control scrambled shRNA and P2Y1 shRNA by lipofection in 7 or 10 DIV neurons. Neurons were left 2–3 days and ankyrinG signal was analyzed (**Figure 2H**). Lipofected neurons expressing shP2Y1 did not show any reduction of ankyrinG levels at neither 10 or 12 DIV, confirming that in cultured hippocampal neurons P2Y1 exerts its action only during the initial steps of AIS development. This timing correlates with the stages prior to which the AIS diffusion barrier is developed at 10 DIV (Brachet et al., 2010).

In view of these results, we next checked whether P2Y1 pharmacological inhibition was enough to reduce ankyrinG levels. For this purpose, we used the non-nucleotide allosteric and none ADP-competitive P2Y1 antagonist, BPTU (1-(2-(2-(tert-butyl)phenoxy)pyridin-3-yl)

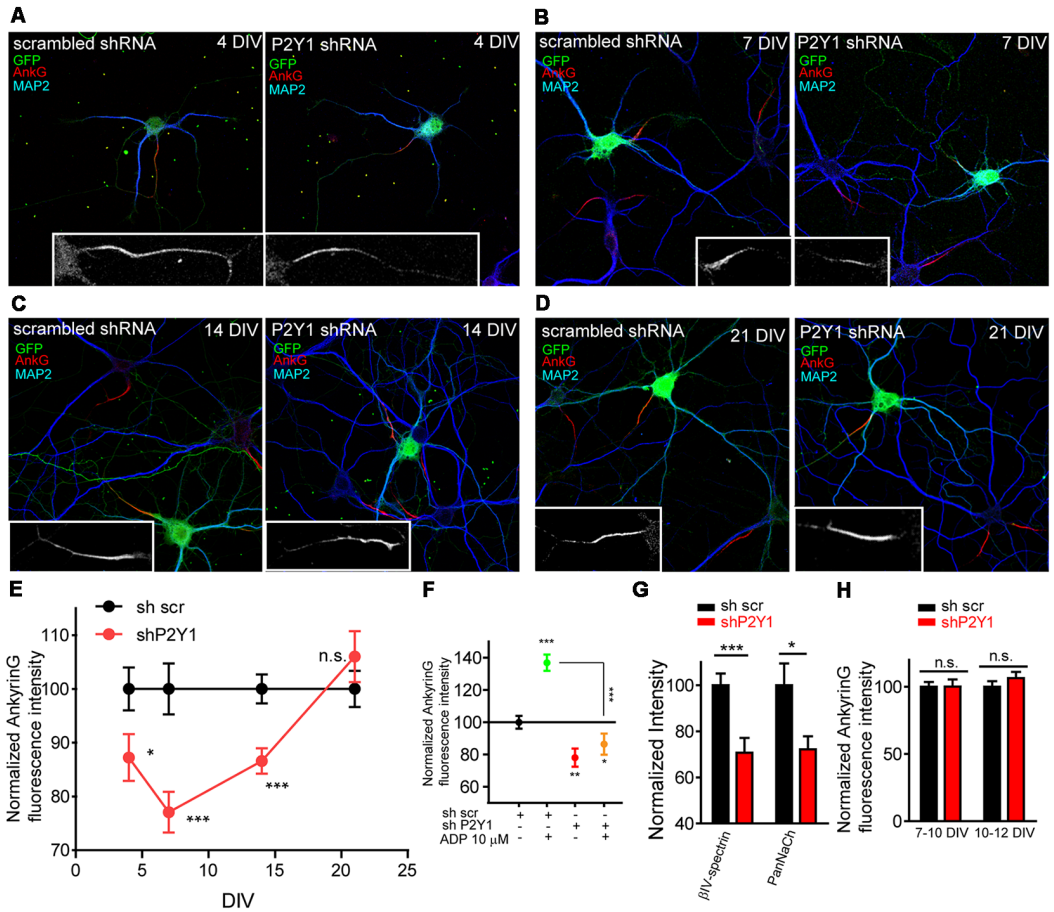

FIGURE 2 | P2Y1 receptor is necessary to maintain ankyrinG density during early stages of AIS development. **(A–D)** 4, 7, 14 and 21 DIV hippocampal neurons nucleofected with scrambled and P2Y1 shRNAs. After nucleofection neurons were kept in culture for 4 **(A)**, 7 **(B)**, 14 **(C)** and 21 days **(D)** and stained with MAP2 (blue) and ankyrinG (red) antibodies. Nucleofected neurons were identified by GFP expression (green). Inserts show magnifications of AISs (gray) of each neuron. **(E)** Normalized ankyrinG intensity at different days post-nucleofection with scrambled shRNA (shscr, black) or P2Y1 shRNA (shP2Y1, red). shP2Y1 data are normalized to their respective shscr controls at each developmental stage. $^{*}p < 0.05$, $^{**}p < 0.01$, $^{***}p < 0.001$, two-tail *t*-test. **(F)** Normalized ankyrinG intensity in 10 DIV neurons expressing shscr or shP2Y1 plasmids, treated with vehicle or ADP from 7 to 10 DIV. $^{*}p < 0.05$, $^{**}p < 0.01$, $^{***}p < 0.001$, two-tail *t*-test. Data were acquired from three independent experiments (30 neurons/experimental condition in each experiment). **(G)** βIV-spectrin and voltage-gated sodium channels (PanNaCh) normalized intensity in 7 DIV control shscr and shP2Y1 expressing neurons. $^{*}p < 0.05$, $^{***}p < 0.001$, two-tail *t*-test. Data were acquired from three independent experiments (at least 25 neurons/experimental condition in each experiment). **(H)** Normalized ankyrinG intensity in 10 and 12 DIV hippocampal transfected at 7 or 10 DIV, respectively, to express shscr or shP2Y1 interference RNAs. Data were acquired from three independent experiments (at least 20 neurons/experimental condition in each experiment). n.s., not significant, two tail *t*-test. Data in graphs are represented as the mean ± SEM.

-3-(4-(trifluoromethoxy)phenyl)urea; Mañé et al., 2016). First, we determined the most efficient dose in cultured hippocampal neurons. Seven DIV neurons were treated for 3 days with BPTU at concentrations of 0.5, 1, 2, 5, 7, 10 and 20 nM and ankyrinG levels were evaluated (**Figure 3A**). AnkyrinG levels decreased linearly with increasing BPTU concentration. BPTU doses under 10 nM did not affect neuronal viability, but concentrations higher than 10 nM had a detrimental effect on neuronal survival due to alterations on glial cell layer morphology and viability (data not shown). Consequently, we decided to inhibit P2Y1 using 5 nM BPTU treatments in 7 DIV neurons for 3 days (**Figure 3C**). While 7–10 DIV neurons increased ankyrinG levels after ADP treatment, 5 nM BPTU reduced ankyrinG levels (**Figure 3B**) to similar levels (75.21 ± 1.54%) than those observed in shP2Y1 neurons (77.07 ± 3.79%, **Figure 2E**, or 63.86 ± 4.95%, **Figure 3E**). No difference was observed between the ADP and BPTU vehicles, water and DMSO, respectively (**Figure 3B**). Moreover, BPTU treatment impaired the positive effect of ADP on ankyrinG (**Figure 3D**). Finally, we combined shP2Y1 with BPTU and again assessed ankyrinG. 10 DIV neurons expressing shP2Y1 had decreased ankyrinG expression (63.86 ± 4.95%), which was significantly reduced (49.38 ± 2.76%) by BPTU treatment in shP2Y1 neurons (**Figure 3E**). The fact that BPTU has an additive effect with P2Y1 suppression may be explained by the fact that still some P2Y1 receptors are available and BPTU is a potent P2Y1 inhibitor. shP2Y1 has an efficiency of 70% reducing P2Y1 expression in cell lines (del Puerto et al., 2012). On the

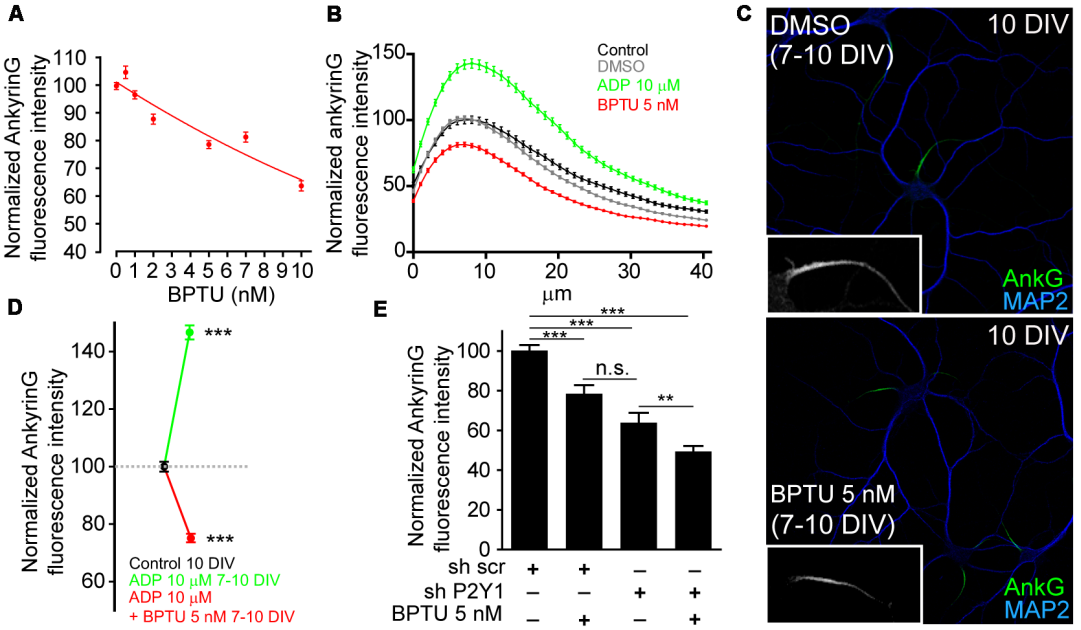

FIGURE 3 | P2Y1 pharmacological inhibition decreases ankyrinG accumulation at the AIS. **(A)** Normalized ankyrinG intensity on 10 DIV hippocampal neurons treated from 7 DIV with increasing concentrations of the P2Y1 antagonist, BPTU (0.5, 1, 2, 5, 7 and 10 nM). Concentrations higher than 10 nM affected the morphology of supporting glial cells and were discarded to avoid secondary effects on neurons. **(B)** AnkyrinG intensity profile along the AIS of hippocampal neurons treated from 7 to 10 DIV with vehicle black line), DMSO (BPTU vehicle, gray line), ADP (green line) and BPTU (red line). **(C)** 10 DIV neurons stained with MAP2 (blue) and ankyrinG antibodies (green) and treated with vehicle (control) or 5 nM BPTU from 7 to 10 DIV. Inserts show a magnification of the respective AIS. **(D)** Normalized ankyrinG intensity on 10 DIV hippocampal neurons treated from 7 DIV with 10 μM ADP and BPTU 5 nM, alone or in combination. **(E)** Normalized ankyrinG intensity on 10 DIV shscr or shP2Y1 nucleofected hippocampal neurons treated with BPTU from 7 DIV. Data were acquired from three independent experiments (at least 30 neurons/experimental condition in each experiment). $^{**}p < 0.01$, $^{***}p < 0.001$, n.s. not significant, two-tail *t*-test. Data in graphs are represented as the mean ± SEM.

other hand, it is the first time that BPTU is used in neurons. We can not discard that BPTU is partially affecting other purinergic receptors. However, BPTU impairs ADP-mediated increase of ankyrinG fluorescence. Therefore, our results suggest that P2Y1 activation is necessary to maintain ankyrinG levels at the AIS during the first stages of AIS development. This led to the question which are the mechanisms or developmental events that are under P2Y1 regulation that contribute to AIS proteins accumulation.

AnkyrinG and Dendrites or AIS Length do Not Correlate in Neurons Lacking P2Y1 Receptor

P2Y1 receptor is not detected at the AIS but is located in dendrites, distal axon and presynaptic terminals in cultured hippocampal neurons (del Puerto et al., 2012). We recently demonstrated that ankyrinG decrease at AIS was correlated with impaired dendrite development mediated by CB1R inhibition (Tapia et al., 2017) and previous studies demonstrated that P2Y1 modulate neuronal morphology during the initial stages of development (del Puerto et al., 2012). Dendrites start their development in cultured hippocampal neurons at 4 DIV (Dotti et al., 1988). In order to test whether P2Y1 may control dendrite development and also influence AIS development, we measured the cell-to-cell dendritic length and ankyrinG fluorescence intensity in 7 DIV shscr and shP2Y1 nucleofected neurons (**Figures 4A,B**). As happened when CB1 expression was reduced (Tapia et al., 2017), dendrites of 7 DIV shP2Y1 neurons were shorter (320.2 ± 14.1 μm) than in control neurons (397.1 ± 20.37 μm, **Figures 4C,E**). Moreover, ankyrinG expression at the AIS was also reduced by 20% (**Figures 4D,E**). Even though a similar percentage reduction of dendrites length and ankyrinG was observed (**Figure 4E**), we analyzed both parameters in each individual neuron (**Figure 4F**). While we found a significant correlation between dendritic arbor length and ankyrinG expression in sh scrambled control neurons (Spearman $r = 0.3037$, $p = 0.0055$), there was no significant correlation in shP2Y1 neurons (Spearman $r = -0.1522$, $p = 0.1955$).

On the other hand, the AIS is known to respond to stimulus or absence of stimulus with plasticity mechanisms that include changes in composition, length and position (Grubb and Burrone, 2010; Kuba et al., 2010; Del Puerto et al., 2015). Therefore, we analyzed AIS length in 7 and 14 DIV shscr and shP2Y1 neurons (**Figure 5**). No significant AIS length differences were found in 7 DIV shP2Y1 neurons (26.06 ± 1.03 μm) compared to control 7 DIV sh scrambled neurons (23.52 ± 0.97 μm), neither in AIS position or

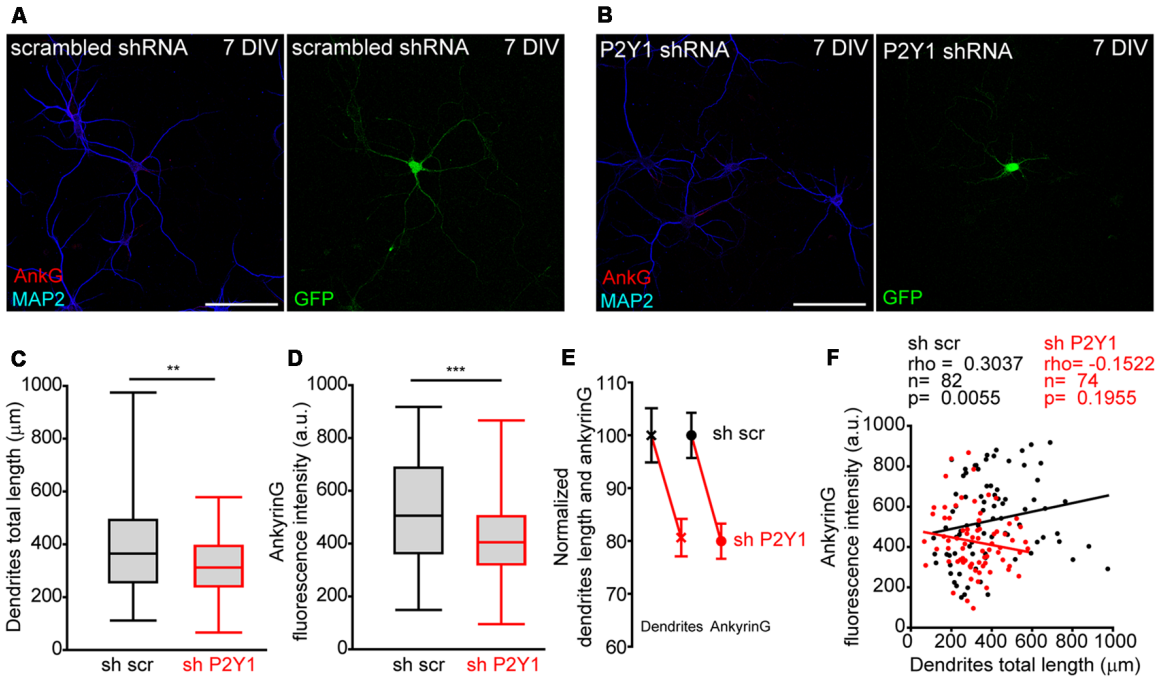

FIGURE 4 | No correlation between P2Y1 suppression-mediated decrease of dendrites length and ankyrinG density. **(A,B)** Representative images of 7 DIV hippocampal neurons nucleofected with scrambled or P2Y1 shRNAs. After nucleofection neurons were kept in culture for 7 DIV and stained with MAP2 (blue) and ankyrinG (red) antibodies. Nucleofected neurons were identified by GFP expression (green). **(C,D)** Box-plots represent total dendritic length **(C)** and ankyrinG intensity **(D)** of 7 DIV scrambled sh (sh scr) or shP2Y1 nuclefected neurons from the same pools in three different experiments. Line inside the box represents the median, and upper and bottom lines represent the maximum and minimum values. $^{**}p < 0.01$, $^{***}p < 0.001$, two-tail *t*-test. **(E)** Normalized mean ± SEM of dendrites length and ankyrinG intensity of data represented in **(C,D)**. **(F)** Correlation graph of dendrites length and ankyrinG intensity for each individual neuron analyzed in the study. Control neurons (shscr) are represented in black and neurons expressing P2Y1 interference RNA (shP2Y1) are in red. Data were analyzed first with two normality tests (Shapiro-Wilk and Kolmogorov-Smirnov). Not all data sets did fit a normal distribution and a non-parametric correlation test (Spearman) was performed. Regression lines are shown for shscr (black) and shP2Y1 (red) neurons. The number of neurons, Spearman *r* coefficient and *p* values are indicated in **(F)**. A positive correlation is observed in control neurons, while there is no significant correlation in neurons expressing shP2Y1 interference RNA.

maximum ankyrinG intensity position (**Figures 5A,B**). No significant change in AIS length was also obtained in 14 DIV neurons, being AIS length around 33 μm in sh scrambled and shP2Y1 neurons (**Figure 5E**). However, in 14 DIV neurons, P2Y1 suppression generated a significant proximal shift of ankyrinG maximum intensity of 2–3 μm (7.37 ± 0.41 μm vs. 9.58 ± 0.53 μm in sh scrambled neurons, **Figure 5I**), which can be observed in the mean profile of ankyrinG expression along the AIS (**Figure 5J**). Despite no AIS length mean changes were observed between scrambled sh and shP2Y1 neurons, there is variability of AIS length within each experimental group. Thus, we analyzed ankyrinG intensity within the AIS length of each neuron (**Figures 5C,F**). Our results show a significant reduction of the mean ratio ankyrinG/AIS length in shP2Y1 neurons at 7 DIV (around 30%, **Figure 5D**) and 14 DIV (around 10%, **Figure 5G**). Furthermore, we analyzed whether AIS length and ankyrinG intensity are correlated in 14 DIV scrambled sh and shP2Y1 neurons (**Figure 5H**). Both parameters were significantly correlated in control scrambled sh neurons, while no significant correlation was found in shP2Y1 neurons, demonstrating that ankyrinG intensity reduction in shP2Y1 neurons is not related to changes in AIS length. This data suggest that besides neuronal morphology regulation, P2Y1 receptor maintain other mechanisms to regulate AIS development.

P2X7 Inhibition Recovers AnkyrinG Expression

Our previous results showed that P2Y1 suppression produced a shorter axon, which was recovered by P2X7 inhibition with BBG (del Puerto et al., 2012). P2Y1-Gq and P2X7-mediated calcium entry are coordinated through AC5 activation (P2Y1) or inhibition (P2X7). This generates a cAMP balance that modulates the PI3K/Akt/GSK3 pathway. In addition, P2X7 modulate ankyrinG expression at the AIS through a calcium-calpain-dependent mechanism (Del Puerto et al., 2015). In order to test whether the same coordinated pathway is also related to AIS modulation, we treated neurons from 7 to 10 DIV with the adenylate cyclase inhibitor NKY80 (10 μM) and analyzed ankyrinG (**Figure 6A**). NKY80 significantly reduced ankyrinG expression by around 10%, suggesting a coordinated action of P2Y1 and P2X7. Next, 6 DIV sh scrambled and shP2Y1 neurons were treated for 24 h with BBG (100 nM), a well-characterized P2X7 inhibitor (**Figures 6B,D**). P2X7 inhibition resulted in a non-significant trend to increase ankyrinG fluorescence in sh scrambled neurons

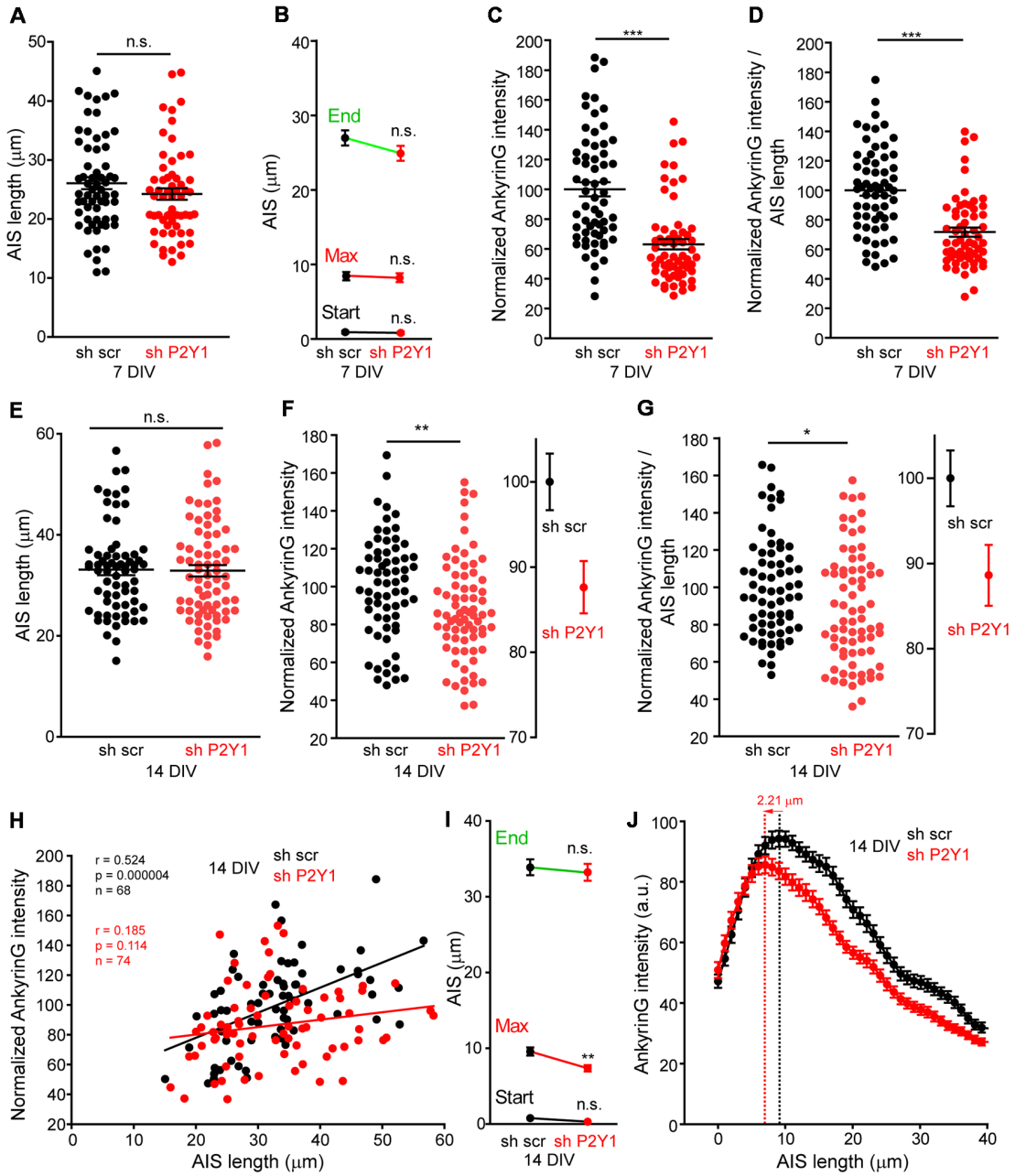

FIGURE 5 | No correlation between P2Y1 suppression-mediated decrease of ankyrinG density and AIS length. **(A)** Graph represents AIS length of each 7 DIV neuron nucleofected with scrambled sh (black dots) or shP2Y1 (red dots). Lines represent the mean ± SEM. **(B)** Graph represents the mean ± SEM of AIS start point, maximum intensity point and end point of AIS in 7 DIV scrambled shRNA or P2Y1 shRNA nucleofected neurons. **(C)** Normalized ankyrinG intensity within the respective AIS length of neurons represented in **(A)**. **(D)** Normalized AnkyrinG/AIS length ratio for each 7 DIV scrambled shRNA or P2Y1 shRNA nucleofected neuron. **(E)** Graph represents AIS length of each 14 DIV neuron nucleofected with scrambled sh (black dots) or shP2Y1 (red dots). Lines represent the mean ± SEM. **(F)** Normalized ankyrinG intensity within the respective AIS length of neurons represented in **(E)**. Adjacent graph represents the mean ± SEM. **(G)** Normalized AnkyrinG/AIS length ratio for each 14 DIV scrambled shRNA or P2Y1 shRNA nucleofected neuron. Adjacent graph represents the mean ± SEM. **(H)** Correlation graph of AIS length and ankyrinG intensity for each individual 14 DIV neuron nucleofected with scrambled (black dots) or P2Y1 (red dots) shRNAs. Values are the same represented in **(E,F)**. Data were analyzed first with two normality tests (Shapiro-Wilk and Kolmogorov-Smirnov). All data sets did fit a normal distribution and a Pearson correlation test was used. Regression lines are shown for shscr (black) and shP2Y1 (red) neurons. The number of neurons, Pearson *r* coefficient and *p* values are indicated in **(H)**. A positive correlation is observed in control neurons, while there is no significant correlation in neurons expressing shP2Y1 interference RNA. **(I)** Graph represents the mean ± SEM of AIS start point, maximum intensity point and end point of AIS in 14 DIV scrambled shRNA or P2Y1 shRNA nucleofected neurons. Note a significant proximal shift of the maximum intensity point. **(J)** AnkyrinG profile along AIS length of 14 DIV neurons, indicating the proximal shift of the maximum ankyrinG intensity. Data are represented as the mean ± SEM of ankyrinG intensity every 1 micron. $^{*}p < 0.05$, $^{**}p < 0.01$, $^{***}p < 0.001$, n.s., non-significant.

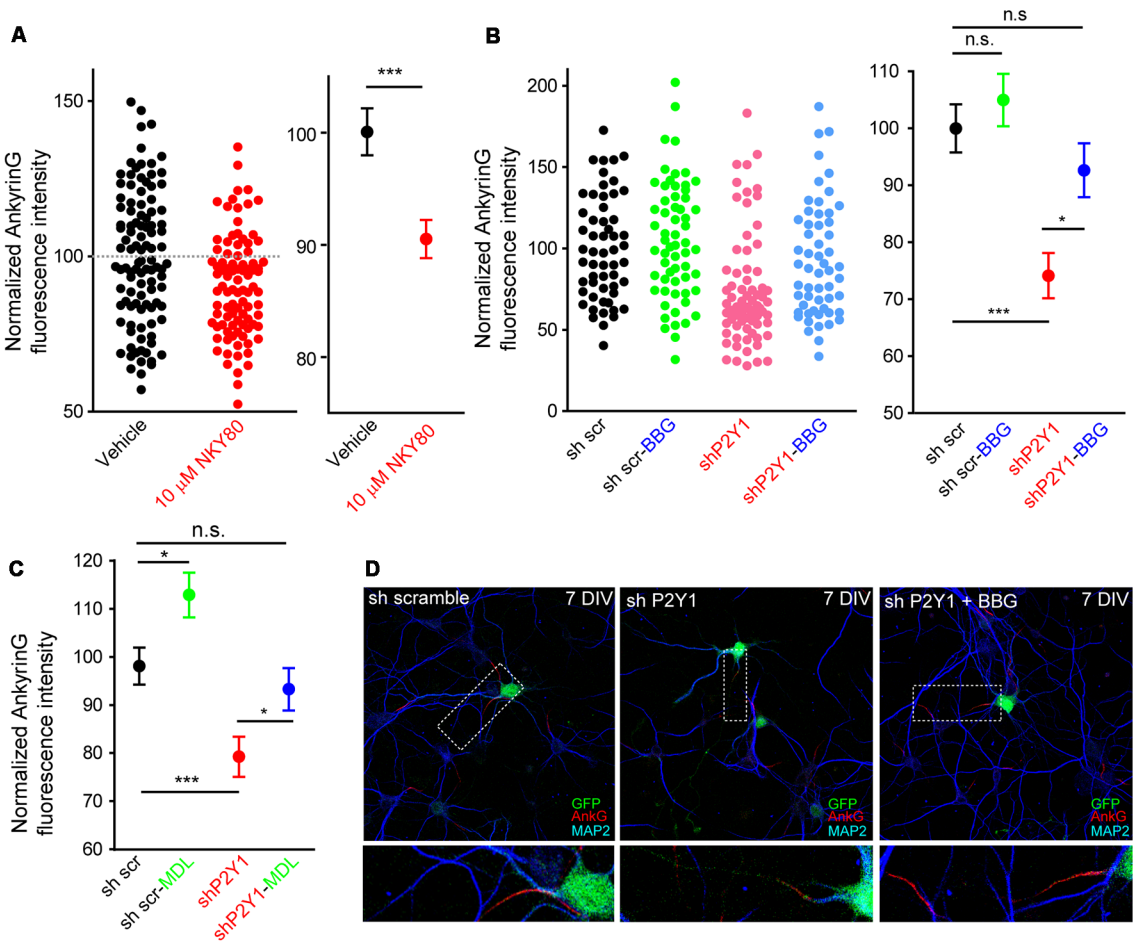

FIGURE 6 | P2X7 inhibition recovers ankyrinG density in shP2Y1 nucleofected neurons. **(A)** Scatter plot showing normalized ankyrinG intensity in 10 DIV control neurons or treated with the adenylate cyclase 5 (AC5) inhibitor NKY80 (10 μM) from 7 to 10 DIV. Mean ± SEM for each condition is shown in the adjacent graph. ***$p < 0.001$, n.s. no significant, two-tail *t*-test. **(B)** Scatter plot of normalized ankyrinG intensity in 7 DIV transfected with scrambled shRNA or P2Y1 shRNA and treated with the P2X7 antagonist, BBG (100 nM) from 6 to 7 DIV. Mean ± SEM for each condition is shown in the adjacent graph. Statistical differences were analyzed by a Kruskal-Wallis test followed by a Dunn's multiple comparisons post-test. *$p < 0.05$, ***$p < 0.001$, n.s., non-significant. **(C)** Mean ± SEM of normalized ankyrinG intensity in 7 DIV nucleofected with scrambled shRNA or P2Y1 shRNA and treated with the calpain inhibitor, MDL-28170 (50 nM) from 6 to 7 DIV. Statistical differences were analyzed by a Kruskal-Wallis test followed by a Dunn's multiple comparisons post-test. *$p < 0.05$, ***$p < 0.001$, n.s., non-significant. **(D)** Representative images of scrambled shRNA or P2Y1 shRNA treated with the P2X7 antagonist, BBG (100 nM). Neurons were stained with MAP2 (blue) and ankyrinG (red) antibodies. Nucleofected neurons were identified by GFP signal (green). Axon initials segments were magnified and presented in panels below.

(105.0 ± 4.59%), while P2Y1 suppression (shP2Y1 neurons) reduced ankyrinG fluoresecence around 25% (74.13 ± 3.98%). Interestingly, 24 h inhibition of P2X7 recovered ankyrinG intensity to control levels (92.7 ± 4.71%, **Figures 6B,D**). Further, 24 h treatment with the calpain inhibitor MDL-28170 (50 nM) recovered ankyrinG fluorescence (95.1 ± 4.49%) in shP2Y1 neurons (**Figure 6C**). This data suggests a coordinated and antagonistic action of P2Y1 and P2X7 receptors during initial stages of AIS development, which may depend on the amount of ATP and ADP in extracellular medium and their expression levels during AIS development. However, P2X7 inhibition did not completely recover ankyrinG intensity as previously observed in mature neurons (Del Puerto et al., 2015), suggesting that P2X7 participation is limited in young neurons. Thus, other AIS intrinsic mechanisms may be regulated by P2Y1 in AIS initial developmental stages.

P2Y1 Suppression Modifies AIS Actin Cytoskeleton and Myosin II Light Chain Phosphorylation

Recently, actin dynamics at the AIS were related to AIS plasticity (Berger et al., 2018). Activity-dependent AIS plasticity can produce a dramatic reorganization of the actin periodic structure (Berger et al., 2018) and P2Y1 signaling pathways can activate the RhoGTPase Rac, which modulates actin dynamics in migration and differentiation processes (Soulet et al., 2005). To understand whether our results can be attributable to actin cytoskeleton modifications mediated by

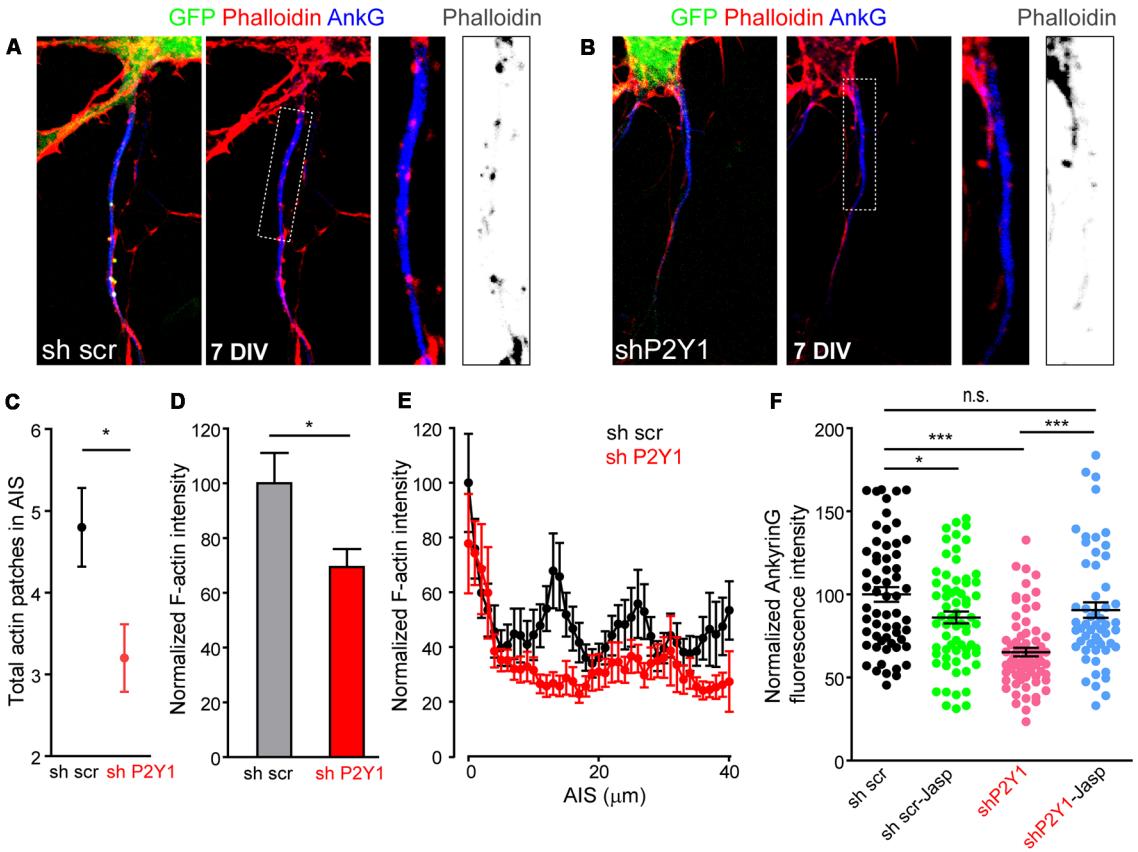

FIGURE 7 | P2Y1 suppression alters AIS F-actin. **(A,B)** Representative images of 7 DIV neurons nucleofected with scrambled **(A)** or P2Y1 **(B)** shRNAs. AISs were identified by ankyrinG staining (blue) and Phalloidin-Alexa594 served to identify F-actin (red). Nucleofected neurons were identified by their GFP expression (green). Panels show AIS region of the respective neurons and a 2.5× magnification of AIS. Gray scale images show phalloidin staining at the respective AISs. **(C)** Graph represents the mean ± SEM number of actin patches identified in scrambled (black, $n = 20$) and shP2Y1 (red, $n = 20$) AISs. *$p < 0.05$, two-tail t-test. **(D)** Total AIS F-actin intensity based on Phalloidin-Alexa 594 fluorescence intensity along ankyrinG signal in 7 DIV shscr and shP2Y1 neurons. *$p < 0.05$, two-tail t-test. **(E)** Plot profile of F-actin intensity along AIS in 7 DIV scrambled shRNA ($n = 24$, black) or P2Y1 shRNA ($n = 22$, red) neurons. Data are represented as the mean ± SEM of values every micron. **(F)** Scatter plot and mean ± SEM representing normalized ankyrinG intensity of each 7 DIV scrambled shRNA (sh scr) or P2Y1 shRNA (shP2Y1) nucleofected neuron, treated or not with the actin stabilizer jasplakinolide (10 nM) during 4 h prior to fixation. Statistical differences were analyzed by a Kruskal-Wallis test followed by a Dunn's multiple comparisons post-test. *$p < 0.05$, ***$p < 0.001$, n.s., non-significant.

P2Y1 receptor, we stained neurons 7 DIV scrambled sh and shP2Y1 neurons with fluorescence phalloidin (**Figures 7A,B**) and quantified F-actin intensity along the AIS, as well as the number of actin patches (**Figures 7C,D**). Total F-actin intensity was reduced by around 30% in shP2Y1 neurons (**Figure 7D**), and so was ankyrinG intensity (**Figure 7F**). Besides, the F-actin intensity decrease in the AIS was confirmed by the profile (**Figure 7E**). While actin patches were visible in control AISs, these were highly reduced in intensity and visibility in shP2Y1 neurons (**Figures 7A,B**). Actin patches quantification, independently of their intensity, showed that scrambled sh neurons contained 4.8 ± 0.48 actin patches, while shP2Y1 neurons only 3.2 ± 0.41 patches (**Figure 7C**). If loss of P2Y1-dependent stabilization of the actin cytoskeleton results in the decrease in ankyrinG, then it may be recovered by actin stabilization. Thus, we treated scrambled and shP2Y1 neurons with an F-actin stabilizing agent, Jasplakinolide (10 nM) for 4 h (**Figure 7F**). AnkyrinG expression in shP2Y1 neurons was significantly recovered by Jasplakinolide treatment (90.6 ± 4.7%) when compared to shP2Y1 neurons with no treatment (65.27 ± 2.59%, $p = 0.0002$). After recovery, the level was equivalent to sh scrambled control neurons (100 ± 4.36%). In control sh scrambled neurons, Jasplakinolide generated a decrease in ankyrinG expression (around 14%), which may be due to a deregulation of actin dynamics and higher actin stabilization.

How can actin cytoskeleton instability resulting from lack of P2Y1 activity modify ankyrinG in the AIS? Recently published work has highlighted the role of myosin II and myosin light chain phosphorylation (pMLC) on AIS (Evans et al., 2017; Berger et al., 2018). In platelets, ADP and P2Y1 activity contribute to shape changes by increasing pMLC levels in a calcium-calmodulin dependent manner (Paul et al., 1999). Therefore, we analyzed pMLC levels and localization in 7 DIV shP2Y1 neurons (**Figure 8A**). As previously demonstrated (Berger et al., 2018), pMLC was localized at the AIS in

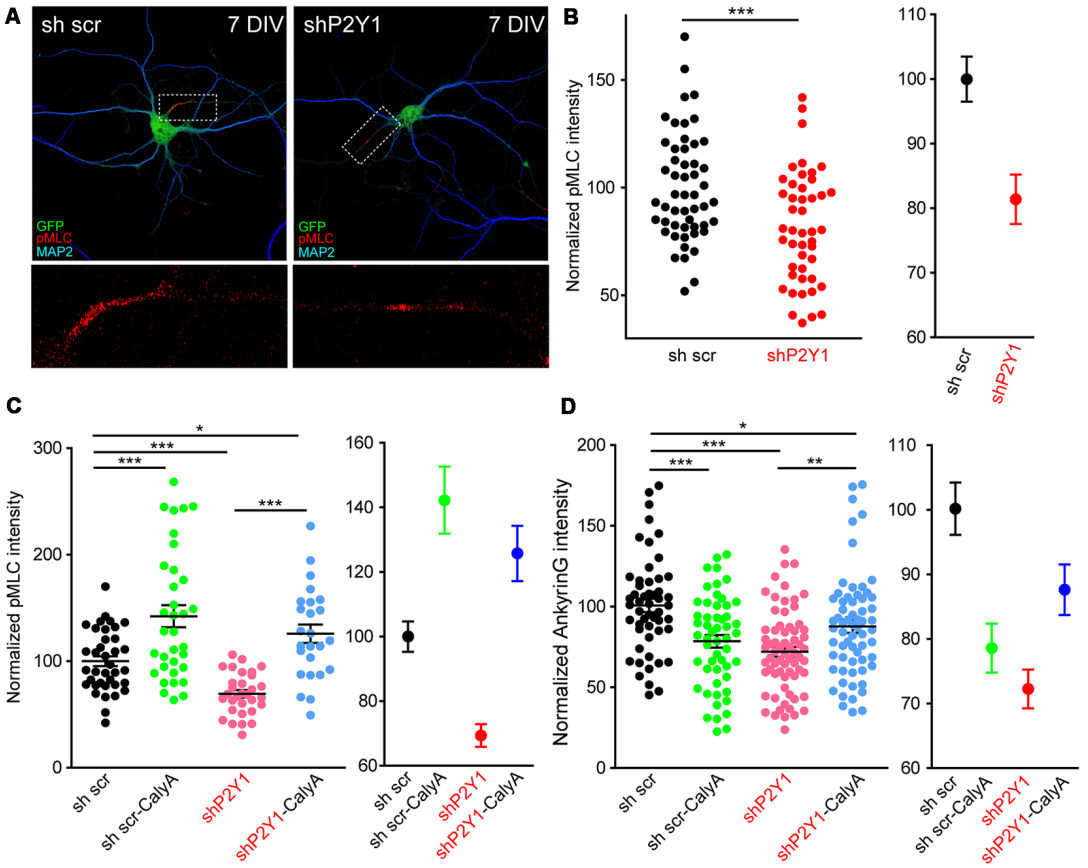

FIGURE 8 | P2Y1 is necessary to maintain myosin light chain (MLC) phosphorylation at the AIS. **(A)** Representative images of 7 DIV scrambled shRNA or P2Y1 shRNA nucleofected neurons showing phosphorylation of MLC (pMLC) staining in the AIS. Neurons were stained with MAP2 (blue) and pMLC (red) antibodies. Nucleofected neurons were identified by GFP signal (green). pMLC staining at axon initials segments was magnified and presented in panels below (red). **(B)** Scatter plot for each neuron (left) and mean ± SEM (right) representing normalized pMLC intensity at the AIS of 7 DIV neurons nucleofected with scrambled shRNA or P2Y1 shRNA. ***$p < 0.001$, two-tail *t*-test. **(C)** Scatter plot representing normalized pMLC intensity at the AIS of 7 DIV neurons nucleofected with scrambled shRNA or P2Y1 shRNA and treated with 1 nM calyculinA (CalyA) for 3 h before fixation. Mean ± SEM of these values is represented in the adjacent graph. **(D)** Scatter plot representing normalized ankyrinG intensity at the AIS of 7 DIV neurons nucleofected with scrambled shRNA or P2Y1 shRNA and treated with 1 nM calyculinA (CalyA) for 3 h before fixation. Mean ± SEM are represented in the adjacent graph. Statistical differences in **(C,D)** were analyzed by a Kruskal-Wallis test followed by a Dunn's multiple comparisons post-test. *$p < 0.05$, **$p < 0.01$, ***$p < 0.001$.

7 DIV control neurons. However, pMLC staining in the AIS was 20% lower in shP2Y1 neurons (**Figure 8B**). Next, we analyzed whether treating neurons with CalyculinA to inhibit PP1/PP2A, the phosphatases acting on pMLC, could recover pMLC levels and, consequently, ankyrinG. Calyculin A (1 nM) treatment for 3 h increased pMLC intensity at the AIS of control neurons by 40%, while in non-treated shP2Y1 neurons it was reduced by 31% (**Figure 8C**). Calyculin A treatment in shP2Y1 neurons increased pMLC intensity by 25% when compared to control neurons without Calyculin A treatment. AnkyrinG intensity analysis in the same experimental conditions revealed a recovery of ankyrinG in shP2Y1 neurons treated with Calyculin A (87.82 ± 4.01%) compared to shP2Y1 neurons (72.04 ± 3.08%), which did not completely reach reference control levels (100 ± 4.16%, **Figure 8D**). Interestingly, 3 h treatment of calyculin A in control neurons reduced ankyrinG intensity (78.5 ± 3.89%). This may suggest that increased pMLC levels are also detrimental to ankyrinG clustering at the AIS, as happened with F-actin stabilization with jasplakinolide (**Figure 7F**).

Altogether, our results underscore the role of P2Y1 as one of the receptors that contribute to AIS plasticity during early events of AIS maturation. Further investigations are required to completely understand the signaling pathway and interactions with other receptors and neurotransmitters.

DISCUSSION

Relevant studies have recently underscored the importance of AIS in neurodevelopmental disorders and neurodegenerative diseases (Kaphzan et al., 2011; Sun et al., 2014; van der Werf et al., 2017). Changes in AIS protein composition have been detected in models of disease, such as Angelman syndrome or

Alzheimer's disease (Kaphzan et al., 2011; Sun et al., 2014). However, our understanding of AIS composition, development and regulation is still limited. Which are the extrinsic and intrinsic mechanisms that modulate the AIS? The AIS has been proven to respond to external stimuli with a high degree of structural plasticity. However, our knowledge of the receptors, neurotransmitters and extracellular factors that modulate AIS remains limited. Understanding how the AIS can be deregulated may contribute to control and recover physiological neuronal function.

Prior studies demonstrated that the purinergic receptor P2X7 modulates AIS composition under pathological conditions (Del Puerto et al., 2015). Due to its relation with the P2Y1 receptor, the objective of our study was to decipher whether the purinergic receptor P2Y1 plays a role in AIS development and maintenance. Our results show that ADP-P2Y1 receptor contributes to the initial accumulation of ankyrinG at the AIS. P2Y1 suppression or inhibition decreases ankyrinG levels, as well as, voltage-gated sodium channels, βIV-spectrin and pMLC. P2Y1 is necessary for a proper elongation of the axon in early stages and is expressed in dendrites and axon terminals in cultured hippocampal neurons (del Puerto et al., 2012). P2Y1 expression is not detected in AIS, as previously mentioned for P2X7 (Del Puerto et al., 2015). Previous studies demonstrated a correlation between dendrites length or caliber and AIS properties (Hamada et al., 2016; Tapia et al., 2017). Our results show that, in control neurons, dendrites length and ankyrinG density is correlated, albeit there is no statistical correlation between both parameters after P2Y1 suppression. This suggests that P2Y1-mediated ankyrinG density regulation entails additional mechanisms triggered by P2Y1 alone or in coordination with other receptors. In fact, ankyrinG levels can be recovered through ATP-P2X7 receptor inhibition in neurons lacking P2Y1 receptor. A previous study demonstrated that high extracellular concentrations of ATP decrease ankyrinG density through P2X7 and calpain activation in mature cultured hippocampal neurons (Del Puerto et al., 2015). Here, we show that extracellular ADP or P2Y1 inhibition do not modify ankyrinG density in these mature neurons. However, through P2Y1 receptor, ADP is necessary to maintain ankyrinG density in young cultured hippocampal neurons. The P2Y1 regulation coincides with the initial stages of AIS development, between 4 and 10 DIV, when the diffusion barrier is being generated (Brachet et al., 2010) and is lost once the AIS achieve a certain degree of maturity and stability, around 10–14 DIV. In fact, P2Y1 suppression or ADP treatment after 7 DIV has no effect on ankyrinG density, while P2Y1 inactivation at 7 DIV or before decreases ankyrinG density. As happened during early axonal elongation (del Puerto et al., 2012), BBG-mediated P2X7 inhibition reverts the effects of P2Y1 suppression on ankyrinG density. However, P2X7 inhibition mediated recovery was not as high as previously observed in mature neurons (Del Puerto et al., 2015), suggesting that P2Y1 receptors decrease their expression or function during AIS development, while the importance of P2X7 increases. This recovery can be the result of decreased P2X7-mediated calcium entry and reduced calpain activation, but other mechanisms may also participate in this regulation. P2Y1 and P2X7 receptors are important regulators of neuronal excitability. P2Y1 receptors are expressed postsynaptically on dendrites of pyramidal cells and presynaptic terminals and participate in the regulation of neuronal plasticity (Barańska et al., 2017). Interestingly, P2X7 and P2Y1 are balanced over the regulation of cAMP and PKA activity, where P2Y1 contributes to increased cAMP levels (del Puerto et al., 2012). It was postulated that a PKA and phosphatases PP1 and calcineurin loop may regulate sodium channels phosphorylation modulating spike firing that correlates with AIS length in dentate granule cells (DGCs). In this study (Evans et al., 2015), PKA activation did not modify AIS length but did reverse the depolarization-induced changes in sodium channels properties, increasing their phosphorylation and decreasing conductance. Our results show P2Y1 inhibition or suppression does not alter AIS length, but rather proximally shifts the maximum ankyrinG intensity while decreasing ankyrinG density. It remains to be determined whether this shift is due to PKA activity levels or modifications of sodium channels conductance. Nevertheless, our results show that PP1/PP2A inhibition with calyculin A is able to counteract the lack of P2Y1 expression, which may balance PKA-phosphatases loop. On the other hand, P2Y1 may participate in AIS modulation through regulation of its actin cytoskeleton. In support, P2Y1 regulates Rac and actin cytoskeleton in other cell types (Soulet et al., 2005). We show that F-actin distribution and intensity in AIS is modified after P2Y1 suppression, and actin cytoskeleton stabilization with jasplakinolide recovers ankyrinG density. In fact, short-time treatment with potassium chloride decreases ankyrinG density at the AIS while at the same time actin is destabilized (Berger et al., 2018). This may be caused by decreased phosphorylation of myosin II light chain (pMLC) at the AIS (Berger et al., 2018). Our results demonstrate that P2Y1 suppression decreases pMLC levels at the AIS at the same time that ankyrinG density is reduced in a similar percentage. The lack of P2Y1 receptor is compensated by inhibition of MLC phosphatase using calyculin A. Interestingly, P2Y1 agonist, 2MeSADP, increases pMLC phosphorylation in platelets generating a shape change (Getz et al., 2010), through a Gq dependent mechanism. All these data suggest that P2Y1 receptor participate in the global regulation of AIS cytoskeleton dynamics during its initial development.

CONCLUSION

In conclusion, our work demonstrates that P2Y1 receptor participates only during initial AIS development. This may represent decreased expression or function during neuronal maturation, while other receptors, such as P2X7, increase their participation and function in more mature neurons. P2Y1 expression levels or functional activation/deactivation in coordination with other receptors and mechanisms may participate in the fine modulation of AIS development. Future work will be necessary to completely understand the molecular mechanisms underlying P2Y1 receptor; both at the level of plasticity and the modulation of AIS cytoskeleton.

DATA AVAILABILITY

All datasets generated for this study are included in the manuscript.

ETHICS STATEMENT

Animals were housed in a room at controlled temperature and relative humidity with alternating 12 h light and dark cycles and free access to food and water "*ad libitum*." Animal care protocols used in our laboratory are in conformity with the appropriate national legislation (53/2013, BOE no. 1337) and guidelines of the Council of the European Communities (2010/63/UE). All protocols were previously approved by the CSIC bioethics committee.

AUTHOR CONTRIBUTIONS

JG, WZ and AB conceived and designed the experiments. JG, WZ, AB, MC and MB performed the experiments and data acquisition. JG and WZ analyzed and interpreted the data. JG wrote the manuscript. AB, MB and MC contributed to acquiring and analyzing data. All authors read and approved the final manuscript.

FUNDING

This work was supported by a research grant from Ministerio de Economía, Industria y Competitividad, Gobierno de España (MINECO) to JG (SAF2015-65315-R). We thank the China Scholarship Council for their support to WZ (fellowship number (No. 201506300085) and the support of the Erasmus+ Program and University of Trento for AB.

ACKNOWLEDGMENTS

We thank Dr Chaska Walton for critical reading of the manuscript, Cajal institute imaging service for their help in confocal images acquisition.

REFERENCES

Balasanyan, V., Watanabe, K., Dempsey, W. P., Lewis, T. L. Jr., Trinh, L. A., and Arnold, D. B. (2017). Structure and function of an actin-based filter in the proximal axon. *Cell Rep.* 21, 2696–2705. doi: 10.1016/j.celrep.2017.11.046

Barańska, J., Czajkowski, R., and Pomorski, P. (2017). P2Y1 receptors—properties and functional activities. *Adv. Exp. Med. Biol.* 1051, 71–89. doi: 10.1007/5584_2017_57

Bas Orth, C., Schultz, C., Müller, C. M., Frotscher, M., and Deller, T. (2007). Loss of the cisternal organelle in the axon initial segment of cortical neurons in synaptopodin-deficient mice. *J. Comp. Neurol.* 504, 441–449. doi: 10.1002/cne.21445

Bender, K. J., Ford, C. P., and Trussell, L. O. (2010). Dopaminergic modulation of axon initial segment calcium channels regulates action potential initiation. *Neuron* 68, 500–511. doi: 10.1016/j.neuron.2010.09.026

Benedeczky, I., Molnar, E., and Somogyi, P. (1994). The cisternal organelle as a Ca^{2+}-storing compartment associated with GABAergic synapses in the axon initial segment of hippocampal pyramidal neurones. *Exp. Brain Res.* 101, 216–230. doi: 10.1007/bf00228742

Berger, S. L., Leo-Macias, A., Yuen, S., Khatri, L., Pfennig, S., Zhang, Y., et al. (2018). Localized myosin II activity regulates assembly and plasticity of the axon initial segment. *Neuron* 97, 555.e6–570.e6. doi: 10.1016/j.neuron.2017.12.039

Brachet, A., Leterrier, C., Irondelle, M., Fache, M. P., Racine, V., Sibarita, J. B., et al. (2010). Ankyrin G restricts ion channel diffusion at the axonal initial segment before the establishment of the diffusion barrier. *J. Cell Biol.* 191, 383–395. doi: 10.1083/jcb.201003042

Burnstock, G. (2007). Purine and pyrimidine receptors. *Cell. Mol. Life Sci.* 64, 1471–1483. doi: 10.1007/s00018-007-6497-0

Burnstock, G. (2017). Purinergic signalling and neurological diseases: an update. *CNS Neurol Disord Drug Targets* 16, 257–265. doi: 10.2174/1871527315666160922104848

Clarkson, R. L., Liptak, A. T., Gee, S. M., Sohal, V. S., and Bender, K. J. (2017). D3 receptors regulate excitability in a unique class of prefrontal pyramidal cells. *J. Neurosci.* 37, 5846–5860. doi: 10.1523/JNEUROSCI.0310-17.2017

del Puerto, A., Díaz-Hernández, J. I., Tapia, M., Gomez-Villafuertes, R., Benitez, M. J., Zhang, J., et al. (2012). Adenylate cyclase 5 coordinates the action of ADP, P2Y1, P2Y13 and ATP-gated P2X7 receptors on axonal elongation. *J. Cell Sci.* 125, 176–188. doi: 10.1242/jcs.091736

Del Puerto, A., Fronzaroli-Molinieres, L., Perez-Alvarez, M. J., Giraud, P., Carlier, E., Wandosell, F., et al. (2015). ATP-P2X7 receptor modulates axon initial segment composition and function in physiological conditions and brain injury. *Cereb. Cortex* 25, 2282–2294. doi: 10.1093/cercor/bhu035

Del Puerto, A., Wandosell, F., and Garrido, J. J. (2013). Neuronal and glial purinergic receptors functions in neuron development and brain disease. *Front. Cell. Neurosci.* 7:197. doi: 10.3389/fncel.2013.00197

Dotti, C. G., Sullivan, C. A., and Banker, G. A. (1988). The establishment of polarity by hippocampal neurons in culture. *J. Neurosci.* 8, 1454–1468. doi: 10.1523/JNEUROSCI.08-04-01454.1988

Evans, M. D., Dumitrescu, A. S., Kruijssen, D. L. H., Taylor, S. E., and Grubb, M. S. (2015). Rapid modulation of axon initial segment length influences repetitive spike firing. *Cell Rep.* 13, 1233–1245. doi: 10.1016/j.celrep.2015.09.066

Evans, M. D., Tufo, C., Dumitrescu, A. S., and Grubb, M. S. (2017). Myosin II activity is required for structural plasticity at the axon initial segment. *Eur. J. Neurosci.* 46, 1751–1757. doi: 10.1111/ejn.13597

Garrido, J. J., Giraud, P., Carlier, E., Fernandes, F., Moussif, A., Fache, M. P., et al. (2003). A targeting motif involved in sodium channel clustering at the axonal initial segment. *Science* 300, 2091–2094. doi: 10.1126/science.1085167

Getz, T. M., Dangelmaier, C. A., Jin, J., Daniel, J. L., and Kunapuli, S. P. (2010). Differential phosphorylation of myosin light chain (Thr)18 and (Ser)19 and functional implications in platelets. *J. Thromb. Haemost.* 8, 2283–2293. doi: 10.1111/j.1538-7836.2010.04000.x

Grubb, M. S., and Burrone, J. (2010). Activity-dependent relocation of the axon initial segment fine-tunes neuronal excitability. *Nature* 465, 1070–1074. doi: 10.1038/nature09160

Grubb, M. S., Shu, Y., Kuba, H., Rasband, M. N., Wimmer, V. C., and Bender, K. J. (2011). Short- and long-term plasticity at the axon initial segment. *J. Neurosci.* 31, 16049–16055. doi: 10.1523/JNEUROSCI.4064-11.2011

Hamada, M. S., Goethals, S., de Vries, S. I., Brette, R., and Kole, M. H. (2016). Covariation of axon initial segment location and dendritic tree normalizes the somatic action potential. *Proc. Natl. Acad. Sci. U S A* 113, 14841–14846. doi: 10.1073/pnas.1607548113

Hedstrom, K. L., Xu, X., Ogawa, Y., Frischknecht, R., Seidenbecher, C. I., Shrager, P., et al. (2007). Neurofascin assembles a specialized extracellular matrix at the axon initial segment. *J. Cell Biol.* 178, 875–886. doi: 10.1083/jcb.200705119

Janssen, A. F. J., Tas, R. P., van Bergeijk, P., Oost, R., Hoogenraad, C. C., and Kapitein, L. C. (2017). Myosin-V induces cargo immobilization and clustering at the axon initial segment. *Front. Cell. Neurosci.* 11:260. doi: 10.3389/fncel.2017.00260

Jenkins, S. M., and Bennett, V. (2001). Ankyrin-G coordinates assembly of the spectrin-based membrane skeleton, voltage-gated sodium channels, and L1 CAMs at Purkinje neuron initial segments. *J. Cell Biol.* 155, 739–746. doi: 10.1083/jcb.200109026

Kaphzan, H., Buffington, S. A., Jung, J. I., Rasband, M. N., and Klann, E. (2011). Alterations in intrinsic membrane properties and the axon initial segment in a mouse model of Angelman syndrome. *J. Neurosci.* 31, 17637–17648. doi: 10.1523/JNEUROSCI.4162-11.2011

Ko, K. W., Rasband, M. N., Meseguer, V., Kramer, R. H., and Golding, N. L. (2016). Serotonin modulates spike probability in the axon initial segment through HCN channels. *Nat. Neurosci.* 19, 826–834. doi: 10.1038/nn.4293

Kole, M. H., Ilschner, S. U., Kampa, B. M., Williams, S. R., Ruben, P. C., and Stuart, G. J. (2008). Action potential generation requires a high sodium channel density in the axon initial segment. *Nat. Neurosci.* 11, 178–186. doi: 10.1038/nn2040

Komada, M., and Soriano, P. (2002). βIV-spectrin regulates sodium channel clustering through ankyrin-G at axon initial segments and nodes of Ranvier. *J. Cell Biol.* 156, 337–348. doi: 10.1083/jcb.200110003

Konishi, Y., and Setou, M. (2009). Tubulin tyrosination navigates the kinesin-1 motor domain to axons. *Nat. Neurosci.* 12, 559–567. doi: 10.1038/nn.2314

Kuba, H., Oichi, Y., and Ohmori, H. (2010). Presynaptic activity regulates Na^+ channel distribution at the axon initial segment. *Nature* 465, 1075–1078. doi: 10.1038/nature09087

Kuba, H., Yamada, R., Ishiguro, G., and Adachi, R. (2015). Redistribution of Kv1 and Kv7 enhances neuronal excitability during structural axon initial segment plasticity. *Nat. Commun.* 6:8815. doi: 10.1038/ncomms9815

Leterrier, C. (2018). The axon initial segment: an updated viewpoint. *J. Neurosci.* 38, 2135–2145. doi: 10.1523/JNEUROSCI.1922-17.2018

Leterrier, C., Potier, J., Caillol, G., Debarnot, C., Rueda Boroni, F., and Dargent, B. (2015). Nanoscale architecture of the axon initial segment reveals an organized and robust scaffold. *Cell Rep.* 13, 2781–2793. doi: 10.1016/j.celrep.2015.11.051

Mañé, N., Jiménez-Sábado, V., and Jiménez, M. (2016). BPTU, an allosteric antagonist of P2Y1 receptor, blocks nerve mediated inhibitory neuromuscular responses in the gastrointestinal tract of rodents. *Neuropharmacology* 110, 376–385. doi: 10.1016/j.neuropharm.2016.07.033

Ogawa, Y., Horresh, I., Trimmer, J. S., Bredt, D. S., Peles, E., and Rasband, M. N. (2008). Postsynaptic density-93 clusters Kv1 channels at axon initial segments independently of Caspr2. *J. Neurosci.* 28, 5731–5739. doi: 10.1523/JNEUROSCI.4431-07.2008

Ogawa, Y., Oses-Prieto, J., Kim, M. Y., Horresh, I., Peles, E., Burlingame, A. L., et al. (2010). ADAM22, a Kv1 channel-interacting protein, recruits membrane-associated guanylate kinases to juxtaparanodes of myelinated axons. *J. Neurosci.* 30, 1038–1048. doi: 10.1523/JNEUROSCI.4661-09.2010

Pan, Z., Kao, T., Horvath, Z., Lemos, J., Sul, J. Y., Cranstoun, S. D., et al. (2006). A common ankyrin-G-based mechanism retains KCNQ and NaV channels at electrically active domains of the axon. *J. Neurosci.* 26, 2599–2613. doi: 10.1523/JNEUROSCI.4314-05.2006

Paul, B. Z., Daniel, J. L., and Kunapuli, S. P. (1999). Platelet shape change is mediated by both calcium-dependent and -independent signaling pathways. Role of p160 Rho-associated coiled-coil-containing protein kinase in platelet shape change. *J. Biol. Chem.* 274, 28293–28300. doi: 10.1074/jbc.274.40.28293

Rasband, M. N. (2010). The axon initial segment and the maintenance of neuronal polarity. *Nat. Rev. Neurosci.* 11, 552–562. doi: 10.1038/nrn2852

Sánchez-Ponce, D., Blázquez-Llorca, L., DeFelipe, J., Garrido, J. J., and Muñoz, A. (2012). Colocalization of α-actinin and synaptopodin in the pyramidal cell axon initial segment. *Cereb. Cortex* 22, 1648–1661. doi: 10.1093/cercor/bhr251

Schafer, D. P., Jha, S., Liu, F., Akella, T., McCullough, L. D., and Rasband, M. N. (2009). Disruption of the axon initial segment cytoskeleton is a new mechanism for neuronal injury. *J. Neurosci.* 29, 13242–13254. doi: 10.1523/JNEUROSCI.3376-09.2009

Schlüter, A., Del Turco, D., Deller, T., Gutzmann, A., Schultz, C., and Engelhardt, M. (2017). Structural plasticity of synaptopodin in the axon initial segment during visual cortex development. *Cereb. Cortex* 27, 4662–4675. doi: 10.1093/cercor/bhx208

Seagar, M., Russier, M., Caillard, O., Maulet, Y., Fronzaroli-Molinieres, L., De San Feliciano, M., et al. (2017). LGI1 tunes intrinsic excitability by regulating the density of axonal Kv1 channels. *Proc. Natl. Acad. Sci. U S A* 114, 7719–7724. doi: 10.1073/pnas.1618656114

Soulet, C., Hechler, B., Gratacap, M. P., Plantavid, M., Offermanns, S., Gachet, C., et al. (2005). A differential role of the platelet ADP receptors P2Y1 and P2Y12 in Rac activation. *J. Thromb. Haemost.* 3, 2296–2306. doi: 10.1111/j.1538-7836.2005.01588.x

Stuart, G., Schiller, J., and Sakmann, B. (1997). Action potential initiation and propagation in rat neocortical pyramidal neurons. *J. Physiol.* 505, 617–632. doi: 10.1111/j.1469-7793.1997.617ba.x

Sun, X., Wu, Y., Gu, M., Liu, Z., Ma, Y., Li, J., et al. (2014). Selective filtering defect at the axon initial segment in Alzheimer's disease mouse models. *Proc. Natl. Acad. Sci. U S A* 111, 14271–14276. doi: 10.1073/pnas.1411837111

Tapia, M., Dominguez, A., Zhang, W., Del Puerto, A., Ciorraga, M., Benitez, M. J., et al. (2017). Cannabinoid receptors modulate neuronal morphology and ankyring density at the axon initial segment. *Front. Cell. Neurosci.* 11:5. doi: 10.3389/fncel.2017.00005

Tapia, M., Wandosell, F., and Garrido, J. J. (2010). Impaired function of HDAC6 slows down axonal growth and interferes with axon initial segment development. *PLoS One* 5:e12908. doi: 10.1371/journal.pone.0012908

van der Werf, I. M., van Dam, D., Missault, S., Yalcin, B., De Deyn, P. P., Vandeweyer, G., et al. (2017). Behavioural characterization of AnkyrinG deficient mice, a model for ANK3 related disorders. *Behav. Brain Res.* 328, 218–226. doi: 10.1016/j.bbr.2017.04.014

Watanabe, K., Al-Bassam, S., Miyazaki, Y., Wandless, T. J., Webster, P., and Arnold, D. B. (2012). Networks of polarized actin filaments in the axon initial segment provide a mechanism for sorting axonal and dendritic proteins. *Cell Rep.* 2, 1546–1553. doi: 10.1016/j.celrep.2012.11.015

Yin, L., Rasch, M. J., He, Q., Wu, S., Dou, F., and Shu, Y. (2017). Selective modulation of axonal sodium channel subtypes by $5\text{-}HT_{1A}$ receptor in cortical pyramidal neuron. *Cereb. Cortex* 27, 509–521. doi: 10.1093/cercor/bhv245

Zhu, S., Cordner, Z. A., Xiong, J., Chiu, C. T., Artola, A., Zuo, Y., et al. (2017). Genetic disruption of ankyrin-G in adult mouse forebrain causes cortical synapse alteration and behavior reminiscent of bipolar disorder. *Proc. Natl. Acad. Sci. U S A* 114, 10479–10484. doi: 10.1073/pnas.1700689114

Conflict of Interest Statement: The authors declare that the research was conducted in the absence of any commercial or financial relationships that could be construed as a potential conflict of interest.

SCIENTIFIC REPORTS

OPEN

Primary neurons can enter M-phase

Chaska C. Walton, Wei Zhang, Iris Patiño-Parrado, Estíbaliz Barrio-Alonso, Juan-José Garrido & José M. Frade

Received: 11 September 2018
Accepted: 14 February 2019
Published online: 14 March 2019

Differentiated neurons can undergo cell cycle re-entry during pathological conditions, but it remains largely accepted that M-phase is prohibited in these cells. Here we show that primary neurons at post-synaptogenesis stages of development can enter M-phase. We induced cell cycle re-entry by overexpressing a truncated Cyclin E isoform fused to Cdk2. Cyclin E/Cdk2 expression elicits canonical cell cycle checkpoints, which arrest cell cycle progression and trigger apoptosis. As in mitotic cells, checkpoint abrogation enables cell cycle progression through S and G2-phases into M-phase. Although most neurons enter M-phase, only a small subset undergo cell division. Alternatively, neurons can exit M-phase without cell division and recover the axon initial segment, a structural determinant of neuronal viability. We conclude that neurons and mitotic cells share S, G2 and M-phase regulation.

Neurons that are not fully differentiated can enter M-phase and undergo cell division[1–6], and they may keep dividing even after full differentiation[7–9]. In contrast, in the absence of dedifferentiation[10], fully differentiated neurons do not undergo M-phase entry and cell division upon acute induction of cell cycle re-entry[1,11–14]. In pathologies such as Alzheimer's disease (AD), Parkinson's disease (PD), amyotrophic lateral sclerosis (AML) or brain injury, neuronal cell cycle re-entry is associated to increased susceptibility to cell death instead of cell division[15,16]. This observation has led to suggest that M-phase entry is prohibited in neurons[16], and that the cell cycle machinery becomes pro-apoptotic in these cells[17]. However, the neuron-specific mechanisms that block M-phase entry remain unidentified. Furthermore, whether M-phase entry is irreversibly prohibited remains to be determined as well.

The block on M-phase entry could be explained by the presence of canonical cell cycle checkpoints. In mitotic cells, non-physiological cell cycle re-entry activates checkpoints that arrest the cell cycle[18–20] and can result in cell death to prevent potentially cancerous cell division[18,21]. Cell cycle checkpoint abrogation in mitotic cells can prevent cell death, and enable M-phase entry and cell division[18,19,22]. This suggests that, by abrogating cell cycle checkpoint activity, neuronal M-phase entry and cell division in neurons that undergo cell cycle re-entry should be possible. This possibility remains untested.

To study whether cell cycle checkpoints regulate cell cycle progression in neurons as in mitotic cells, we induced neuronal cell cycle re-entry with a low molecular weight (LMW) Cyclin E isoform (Cyclin ET1), which shows higher oncogenic potential when compared to full length Cyclin E[23], fused to Cdk2 (t1EK2). This fusion protein is similar to a Cyclin E/Cdk2 chimeric protein previously shown to be active[24]. t1EK2 overexpression was coupled with genetic and pharmacological checkpoint signaling abrogation. We assessed cell cycle progression through each of its phases. We show that the regulation of S, G2 and M phases in neurons is as in standard mitotic cells. Neurons readily enter M-phase and a small subset can undergo cell division. We also assessed the integrity of the axon initial segment (AIS) after M-phase exit without cell division in multinucleated neurons. We show that multinucleated neurons recover the AIS, indicating that aberrant cell cycle re-entry is not necessarily fatal.

Results

t1EK2 induces DNA synthesis in differentiated neurons. Cyclin E is the canonical late G1 cyclin that triggers transition into S-phase by activating Cyclin-dependent kinase 2 (Cdk2)[25] and is necessary for cell cycle re-entry from quiescence[26]. Strikingly, Cyclin E is highly expressed in neurons under physiological conditions[27], and Cyclin E upregulation is associated to aberrant neuronal cell cycle re-entry[14,28–34] and in AD[35,36]. Under physiological conditions, Cyclin E forms catalytically inactive complexes with Cdk5 to promote synapse maturation[27]. However, Cdk5 deregulation is associated to neuron diseases[37]. To avoid interfering with endogenous Cdk5 signaling by off target binding of Cyclin ET1 to Cdk5, we generated a t1EK2 fusion product and used it to induce neuronal cell cycle re-entry.

t1EK2 or control LacZ were co-lipofected with red fluorescent protein (RFP) in hippocampal cultures maintained for 15 days *in vitro* (DIV), a stage in which dendritic spines and synapses have already been developed and neurons are electrophysiologically active[38,39]. Transfected neurons were identified by MAP2-specific

Department of Molecular, Cellular and Developmental Neurobiology, Cajal Institute (CSIC), Madrid, 28002, Spain. Correspondence and requests for materials should be addressed to J.M.F. (email: frade@cajal.csic.es)

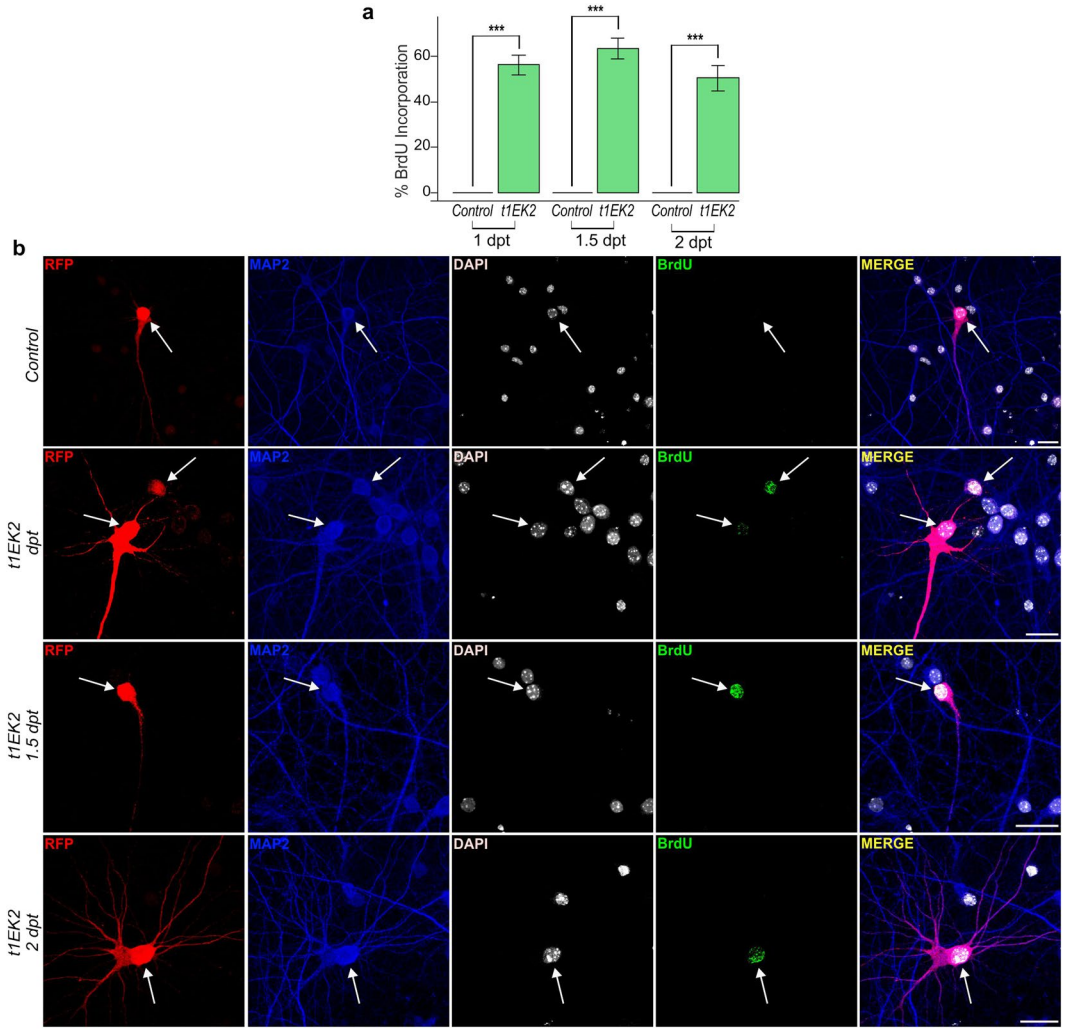

Figure 1. t1EK2 induces DNA synthesis in differentiated neurons. (**a**) Percentage of BrdU positive neurons expressing LacZ (Control) or t1EK2 at 1 (Control: n = 129; t1EK2: n = 153), 1.5 (Control: n = 201; t1EK2: n = 129), and 2 (Control: n = 161; t1EK2: n = 94) dpt (16–17 DIV). Control neurons never incorporate BrdU. Three independent experiments for each dpt were carried out. As control neurons never incorporated BrdU, statistical analysis was performed by comparing percent BrdU incorporation in t1EK2-expressing neurons with zero (***$p < 0.001$; one-tailed *t* test for each dpt). BrdU incorporation could not be assessed at 3 dpt due to widespread neuronal death of t1EK2-expressing neurons. (**b**) Representative confocal images of BrdU incorporation in a LacZ control neuron (1 dpt) and t1EK2-expressing neurons at 1, 1.5 and 2 dpt. Graphs represent mean ± s.e.m. Scale bar: 25 µm.

labeling in RFP-positive cells. We studied cell cycle S-phase entry by assessing 5-bromo-2′-deoxyuridine (BrdU) incorporation 1, 1.5, and 2 days post-transfection (dpt). Transfected control neurons never incorporated BrdU (n = 491) (Fig. 1a,b), confirming that neurons in primary culture at these stages of maturation do not spontaneously re-enter the cell cycle. In contrast, t1EK2 induced DNA synthesis in neurons (Fig. 1a,b). At 1 dpt, 52.3% t1EK2-expressing neurons incorporated BrdU ($t_{152} = 12.906$, $p < 0.001$). This increased at 1.5 dpt to 58.9% ($t_{128} = 13.548$, $p < 0.001$), and then declined to 46.8% at 2 dpt ($t_{93} = 9.047$, $p < 0.001$). The apparent decrease in BrdU incorporation from 1.5 to 2 dpt likely reflected selective death of t1EK2 transfected neurons since, at 3 dpt, BrdU incorporation could no longer be assessed due to widespread deterioration of the t1EK2-expressing neurons.

t1EK2 induces p53-dependent apoptosis in differentiated neurons. Cell cycle related cell death was expected, as Cyclin E is consistently associated to apoptotic cell death during aberrant neuronal cell cycle re-entry[14,28,30,32–34]. To confirm whether t1EK2 was inducing apoptosis we performed active caspase-3 immunolabeling[40]. The proportion of neurons expressing t1EK2 that were positive for active caspase-3 (34.7%) was already significantly higher than control neurons (6.0%) at 1.5 dpt ($p < 0.001$, Fisher's exact test) (Fig. 2a). As expected, apoptotic neurons displayed pyknotic nuclei (Fig. 2b). We therefore concluded that t1EK2 induced neuronal S-phase entry and this was followed by apoptotic cell death.

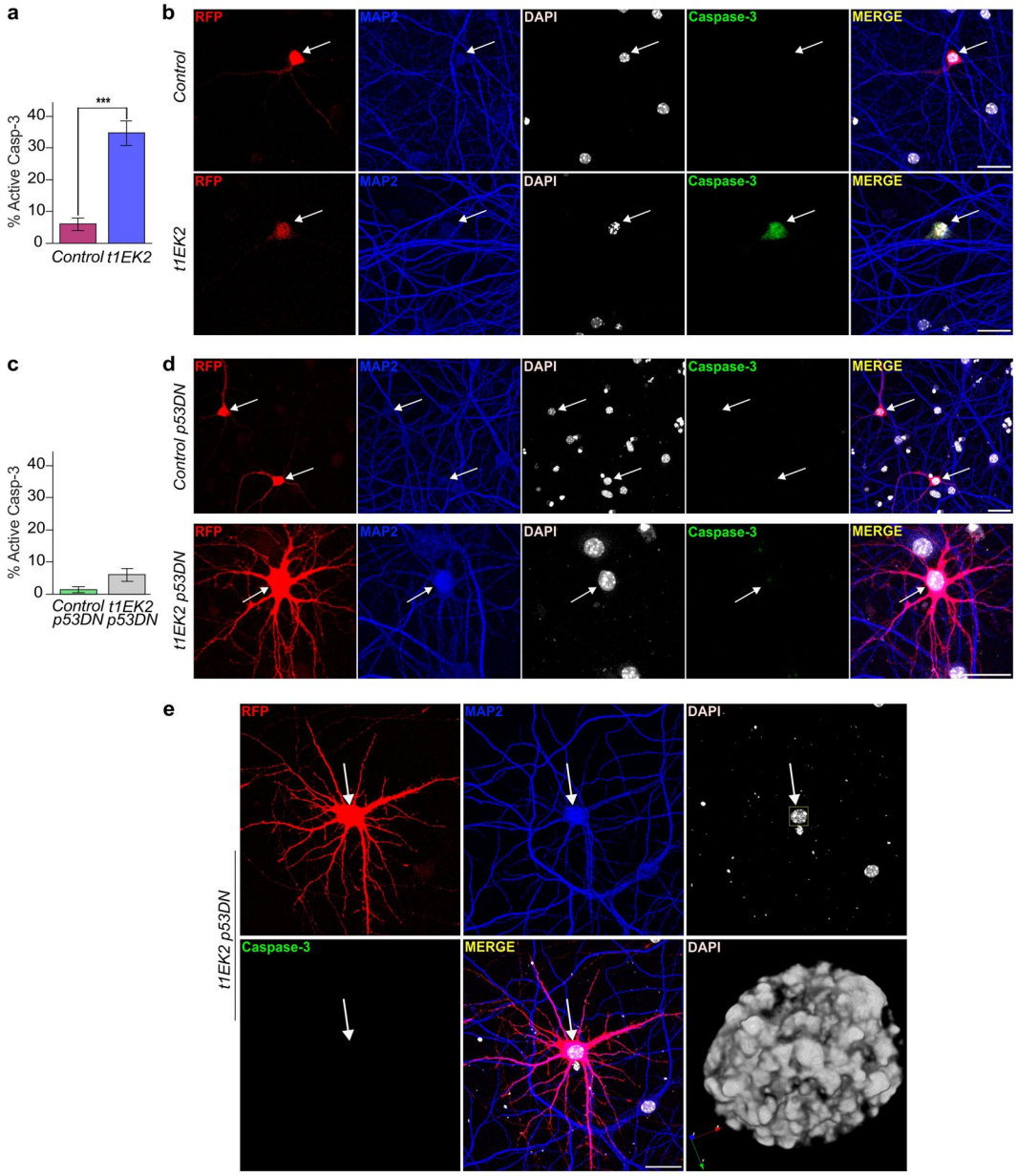

Figure 2. t1EK2 induces p53-dependent apoptosis in differentiated neurons. (**a**) Percentage of active caspase-3 positive neurons expressing LacZ (n = 150) or t1EK2 (n = 150) at 1.5 dpt (17 DIV). Three independent experiments were carried out (***$p < 0.001$; two-sided Fisher's exact test). (**b**) Representative confocal images of active caspase-3-specific immunostaining in a LacZ control neuron and a t1EK2-expressing neuron. Note that the active caspase-3-positive nuclei is pyknotic. Arrows identify RFP positive neurons. (**c**) Percentage of active caspase-3 positive neurons expressing LacZ/p53DN (n = 150) or t1EK2/p53DN (n = 150) at 1.5 dpt (17 DIV). Three independent experiments were carried out (***$p < 0.001$; two-sided Fisher's exact test). (**d**) Representative confocal images of active caspase-3-negative LacZ/p53DN (Control) and t1EK2/p53DN expressing neurons. (**e**) Confocal image of an active caspase-3-negative neuron presenting chromatin condensation characteristic of prophase with 3D reconstruction of the nucleus. Blue, red and green arrows represent 3D orientation. Graphs represent mean ± s.e.m. Scale bar: 25 µm.

A key barrier to Cyclin E/Cdk2 deregulation is the p53 tumor suppressor protein[41]. It is therefore possible that p53 activity could underlie the apoptotic response of hippocampal neurons to t1EK2-induced cell cycle re-entry. In consequence, cell cycle-related cell death in t1EK2-expressing neurons should be blocked by suppressing p53 signaling. To test this hypothesis, we prevented p53 function in t1EK2-expressing neurons by expressing a dominant negative mutant (p53DN)[42]. We assessed apoptosis using active caspase-3 immunostaing. p53 blockade prevented cell cycle re-entry-induced apoptosis in neurons (Fig. 2c–e). The proportion of active caspase-3-positive t1EK2/p53DN-expressing neurons (6.0%) was not statistically significantly different from control neurons expressing p53DN (1.3%) at 1.5 dpt ($p = 0.061$, Fisher's exact test) (Fig. 2c). Moreover, rescued

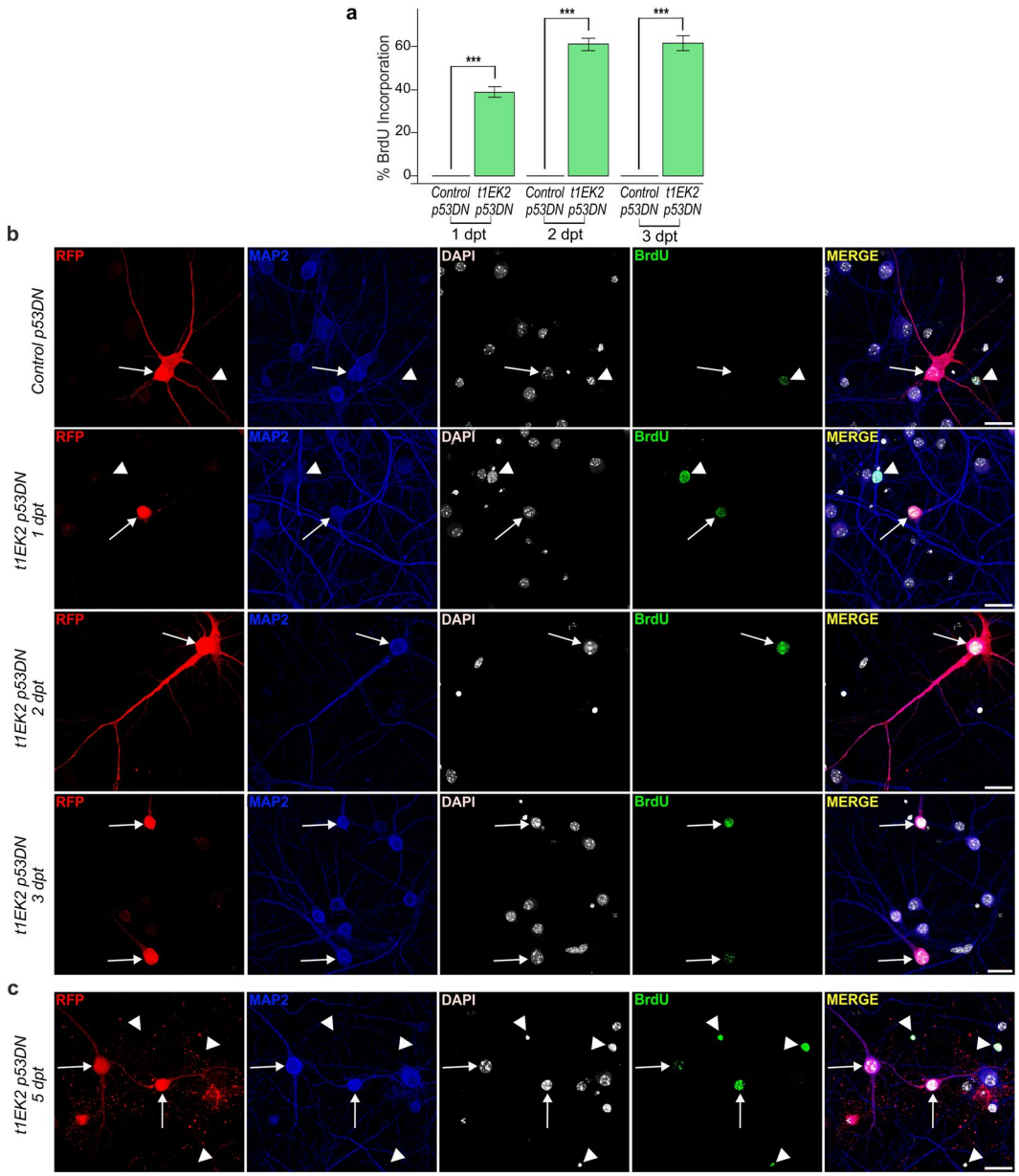

Figure 3. p53 tumor suppressor blockade rescues t1EK2-induced BrdU incorporation. (**a**) Percentage of BrdU positive neurons expressing LacZ/p53DN (Control) or t1EK2/p53DN at 1 (Control: n = 325; t1EK2/p53DN: n = 376), 2 (Control: n = 406; t1EK2/p53DN: n = 294), and 3 (Control: n = 312; t1EK2/p53DN: n = 204) dpt (16–18 DIV). Control neurons never incorporate BrdU. Three independent experiments for each dpt were carried out. As control neurons never incorporated BrdU, statistical analysis was performed by comparing percent BrdU incorporation in t1EK2/p53DN-expressing neurons with zero (***$p < 0.001$; one-tailed *t* test for each dpt). (**b**) Representative confocal images of BrdU incorporation of a LacZ/p53DN control neuron (3 dpt) and t1EK2/p53DN-expressing neurons at 1, 2, and 3 dpt. (**c**) Confocal images showing BrdU incorporation in t1EK2/p53DN-expressing neurons at 5 dpt. Arrows identify RFP positive neurons and arrowheads MAP2-negative (non-neuronal) cells. Graphs represent mean ± s.e.m. Scale bar: 25 µm.

neurons occasionally showed chromatin condensation (Fig. 2e), suggesting that t1EK2 overexpression plus p53 blockade can enable neuronal cell cycle progression into M-phase.

p53 tumor suppressor blockade rescues t1EK2-induced BrdU incorporation. We quantified BrdU incorporation at 1, 2, and 3 dpt to confirm that preventing p53-dependent apoptosis rescued BrdU-positive neurons. As we could not analyze BrdU incorporation at 3 dpt when expressing t1EK2 without p53DN (Fig. 1a), we included this time point to determine whether the effects of p53DN were sustained. Control neurons never incorporated BrdU (n = 1,043) (Fig. 3a,b). In contrast, a substantial proportion of t1EK2/p53DN-expressing neurons was positive for BrdU labelling at 1 (38.8%) ($t_{375} = 15.429$, $p < 0.001$), 2 (61.2%) ($t_{293} = 21.509$, $p < 0.001$), and 3 dpt (61.8%) ($t_{203} = 18.109$, $p < 0.001$) (Fig. 3a,b). Co-expressing p53DN with t1EK2 rescued BrdU incorporation

at 3 dpt and, although we did not quantify it, neurons with BrdU incorporation could still be found at 5 dpt (Fig. 3c). In summary, p53 tumor suppressor loss of function prevented t1EK2-induced apoptosis and rescued S-phase viability.

Wee1 inhibition enables G2/M transition in differentiated neurons. Next, we wanted to determine whether neurons could continue cell cycle progression beyond S-phase. To assess this possibility, we performed Phospho-Ser10 Histone H3 (pH3) immunostaining to identify t1EK2-expressing neurons in late G2 and M-phase[43]. Cdk1 activity is required for the phosphorylation of Histone H3[44] and, although detected at low levels during G2[45], the onset of pH3 staining starts at late G2, prior to M-phase, in the form of nuclear pH3 foci[43]. This transitions to pan-nuclear pH3 staining just prior to the formation of prophase chromosomes and remains from prophase to metaphase[43]. However, the loss of pH3 staining begins while cells are still in M-phase, at anaphase onset[43]. Thus, we blocked anaphase onset with the proteasome inhibitor MG132[46] to identify all neurons that entered M-phase (see Supplementary Fig. S1a,b for protocol details). Consistent with the absence of spontaneous DNA replication, control MAP2-positive neurons were never positive for pH3 (n = 150) (Fig. 4a). In contrast, 45.3% ($t_{149} = 11.116$, $p < 0.001$) of t1EK2/p53DN-expressing neurons reached late G2 (evidenced by pH3-specific foci). In addition, 2.7% ($t_{149} = 2.020$, $p < 0.05$) of t1EK2/p53DN-expressing neurons showed pan-nuclear pH3 labelling (Fig. 4a), an observation consistent with the capacity of active caspase-3-negative neurons expressing t1EK2/p53DN to occasionally enter M-phase (Fig. 2e). Therefore, although most neurons could not undergo G2/M transition, some neurons did enter M-phase upon t1EK2 expression and p53 inhibition.

In mitotic cells, G2/M transition can be blocked by G2 checkpoint activation[19], which is triggered by DNA damage acquired during a genotoxic S-phase. Deregulated Cyclin E can induce DNA damage resulting from the aberrant activation of the DNA replication machinery[47–50]. Thus, we assessed whether DNA damage in t1EK2/p53DN neurons was present and could account for the overall block in G2/M transition. DNA damage was assessed by Phospho-Ser139 Histone H2AX (γ-H2AX) immunostaining[51]. We quantified the amount of neurons that were negative for γ-H2AX, had 1–5, 6–10, or more than 10 γ-H2AX foci, or showed γ-H2AX pan-nuclear staining. At 1.5 dpt, t1EK2/p53DN-expressing neurons generally presented more than 5 γ-H2AX foci and control neurons 5 or less foci (Supplementary Fig. S1c). Thus, we analyzed whether the proportion of t1EK2/p53DN-expressing neurons with more than 5 γ-H2AX foci was significantly higher than that of control neurons. This analysis indicated that the proportion of neurons presenting more than 5 γ-H2AX foci was significantly higher in the t1EK2/p53DN-expressing group (78%) than in the p53DN-expressing controls (24%) ($p < 0.001$, Fisher's exact test) (Fig. 4b). Neurons with pan-nuclear γ-H2AX staining generally displayed interphase nuclei (Fig. 4c left neuron; for 360° view of DAPI-stained nuclei see Supplementary Video S1). Neurons presenting reduced γ-H2AX foci formation could be occasionally found with prophasic-like mitotic chromatin condensation (Fig. 4c right; Supplementary Video S1). These results support the possibility that DNA damage in neurons could be blocking M-phase entry by activating the canonical G2 checkpoint.

M-phase block exerted by G2 checkpoint signaling is reversible[19]. This checkpoint largely relies on the phosphorylation of Cdk1 in Tyr15 by Wee1 kinase, and the subsequent inhibition of Cyclin B1/Cdk1 activity[52]. We found that Cyclin B1 and Cdk1 are expressed by t1EK2/p53DN-transfected neurons. Cyclin B1 is present in both non-transfected and transfected t1EK2/p53DN expressing neurons (Supplementary Fig. S1e,f). This is not unexpected, as several cell cycle regulators are present in neurons[53,54], where they perform non-cell cycle functions related to neuronal maturation and synaptic activity[55]. The expression pattern shown in Supplementary Fig. S1e,f is consistent with t1EK2 inducing an increase in expression of Cyclin B1, both in interphase (Supplementary Fig. S1e) and in neurons presenting chromatin condensation (Supplementary Fig. S1f). In contrast, neurons presenting apoptotic chromatin condensation (Supplementary Fig. S1g) do not show Cyclin B1 expression. As a proof of specificity, non-neuronal cells lack cyclin B1 expression (yellow arrows in Supplementary Fig. S1e), as previously described[54]. To verify that Cdk1 is present in t1EK2/p53DN-transfected neurons, becoming active in those that spontaneously enter M-phase, we resorted to double labeling of Cdk1 and phosphoTyr15 phosphorylation of Cdk1 (pTyr15-Cdk1) (Supplementary Fig. S1h,i). t1EK2/p53DN-transfected neurons showing uncondensed DNA were positive for Cdk1 and pTyr15-Cdk1 (Supplementary Fig. S1h). This is consistent with neurons in G2. As expected, transfected neurons presenting chromatin condensation consistent with M-phase entry were positive for Cdk1 and negative for pTyr15-Cdk1 (Supplementary Fig. S1i), reflecting Cdk1 activation.

In mitotic cells, G2/M transition can be induced by inhibiting Wee1 kinase with MK1775[56]. To test whether Wee1 kinase was preventing neurons from entering M-phase, we abrogated G2 checkpoint signaling by inhibiting Wee1 with MK1775 and assessed pH3 immunostaining. Again, we blocked anaphase onset with MG132[46] to capture all neurons that entered M-phase (see Supplementary Fig. S1a,d for protocol details). Control MAP2-positive neurons were not found in late G2 or M-phase (n = 150) (Fig. 4d). In contrast, Wee1 inhibition with MK1775 resulted in a substantial increase of t1EK2/p53DN-expressing neurons in M-phase with pan-nuclear pH3 labeling (31.3%) ($t_{149} = 8.246$, $p < 0.001$) and chromatin condensation (Fig. 4d,f,g, Supplementary Fig. S1k–p; for 360° view of RFP/pH3 labeling illustrated in Fig. 4f, see Supplementary Video S2). Chromatin condensation in these neurons was not apoptotic since it was negative for active caspase-3 (Supplementary Fig. S1q,r). In addition, 37.3% ($t_{149} = 9.422$, $p < 0.001$) of t1EK2/p53DN-expressing neurons were still found in late G2 as reflected by pH3 foci (Fig. 4d,e, Supplementary Fig. S1j). The total percentage of neurons in late G2 and M-phase after Wee1 inhibition (68.6%) was consistent with the percent of BrdU positive neurons at 2 (61.2%) or 3 dpt (61.8%) (Fig. 3a).

We confirmed that MK1775-dependent G2/M transition in t1EK2/p53DN-transfected neurons relies on canonical Cdk1 activity since the Cdk1-specific inhibitor RO-3306 prevented both pH3 labeling and mitotic-like chromatin condensation in these neurons (n = 115) (Supplementary Fig. S1s). As an internal control, MAP2-negative cells in the cultures also lacked pH3 immunostaining and lacked mitotic chromatin condensation (see low magnification in Supplementary Fig. S1t).

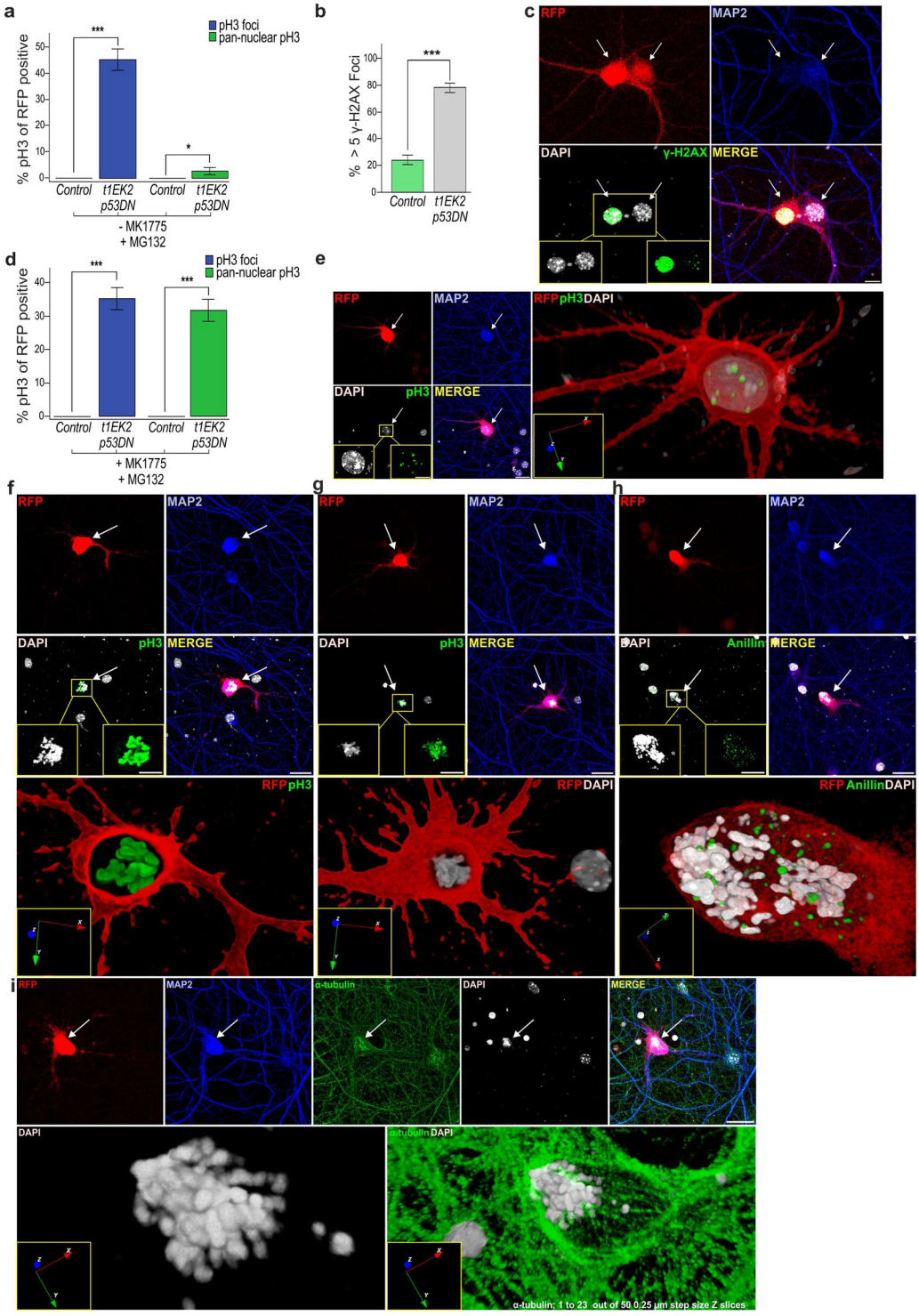

Figure 4. Wee1 inhibition enables G2/M transition in differentiated neurons. (**a**) Percentage of LacZ/p53DN- (Control) or t1EK2/p53DN-expressing neurons with pH3 foci (Control: n = 150; t1EK2/p53DN: n = 150) or pan-nuclear pH3 staining (Control: n = 150; t1EK2/p53DN: n = 150) at 1.5 dpt. Anaphase onset was blocked with MG132. Control neurons were never positive for pH3. Three independent experiments were carried out. As control neurons never were never positive for pH3, statistical analysis was performed by comparing pH3-positive t1EK2 neurons with zero (***$p < 0.001$, *$p < 0.05$; one-tailed *t* test). (**b**) Percentage of LacZ/p53DN- (Control) or t1EK2/p53DN-expressing neurons with more than 5 γ-H2AX foci (Control: n = 150; t1EK2/p53DN: n = 150) at 1.5 dpt (see Supplementary Fig. S1c for additional γ-H2AX results). Three independent experiments were carried out (***$p < 0.001$; Fisher's exact test). (**c**) Confocal image of pan-nuclear γ-H2AX staining of an interphase nucleus (left neuron) and γ-H2AX foci of a prophase-like nucleus (right neuron) (see Supplementary Video S1). (**d**) Percentage of LacZ/p53DN- (Control) or t1EK2/p53DN-expressing neurons (Control: n = 150; t1EK2/p53DN: n = 150) at 1.5 dpt with pH3 foci or pan-nuclear pH3 staining after G2

checkpoint abrogation with MK1775. Anaphase onset was blocked with MG132. Control neurons are never positive for pH3. Three independent experiments were carried out. As control neurons never were never positive for pH3, statistical analysis was performed by comparing pH3-positive t1EK2/p53DN neurons with zero (***$p < 0.001$, *$p < 0.05$; one-tailed *t* test). (**e**–**g**) Confocal images and 3D reconstructions of a pH3 foci-positive neuron consistent with late G2 (**e**) and neurons with pan-nuclear pH3 staining consistent with prometaphase/metaphase (**f**, see also Supplementary Video S2, **g**). See also Supplementary Fig. S1j–p. Blue, red and green arrows represent 3D orientation. (**h**) Confocal images and 3D reconstruction showing diffuse anillin staining in a t1EK2/p53DN-expressing neuron treated with MK1775 in prometaphase. Blue, red and green arrows represent 3D orientation. (**i**) Confocal images of a neuron with α-tubulin staining of putative mitotic spindle. Bottom panels: three-dimensional reconstruction of DAPI (left) and of slices 1 to 23 out of 50 from cytoskeleton α-tubulin staining to eliminate background (right). Graphs represent mean ± s.e.m. Arrows identify RFP positive neurons. Scale bars: 25 µm (**c**,**e**–**i**), 10 µm (**i**, bottom panels).

Neuronal M-phase progression was confirmed by the loss of lamin B1, the major component of the nuclear lamina[57], which becomes disassembled during mitosis[58], thus providing evidence of nuclear envelope breakdown. As expected, t1EK2/p53DN-transfected neurons without chromatin condensation conserve Lamin B1 immunolabeling (Supplementary Fig. S1u), while t1EK2/p53DN-transfected neurons with chromatin condensation do not (Supplementary Fig. S1v).

Neuronal M-phase progression was further confirmed by anillin immunolabeling, which localizes to the nucleus during interphase, the cortex following nuclear envelope breakdown, and the cleavage furrow during cytokinesis[59,60]. In neurons with nuclei displaying characteristics of prometaphase/metaphase, anillin immunostaining was released from the cell nucleus (Fig. 4h). In contrast, anillin was located in the nucleus in t1EK2-transfected neurons in interphase (Supplementary Fig. S1w).

We also performed α-tubulin immunostaining of the mitotic spindle of neurons in M-phase to confirm mitosis progression in t1EK2/p53DN-transfected neurons. Although α-tubulin staining resulted in extensive background signal due to its presence in the cytoskeleton[61,62], putative mitotic spindles with intense α-tubulin labeling could be identified in neurons with chromatin condensation, consistent with prometaphase/metaphase (Fig. 4i). This α-tubulin labeling is clearly different from that observed in non-transfected neurons (arrows in Supplementary Fig. S1x) and transfected neurons undergoing apoptosis (Supplementary Fig. S1y), which in these cases is absent from the nuclear compartment.

Finally, we performed time-lapse experiments to follow live neurons into M-phase. We expressed Histone H2B tagged with EGFP (H2B-GFP) to follow DNA dynamics and RFP reporter protein to study morphology. H2B-EGFP signal was consistent with mitotic chromatin condensation (Supplementary Video S3, right). Chromatin condensation was usually accompanied by a loss of RFP signal from dendrites. This may reflect a thinning and or retraction of the dendrites that is coordinated with M-phase entry. In contrast, t1EK2/p53DN expressing neurons in interphase remained with unaltered gross morphology (Supplementary Video S3, left). Occasionally, neurons underwent cell death either during interphase (Supplementary Video S4) or after attempting M-phase progression (Supplementary Video S5). In summary, primary neurons can progress through S and G2-phases and enter M-phase. M-phase entry in neurons is gated by G2 cell cycle checkpoint signaling as in mitotic cells.

Differentiated neurons can undergo cytokinesis. We again performed time-lapse experiments to see whether neurons can undergo cytokinesis. To improve the chances of cytokinesis, we used caffeine to inhibit G2 checkpoint signaling[63] upstream of Wee1[19] and co-expressed Topoisomerase-2α (TOP2α) to aid in the decatenation of intertwined sister chromatids[64] (see Supplementary Fig. S2a for protocol details). Although sparse and highly asynchronous, attempts at anaphase/cytokinesis could be detected in 12.9% (n = 93) of recorded neurons. Neurons largely underwent anaphase/cytokinesis failure (n = 8) (Supplementary Videos S6, S7). Despite this, some neurons were able to complete cell division (n = 4). One of the daughter neurons could die whilst the other remained viable (Fig. 5a,b; Supplementary Video S8; see Supplementary Fig. S2a,b for protocol details), evidencing that neuronal cell division was complete. Alternatively, both neurons could remain viable for hours after abscission (Fig. 5c,d; Supplementary Video S9; see Supplementary Fig. S2a,c for protocol details).

We also assessed the assembly of the cytokinesis machinery by anillin immunocytochemistry. Anillin localizes to the cleavage furrow at cytokinesis onset and remains in the intercellular bridge after cleavage furrow ingression[59]. The detection of cytokinesis by immunocytochemistry only captures neurons undergoing cytokinesis at a single time-point. However, cytokinesis onset in different neurons could be hours apart (Fig. 5a,c; Supplementary Videos S8 and S9). To achieve some degree of synchronization, we forced anaphase/cytokinesis onset by abrogating the Spindle Assembly Checkpoint (SAC) with the Mps1 inhibitor AZ3146[65] (see Supplementary Fig. S2d,e for protocol details). Confirming our time-lapse experiments, neurons assembled the cytokinesis machinery (Fig. 5e,f; Supplementary Fig. S2f–h). We found that, in most cases, cleavage furrow ingression began (Supplementary Fig. S2f) and proceeded asymmetrically (Supplementary Fig. S2g,h) up to the formation of the intercellular bridge/midbody (Fig. 5e,f; for 360° view of Fig. 5f see Supplementary Video S10). We were also able to detect putative daughter neurons after abscission completion (Fig. 5g,h). We also performed pH3 immunolabelling to characterize chromatin decondensation during anaphase/telophase. The loss of pH3 staining begins at anaphase and is completed prior to detectable chromosome decondensation in telophase[43]. In agreement, neurons locked in cytokinesis by chromatin bridges displayed both patterns of staining (Fig. 5i; for 360° view of Fig. 5i, see Supplementary Video S11). This suggests that the pH3-positive chromatin trapped in the intercellular bridge was still condensed while the portion of the chromatin outside the intercellular bridge lacking pH3 staining was already decondensed in a telophase-like state.

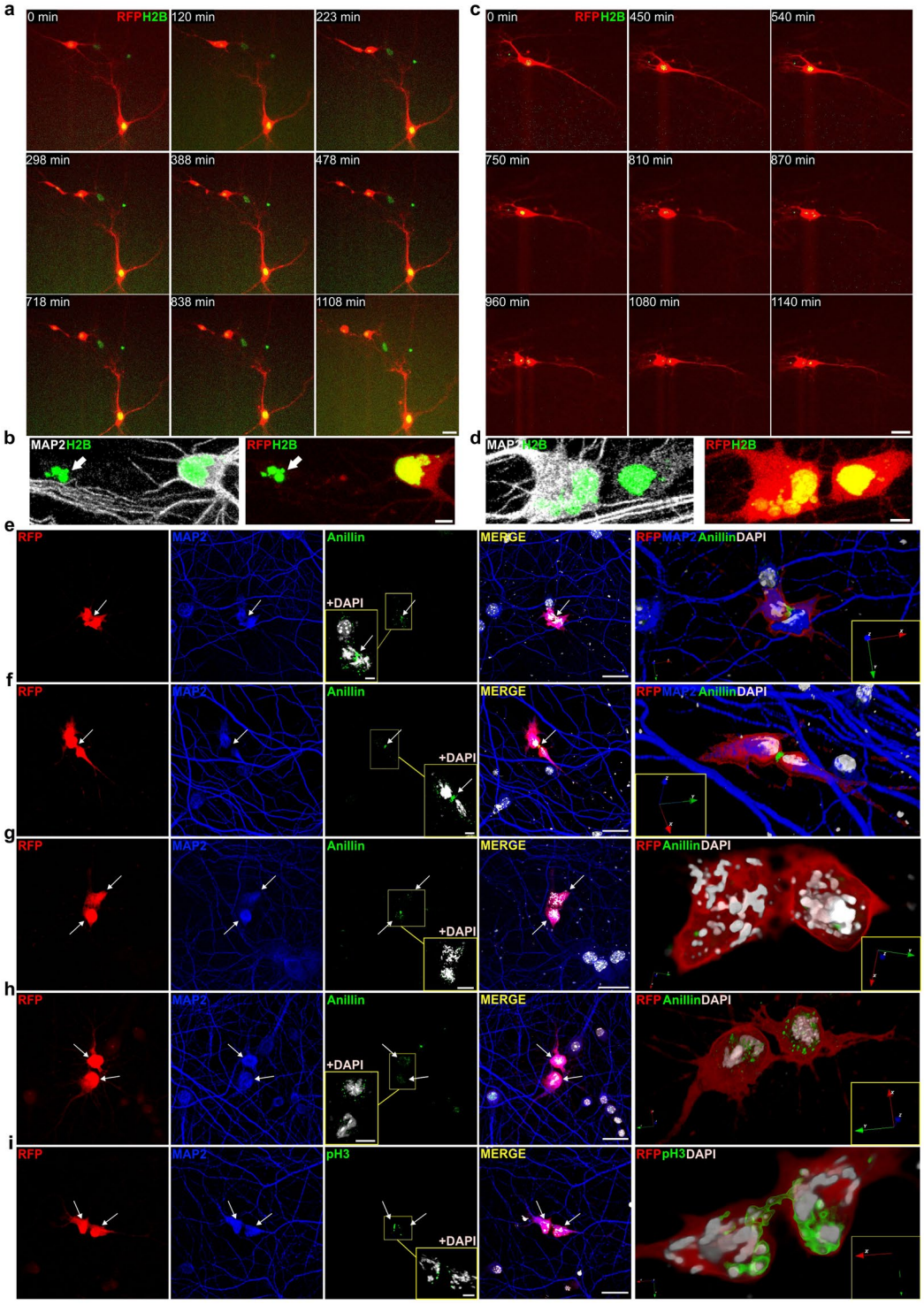

Figure 5. Differentiated neurons can undergo cytokinesis. (**a**) Time-lapse video frames of a neuron undergoing cytokinesis (Supplementary Video S9). There is a delay between the formation of the intercellular bridge and final abscission, suggestive of the presence of a chromatin bridge. (**b**) Confocal images of daughter neurons (evidenced by MAP2 immunostaining) in a, confirming that abscission was complete. One daughter neuron survived (right) while the other (left) displayed pyknotic nucleus (white arrow). (**c**) Time-lapse video frames of a neuron undergoing cytokinesis (Supplementary Video S10). (**d**) Confocal images of daughter neurons (evidenced by MAP2 immunostaining) in c, confirming that abscission was complete. The daughter neuron on the left is multinucleated, indicative of aneuploidy. (**e**–**h**) Confocal images of anillin immunolabelling. Anillin stains the cleavage furrow/midbody during neuronal cytokinesis (**e**,**f**; for 360° view of f see Supplementary Video S10). White arrows indicate intercellular bridge/midbody. See also Supplementary Fig. S2f–h. Anillin is recycled from the midbody in putative daughter neurons after completing abscission (**g**,**h**). (**i**) Confocal images of a pH3 positive neuron undergoing cytokinesis (for 360° view see Supplementary Video S11). The intercellular

bridge is traversed by pH3 positive chromatin, evidencing the presence of a chromatin bridge. White arrows identify daughter neurons (**g**–**i**). Blue, red and green arrows represent 3D orientation (**e**–**i**). H2B: Histone H2B tagged with EGFP. Scale bars: 25 µm (**a**,**c**, RFP and H2B-EGFP stills), 5 µm (**a**,**b**, bottom panels), 25 µm (**e**–**i**).

In sum, we conclude that cell cycle regulation in S, G2, and M phases in neurons is shared with mitotic cells.

Neurons recover AIS integrity after M-phase exit without cell division. Neuronal cell cycle re-entry in neuron disease is associated to cell death instead of cell division[15,16]. To determine whether cell cycle re-entry without cell division is necessarily fatal, we assessed the viability of t1EK2/p53DN/TOP2α-expressing multinucleated neurons, which were frequently detected in our cultures. Multinucleation requires M-phase entry and, therefore, enabled the identification of neurons that had entered and exited the cell cycle without cell division. As a control, we did not detect any evidence of multinucleation in controls transfected neurons in BrdU (n = 491, Fig. 1a; n = 1,043, Fig. 3a) or pH3 (n = 150, Fig. 4a; n = 150, Fig. 4d) experiments. As neurons expressed the p53DN mutant, we assessed AIS integrity rather than active caspase-3 to study viability. The AIS sustains neuronal polarity and integrates synaptic input to generate action potentials[66,67], and previous studies demonstrate that AIS integrity is required to maintain neuronal viability[67,68]. Within the AIS, AnkyrinG (AnkG) is the main structural constituent, necessary to maintain AIS functions and neuronal integrity[66]. We analyzed AnkG dynamics in t1EK2/p53DN/TOP2α-expressing neurons in interphase, prophase, and prometaphase/telophase 3 h after G2 checkpoint abrogation. In multinucleated neurons we assessed AnkG 6 and 9 h after abrogating the G2 checkpoint. In control LacZ/p53DN/TOP2α-expressing neurons AnkG was assessed 9 h after G2 checkpoint abrogation.

AnkG signal varied significantly across cell cycle stages [Welch's F test (5; 20,479) = 11.617, $p < 0.001$] (Fig. 6a,b), evidencing that AIS integrity fluctuated during the cell cycle. Multiple comparisons using the Games-Howell post-hoc test indicated that the AnkG signal of neurons in prophase was not significantly different from that of neurons in interphase ($p = 0.448$) or control transfected neurons ($p = 0.703$) (Fig. 6a,b). However, the AnkG signal did decrease significantly in prometaphase to telophase when compared to interphase ($p = 0.003$), prophase ($p = 0.023$) or control neurons ($p = 0.009$). These results evidence a loss of AIS integrity in M-phase, in between prometaphase and telophase. 6 h after inducing G2/M transition, multinucleated neurons had still not recovered the AnkG signal when compared to interphase ($p = 0.033$), prophase ($p = 0.033$), or control neurons ($p = 0.041$). However, 9 h after inducing G2/M transition, multinucleated neurons significantly increased their AnkG signal with respect to neurons in between prometaphase and telophase ($p = 0.005$), achieving an AnkG signal that was non-significantly different from control ($p = 0.957$), interphase ($p = 0.999$), or prophase ($p = 0.349$) neurons. The recovery of AnkG signal in multinucleated neurons was gradual, as multinucleated neurons 9 h after inducing G2/M transition displayed a non-significant trend to increase the AnkG signal when compared to 6 h ($p = 0.065$). Therefore, the AIS is coordinated with the neuronal cell cycle. After cell cycle exit without cell division, neurons can progressively yet fully recover the AIS.

Discussion

It was originally believed that the postmitotic status of neurons prohibited any form of cell cycle activity. This view is now outdated. There is ample evidence of neuronal cell cycle re-entry in human pathologies such as AD, PD, AML or brain injury, as well as in animal models and in primary neuronal cultures[15,16]. Notwithstanding, neuronal cell cycle re-entry in differentiated mature neurons does not result in cell division but it is instead associated to increased susceptibility to cell death[16]. Congruently, the activation of the cell cycle machinery itself has been deemed pathological[17]. We provide evidence that the lack of cell division and the susceptibility to cell death in neurons that reactivate the cell cycle likely relies on canonical cell cycle regulatory mechanisms. Primary neurons undergo apoptosis upon cell cycle re-entry. As with cycling cells, apoptosis in S-phase can be prevented by suppressing p53 signaling. Rescued neurons progress through S-phase into G2, where they are arrested at the G2/M transition. Inhibition of G2 checkpoint kinase Wee1 reveals neurons readily enter M-phase and a subset of neurons can undergo cytokinesis. Therefore, although our results have to be confirmed *in vivo*, we have shown that a large part of the regulation of the cell cycle in S, G2 and M-phase in primary neurons at post-synaptogenesis stages of development is shared with mitotic cells. Hence, cell cycle-induced cell death, lack of M-phase entry, or lack of cell division in neurons can be accounted for by standard cell cycle regulation present in mitotic cells.

Multinucleated neurons have been previously reported in Alzheimer's disease (AD)[69]. Cellular multinucleation can result from premature exit from the cell cycle in M-phase, after aberrant anaphase and/or failed cytokinesis[21]. Cells that prematurely exit the cell cycle and attain viability are largely in a senescent state, which entails a permanent withdrawal from the cell cycle[70]. Most senescent cells develop the senescence associated secretory phenotype (SASP), which can be pro-inflammatory, pro-oxidative and pro-mitogenic[70]. There is already evidence to support that the selective killing of senescent cells in the brain can be therapeutic[71]. Whether it is the selective killing of senescent neurons, non-neuronal cells or both is unclear because we are still lacking conclusive proof that neurons can undergo bona fide senescence[71]. Our results show that cytokinesis failure results in multinucleated neurons that recover the AIS, a structural determinant of neuronal viability[67,68]. Hence, as with cells that undergo senescence, neurons prematurely exit the cell cycle into a viable state. The extent to which neurons that exit the cell cycle are viable, and whether they are indeed senescent will have to be determined by future studies. The recovery of the AIS in multinucleated neurons indicates that our protocol to induce cell cycle progression does not result in neuronal dedifferentiation.

Viable cell cycle exit is consistent with reports showing that neurons that re-enter the cell cycle in AD can remain viable for months to years[16,72]. Furthermore, the existence of multinucleated neurons in AD suggest that

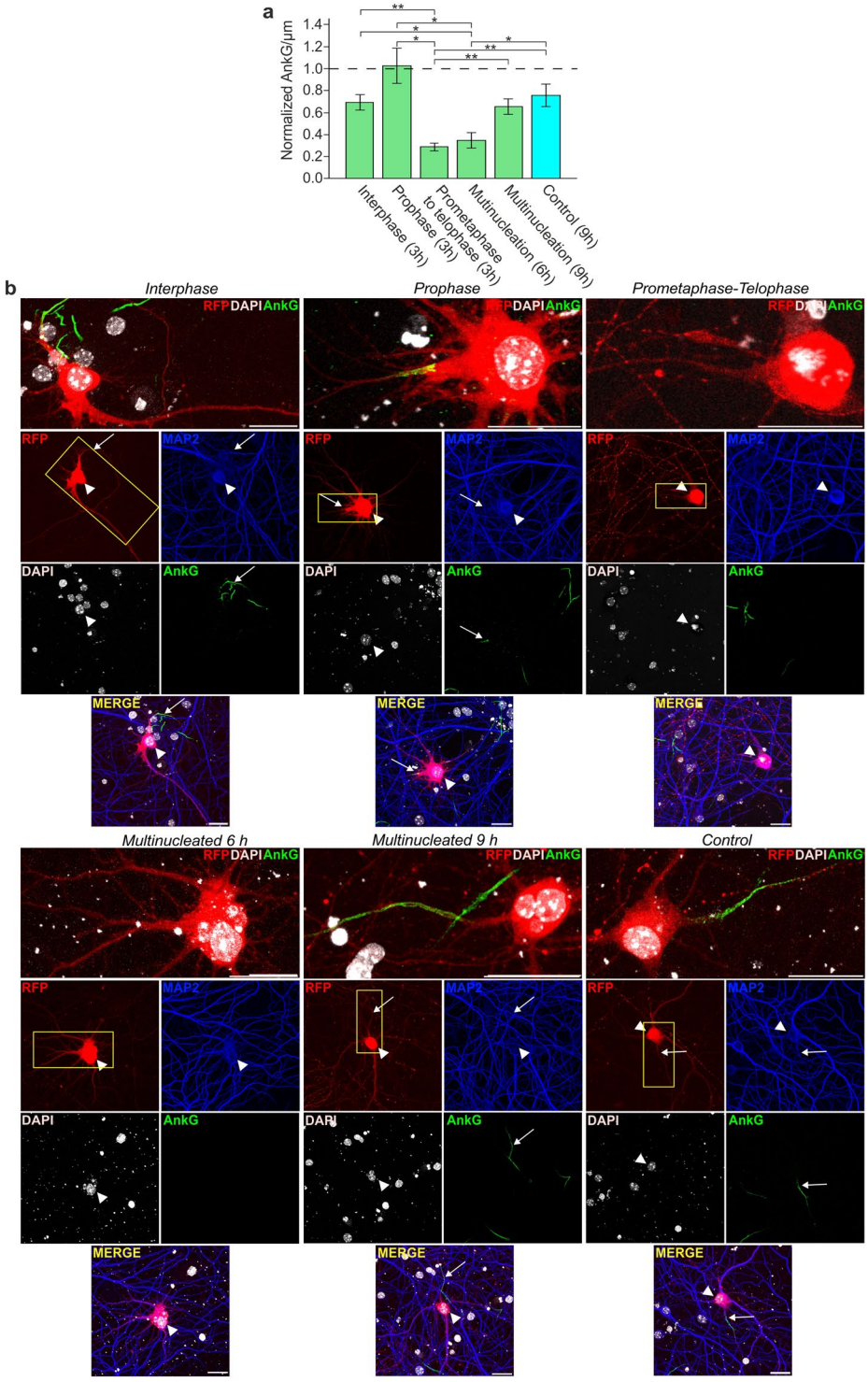

Figure 6. Neurons recover AIS integrity after M-phase exit without cell division. (**a**) AnkG signal per µm in t1EK2/p53DN/TOP2α-expressing neurons in different stages of the cell cycle (green) and in control neurons expressing LacZ/p53DN/TOP2α (blue) at the indicated time points after suppressing the G2 checkpoint with MK1775, normalized to neighboring RFP-negative/MAP2-positive neurons. All groups were treated with AZ3146 to abrogate the SAC 2.5 h after MK1775 treatment. A single experiment was carried out (**$p < 0.01$, *$p < 0.05$; Welch's F test and two-sided Games-Howell post-hoc tests; Interphase: $n = 9$, Prophase: $n = 7$, Prometaphase to telophase: $n = 9$, Multinucleation 6 h: $n = 8$, Multinucleation 9 h: $n = 10$, Control: $n = 10$). (**b**) Confocal images of AnkG-immunolabelled neurons in interphase, prophase, and prometaphase to telophase, multinucleated neurons 6 and 9 h post transfection, and control neurons. High magnification of AIS (boxes) is shown for each case. Arrowheads identify RFP positive neurons and arrows their respective AIS when present. Graphs represent mean ± s.e.m. Scale bar: 25 µm.

at least some neurons that re-enter the cell cycle can reach M-phase[69]. However, in current models, cell cycle re-entry invariantly results in cell death. This prevents understanding how neurons can survive cell cycle re-entry in neurodegenerative diseases and underscores the need for models of viable neuronal cell cycle entry[16]. In this study, we provide a model in which cell cycle-related cell death is prevented, and that allows the study of dividing or multinucleated neurons. We propose that canonical cell cycle regulation in neurons will afford a new framework to study cell cycle deregulation in neurodegeneration and basic research.

We have shown that neurons possess functional cell cycle machinery and, although in rare occasions, can undergo cell division. Therefore, the manipulation of the neuronal cell cycle could theoretically be employed to modulate neuronal maturation and synaptic activity, as these processes are known to rely on mitotic mechanisms[55]. Further, the loss of the AIS during M-phase entry and its recovery after premature cell cycle exit suggest the possibility that the neuronal cell cycle is a coordinated program. Rather than cell cycle activity in itself being deleterious for neurons, it is possible aberrant drivers of cell cycle re-entry such as t1EK2 and those reported in the literature[15] deregulate the neuronal cell cycle machinery, trigger cell cycle checkpoints, and prevent cell cycle completion. Hence, the aberrant re-activation of an otherwise functional neuronal cell cycle program may explain why neuronal cell division is limited after unscheduled re-entry. Future work that improves on our methods will have to determine whether the neuronal cell cycle can be activated in ways that can bestow neuronal proliferation. This will require the development of an improved procedure aimed at organizing bipolar spindles and successful segregation of chromosomes in all neurons undergoing mitosis. For now, we have established that cell division in differentiated primary neurons can no longer be considered impossible.

Methods

Ethics statement. All of the procedures for handling and sacrificing animals were approved by the CSIC Ethics Committee in accordance with the EU guidelines for the care and use of laboratory animals.

Plasmids. Construction of a vector encoding a truncated form of Cyclin E (Trunk 1), which lacks the first 39 amino acids of Cyclin E[23], fused to Cdk2 isoform 1 (NCBI accession number NP_001789) (t1EK2) was based on the EK2 fusion protein described previously[24]. Briefly, a synthetic DNA construct encoding for t1EK2 was firstly cloned into the pUC vector, then subcloned into the HindIII and XbaI sites of pcDNA3 vector (ThermoFisher Scientific) and finally sequence verified. The pcDNA6/V5-His/lacZ vector expressing LacZ was purchased from Invitrogen. The pRFPRNAiC vector expressing red fluorescent protein (RFP), provided by Stuart Wilson (University of Sheffield, UK), has been previously described[73]. The T7-p53DD-pcDNA3 vector expressing a dominant negative form of p53[42] was a gift from William Kaelin (Addgene plasmid # 25989). The H2B-GFP vector expressing a Histone-GFP fusion protein[74] was a gift from Geoff Wahl (Addgene plasmid #11680). The TOP2α-WT pcDNA3.1(+) vector expressing topoisomerase IIα[75] was a kind gift from Corrado Santocanale (National University of Ireland).

Antibodies and inhibitory compounds. Primary antibodies: The anti-BrdU rat monoclonal antibody (mAb) [BU1/75 (ICR1)] (AbDSerotec) was used at 1:200 dilution. The anti-RFP rabbit polyclonal antibody ab62341 (Abcam) was used at 1:100 dilution. The anti-MAP2 chicken antibody ab5392 (Abcam) was diluted 1:5000-1:12000. The cleaved Caspase-3 rabbit antibody (Cell Signaling Technology) was used at 1:400 dilution. The anti-phospho Histone H3 (ser10) rabbit polyclonal antibody 06–570 (Millipore) was used at 1:500 dilution. The anti-anillin rabbit polyclonal antibody ab154337 (Abcam) was used at 1:100 dilution. The anti-α-tubulin mouse monoclonal antibody [DM1A] ab2791 (Abcam) was used at 1:10000 dilution. The anti-phosphoH2AX (ser139) mouse monoclonal antibody [9F3] ab26350 (Abcam) was used at 1:500 dilution. The anti-Ankyrin-G mouse antibody [N106/36] (NeuroMab) was diluted at 1:150. The anti-CDK1 mouse monoclonal antibody [A17] (Abcam) was used at 1/100 dilution. The anti-CDK1/2/3/5 (phospho Y15) rabbit monoclonal antibody [EPR7875] (Abcam) was diluted 1/100. The anti-Cyclin B1 rabbit monoclonal antibody [EPR17060] (Abcam) was used at 1/500 dilution. The anti-Lamin B1 rabbit monoclonal antibody (Abcam) was diluted 1/100. Secondary antibodies: Alexa Fluor 488 Goat Anti-Rat IgG (H + L) (Life Technologies), Alexa Fluor 488 Goat Anti-Mouse IgG (H + L) (Life Technologies), Alexa Fluor 488 Goat anti-Mouse IgG2a A-21131 (Invitrogen), Alexa Fluor 488 Affinipure Goat Anti-Rabbit IgG (H + L) (Jackson Immunoresearch), Alexa Fluor 594 Goat Anti-Rabbit IgG (H + L) (Life Technologies), and Alexa Flour 647 Goat Anti-Chicken IgY (H + L) A-21449 (Invitrogen) were used at 1:1000 dilution. Inhibitors: Cdk1 inhibitor RO-3306 (ref. 1530) was used at 9 μM, Wee1 inhibitor MK1775 (ref. 1494), used at 900 nM, and Mps1 inhibitor AZ3146 (ref. 1642), used at 10 μM, were purchased from Axon Medchem. The Eg5 inhibitor monastrol (ab14087), used at 100 μM, and the proteasome inhibitor MG132 (ab141003), used at 10 μM, were purchased from Abcam. Caffeine (Sigma), used at 3 mM, was diluted in Neurobasal without L-Glutamine (ThermoFisher Scientific) and filter sterilized with 0.2 μm syringe filters (Acrodisc).

Hippocampal Cultures. 10-mm diameter coverslips (Menzel Glässer) were placed in 65% nitric acid (Merck) overnight. Coverslips were then washed 4 times in Milli-Q water (Millipore), once in pure ethanol (Merck) and air-dried. Coverslips were sterilized overnight in oven at 185 °C, placed in CELLSTAR cell culture dishes with 4 inner rings (Greiner bio-one) and UV sterilized for 1 h. Coverslips were coated with 0.5 mg/ml polyornithine (PLO) (Sigma-Aldrich) (prepared in 150 mM borate buffer, pH8.4) for at least 24 h. PLO was washed twice in sterilized Milli-Q water. CELLSTAR culture dishes were left in a humidified atmosphere containing 5% CO_2 at 37 °C with 2 ml of neuronal plating medium consistent of Dulbecco's modified Eagle medium (DMEM) with D-Glucose, L-Glutamine and Pyruvate (ThermoFisher Scientific) containing 10% fetal bovine serum (FBS) (Life technologies) and penicillin-streptomycin (25 U/ml) (Gibco). Primary hippocampal neurons derived from CD-1 mice (Charles River) were harvested from embryonic day 17, staged as previously described[76]. Pups were decapitated and brains were placed in cold Hanks' balanced salt solution (HBSS) without calcium

chloride, magnesium chloride, nor magnesium sulphate (Gibco). Hippocampi were then dissected and incubated for 15 min at 37 °C in 5 ml HBSS containing 2.5 mg/ml trypsin (Gibco) in a 15 ml conical centrifuge tube. 1 mg/ml DNAse (Roche) was added for the last 30 s. Hippocampi were then washed 5 times in 5 ml of HBSS at 37 °C each time. Mechanical dissociation followed in 1 ml of HBSS at 37 °C by passing hippocampi through a Pasteur pipette 10–15 times. Non-dissociated tissue was allowed to collect at the bottom by gravity and clean supernatant with dissociated cells transferred to a new 15 ml centrifuge tube. 1 ml of HBSS at 37 °C was added to the remaining tissue and dissociated again with a flame polished Pasteur pipette to reduce the diameter of the tip 10–15 times. Non-dissociated tissue was allowed to collect at the bottom by gravity. Clean supernatant with dissociated cells was transferred to the same centrifuge tube in which cells from the first dissociation were collected. Neurons were transferred at a density of 24.000 cells/cm^2 to CELLSTAR cell culture dishes (Greiner bio-one) with neuronal plating medium. Neurons were allowed to attach to coverslips for 3 to 4 h in a humidified atmosphere containing 5% CO_2 at 37 °C. Once neurons were settled onto the coverslips, neuronal plating medium was washed with maintenance medium consistent of Neurobasal without L-Glutamine (ThermoFisher Scientific) medium supplemented with B27 (ThermoFisher Scientific), penicillin-streptomycin (25 U/ml) (Gibco) and GlutaMAX (Gibco) and differentiated with the same medium up to 3–4 DIV. Half of the culture medium was exchanged by fresh maintenance medium without penicillin-streptomycin every 3–4 days.

Lipofection. All lipofections were carried out in hippocampal neurons differentiated for 15 DIV. Two or three days prior to lipofection, half of the culture medium was changed for fresh growth medium without penicillin-streptomycin. In order to increase viability, recovery medium was prepared from conditioned medium of neuronal cultures and used after lipofection. Thus, 30–60 min prior to lipofection, half of the conditioned medium of each neuronal culture (1 ml) was removed and collected into a clean culture dish containing 1 ml of fresh growth medium. BrdU (5 µg/ml) and or inhibitors were added to the recovery medium as needed. The recovery medium was then incubated in a humidified atmosphere containing 5% CO_2 at 37 °C for the duration of the lipofection. Neurobasal medium without supplements pre-warmed to 37 °C was added to each of the neuronal cultures. Cultures were returned to the incubator for a minimum of 30 min to stabilize CO_2 levels. To maximize viability, neurons were lipofected in their own culture dish and remaining conditioned medium, which was free of penicillin-streptomycin by 15 DIV. Neurons were transfected with Lipofectamine 2000 (Invitrogen). Lipoplexes were prepared at a ratio of 1 µl of Lipofectamine per 1 µg of DNA. For immunocytochemistry experiments, RFP DNA was always transfected at a 1:20 ratio. Total transfected DNA per culture dish for t1EK2/RFP and LacZ/RFP experiments was 6.4 µg and total transfected DNA per culture dish for t1EK2/p53DN/RFP, LacZ/p53DN/RFP, t1EK2/p53DN/TOP2α/RFP, LacZ/p53DN/TOP2α-RFP experiments was 12.85 µg. For time-lapse experiments, RFP DNA was also transfected at 1:20. Total transfected DNA for t1EK2/p53DN/H2B-EGFP was 10.27 µg and for t1EK2/p53DN/TOP2α/H2B-EGFP it was 12.44 µg. Lipofectamine was mixed with Neurobasal to a final volume of 250 µl per culture dishand left for 3–5 min. Next, plasmid DNA diluted in 250 µl of Neurobasal per culture dish was added and left for 20 min at room temperature. Thereafter, 0.5 ml of the mix was added to each culture dish and left for 90 min. Lipofectamine was then washed out 3 times with 2 ml of growth medium medium pre-warmed to 37 °C. After washout, the recovery medium was added to its corresponding neuronal culture. For cytokinesis experiments, cultures were supplemented with 1xEmbryoMax Nucleosides (Merck)[49].

Immunocytochemistry. Hippocampal cultures were fixed for 15 min with 4% paraformaldehyde (PFA) at RT, and permeabilized for 30 min with phosphate buffered saline (PBS) containing 0.05% Triton X-100 (Sigma-Aldrich) (0.1% for AnkG staining) (PBTx). To detect Lamin B1, a quick wash with methanol (−20 °C) was given after 10 min fixation with 4% PFA, followed by 3 PBS washes and permeabilization with 0.05% PBTx as described above. For BrdU inmunolabeling, DNA was denatured for 30 min at RT with 2 N HCl/0.33× PBS, and then neutralized with three 15-min washes with 0.1 M sodium borate, pH 8.9, and a wash of 5 min with PBTx. Cultures were then incubated for 30 min at RT with PBTx containing 10% FBS to block antibody unspecific binding, followed by a 1-h incubation at RT with PBTx/1% FBS and the appropriate primary antibodies. After 4 washes in PBTx, cultures were incubated for 1 h at RT in PBTx containing 1% FBS and the appropriate secondary antibodies. After 4 additional washes as above, DNA labelling was performed using PBS containg 100 ng/ml 4′,6-diamidino-2-phenylindole (DAPI) (Sigma-Aldrich) and the preparations were mounted in glycerol (Panreac)/PBS (1:1).

Image analysis and cell counting studies. For BrdU incorporation time-course experiments, the proportion of BrdU positive neurons out of all MAP2 positive transfected neurons of 10-mm diameter coverslips (Menzel Glässer) was calculated in 3 independent experiments. To assess apoptosis, the proportion of active Caspase-3[40] positive neurons of all MAP2 positive transfected neurons was calculated in each of 3 independent experiments. DNA damage was assessed with Phospho-Ser139 Histone H2AX (γ-H2AX)[51]. The proportion of neurons with more than 5 γ-H2AX foci or γ-H2AX pan-nuclear staining out of all MAP2 positive transfected neurons was calculated in each of 3 independent experiments. Phospho-Ser10 Histone H3 (pH3) immunostaining was used to assess late G2 and M-phase entry[46], wherein the proportion of neurons positive for foci (late G2) or pan-nuclear (M-phase) staining out of all MAP2 positive transfected neurons was calculated in each of 3 independent experiments in each treatment condition. Cell counting in BrdU, active Caspase-3, pH3 and γ-H2AX experiments was done with 20x (Zoom, 1.5) or 40x objectives with AF 6500–7000 fluorescence microscope (Leica) and a DU8285 VP-4324 camera (Andor). Confocal microscope images were acquired with 40x or 63x objectives using upright or inverted TCS SP5 confocal microscopes (Leica). For three-dimensional (3D) image reconstructions, images were taken with a 63x objective with 1.7- to 3.6-times zoom, in 50 to 69 z-stacks of 0.13 to 0.25 µm step-sizes. 3D reconstructions and rotating 3D videos were generated using Icy bioimage informatics platform[77].

Live imaging of neuronal cell cycle. Neurons were cultured as described above in µ-Dish 35 mm, high Grid-500 cell culture dishes with ibidi polymer coverslip bottom (Ibidi) coated with 0.5 mg/ml polyornithine (Sigma-Aldrich). Live neuronal imaging was performed in a sealed chamber at 37 °C and 5% CO_2 with 20x objective of an AF 6500–7000 fluorescence microscope and recorded with DU8285 VP-4324 camera. Pictures and videos were generated using Leica Application Suite X (Leica). Time intervals between pictures and experiments duration are described in each video. For cell counting studies of anaphase and cytokinesis, neurons were identified by morphological criteria based on RFP signal. When in doubt, cells were either not included in the quantification or neuronal identity confirmed by MAP2 immunostaining and included in the quantification. Binucleated neurons were not quantified. Neurons that presented obvious signs of cell death during the first hour of recording were not included in the quantification. Chromosome segregation during anaphase was identified by H2B-GFP[74] and cleavage furrow ingression by RFP.

Measurement of the AIS. AnkyrinG (AnkG) was used to evaluate changes in the AIS of neurons at different stages of the cell cycle. All groups were treated with Wee1 inhibitor MK1775[56] (900 nM) to abrogate the G2 checkpoint and with the Mps1 inhibitor AZ3146[65] (10 µM) 2.5 h later to abrogate the SAC. Neurons in the interphase, prophase and prometaphase to telophase groups were fixed 3 h after G2 checkpoint abrogation. Stages in between prometaphase and telophase could not be reliably distinguished by nuclear morphology and were thus grouped together. Multinucleated neurons were used to assess premature M-phase exit and were fixed 6 and 9 h after G2 checkpoint abrogation. Multinucleated neurons still presenting mitotic chromatin condensation or evidence of pyknosis were not included in the quantification. Neurons in all of the aforementioned groups co-expressed t1EK2/p53DN/TOP2α/RFP. Control neurons expressing LacZ/p53DN/TOP2α/RFP were fixed 9 h after G2 checkpoint abrogation. Images were acquired on an upright Leica SP5 confocal microscope with a 63× objective, 1024 × 1024 pixels in z stacks with 0.5-µm steps and a Z-projection was obtained. Measurements of AnkG fluorescence intensity were performed by Fiji-ImageJ software. We drew a line starting at the limit of neuronal soma identified by MAP2 staining, and extended it along the AnkG staining or the RFP signal of the axon. Data were obtained after background subtraction. Then, data were smoothed every 1 µm using Sigma Plot 12.5 software. AIS start and end positions were obtained following the criteria described previously[78]. Then total fluorescence intensity for each AIS was obtained. Total fluorescent intensity was then divided by the length of the AIS to obtain the mean AnkG fluorescence per 1 µm (AnkG/µm). To avoid variability between cell cultures and treatment exposure times, we normalized the mean AnkG/µm of transfected neurons to the nearest neighboring non-transfected neurons in the same image.

Statistical Analysis. Statistical analysis was performed using SPSS (version 24.0). Statistical analysis of BrdU time-course experiments of pH3 experiments were done with one-sample *t* test against 0 because control neurons never incorporated BrdU or were positive for pH3 ($\alpha = 0.05$, one-tailed). For BrdU time-course experiments, the mean percent BrdU incorporation of the treatment group was compared to 0 in each time-point. Analysis of active-caspase-3 and γ-H2AX experiments were done with Fisher's exact test ($\alpha = 0.05$, two-tailed). For AnkG/µm in AIS experiments, outliers were identified by boxplots. Normality was assessed with Shapiro-Wilk test of normality and Normal Q-Q Plots. Homogeneity of variances with Levene's test for equality of variances. Omnibus testing was performed with Welch's F test and post-hoc multiple comparisons with the Games-Howell method ($\alpha = 0.05$, two-tailed). Quantitative data are expressed as mean ± standard error of the mean (s.e.m.). Significance was $p < 0.05$ (*), $p < 0.01$ (**), and $p < 0.001$ (***).

Data Availability

The datasets generated during and/or analyzed during the current study are available from the corresponding author on reasonable request.

References

1. Anda, F. C. *et al*. Cortical neurons gradually attain a post-mitotic state. *Cell Res.* **26**, 1033–1047 (2016).
2. Chen, D. *et al*. Cell-specific effects of RB or RB/p107 loss on retinal development implicate an intrinsically death-resistant cell-of-origin in retinoblastoma. *Cancer Cell* **5**, 539–551 (2004).
3. Ferguson, K. L. *et al*. Telencephalon-specific Rb knockouts reveal enhanced neurogenesis, survival and abnormal cortical development. *EMBO J.* **21**, 3337–3346 (2002).
4. Ray, J., Peterson, D. A., Schinstine, M. & Gage, F. H. Proliferation, differentiation, and long-term culture of primary hippocampal neurons. *Proc. Natl. Acad. Sci. USA* **90**, 3602–3606 (1993).
5. Xu, X. L. *et al*. Rb suppresses human cone-precursor-derived retinoblastoma tumours. *Nature* **514**, 385–388 (2014).
6. Zindy, F. *et al*. Postnatal neuronal proliferation in mice lacking Ink4d and Kip1 inhibitors of cyclin-dependent kinases. *Proc. Natl. Acad. Sci. USA* **96**, 13462–13467 (1999).
7. Ajioka, I. *et al*. Differentiated horizontal interneurons clonally expand to form metastatic retinoblastoma in mice. *Cell* **131**, 378–390 (2007).
8. Oshikawa, M., Okada, K., Nakajima, K. & Ajioka, I. Cortical excitatory neurons become protected from cell division during neurogenesis in an Rb family-dependent manner. *Development* **140**, 2310–2320 (2013).
9. Oshikawa, M., Okada, K., Tabata, H., Nagata, K. I. & Ajioka, I. Dnmt1-dependent Chk1 pathway suppression is protective against neuron division. *Development* **144**, 3303–3314 (2017).
10. Friedmann-Morvinski, D. *et al*. Dedifferentiation of neurons and astrocytes by oncogenes can induce gliomas in mice. *Science* **338**, 1080–1084 (2012).
11. Al-Ubaidi, M. R., Hollyfield, J. G., Overbeek, P. A. & Baehr, W. Photoreceptor degeneration induced by the expression of simian virus 40 large tumor antigen in the retina of transgenic mice. *Proc. Natl. Acad. Sci. USA* **89**, 1194–1198 (1992).
12. Feddersen, R. M., Ehlenfeldt, R., Yunis, W. S., Clark, H. B. & Orr, H. T. Disrupted cerebellar cortical development and progressive degeneration of Purkinje cells in SV40 T antigen transgenic mice. *Neuron* **9**, 955–966 (1992).
13. Kuan, C. Y. *et al*. Hypoxia-ischemia induces DNA synthesis without cell proliferation in dying neurons in adult rodent brain. *J. Neurosci.* **24**, 10763–10772 (2004).

14. Verdaguer, E. *et al*. Kainic acid-induced apoptosis in cerebellar granule neurons: an attempt at cell cycle re-entry. *Neuroreport* **13**, 413–416 (2002).
15. Frade, J. M. & Ovejero-Benito, M. C. Neuronal cell cycle: the neuron itself and its circumstances. *Cell Cycle* **14**, 712–720 (2015).
16. Herrup, K. & Yang, Y. Cell cycle regulation in the postmitotic neuron: oxymoron or new biology? *Nat. Rev. Neurosci.* **8**, 368–378 (2007).
17. Greene, L. A., Liu, D. X., Troy, C. M. & Biswas, S. C. Cell cycle molecules define a pathway required for neuron death in development and disease. *Biochim. Biophys. Acta.* **1772**, 392–401 (2007).
18. Halazonetis, T. D., Gorgoulis, V. G. & Bartek, J. An oncogene-induced DNA damage model for cancer development. *Science* **319**, 1352–1355 (2008).
19. Manic, G., Obrist, F., Sistigu, A. & Vitale, I. Trial watch: targeting ATM–CHK2 and ATR–CHK1 pathways for anticancer therapy. *Mol. Cell. Oncol.* **2**, e1012976 (2015).
20. Musacchio, A. & Salmon, E. D. The spindle-assembly checkpoint in space and time. *Nat. Rev. Mol. Cell Biol.* **8**, 379–393 (2007).
21. Vitale, I., Galluzzi, L., Castedo, M. & Kroemer, G. Mitotic catastrophe: a mechanism for avoiding genomic instability. *Nat. Rev. Mol. Cell Biol.* **12**, 385–392 (2011).
22. Lan, W. & Cleveland, D. W. A chemical tool box defines mitotic and interphase roles for Mps1 kinase. *J. Cell Biol.* **190**, 21–24 (2010).
23. Porter, D. C. *et al*. Tumor-specific proteolytic processing of cyclin E generates hyperactive lower-molecular-weight forms. *Mol. Cell. Biol.* **21**, 6254–6269 (2001).
24. Jahn, S. C. *et al*. Assembly, activation, and substrate specificity of cyclin D1/Cdk2 complexes. *Biochemistry* **52**, 3489–3501 (2013).
25. Teixeira, L. K. & Reed, S. I. Cyclin E Deregulation and Genomic Instability. *Adv. Exp. Med. Biol.* **1042**, 527–547 (2017).
26. Geng, Y. *et al*. Cyclin E ablation in the mouse. *Cell* **114**, 431–443 (2003).
27. Odajima, J. *et al*. Cyclin E constrains Cdk5 activity to regulate synaptic plasticity and memory formation. *Dev. Cell* **21**, 655–668 (2011).
28. Copani, A. *et al*. Mitotic signaling by β-amyloid causes neuronal death. *FASEB J.* **13**, 2225–2234 (1999).
29. Staropoli, J. F. *et al*. Parkin is a component of an SCF-like ubiquitin ligase complex and protects postmitotic neurons from kainate excitotoxicity. *Neuron* **37**, 735–749 (2003).
30. Schwartz, E. I. *et al*. Cell cycle activation in postmitotic neurons is essential for DNA repair. *Cell Cycle* **6**, 318–329 (2007).
31. Harbison, R. A. *et al*. Calpain plays a central role in 1-methyl-4-phenylpyridinium (MPP+)-induced neurotoxicity in cerebellar granule neurons. *Neurotox. Res.* **19**, 374–388 (2011).
32. Absalon, S., Kochanek, D. M., Raghavan, V. & Krichevsky, A. M. MiR-26b, upregulated in Alzheimer's disease, activates cell cycle entry, tau-phosphorylation, and apoptosis in postmitotic neurons. *J. Neurosci.* **33**, 14645–14659 (2013).
33. Veas-Pérez de Tudela, M., Maestre, C., Delgado-Esteban, M., Bolaños, J. P. & Almeida, A. Cdk5-mediated inhibition of APC/C-Cdh1 switches on the cyclin D1-Cdk4-pRb pathway causing aberrant S-phase entry of postmitotic neurons. *Sci. Rep.* **5**, 18180 (2015).
34. Lee, K. H. *et al*. Amyloid β1-42 (Aβ1-42) induces the CDK2-mediated phosphorylation of Tau through the activation of the mTORC1 signaling pathway while promoting neuronal cell death. *Front. Mol. Neurosci.* **10**, 229 (2017).
35. Hoozemans, J. J. *et al*. Cyclin D1 and cyclin E are co-localized with cyclo-oxygenase 2 (COX-2) in pyramidal neurons in Alzheimer disease temporal cortex. *J. Neuropathol. Exp. Neurol.* **61**, 678–688 (2002).
36. Nagy, Z., Esiri, M. M., Cato, A. M. & Smith, A. D. Cell cycle markers in the hippocampus in Alzheimer's disease. *Acta Neuropathol.* **94**, 6–15 (1997).
37. Su, S. C. & Tsai, L. H. Cyclin-dependent kinases in brain development and disease. *Annu. Rev. Cell Dev. Biol.* **27**, 465–491 (2011).
38. Chin, L. S., Li, L., Ferreira, A., Kosik, K. S. & Greengard, P. Impairment of axonal development and of synaptogenesis in hippocampal neurons of synapsin I-deficient mice. *Proc. Natl. Acad. Sci. USA* **92**, 9230–9234 (1995).
39. Sala, C. *et al*. Inhibition of dendritic spine morphogenesis and synaptic transmission by activity-inducible protein Homer1a. *J. Neurosci.* **23**, 6327–6337 (2003).
40. Mazumder, S., Plesca, D. & Almasan, A. Caspase-3 activation is a critical determinant of genotoxic stress-induced apoptosis. *Methods Mol. Biol.* **414**, 13–21 (2008).
41. Minella, A. C. *et al*. p53 and p21 form an inducible barrier that protects cells against cyclin E-cdk2 deregulation. *Curr. Biol.* **12**, 1817–1827 (2002).
42. Irwin, M. *et al*. Role for the p53 homologue p73 in E2F-1-induced apoptosis. *Nature* **407**, 645–648 (2000).
43. Hendzel, M. J. *et al*. Mitosis-specific phosphorylation of histone H3 initiates primarily within pericentromeric heterochromatin during G2 and spreads in an ordered fashion coincident with mitotic chromosome condensation. *Chromosoma* **106**, 348–360 (1997).
44. Vassilev, L. T. *et al*. Selective small-molecule inhibitor reveals critical mitotic functions of human CDK1. *Proc. Natl. Acad. Sci. USA* **103**, 10660–10665 (2006).
45. Juan, G. *et al*. Histone H3 phosphorylation and expression of cyclins A and B1 measured in individual cells during their progression through G2 and mitosis. *Cytometry* **32**, 71–77 (1998).
46. Brito, D. A. & Rieder, C. L. Mitotic checkpoint slippage in humans occurs via cyclin B destruction in the presence of an active checkpoint. *Curr. Biol.* **16**, 1194–1200 (2006).
47. Bartkova, J. *et al*. DNA damage response as a candidate anti-cancer barrier in early human tumorigenesis. *Nature* **434**, 864–870 (2005).
48. Bester, A. C. *et al*. Nucleotide deficiency promotes genomic instability in early stages of cancer development. *Cell* **145**, 435–446 (2011).
49. Jones, R. M. *et al*. Increased replication initiation and conflicts with transcription underlie Cyclin E-induced replication stress. *Oncogene* **32**, 3744–3753 (2013).
50. Neelsen, K. J., Zanini, I. M., Herrador, R. & Lopes, M. Oncogenes induce genotoxic stress by mitotic processing of unusual replication intermediates. *J. Cell Biol.* **200**, 699–708 (2013).
51. Kinner, A., Wu, W., Staudt, C. & Iliakis, G. γ-H2AX in recognition and signaling of DNA double-strand breaks in the context of chromatin. *Nucl. Acids Res.* **36**, 5678–5694 (2008).
52. McGowan, C. H. & Russell, P. Human Wee1 kinase inhibits cell division by phosphorylating p34cdc2 exclusively on Tyr 15. *EMBO J.* **12**, 75–85 (1993).
53. Schmetsdorf, S., Gärtner, U. & Arendt, T. Expression of cell cycle-related proteins in developing and adult mouse hippocampus. *Int. J. Dev. Neurosci.* **23**, 101–112 (2005).
54. Schmetsdorf, S., Gärtner, U. & Arendt, T. Constitutive expression of functionally active cyclin-dependent kinases and their binding partners suggests noncanonical functions of cell cycle regulators in differentiated neurons. *Cereb. Cortex.* **17**, 1821–1829 (2007).
55. Frank, C. L. & Tsai, L. H. Alternative functions of core cell cycle regulators in neuronal migration, neuronal maturation, and synaptic plasticity. *Neuron* **62**, 312–326 (2009).
56. Hirai, H. *et al*. Small-molecule inhibition of Wee1 kinase by MK-1775 selectively sensitizes p53-deficient tumor cells to DNA-damaging agents. *Mol. Cancer Ther.* **8**, 2992–3000 (2009).
57. Lin, F. & Worman, H. J. Structural organization of the human gene (LMNB1) encoding nuclear lamin B1. *Genomics* **27**, 230–236 (1995).

58. Panorchan, P., Schafer, B. W., Wirtz, D. & Tseng, Y. Nuclear envelope breakdown requires overcoming the mechanical integrity of the nuclear lamina. *J. Biol. Chem.* **279**, 43462–43467 (2004).
59. Piekny, A. J. & Maddox, A. S. The myriad roles of Anillin during cytokinesis. *Semin. Cell Dev. Biol.* **21**, 881–891 (2010).
60. Oegema, K., Savoian, M. S., Mitchison, T. J. & Field, C. M. Functional analysis of a human homologue of the Drosophila actin binding protein anillin suggests a role in cytokinesis. *J. Cell Biol.* **150**, 539–552 (2000).
61. Baas, P. W. & Black, M. M. Compartmentation of alpha-tubulin in neurons: identification of a somatodendritic-specific variant of alpha-tubulin. *Neuroscience* **30**, 795–803 (1989).
62. Song, Y. & Brady, S. T. Post-translational modifications of tubulin: pathways to functional diversity of microtubules. *Trends Cell Biol.* **25**, 125–136 (2015).
63. Sarkaria, J. N. *et al*. Inhibition of ATM and ATR kinase activities by the radiosensitizing agent, caffeine. *Cancer Res.* **59**, 4375–4382 (1999).
64. Chen, T., Sun, Y., Ji, P., Kopetz, S. & Zhang, W. Topoisomerase IIα in chromosome instability and personalized cancer therapy. *Oncogene* **34**, 4019–4031 (2015).
65. Hewitt, L. *et al*. Sustained Mps1 activity is required in mitosis to recruit O-Mad2 to the Mad1–C-Mad2 core complex. *J. Cell Biol.* **190**, 25–34 (2010).
66. Rasband, M. N. The axon initial segment and the maintenance of neuronal polarity. *Nat. Rev. Neurosci.* **11**, 552–562 (2010).
67. Schafer, D. P. *et al*. Disruption of the axon initial segment cytoskeleton is a new mechanism for neuronal injury. *J. Neurosci.* **29**, 13242–13254 (2009).
68. Del Puerto, A. *et al*. ATP-P2X7 receptor modulates axon initial segment composition and function in physiological conditions and brain injury. *Cereb. Cortex* **25**, 2282–2294 (2015).
69. Zhu, X. *et al*. Neuronal binucleation in Alzheimer disease hippocampus. *Neuropathol. Appl. Neurobiol.* **34**, 457–465 (2008).
70. Campisi, J. Aging, cellular senescence, and cancer. *Annu. Rev. Physiol.* **75**, 685–705 (2013).
71. Walton, C. C. & Andersen, J. K. Unknown fates of (brain) oxidation or UFO: close encounters with neuronal senescence. *Free. Radic. Biol. Med*. https://doi.org/10.1016/J.FREERADBIOMED.2019.01.012 (2019). In press.
72. Arendt, T., Brückner, M. K., Mosch, B. & Lösche, A. Selective cell death of hyperploid neurons in Alzheimer's disease. *Am. J. Pathol.* **177**, 15–20 (2010).
73. Das, R. M. *et al*. A robust system for RNA interference in the chicken using a modified microRNA operon. *Dev. Biol.* **294**, 554–563 (2006).
74. Kanda, T., Sullivan, K. F. & Wahl, G. M. Histone–GFP fusion protein enables sensitive analysis of chromosome dynamics in living mammalian cells. *Curr. Biol.* **8**, 377–385 (1998).
75. Wu, K. Z. *et al*. DDK dependent regulation of TOP2A at centromeres revealed by a chemical genetics approach. *Nucleic Acids Res.* **44**, 8786–8798 (2016).
76. Kaufman, M. H. The atlas of mouse development. London: Academic press (1992).
77. de Chaumont, F. *et al*. Icy: an open bioimage informatics platform for extended reproducible research. *Nat. Methods* **9**, 690–696 (2012).
78. Grubb, M. S. & Burrone, J. Activity-dependent relocation of the axon initial segment fine-tunes neuronal excitability. *Nature* **465**, 1070–1074 (2010).

Acknowledgements

We thank Stuart Wilson, William Kaelin, Geoff Wahl, and Corrado Santocanale for the plasmids used in this study, and S. Casas-Tintó, and F. Wandosell for the critical reading of the manuscript. We also thank the Department of Statistics of SGAI-CSIC. This study was supported by Ministerio de Economía y Competitividad grant SAF2015-68488-R (J.M.F.), SAF2015-65315-R (J.J.G.), and Ministerio de Educación, Cultura y Deporte grant FPU1305084 (C.C.W.).

Author Contributions

C.C.W., J.M.F. and J.J.G. conceived the study, C.C.W. performed the experiments and analyzed data, W.Z. analyzed data, I.P.-P. analyzed data, E.B.-A. provided expertise and feedback, C.C.W. and J.M.F. wrote the manuscript.

Additional Information

Supplementary information accompanies this paper at https://doi.org/10.1038/s41598-019-40462-4.

Competing Interests: The authors declare no competing interests.

Publisher's note: Springer Nature remains neutral with regard to jurisdictional claims in published maps and institutional affiliations.